UNIVERSITÁ DEGLI STUDI DELLA TUSCIA

Department of Economics, Engineering, Society and Business Organization

PhD Program in
Engineering for Energy and Environment
Curriculum Energy and Engineering Systems
XXXVI Cycle

Valorization of biomass wastes from different industrial supply chains through HTC process to produce value-added products based on a circular economy approach

S.S.D. ING/IND 11

PhD Candidate
Dott. Alessandro Cardarelli

PhD Coordinator
Prof. Andrea Luigi Facci

Supervisors
Prof. Marco Barbanera
Prof. Giuseppe Calabrò

Academic Year 2023-2024

« Macte nova virtute, sic itur ad astra »
Virgilio (Aen. IX, 641)

Abstract

In light of the pressing issues of resource depletion and waste accumulation, it becomes imperative to embrace inventive strategies that align with the fundamental principles of a circular economy. By embracing a circular economy and adopting a waste-to-resource approach, we have the potential to minimize resource extraction, waste generation, and our carbon footprint. An area of great untapped potential lies in the biomass wastes produced across diverse industrial supply chains. This work presents the findings of a comprehensive research project focused on exploring the valuable and sustainable application of hydrochar in various sectors, including energy, industrial, and building. The primary objective of this study was to demonstrate the potential benefits of hydrochar utilization, and the effectiveness of the hydrothermal carbonization conversion process, with an emphasis on valorizing the use of biomass waste, promoting a circular economy and a waste-to-resource approach, and encouraging sustainable development in industries, as well as identifying areas for improvement. Via a combination of experimental investigations, data analysis, and case studies, this research project highlights the significant advantages of incorporating hydrochar derived from winemaking industry residues and municipal solid waste management into different applications. Through the optimization of the hydrothermal carbonization process and a thorough kinetic analysis, the study showcases how hydrochar, from the winemaking industry residues, is a valuable carbon-rich material that can be utilized as a renewable energy source contributing to the transition towards a more sustainable energy landscape. Furthermore, the thesis examines the industrial applications of hydrochar, revealing its potential as a valuable resource in the electric arc furnace steelmaking industry. With the support of computational fluid dynamics and life cycle assessment analysis was recognized that by substituting fossil-based carbonaceous materials with hydrochar-based alternatives, industries can reduce their reliance on non-renewable resources, minimize environmental impact, and enhance overall sustainability. Moreover, to provide a sustainable solution to the challenges associated with municipal solid waste management, hydrothermal carbonization process conditions were deeply investigated to obtain hydrochar with enhanced properties to be used as an admixture for the production of a sustainable plaster as carbon-capture, thermal insulation, moisture absorption, and acoustic insulation material. As a result, insights were provided into its suitability and potential for improving sustainable building practices. The outcomes of this research work shed light on the multifaceted benefits of hydrochar utilization, demonstrating its capacity to address pressing environmental challenges and contribute to a more sustainable future. The findings provide valuable insights for policymakers, industries, and researchers, paving the way for the widespread adoption and further advancement of hydrochar applications across different fields.

Table of contents

Chapter 1

Introduction

1.1 Motivation

Among the main challenges for society today, climate change and the sustainable and responsible use of natural resources are on top of the political environmental agenda. Governments, organizations, and individuals are increasingly recognizing the importance of adopting sustainable practices and supporting research initiatives that drive innovation in renewable energy, resource efficiency, and waste management. As we face the challenges of resource depletion and waste accumulation, it is crucial to explore innovative approaches that align with the principles of a circular economy. By adopting a circular economy and a waste-to-resource approach, resource extraction, waste generation, and our carbon footprint might be minimized. Biomass wastes generated from various industrial supply chains represent a significant untapped resource. By harnessing thermo-chemical processes, we have the opportunity to transform these wastes into valuable products, thereby contributing to the development of a sustainable and circular bioeconomy. Through comprehensive research and analysis, the potential of biomass waste valorization may be unlocked, identifying efficient and economically viable pathways to convert these wastes into value-added products such as biofuels, biochemicals, and biopolymers. This research endeavor holds tremendous promise in not only reducing waste and environmental impact but also creating new economic opportunities and fostering a more sustainable future for industries and communities alike. By shifting towards renewable and bio-based alternatives, the reliance on fossil fuels can be reduced, mitigating environmental pollution, and promoting a more equitable and resilient society. In this context, research on the valorization of biomass wastes through thermo-chemical processes contributes to the broader objectives of climate change mitigation and sustainable resource management.
In light of what is aforementioned, the scope of this research is to explore alternative approaches for treating biomass wastes, intending to enhance the attractiveness of hydrochar. Hopefully, the insights gained from the findings of this research may have the potential to contribute towards a more sustainable transition.

1.2 Objectives

Overall, this thesis on the valorization of biomass wastes through thermochemical processes for value-added product production in a circular economy ap-

proach contributes to the field of sustainable waste management and resource utilization. A conceptual layout of the proposed research line is presented in ***Figure 1.1***.

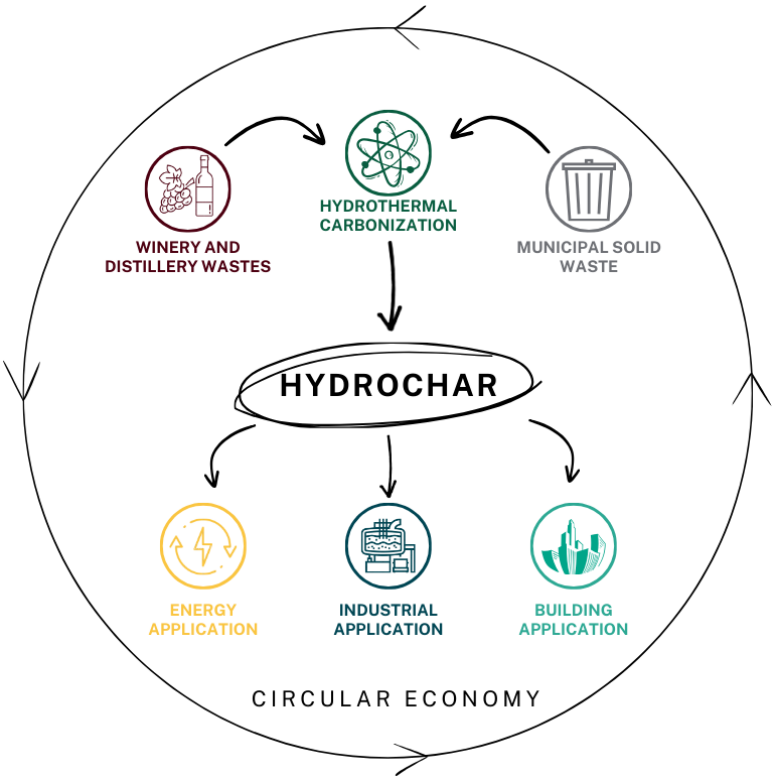

Figure 1.1: *Conceptual layout of the proposed research line, which is the main focus of the present thesis work.*

The research aims to provide practical insights, innovative solutions, and a comprehensive understanding of the environmental implications of biomass waste valorization. By promoting a circular economy approach, the study seeks to pave the way for a more sustainable and resource-efficient future. By adopting circularity, the aim is to create a closed-loop system where biomass wastes are diverted from traditional disposal practices and instead transformed into valuable outputs through thermo-chemical processes.
Besides, the environmental benefits and potential trade-offs associated with the production of hydrochar through the hydrothermal carbonization (HTC) of biomass residue from the winemaking industry and municipal solid waste were examined. Critical HTC parameters, physical-chemical characteristics of products, deep understanding of hydrochar formation mechanisms, process improvement, and potential hydrochar applications have been thoroughly assessed. Moreover, a comprehensive assessment of the environmental impact of the production, usage, and application of hydrochar as a substitute for fossil coal in the steelmaking industry was provided.

The main outcomes of this research project aim to demonstrate the valuable and sustainable application of hydrochar in several fields, energy, industrial, and building. This approach maximizes the utilization of biomass resources, minimizes waste generation, contributes to the sustainable development of industries, and provides insights into potential areas for improvement.

1.3 Thesis structure

This section provides a comprehensive overview of the organization and framework of this PhD thesis. A visual representation of the thesis structure based on the research Papers elaborated to demonstrate the potential, and sustainable application of hydrochar in the energy, industrial, and building sectors is displayed in ***Figure 1.2***.

The structure of the thesis is planned as follows:

⇒ A brief introduction on motivations, research objectives and structure of the thesis is provided in ***Chapter 1***.

⇒ In ***Chapter 2***, an overview necessary to thoroughly understand the developed research scope is provided. In detail, it clarifies the environmental burdens and the concerns of biomass waste management, prioritizing the valorization of winemaking industry residues and municipal solid waste. The chapter continues by introducing the thermochemical processes as effective solutions to valorize biomass wastes, focusing on hydrothermal carbonization. Finally, explains the wide potential application of hydrochar across different fields and the aim of this work to utilize it in the energy, industrial, and building sectors.

⇒ Once an explanation and discussion of the research project was provided, the materials and methods employed in the experimental work are presented in ***Chapter 3***.

⇒ ***Chapter 4*** introduces the readers to the utilization of agricultural residues and by-products for sustainable energy production and waste management. In detail, the research Paper A on the HTC of winery and distillery by-products provides crucial insights into the most suitable HTC process conditions to obtain high-quality hydrochar. Afterward, the chapter delves into the research Paper B by examining the pyrolysis and combustion kinetics of the hydrochar produced under the optimized HTC conditions obtained in Paper A. The chapter ends by describing the research activities carried out during the months spent as a Visiting PhD Fellow at the Universidad de Córdoba, Spain.

⇒ Following, ***Chapter 5*** extends the research work by exploring the applicability of hydrochar in the industrial sector. It begins by describing the research Paper C focused on the computational fluid dynamic analysis of the possible use of different biochars as substitutes for fossil coal in the electrical arc furnace steelmaking process. Next, the chapter looks into Paper D which presents a a comprehensive assessment of the environmental impacts associated with the production of steel using electric arc furnaces, wherein pulverized hydrochar is utilized as a substitute for fossil coal, both as a charged and injected material.

⇒ ***Chapter 6*** delves into the application of hydrochar in the building sector and emphasizes how hydrochar from HTC can provide a sustainable solution

to the challenges associated with municipal solid waste management (Paper E).

⇒ The overall conclusions, challenges, and perspectives that can be drawn from this thesis are then presented in ***Chapter 7***.

⇒ The thesis concludes with the appendices.

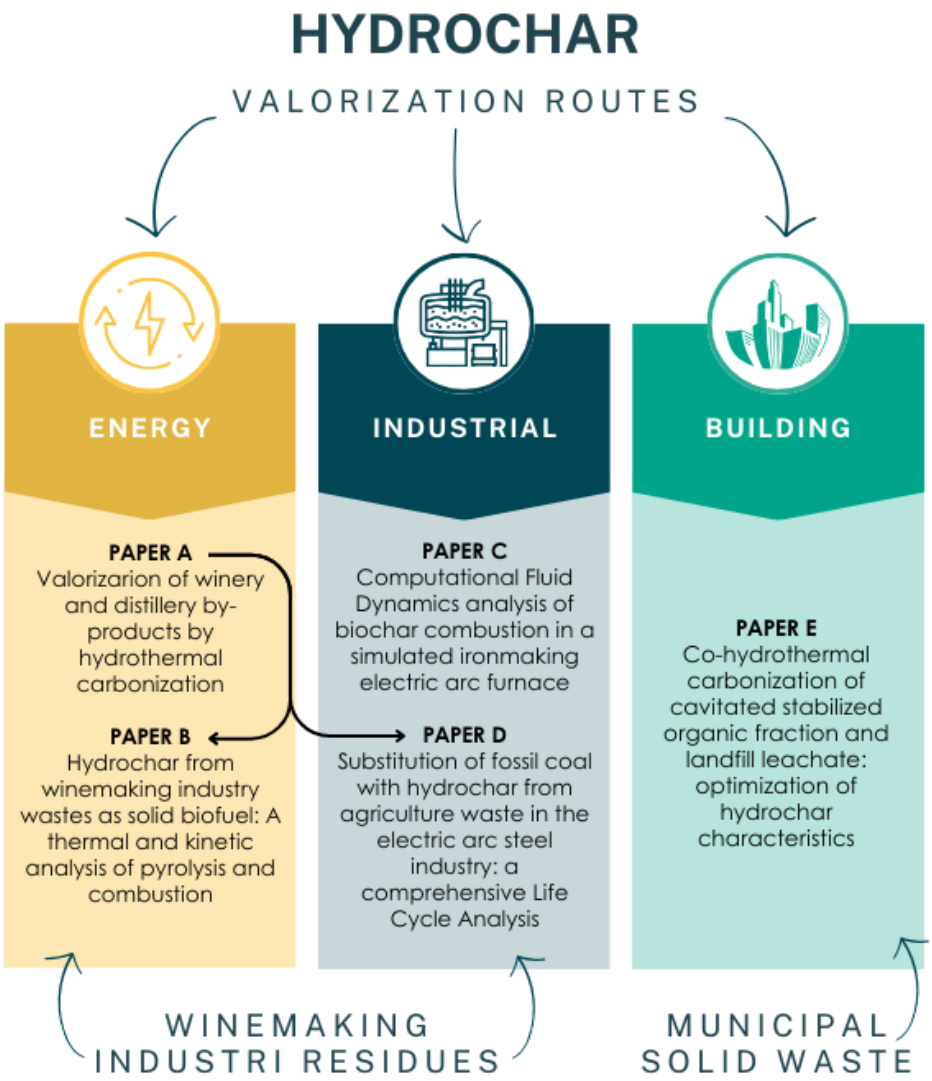

Figure 1.2: *Visual representation of the research papers in relation to the main hydrochar application fields.*

Chapter 2

Overview

2.1 Biomass waste management

Carbon is one of the most widespread and versatile elements in nature and is responsible for our existence. Humans have been using carbon since the beginning of our civilization. There are millions of known carbon compounds and many thousands of these are essential for vital processes and important for organic-based reactions. With the development of modern technology and the need for better-performing materials, a larger number of new carbon materials with well-defined nanostructures have been synthesized by various physical and chemical processes [1]. Despite its widespread and natural occurrence on Earth, carbon has been mainly synthesized from fossil-based precursors with sophisticated and energy-consuming methodologies, consequently generating greenhouse gasses (GHG) and toxic chemicals. The requirements of an evolving sustainable society are encouraging and developing awareness among the materials science community for a need to introduce, improve, and develop novel technology in the most eco-friendly, resource-efficient manner possible. In particular, the progress of innovative carbon materials from renewable resources is a quickly recognized area. The production of low-cost and environmentally friendly high-performing carbon materials is crucial for a sustainable future. Carbon has been created from biomass from the very beginning, throughout the natural process of coal formation. Nature has been the ancestor of carbon production from biomass and we only need to translate it into a synthetic process.

It is considered biomass every organic substance deriving directly or indirectly from the photosynthesis process. Biomass is a carbon-neutral resource because CO_2 released through its combustion and utilization processes does not lead to an increase in atmospheric carbon dioxide as it is of biogenic origin. Biomass originates from many different sources, generally as a main product or by-product and residue from agriculture, forestry, and organic waste [2], as displayed in ***Figure 2.1***.
Annually, the total sources of biomass in the EU-27 are estimated for approximately 1 billion tonnes of dry matter (tdm), of which 46% are unexploited residue derived from agriculture (120 Mtdm), forestry (195 Mtdm), and organic waste (147 Mtdm) [3]. Significant quantities of these residues are often disposed of improperly, burned, dumped, or unplan landfilled, resulting in environmental pollution and public health problems.

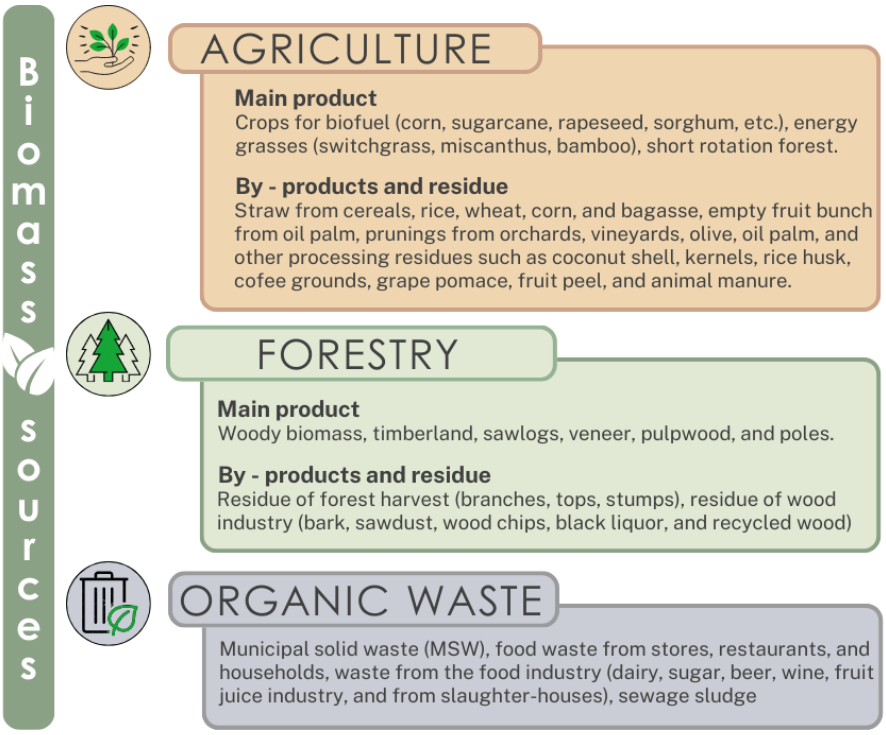

Figure 2.1: *Different types of biomass source.*

Therefore, biomass waste management must be given due consideration to ensure the proper generation, collection, transfer, and disposal. Waste management is an expanding sector in the global environmental industry. When evaluating different biomass waste management industrial supply chains, a careful analysis has to be conducted to identify the most suitable waste streams for valorization. In this sense, various factors should be considered, such as their abundance, the presence of valuable components, the need to address waste management challenges, and the environmental impact of their disposal.

In this research work, prioritizing the valorization of winemaking industry residues and municipal solid waste was a strategic decision driven by the recognition of their significant potential for resource recovery, environmental sustainability, and the promotion of a circular economy.

2.1.1 Winemaking industry waste

The winemaking industry produces a huge amount of waste, both in the form of liquid and solid materials, the management of which causes economic and environmental problems. This waste, with no economic value, is produced by viticulture, wine industry, and alcohol distillery activities. Their inadequate management or disposal can cause environmental burdens [4].
Viticulture generates vine pruning (VP), which is the main solid by-product of the in-field interventions. Typically vine pruning is left or open-burned in the agricultural fields with significant emissions of pollutants, in both gas and particulate phases [5]. Besides, the wine industry is responsible for the production of fresh grape marc biomass, mainly constituted by grape skins, seeds, pulp, and stalks obtained from grape pressing after wine production [6]. In Europe, according to the European Council Regulation (EC) 491/2009, grape marc biomass

should be sent to alcohol distilleries to recover ethanol, tartrates, and produce spirit liquors [7]. However, this process produces two other flow wastes, a solid fraction, the exhausted grape marc (EGM), and a liquid stream, vinasse, whose disposal and recycling represent a serious environmental problem. A large fraction of EGM is simply disposed of and then dumped or settled in ponds constituting a relevant environmental burden due to its high organic carbon content (31–54%) [8]. EGM is also employed as compost or animal feed, or simply discarded as natural waste in landfills. Recent studies have demonstrated that EGM can be fruitfully employed to extract high-added polyphenols, contributing to the development of the bioeconomy in the wine industry [9]. Grape phenolic compounds are of great interest for use as antioxidants, antimicrobials, and enzyme modulators [10]. Moreover, the inadequate disposal of vinasse can cause salinization, sodification, and acidification of soil, due to its low pH, high biochemical oxygen demand (BOD), high chemical oxygen demand (COD), and high solid content [11].
Italy is one of the major wine producers with an area dedicated to vine cultivation of 657700 hectares in 2018 [12]. The wine industry produces approximately 3.0 t/ha of vine pruning, with an average moisture content of 45%, and about 2.7 t/ha of fresh grape marc, with a moisture content of 60% [13, 14]. Considering also that about 10–15 L of vinasse are obtained per 1 L of ethanol produced [15], the efficient disposal of winery waste is a serious problem from an economic and environmental point of view.
However, the main drawback to the recovery of winery and distillery waste is their high moisture content which leads to an increase in transport costs and consumption of energy needed for drying before use. In this context, the hydrothermal carbonization (HTC) process could be a valuable and profitable option to valorize the winery and distillery waste. Only a few studies on hydrothermal carbonization of waste from the winemaking industry are available in the literature. Basso et al. [16] conducted several HTC tests at different temperatures and residence times on fresh grape marc, obtaining an increase of higher heating value (HHV) of the hydrochar from 43% to 54%, at 250°C depending on residence time. Basso et al. Also, the behavior of grape marc constituents (seeds, skins) during HTC at several process conditions (temperature: 180, 220, and 250 °C; reaction time: 0.5, 1, 3, and 8 h) was analyzed [17]. Duman et al. [18] analyzed the effects of the HTC process on fuel characteristics and combustion behavior of hydrochar obtained from vine pruning. In all these investigations distilled water was used as reaction media to reach the useful moisture content of the substrate. However, the use of pure water as a liquid source cannot be considered as an environmentally sustainable practice in light of the global water scarcity. Venna et al. [19] and Li et al. [20] used landfill leachate as liquid source during HTC of yard waste and food waste, highlighting that it had minimal impact on the fuel characteristics of the hydrochars than distilled water. Also, Weiner et al. [21] demonstrated that the use of organosolv wastewater had no negative effects on the HTC process of chaff and hydrochar properties.
In this way, liquid waste effluents, such as vinasse, could be an interesting option that should be explored to analyze their influence on the carbonization rate and the physical and chemical properties of the hydrochar.

2.1.2 Municipal solid waste

Approximately 232 million tonnes of municipal solid waste, or 517 kg per capita, were produced in 2020 in the UE27. In the three years 2018–2020, there was an increase of 3.7% in production overall [22]. In 2021, in Italy, the production of municipal waste involved a quantity of about 30 million tons, the final solution of which mainly involves landfilling. Such a solution not only occupies more and more valuable space but also causes air, water, and soil pollution by discharging carbon dioxide (CO_2) and methane (CH_4) into the atmosphere and chemicals and pesticides in the land and the groundwater. This, in turn, is harmful to human health, as well as the environment. Mechanical Biological Treatment (MBT) is widely used as a form of pretreatment for landfills or incineration. It is an essential phase of the waste cycle since allows, through a process of selection (mechanical) and treatment (biological), to:

- recover a further part of recyclable materials;
- make an appropriate selection of waste to be sent for incineration/waste-to-energy plant, obtaining a lower emission of pollutants and a higher energy yield;
- reduce the volume of material for final disposal and therefore the use of landfills and incinerators;
- ensure the conditions of biological stability of the waste to minimize the formation of decomposition gases and leachate.

In an MBT plant, the unsorted MSW is mechanically sorted into three fractions, i.e. material organic, recyclables, and waste. The recyclable fraction includes materials such as glass, metals, plastics, rubber, rags, papers, etc. which can be differentiated by separation and sieving. The recyclable components (glass, metals, etc.) can be sent for recycling, while the non-recyclable components partly contribute to the production of solid fuel to be sent to waste-to-energy plants, and parts are sent to landfill. The organic fraction is addressed to a biological stabilization process (aerobic digestion). The output of the aerobic digestion is called stabilized organic fraction (SOF), or off-specification compost, and it is codified by the European Waste Catalog (EWC) as EWC 19.05.03. This material is currently discarded and landfilled, with additional costs. According to the Urban Waste Report 2022 of ISPRA [23], in 2021 over 8.1 million tons of waste materials were produced by mechanical biological treatment plants, which is about 560.000 tons of SOF. Furthermore, leachate is generated from the MSW landfilling. Landfill leachate (LL) is a tainted liquid arising from the bottom of solid waste disposal facilities that contains both soluble organic and inorganic compounds as well as suspended particles [24]. In Italy, the regulation requires that it must be captured and appropriately treated on the same site of the landfill or transported in an ad hoc plant duly authorized for disposal in the sewers. Currently, physicochemical treatment methods such as reverse osmosis are widely used. Reverse osmosis membrane technology plants are employed for LL treatment, producing two fractions: the permeate (PF) (about 75%) and the concentrate (CF) (about 25%). Since the permeate might be directed to the sewers, the concentrate remains a burden. In this context, alternatives are needed to valorize the SOF, together with landfill

waste reduction, as well as the landfill leachate and/or concentrate, leading the waste management business towards a circular economy perspective. A valuable option is to use all these wastes as precursors in the production of carbon-based materials.
Several studies have investigated the HTC as thermal pre-treatment for different types of MSWs, or streams obtained from it. Ischia et al. [25], performed the HTC to valorize municipal solid waste for biofuel production; the off-specification compost was used by González-Arias et al. [26], to be co-processed by HTC with olive tree pruning and obtaining a coal-like product with a high carbon content; Periyavaram et al. [27], analyzed the thermal behavior of hydrochar derived from HTC of food waste using leachate as moisture source; likewise, Śliz et al. [28], reported the technical feasibility of an industrial scale layout of an HTC plant by using the wet fraction mechanically separated from mixed MSW or under sieve fraction as solid substrate and water as moisture source.
Despite the many probable benefits, the potential application of LL or CF from reverse osmosis plants as liquid substrates for HTC remains less explored.

Overall, by extracting valuable resources from these biomass waste streams, we can reduce waste generation, promote sustainable practices, and contribute to a more circular and resource-efficient industrial system.

2.2 Biomass waste valorization

Among the numerous approaches to address the substantial volume of biomass wastes, one effective solution is to yield bioenergy or produce value-added products from it. In the middle of the current energy crisis, valorization of waste not only presents a great opportunity for economic growth in many countries but also offers the potential to create new jobs and foster international economic competition. Under the Waste Framework Directive (WFD), the EU aims to transition from linear economic processes to circular ones, effectively creating a recycling society [29, 30]. The circular economy minimizes waste generation, maximizes material recycling, and brings cost savings and reduced reliance on primary resources.
Nowadays, researchers are challenged in optimizing and developing technologies to valorize these agro-industrial wastes from a circular economy perspective. The main challenges in the biomass supply chain are seasonal availability, fluctuations in the amount of residual biomass, availability in dispersed locations, the elevated moisture content that makes it prone to degradation, and the low density of biomass resulting in higher costs for storage and transportation [31]. Thus, depending on the biomass residue characteristics need to adopt targeted valorization routes to obtain a value-added product not only to outrage these challenges but also to be suitable for the specific application.

At present, one of the most effective processes of converting biomass wastes into bioenergy or other value-added products is thermochemical conversions (***Figure 2.2***). It includes two different categories: dry technique and hydrothermal processing. The dry thermochemical conversion regards the torrefaction, traditional carbonization, pyrolysis, and gasification processes. Instead, hydrothermal conversion includes hydrothermal carbonization (HTC), hydrothermal liquefaction (HTL), and supercritical gasification.

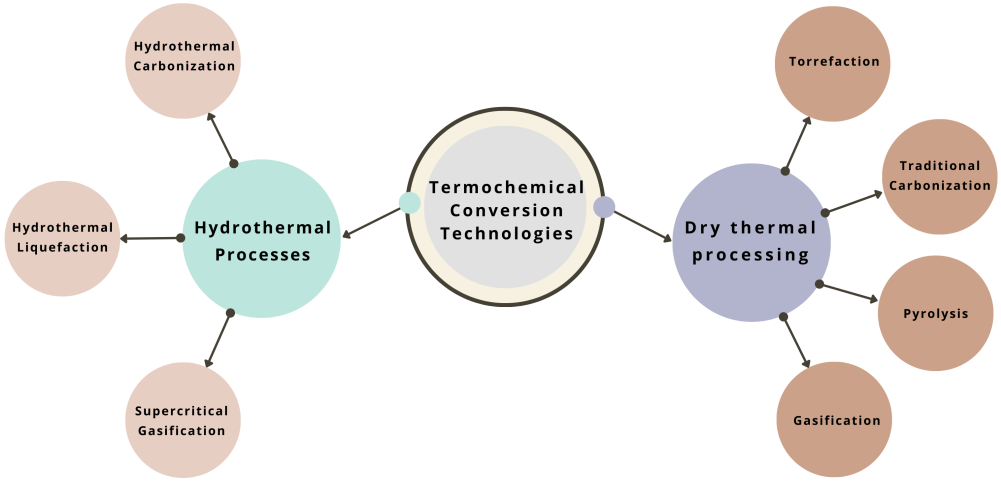

Figure 2.2: *Biomass conversion technologies.*

Each conversion process has its own set of advantages and disadvantages. Dry thermochemical conversion processes require a low moisture content in the biomass, thus drying is normally a necessary process before biofuel production. Furthermore, their efficiency can be affected by feedstock variability, and uniform particle size and shape. Wet thermochemical conversion processes seem to be a good solution to dealing with the high moisture contained in biomass without drying, offering a wider range of feedstock suitability with a broad range of particle sizes and shapes. However, the high pressure and water vaporization required for the process might result in more energy-intensive.
Torrefaction is usually conducted under an inert environment and atmospheric pressure in the temperature range between 200°C and 300°C at a low heating rate [32]. During torrefaction, mainly hemicellulose decomposes and releases most of the moisture, CO, and CO_2. The torrefied biomass normally has reduced volatile content and increased energy density.
Compared to torrefaction, traditional carbonization is a long-term conversion requiring higher temperatures from 300 up to 500°C, leading to maximizing the fixed carbon (charcoal) [33].
Pyrolysis is a typical dry thermochemical decomposition process in the absence of oxygen. It is generally performed between 400 and 700°C, normally at atmospheric pressure. Pyrolysis of biomass mainly produces bio-oil, biochar, and noncondensable gas (CO, CO_2, etc.). The proportions of the products vary depending on the operating conditions, raw materials, and process configuration. Generally, both low temperatures and heating rates result in a high yield of biochar. To maximize the yield of liquid a low temperature, high heating rate, and short gas residence time process would be required. For higher fuel gas production, high temperature, low heating rate, and long gas residence time process would be preferred [34].
Differently from the other dry thermochemical conversion processes aforementioned, gasification is performed with a controlled flow rate of gasification agent (air, oxygen, steam, or CO_2) to convert biomass into a mixture of combustible gases. These gases typically include carbon monoxide, hydrogen, methane, carbon dioxide, and water. Normally operates in the temperature range between 700°C and 1300°C. Oxidation, drying, pyrolysis, and reduction are the four key steps of the gasification mechanism [35]. The oxidation of part of the biomass is neces-

sary to obtain the thermal energy required for the endothermic processes (drying, pyrolysis, and reduction) and maintain the operative temperature at the required value. On the other hand, the reduction step involves all the products of the preceding stages of oxidation, drying, and pyrolysis. The gas mixture and the char react with each other resulting in the formation of the final syngas.
By considering wet thermochemical processes, hydrothermal liquefaction requires temperatures in the range of 280°C – 370°C and high pressures (4 – 22 MPa) for the reaction [36]. It is a complex process that comprises hydrolysis, decomposition, isomerization, dehydration, repolymerization, etc. The main product from HTL is tar (bio-oil), together with by-products of char, water-soluble substances, and gases.
When the temperature and pressure increase to exceed the supercritical state for water (above 370°C and 22 MPa) in nonoxidative conditions, the dominant products are gaseous substances (mainly H_2 and CO_2 with lower amounts of CH_4 and CO), and the process is normally called supercritical water gasification (SCWG) [37]. As with HTL, SCWG can also process biomass directly without additional drying pretreatment. The start temperature for SCWG can be much lower than that for dry gasification but a high pressure is required to reach the supercritical environment.
Among the hydrothermal processes, during HTC the wet biomass remains heated at a lower temperature range (150–350°C) over a few minutes to several hours under autogenic pressure [38]. Under these conditions, wet biomass undergoes a series of complex reactions (hydrolysis, dehydration, decarboxylation, aromatization, and re-condensation), and three types of products are resulting from the process [39, 40]. The main output is a carbon-rich solid material known as hydrochar, which accounts for approximately 45–70% of the product mass. A gas phase, approximately 1–3% of the raw material, consisting mainly of CO_2 (>90% of the gaseous products) with small amounts of CH_4, H_2, and CO. A liquid fraction (spent liquor), 5 and 25% of the mass of products, which is rich in bio-degradable soluble organic compounds [41, 42]. The HTC process has several advantages. Unlike pyrolysis, gasification, torrefaction, and traditional carbonization, HTC can efficiently handle heterogeneous wet feedstock without pre-drying or separation pretreatment, since water works as a reactant, solvent, and catalyst [43–46]. These advantages make the HTC process applicable to various wet residues, including agricultural and forestry residues [47], anaerobic digestate [48], sewage sludge [49], algal biomass [50, 51], olive mill sludge [52], pulp and paper mill sludge [53] and off-specification compost [54]. Nonetheless, within the HTC process, there are present some disadvantages. These include the use of complex and costly systems that use substantial amounts of water and further costs for the separation of the solid and liquid phases, as well as the discharge of significant quantities of wastewater [55, 56]. However, current research examining the possible valorization of the spent liquor derived from the biomass HTC process highlights the commercial rentability in a circular economy approach [56]. Possible solutions cited include processes from which the resultant by-product represents a benefit such as anaerobic digestion, nutrient recovery, bioplastic production, wet oxidation, and liquid fertilizer [57–61].

Nowadays, the idea of eco-sustainability, energy savings, circular economy, and a waste-to-energy approach, ensures that these thermochemical conversion processes are continually improved and developed for different purposes. Among these technologies, HTC is one of the most promising methods for biomass treatment. HTC represents an alternative, eco-friendly technique to produce value-added materials from biomass. In this context, hydrochar has gained great attention as a versatile material with various applications across different industries. Hydrochar can be used as a soil amendment to improve soil fertility and structure. It enhances water retention, nutrient availability, slow-release fertilizers, and microbial activity in the soil, leading to increased crop yields and improved soil health [62, 63]. Its porous structure allows it to effectively remove contaminants such as heavy metals, organic pollutants, and pharmaceuticals from water, making it a promising adsorbent material for wastewater treatment and purification [64, 65]. Hydrochar can be used as a catalyst or support in catalytic aromatization. It can be activated under high-temperature conditions to increase the specific surface area and porosity, and chemically functionalized or decorated with metallic nanoparticles to strengthen their catalytic activity [66]. Furthermore, hydrochar-based scaffolds have shown promise in tissue engineering applications. Scaffolds made from hydrochar can provide a three-dimensional structure that supports cell growth and tissue regeneration. The surface properties of hydrochar can be modified to enhance cell adhesion and promote specific tissue formation [67, 68]. Moreover, Hydrochar can be employed as a component in the production of construction materials such as bricks, cement, plasters, and composites. It can improve the mechanical properties, the thermal and acoustic insulation [69, 70], and act as moisture absorption [71] and carbon-capture material [72, 73]. Also, the great potential of hydrochars as an alternative to fossil fuels due to their high carbon content, calorific value, increased hydrophobicity and grindability (which means reduced problems for storage and transport), and carbon neutral potential has been largely evaluated [74]. Prasongthum et al. [75] investigated the production of hydrochar from oil palm trunks, resulting in lower slagging and fouling issues during combustion in comparison to raw biomass. Sattasathuchana et al. [76] found that the utilization of hydrochar from co-HTC of palm kernel shell and bamboo to produce electricity in a municipal power plant could reduce the fuel storage size by 34%, save around 28000 USD/year of transportation cost and reduce 2300 ton/year of CO_2 emissions during burning in comparison of raw biomass. Yu et al. [77] explained that the combination of HTC and pelletization on Ginkgo leaf residues is an efficient technique to produce a solid biofuel with upgraded characteristics. Furthermore, in the industrial sector the HTC process was demonstrated to be a valuable environmental solution to produce hydrochar as a substitute for fossil coal for metallurgical applications [78].

Considering all the aforementioned factors, in this work the HTC emerged as the most suitable and effective thermochemical process for the valorization of biomass waste and by-products from the winemaking industry and municipal solid waste management. Furthermore, the versatile and sustainable nature of the application of the hydrochar from HTC made this work focused on three main sectors, energy, industrial, and building.

2.3 Unlocking potential hydrochar applications

2.3.1 Energy sector

In connection with the rapid growth of the global population and the modernization of people's lifestyles, our world is grappling with a multitude of pressing environmental challenges. The latest United Nations Climate Change Conference (COP 28), held in December 2023, marked the completion of the initial worldwide assessment of global climate change efforts under the Paris Agreement. The outcomes revealed sluggish progress in various aspects of climate action, spanning from reducing greenhouse gas emissions and enhancing resilience to climate change, to providing financial and technological assistance to vulnerable nations. For the energy sector, to expedite action across all areas by 2030, countries made the call to governments to hasten the shift from fossil fuels to renewable energy sources in their forthcoming climate commitments [79]. Regarding these global agreements, a roadmap towards the reduction of reliance on fossil sources has been devised by the European Union (EU), increasing the production and utilization of renewable energy sources (RES). In 2020 the EU surpassed its 20% target of gross final energy consumption from renewable sources, as outlined in the 2009 Renewable Energy Directive (RED I), by achieving a 22% share [80]. The recent agreement between the European Parliament and the Council in the recast RED II (2018/2001/EU) introduced a new strengthening renewable energy target of at least 42.5% share by 2030 (RED III) [81, 82]. This means almost doubling the current share of RES in the EU. RES achieved their highest level of integration in the power sector, accounting for 37.5% of the total electricity generated in the EU in 2021. Subsequently, the heating and cooling sector followed with a RES share of 22.9% while in transport contributed to 9.1% of the overall share [83]. Solid biomass stands out as the most prominent renewable energy source, dominating the renewable energy supply in Europe [84, 85]. It finds extensive application in heating and industrial sectors, accounting for a substantial 41% share in 2021. Following behind are wind energy (13%), hydropower (12%), liquid biofuels (8%), and biogas (6%), while heat pumps and solar photovoltaic represent less than 6% individually. With its great potential to boost the EU to get on track with the 2030 agenda, biomass has become of central role in the clean energy transition.

As already mentioned, biomasses have several disadvantages to be used as it is for energy purposes. Ence, they need to be pretreated to enhance their chemical-physical characteristics. The hydrothermal carbonization process has been largely evaluated as a valuable option to convert wet biomasses into solid biofuels (hydrochars).

2.3.2 Industrial sector

Among the branches that constitute the industrial sector, metal production has a relevant role. Currently, the iron and steel sector is responsible for about 3 gigatonnes of carbon dioxide (Gt CO_2) emissions, corresponding to around 7% of the global total CO_2 emissions [86]. Therefore, the decarbonization of this sector is crucial to meet the climate targets. The blast furnace-basic oxygen furnace (BF-BOF) and electric arc furnace (EAF) are the two well-established steel-producing routes. However, since the current dominant BF-BOF production route is con-

siderably high energy and CO_2-intensive, the industry is increasingly focusing on diverting large capital investments from BF-BOF production to the scrap-based steel production EAF route [87]. An EAF utilizes graphite electrodes to generate electric arcs that melt the metal scrap. Coal contributes 11%, while electricity, natural gas, and other sources account for 50%, 38%, and 1% of the total energy input, respectively [88]. Typically, anthracite, coke (metallurgical or petroleum), or graphite are employed as sources of carbon with two primary objectives. These are used as charged materials that add extra carbon to the scrap and are burnt to provide additional heat alongside the electrical energy used for melting. Also, they are used as injected carbon to react with iron oxide in the slag during the foaming process. This helps to protect the internal walls of the furnace from the intense radiation of the arc and to enhance energy efficiency [89]. Typically, when fossil coal is used as the chemical energy source in EAF, it accounts for 40–70% of the total direct emissions of the EAF [90]. Therefore, to reduce CO_2 emissions, replacing conventional fossil fuels with substitutes is a highly attractive option. By replacing 60% of fossil carbon with biogenic carbon, the total CO_2 emissions from EAFs could be reduced by 19% [91]. Additionally, using biogenic material in a mini-mill/EAF was found to reduce greenhouse gas (GHG) emissions by 5–11% without by-product credits, and 7–15% with by-product credits [92]. Furthermore, the potential for reducing CO_2 emissions was estimated to be around 8–12% in the Australian EAF opera-tions by using biogenic material in a variety of applications [93]. In this context, the use of char derived from biomass/agricultural waste as a substitute or auxiliary source alongside fossil coal has become increasingly interesting. Moreover, fuels from biomass are considered carbon neutral since the carbon dioxide emitted when they are burnt is offset by the CO_2 that was absorbed by the plants during their growth [94]. Literature studies demonstrated biomass chars application in EAF can partially substitute coal used as an injected powder or charged within the basket. Fidalgo et al. [95] studied the thermochemical properties and reactivities of biochars derived from grape seed and pumpkin seed to address their suitability to be used in EAF steelmaking. It was found that these crop-derived biochars could replicate reactivities comparable to those of coals employed in the EAF steelmaking process. Yunos et al. [96, 97] investigated the interactions of palm shells with EAF slag, involving a quantitative estimation of changes occurring in the slag volume as a function of time. The results indicated that the partial replacement of coal with palm shells is viable. Demus et al. [90] tested biochars from agricultural residues as charge carbon in pilot EAF melting trials. The evaluation of the results of these trials regarding steel, slag and off-gas composition showed no negative impact on the slag and steel chemistry in comparison to fossil coal. These results are in line with the lab-scale test of Robinson et al. [98] which demonstrated that partial substitution of standard anthracite carbon charge with biochar from woody biomass gave no deviation from normal operating conditions in the EAF.
Recently, the effective application of lignocellulosic-derived hydrochar as a carbonaceous foaming agent in EAF was investigated [99].

Despite biomass chars presenting great potential for the metallurgical sector, their use instead of fossil coal in EAF steelmaking is still challenging and needs to be further investigated.

2.3.3 Building sector

Overall, buildings account for 40% of energy consumption and 36% of GHG emissions in Europe [100]. Improving the energy efficiency of buildings is therefore crucial to achieving the ambitious target of carbon neutrality by 2050, as defined in the European Green Deal [101]. Since around 35% of EU buildings are over 50 years old, and 75% are energy inefficient, there is an urgent need for intensive action both on the design of new buildings and on the redevelopment of existing ones, looking for smart solutions and energy efficient materials [102]. The renovation of existing buildings could reduce the total EU energy consumption by 5-6% and CO_2 emissions by around 5% [103]. The EU has recently introduced ambitious new policies to help member states improve energy efficiency in buildings. The revised Energy Performance of Buildings Directive (EPBD) [104] and the Energy Efficiency Directive (EED) [105] marked a clear milestone in Europe in the field of building sustainability. Together promote:

- to reduce the average primary energy use of residential buildings;
- the construction of nearly zero energy buildings (NZEBs);
- to increase reliability, quality, and digitalization of Energy Performance Certificates (EPCs) with energy performance classes to be based on common criteria;
- the modernization of buildings and their systems and better energy system integration.

Moreover, have been introduced incentives for the renovation of public and private buildings with high-energy performance improvements. The cumulative impact of these efforts at the national level will contribute to achieving 32.5% of the energy efficiency target for the EU by 2030 [103]. Alongside this, the development of the attention to eco-sustainability has led to the emergence of innovative ways of building design. Many governments have imposed laws to increase sustainability in construction. In Italy, the DM 256/2022 recently revised the minimum environmental criteria for buildings, focusing on a bio-eco-sustainable approach. This implies a dialoguing set between materials with low environmental impact (renewable, durable, reusable, recyclable) and technological know-how for improving energy performance. Green buildings, using sustainable, environmentally friendly materials, can reduce the extraction of raw materials, decrease imports through recycling, and improve energy performance. Recently, many papers have been published on the admixture of chars from biomass into building materials to improve the mechanical and hygrothermal performance of the material itself [106]. The high specific surface area and porosity of biochars play an important role in improving the thermal conductivity, humidity control capability, gaseous pollutant adsorption ability, as well as mechanical strength. Diverse biochars derived from a variety of biomass wastes have been proven as successful admixtures in building materials [107–109]. Among them, hydrochars from different biomass residues were investigated as a potential partial replacement in cementitious mortar [110, 111]. The application of hydrochar as building admixture material provides an opportunity for large-scale recycling of waste biomass, pushing society towards both an

eco-sustainable and circular economy. Furthermore, by using hydrochar as an admixture, plasters and other building materials might benefit from its low thermal conductivity, high surface area, and porous nature. These properties work together to enhance the plaster thermal insulation by disrupting the thermal bridging, rendering the heat propagation routes multi-directional and hindering the effect of unidirectional heat propagation, thus reducing the propagation of heat flow [112, 113]. Additionally, hydrochar could increase the ability of the plaster to absorb sound, as sound waves would disperse and converted into heat through refraction within the increased porosity and interconnected pore networks of the admixture [114, 115]. Furthermore, a high surface area is favorable for the formation of a suitable pore structure for CO_2 uptake, which is subsequently mineralized into stable carbonates after being released into the plaster matrix, and moisture adsorption, which can help to regulate the relative humidity [112, 113, 116–118].
Therefore, further research may be directed towards innovative production technologies that would benefit in terms of environmental sustainability, and public health, and focusing on the virtuosic waste-to-resource approach, increasing the viability of hydrochar applications.

Throughout this overview chapter, the background behind the choice of investigating the application of hydrochar from biomass waste of different industrial supply chains, as a solution to address the environmental impact of the energy, industrial, and building sectors, has been clarified.

Nomenclature

Abbreviation			
GHG	Greenhouse Gas	HTL	Hydrothermal Liquefaction
VP	Vine Pruning	SCWG	Supercritical Water Gasification
EGM	Exhausted Grape Marc	RES	Renewable Energy Sources
HTC	Hydrothermal Carbonization	RED	Renewable Energy Directive
MBT	Mechanical Biological Treatment	BF-BOF	Blast Furnace-Basic Oxygen Furnace
MSW	Municipal Solid Waste	EAF	Electric Arc Furnace
SOF	Stabilized Organic Fraction	EPBD	Energy Performance of Buildings Directive
EWC	European Waste Catalog	EED	Energy Efficiency Directive
LL	Landfill Leachate	NZEBs	Nearly Zero Energy Buildings
PF	Permeate Fraction	EPCs	Energy Performance Certificates
CF	Concentrate Fraction	tdm	tonnes of dry matter
WFD	Waste Framework Directive	COD	Chemical Oxygen Demand
EU	European Union	BOD	Biochemical Oxygen Demand
		HHV	Higher Heating Value

Bibliography

[1] M.-M. Titirici, ed., *Sustainable carbon materials from hydrothermal processes*. Wiley, 2013.

[2] World Bioenergy Association, "Global biomass potential towards 2035 - factsheet," 2016. https://www.worldbioenergy.org/factsheets/.

[3] European Commission - Joint Research Centre, *EU biomass flows: update 2022.* Publications Office, 2022. https://data.europa.eu/doi/10.2760/082220.

[4] Z. Jesus, A. Romaní, R. N. C. Pereira, J. A. Teixeira, M. S. Domingues, Lucília, and Genisheva, "Bioactive compounds recovery optimization from vine pruning residues using conventional heating and microwave-assisted extraction methods.," *Industrial Crops and Products*, vol. 132, pp. 99–110, 2019.

[5] M. Cotana, D. Foschini, E. Lascaro, F. Buratti, Cinzia, and Barbanera, "Preliminary optimization of alkaline pretreatment for ethanol production from vineyard pruning," *Energy Procedia*, vol. 82, pp. 389–394, 2015.

[6] G. Saha, M. Dally, Bassam B., and Gitto, "Burning characteristics of grape marc under mild combustion conditions," *Experimental Thermal and Fluid Science*, vol. 114, 2020.

[7] P. Torres-Climent, J. Martin-Mata, M. A. Bustamante, F. C. Marhuenda-Egea, M. D. Perez-Murcia, A. Perez-Espinosa, C. Paredes, A. Moral, Raúl, and Gomis, "Chemical, thermal and spectroscopic methods to assess biodegradation of winery-distillery wastes during composting," *PloS one*, vol. 10, no. 9, 2015.

[8] S. Ibn Ferjani, H. Akrout, L. Limousy, H. Hamdi, N. Thevenin, A. Jeguirim, Mejdi, and Jellali, "Nutrient retention and release from raw exhausted grape marc biochars and an amended agricultural soil: Static and dynamic investigation," *Environmental Technology & Innovation*, vol. 19, 2020.

[9] A. Natolino, Carla and D. Porto, "Kinetic models for conventional and ultrasound assistant extraction of polyphenols from defatted fresh and distilled grape marc and its main components skins and seeds," *Chemical Engineering Research and Design*, vol. 156, pp. 1–12, 2020.

[10] I. Drevelegka, Athanasia M. and Goula, "Recovery of grape pomace phenolic compounds through optimized extraction and adsorption processes," *Chemical Engineering and Processing - Process Intensification*, vol. 149, 2020.

[11] A. Zhang, J. Patel, S. Lim, N. Li, Chao'en, and Hoadley, "Sustainable options for the utilization of solid residues from wine production.," *Waste management (New York, N.Y.)*, vol. 60, pp. 173–183, 2017.

[12] A. Pomarici, S. Mazzarino, E. Sardone, Roberta, and Corsi, "The italian wine sector: Evolution, structure, competitiveness and future challenges of

an enduring leader," *Italian Economic Journal*, vol. 7, no. 2, pp. 259–295, 2021.

[13] J. Bacenetti, "Heat and cold production for winemaking using pruning residues : environmental impact assessment," *Applied Energy*, vol. 252, 2019.

[14] G. Toscano, D. Duca, E. F. Pedretti, F. Corinaldesi, G. Rossini, Giorgio, and Riva, "Analysis of the characteristics of the residues of the wine production chain finalized to their industrial and energy recovery," *Biomass and Bioenergy*, vol. 55, pp. 260–267, 2013.

[15] M. Tena, B. Luque, M. Perez, and R. Solera, "Enhanced hydrogen production from sewage sludge by cofermentation with wine vinasse," *International Journal of Hydrogen Energy*, vol. 45, no. 32, pp. 15977–15984, 2020.

[16] F. Basso, D. Castello, M. Baratieri, E. C. Rada, E. Weiss-Hortala, D. Fiori, Luca, and Patuzzi, "Agro-industrial waste to solid biofuel through hydrothermal carbonization," *Waste management (New York, N.Y.)*, vol. 47, no. 47, pp. 114–121, 2015.

[17] E. Basso, F. Patuzzi, M. Baratieri, D. Fiori, Luca, and Weiss-Hortala, "In deep analysis on the behavior of grape marc constituents during hydrothermal carbonization," *Energies*, vol. 11, no. 6, 2018.

[18] G. Duman, H. Cay, I. C. Kantarli, G. Yanik, Jale, and Balmuk, "Comparative evaluation of torrefaction and hydrothermal carbonization: Effect on fuel properties and combustion behavior of agricultural wastes," *Energy & Fuels*, vol. 34, no. 9, pp. 11175–11185, 2020.

[19] H. B. Venna, P. H. P. Reddy, S. Chowdhury, S. Dubey, Brajesh, and Sharma, "Landfill leachate as an alternative moisture source for hydrothermal carbonization of municipal solid wastes to solid biofuels.," *Bioresource technology*, vol. 320, 2020.

[20] M. Li, P. Olsen, L. Berge, Nicole D., and Hale, "Using liquid waste streams as the moisture source during the hydrothermal carbonization of municipal solid wastes," *Waste management (New York, N.Y.)*, vol. 34, no. 11, pp. 2185–2195, 2014.

[21] H. Weiner, J. Poerschmann, B. Kopinke, Frank-Dieter, and Wedwitschka, "Utilization of organosolv waste waters as liquid phase for hydrothermal carbonization of chaff," *ACS Sustainable Chemistry & Engineering*, vol. 4, no. 10, pp. 5737–5742, 2016.

[22] Eurostat, "Overview - waste," 2023. https://ec.europa.eu/eurostat/web/waste.

[23] ISPRA, "Rapporto rifiuti urbani edizione 2022," 2022. https://www.isprambiente.gov.it/it/pubblicazioni/rapporti/rapporto-rifiuti-urbani-edizione-2022.

[24] B. Naveen, D. M. Mahapatra, T. Sitharam, P. Sivapullaiah, and T. Ramachandra, "Physico-chemical and biological characterization of urban municipal landfill leachate," *Environmental Pollution*, vol. 220, pp. 1–12, 2017.

[25] G. Ischia, L. Fiori, L. Gao, and J. L. Goldfarb, "Valorizing municipal solid waste via integrating hydrothermal carbonization and downstream extraction for biofuel production," *Journal of Cleaner Production*, vol. 289, p. 125781, 2021.

[26] J. González-Arias, A. Carnicero, M. Sánchez, E. Martínez, R. López, and J. Cara-Jiménez, "Management of off-specification compost by using co-hydrothermal carbonization with olive tree pruning. assessing energy potential of hydrochar," *Waste Management*, vol. 124, pp. 224–234, 2021.

[27] S. R. Periyavaram, L. Uppala, S. Sivaprakash, and P. H. P. Reddy, "Thermal behaviour of hydrochar derived from hydrothermal carbonization of food waste using leachate as moisture source: Kinetic and thermodynamic analysis," *Bioresource Technology*, vol. 373, p. 128734, 2023.

[28] M. Śliz, F. Tuci, K. Czerwińska, S. Fabrizi, L. Lombardi, and M. Wilk, "Hydrothermal carbonization of the wet fraction from mixed municipal solid waste: Hydrochar characteristics and energy balance," *Waste Management*, vol. 151, pp. 39–48, 2022.

[29] European Union, "Directive 2008/98/ec of the european parliament and of the council of 19 november 2008 on waste and repealing certain directives," *Official Journal of the European Union*, 2008.

[30] European Commission, "Waste framework directive," https://environment.ec.europa.eu/topics/waste-and-recycling/waste-framework-directive_en.

[31] P. K. Sarangi and L. Bhatia, *Biotechnology for waste biomass utilization*. Apple Academic Press, 1 ed., 2023.

[32] A. Cardarelli, S. Pinzi, and M. Barbanera, "Effect of torrefaction temperature on spent coffee grounds thermal behaviour and kinetics," *Renewable Energy*, vol. 185, pp. 704–716, 2022.

[33] J. Zhang and X. Zhang, "The thermochemical conversion of biomass into biofuels," pp. 327–368, 2019.

[34] T. P. Wampler, ed., *Applied pyrolysis handbook*. CRC Press/Taylor & Francis, 2nd ed ed., 2007.

[35] A. Molino, S. Chianese, and D. Musmarra, "Biomass gasification technology: The state of the art overview," *Journal of Energy Chemistry*, vol. 25, no. 1, pp. 10–25, 2016.

[36] H. Shahbeik, H. K. S. Panahi, M. Dehhaghi, G. J. Guillemin, A. Fallahi, H. Hosseinzadeh-Bandbafha, H. Amiri, M. Rehan, D. Raikwar, H. Latine,

et al., "Biomass to biofuels using hydrothermal liquefaction: A comprehensive review," *Renewable and Sustainable Energy Reviews*, vol. 189, p. 113976, 2024.

[37] C. Yang, S. Wang, J. Yang, D. Xu, Y. Li, J. Li, and Y. Zhang, "Hydrothermal liquefaction and gasification of biomass and model compounds: a review," *Green Chemistry*, vol. 22, no. 23, pp. 8210–8232, 2020.

[38] J. Villamil, M. De La Rubia, E. Diaz, and A. Mohedano, "Technologies for wastewater sludge utilization and energy production: Hydrothermal carbonization of lignocellulosic biomass and sewage sludge," in *Wastewater Treatment Residues as Resources for Biorefinery Products and Biofuels*, pp. 133–153, Elsevier, 2020.

[39] M. Wilk, A. Magdziarz, I. Kalemba-Rec, and M. Szymańska-Chargot, "Upgrading of green waste into carbon-rich solid biofuel by hydrothermal carbonization: The effect of process parameters on hydrochar derived from acacia," *Energy*, vol. 202, p. 117717, 2020.

[40] Z.-X. Xu, H. Song, P.-J. Li, Z.-X. He, Q. Wang, K. Wang, and P.-G. Duan, "Hydrothermal carbonization of sewage sludge: Effect of aqueous phase recycling," *Chemical Engineering Journal*, vol. 387, p. 123410, 2020.

[41] A. Magdziarz, A. Mlonka-Mędrala, M. Sieradzka, C. Aragon-Briceño, A. Pożarlik, E. A. Bramer, G. Brem, L. Niedzwiecki, and H. Pawlak-Kruczek, "Multiphase analysis of hydrochars obtained by anaerobic digestion of municipal solid waste organic fraction," *Renewable Energy*, vol. 175, pp. 108–118, 2021.

[42] F. F. Roman, J. L. Diaz De Tuesta, P. Praça, A. M. Silva, J. L. Faria, and H. T. Gomes, "Hydrochars from compost derived from municipal solid waste: Production process optimization and catalytic applications," *Journal of Environmental Chemical Engineering*, vol. 9, no. 1, p. 104888, 2021.

[43] M. Cavali, N. Libardi Junior, J. D. De Sena, A. L. Woiciechowski, C. R. Soccol, P. Belli Filho, R. Bayard, H. Benbelkacem, and A. B. De Castilhos Junior, "A review on hydrothermal carbonization of potential biomass wastes, characterization and environmental applications of hydrochar, and biorefinery perspectives of the process," *Science of The Total Environment*, vol. 857, p. 159627, 2023.

[44] S. Zhu, N. Preuss, and F. You, "Advancing sustainable development goals with machine learning and optimization for wet waste biomass to renewable energy conversion," *Journal of Cleaner Production*, vol. 422, p. 138606, 2023.

[45] S. Wu, Q. Wang, D. Cui, H. Sun, H. Yin, F. Xu, and Z. Wang, "Evaluation of fuel properties and combustion behaviour of hydrochar derived from hydrothermal carbonisation of agricultural wastes," *Journal of the Energy Institute*, vol. 108, p. 101209, 2023.

[46] S. Z. Roslan, S. F. Zainudin, A. Mohd Aris, K. B. Chin, M. Musa, A. R. Mohamad Daud, and S. S. A. Syed Hassan, "Hydrothermal carbonization of sewage sludge into solid biofuel: Influences of process conditions on the energetic properties of hydrochar," *Energies*, vol. 16, no. 5, p. 2483, 2023.

[47] S. Başakçılardan Kabakcı and S. S. Baran, "Hydrothermal carbonization of various lignocellulosics: Fuel characteristics of hydrochars and surface characteristics of activated hydrochars," *Waste Management*, vol. 100, pp. 259–268, 2019.

[48] M. Cavali, N. Libardi Junior, R. D. A. Mohedano, P. Belli Filho, R. H. R. Da Costa, and A. B. De Castilhos Junior, "Biochar and hydrochar in the context of anaerobic digestion for a circular approach: An overview," *Science of The Total Environment*, vol. 822, p. 153614, 2022.

[49] X. Luo, Z. Huang, J. Lin, X. Li, J. Qiu, J. Liu, and X. Mao, "Hydrothermal carbonization of sewage sludge and in-situ preparation of hydrochar/MgAl-layered double hydroxides composites for adsorption of pb(II)," *Journal of Cleaner Production*, vol. 258, p. 120991, 2020.

[50] J. D. S. Castro, P. P. Assemany, A. C. D. O. Carneiro, J. Ferreira, M. M. De Jesus Júnior, F. D. A. Rodrigues, and M. L. Calijuri, "Hydrothermal carbonization of microalgae biomass produced in agro-industrial effluent: Products, characterization and applications," *Science of The Total Environment*, vol. 768, p. 144480, 2021.

[51] S. Jabeen, X. Gao, J.-i. Hayashi, M. Altarawneh, and B. Z. Dlugogorski, "Effects of product recovery methods on the yields and properties of hydrochars from hydrothermal carbonization of algal biomass," *Fuel*, vol. 332, p. 126029, 2023.

[52] B. Mendecka, L. Lombardi, F. Micali, and A. De Risi, "Energy recovery from olive pomace by hydrothermal carbonization on hypothetical industrial scale: a LCA perspective," *Waste and Biomass Valorization*, vol. 11, no. 10, pp. 5503–5519, 2020.

[53] A. Mohammadi, G. Venkatesh, M. Sandberg, S. Eskandari, S. Joseph, and K. Granström, "A comprehensive environmental life cycle assessment of the use of hydrochar pellets in combined heat and power plants," *Sustainability*, vol. 12, no. 21, p. 9026, 2020.

[54] D. Basso, E. Weiss-Hortala, F. Patuzzi, D. Castello, M. Baratieri, and L. Fiori, "Hydrothermal carbonization of off-specification compost: A byproduct of the organic municipal solid waste treatment," *Bioresource Technology*, vol. 182, pp. 217–224, 2015.

[55] B. Ercan, K. Alper, S. Ucar, and S. Karagoz, "Comparative studies of hydrochars and biochars produced from lignocellulosic biomass via hydrothermal carbonization, torrefaction and pyrolysis," *Journal of the Energy Institute*, vol. 109, p. 101298, 2023.

[56] T. A. Khan, A. S. Saud, S. S. Jamari, M. H. A. Rahim, J.-W. Park, and H.-J. Kim, "Hydrothermal carbonization of lignocellulosic biomass for carbon rich material preparation: A review," *Biomass and Bioenergy*, vol. 130, p. 105384, 2019.

[57] J. González-Arias, M. E. Sánchez, J. Cara-Jiménez, F. M. Baena-Moreno, and Z. Zhang, "Hydrothermal carbonization of biomass and waste: A review," *Environmental Chemistry Letters*, vol. 20, no. 1, pp. 211–221, 2022.

[58] R. P. Ipiales, M. A. De La Rubia, E. Diaz, A. F. Mohedano, and J. J. Rodriguez, "Integration of hydrothermal carbonization and anaerobic digestion for energy recovery of biomass waste: An overview," *Energy & Fuels*, vol. 35, no. 21, pp. 17032–17050, 2021.

[59] Q. Zhang, B. Wang, Y. Feng, Y. Feng, J. Li, S. Ding, H. He, and H. Xie, "Process water from hydrothermal carbonization: The impacts on the aquatic dissolved organic matter feature and microbial network at the soil-water interface," *Journal of Cleaner Production*, vol. 397, p. 136486, 2023.

[60] A. D. Tripathi, P. K. Mishra, K. K. Darani, A. Agarwal, and V. Paul, "Hydrothermal treatment of lignocellulose waste for the production of polyhydroxyalkanoates copolymer with potential application in food packaging," *Trends in Food Science & Technology*, vol. 123, pp. 233–250, 2022.

[61] M. Langone and D. Basso, "Process waters from hydrothermal carbonization of sludge: Characteristics and possible valorization pathways," *International Journal of Environmental Research and Public Health*, vol. 17, no. 18, p. 6618, 2020.

[62] H. Si, C. Zhao, B. Wang, X. Liang, M. Gao, Z. Jiang, H. Yu, Y. Yang, Z. Gu, K. Ogino, and X. Chen, "Liquid-solid ratio during hydrothermal carbonization affects hydrochar application potential in soil: Based on characteristics comparison and economic benefit analysis," *Journal of Environmental Management*, vol. 335, p. 117567, 2023.

[63] A. Khosravi, Y. Yuan, Q. Liu, H. Zheng, M. Hashemi, Y. Tang, and B. Xing, "Hydrochars as slow-release phosphorus fertilizers for enhancing corn and soybean growth in an agricultural soil," *Carbon Research*, vol. 3, no. 1, p. 7, 2024.

[64] M. Jalilian, R. Bissessur, M. Ahmed, A. Hsiao, Q. S. He, and Y. Hu, "A review: Hydrochar as potential adsorbents for wastewater treatment and CO2 adsorption," *Science of The Total Environment*, vol. 914, p. 169823, 2024.

[65] M. T. Islam, A. I. Sultana, C. Chambers, S. Saha, N. Saha, K. Kirtania, and M. T. Reza, "Recent progress on emerging applications of hydrochar," *Energies*, vol. 15, no. 24, p. 9340, 2022.

[66] C. H. Ng, M. A. Mistoh, S. H. Teo, A. Galassi, Y. H. Taufiq-Yap, N. J. Siambun, J. Foo, C. S. Sipaut, J. Seay, and J. Janaun, "The roles of carbonaceous

wastes for catalysis, energy, and environmental remediation," *Catalysis Communications*, vol. 187, p. 106845, 2024.

[67] B. F. Bukit, F. A. Syamani, E. Rochima, C. Panatarani, W. Widiyastuti, D. Praseptiangga, N. Nazir, Y. Nurhamiyah, and S. Agustina, "Review of alginate-based composites for 3d printing material," *Polymers from Renewable Resources*, p. 20412479241227137, 2024.

[68] J. Fang, L. Zhan, Y. S. Ok, and B. Gao, "Minireview of potential applications of hydrochar derived from hydrothermal carbonization of biomass," *Journal of Industrial and Engineering Chemistry*, vol. 57, pp. 15–21, 2018.

[69] K. Kahandawa Arachchi, A. Selvaratnam, J. Gamage, and G. De Silva, "Green composite plaster with modified morphology for enhanced thermal comfort in buildings," *Case Studies in Construction Materials*, vol. 15, p. e00611, 2021.

[70] G. Srikanth, A. Fernando, K. Selvaranjan, J. Gamage, and L. Ekanayake, "Development of a plastering mortar using waste bagasse and rice husk ashes with sound mechanical and thermal properties," *Case Studies in Construction Materials*, vol. 16, p. e00956, 2022.

[71] R. Mrad and G. Chehab, "Mechanical and microstructure properties of biochar-based mortar: An internal curing agent for PCC," *Sustainability*, vol. 11, no. 9, p. 2491, 2019.

[72] S. Gupta and H. W. Kua, "Factors determining the potential of biochar as a carbon capturing and sequestering construction material: Critical review," *Journal of Materials in Civil Engineering*, vol. 29, no. 9, p. 04017086, 2017.

[73] S. Navaratnam, H. Wijaya, P. Rajeev, P. Mendis, and K. Nguyen, "Residual stress-strain relationship for the biochar-based mortar after exposure to elevated temperature," *Case Studies in Construction Materials*, vol. 14, p. e00540, 2021.

[74] H. B. Sharma, A. K. Sarmah, and B. Dubey, "Hydrothermal carbonization of renewable waste biomass for solid biofuel production: A discussion on process mechanism, the influence of process parameters, environmental performance and fuel properties of hydrochar," *Renewable and Sustainable Energy Reviews*, vol. 123, p. 109761, 2020.

[75] N. Prasongthum, A. Suemanotham, W. Sisuthog, Y. Thanmongkhon, C. Chaiya, and L. Attanatho, "Hydrothermal carbonization of oil palm trunk: Hydrochar properties and combustion behaviors," *Energy Reports*, vol. 9, pp. 380–386, 2023.

[76] S. Sattasathuchana, J. Parnthong, S. Youngian, K. Faungnawakij, P. Rangsunvigit, B. Kitiyanan, R. Khunphonoi, A. Wanichsombat, N. Grisdanurak, and P. Khemthong, "Energy efficiency of bio-coal derived from hydrothermal carbonized biomass: Assessment as sustainable solid fuel for municipal biopower plant," *Applied Thermal Engineering*, vol. 221, p. 119789, 2023.

[77] Y. Yu, Y. Guo, G. Wang, Y. A. El-Kassaby, and S. Sokhansanj, "Hydrothermal carbonization of waste ginkgo leaf residues for solid biofuel production: Hydrochar characterization and its pelletization," *Fuel*, vol. 324, p. 124341, 2022.

[78] C. Wang, Y.-C. Lu, L. Brabie, and G. Wang, "A pilot trial investigation of using hydrochar derived from biomass residues for EAF process," in *Advances in Pyrometallurgy* (C. Fleuriault, J. D. Steenkamp, D. Gregurek, J. F. White, Q. G. Reynolds, P. J. Mackey, and S. A. Hockaday, eds.), pp. 153–163, Springer Nature Switzerland, 2023. Series Title: The Minerals, Metals & Materials Series.

[79] United Nation Climate Change, "Cop 28: What was achieved and what happens next?," 2024. https://unfccc.int/cop28/5-key-takeaways.

[80] Eurostat, *Sustainable development in the European Union: monitoring report on progress towards the SDGs in an EU context : 2022 edition.* Publications Office of the European Union, 6 ed., 2022.

[81] European Commission, "European green deal: EU agrees stronger legislation to accelerate the rollout of renewable energy," 2023. https://ec.europa.eu/commission/presscorner/detail/en/IP_23_2061.

[82] European Union, "Directive (EU) 2023/2413 of the european parliament and of the council of 18 october 2023 on the promotion of energy from renewable sources," *Official Journal of the European Union*, 2023. http://data.europa.eu/eli/dir/2023/2413/oj.

[83] Eurostat, "Share of renewable energy in gross final energy consumption by sector," 2023. https://ec.europa.eu/eurostat/databrowser/product/view/nrg_ind_ren.

[84] European Environment Agency (EEA), "Trends and projections in europe 2022 - EEA report no 10/2022," 2022.

[85] European Environment Agency (EEA), "Share of energy consumption from renewable sources in europe - 8th EAP," 2023. https://www.eea.europa.eu/en/analysis/indicators/share-of-energy-consumption-from.

[86] International Energy Agency - IEA, "Iron and steel technology roadmap, paris," https://www.iea.org/reports/iron-and-steel-technology-roadmap.

[87] European Commission - Joint Research Centre, *Technologies to decarbonise the EU steel industry.* Publications Office, 2022. https://data.europa.eu/doi/10.2760/069150.

[88] World Steel Association, "Energy use in the steel industry - fact sheet," 2021. https://www.worldsteel.org/en/dam/jcr:f07b864c-908e-4229-9f92-669f1c3abf4c/fact%2520sheet%2520energy%25202021.pdf.

[89] X. Huang, K. W. Ng, L. Giroux, M. Duchesne, D. Li, and T. Todoschuk, "Interaction behavior of biogenic material with electric arc furnace slag," *Fuels*, vol. 2, no. 4, pp. 420–436, 2021.

[90] T. Demus, T. Reichel, M. Schulten, T. Echterhof, and H. Pfeifer, "Increasing the sustainability of steel production in the electric arc furnace by substituting fossil coal with biochar agglomerates," *Ironmaking & Steelmaking*, vol. 43, no. 8, pp. 564–570, 2016.

[91] L. Bianco, G. Baracchini, F. Cirilli, L. D. Sante, A. Moriconi, E. Moriconi, M. M. Agorio, H. Pfeifer, T. Echterhof, T. Demus, H. P. Jung, C. Beiler, and H.-J. Krassnig, "Sustainable electric arc furnace steel production: GREENEAF," *BHM Berg- und Hüttenmännische Monatshefte*, vol. 158, no. 1, pp. 17–23, 2013.

[92] T. Norgate, N. Haque, M. Somerville, and S. Jahanshahi, "Biomass as a source of renewable carbon for iron and steelmaking," *ISIJ International*, vol. 52, no. 8, pp. 1472–1481, 2012.

[93] S. Jahanshahi, J. G. Mathieson, M. A. Somerville, N. Haque, T. E. Norgate, A. Deev, Y. Pan, D. Xie, P. Ridgeway, and P. Zulli, "Development of low-emission integrated steelmaking process," *Journal of Sustainable Metallurgy*, vol. 1, no. 1, pp. 94–114, 2015.

[94] J. Zhao, H. Liu, H. Zhang, X. Song, H. Zuo, G. Wang, Z. Xu, M. Wu, Z. Zhang, and R. Chi, "Metallurgical performance and structural characteristics of cokes of hypercoal prepared from the mixture of low-rank coal and biomass residue," *Fuel*, vol. 332, p. 126069, 2023.

[95] B. Fidalgo, C. Berrueco, and M. Millan, "Chars from agricultural wastes as greener fuels for electric arc furnaces," *Journal of Analytical and Applied Pyrolysis*, 2015.

[96] N. F. Mohd Yunos, M. Zaharia, K. R. Ahmad, D. Nath, M. Iwase, and V. Sahajwalla, "Structural transformation of agricultural waste/coke blends and their implications during high temperature processes," *ISIJ International*, vol. 51, no. 7, pp. 1185–1193, 2011.

[97] N. F. M. Yunos, M. Zaharia, M. A. Idris, D. Nath, R. Khanna, and V. Sahajwalla, "Recycling agricultural waste from palm shells during electric arc furnace steelmaking," *Energy & Fuels*, vol. 26, no. 1, pp. 278–286, 2012.

[98] R. Robinson, L. Brabie, M. Pettersson, M. Amovic, and R. Ljunggren, "An empirical comparative study of renewable biochar and fossil carbon as carburizer in steelmaking," *ISIJ International*, p. 7, 2021.

[99] R. Wei, X. Zheng, Y. Zhu, S. Feng, H. Long, and C. C. Xu, "Hydrothermal bio-char as a foaming agent for electric arc furnace steelmaking: Performance and mechanism," *Applied Energy*, vol. 353, p. 122084, 2024.

[100] D. D'Agostino, P. M. Congedo, P. M. Albanese, A. Rubino, and C. Baglivo, "Impact of climate change on the energy performance of building envelopes and implications on energy regulations across europe," *Energy*, vol. 288, p. 129886, 2024.

[101] European Commission, "European green deal," https://climate.ec.europa.eu/eu-action/european-green-deal_en.

[102] C. Zhang, M. Hu, B. Laclau, T. Garnesson, X. Yang, C. Li, and A. Tukker, "Environmental life cycle costing at the early stage for supporting cost optimization of precast concrete panel for energy renovation of existing buildings," *Journal of Building Engineering*, vol. 35, p. 102002, 202.

[103] European Commission, "In focus: Energy efficiency in buildings," 2020. https://commission.europa.eu/news/focus-energy-efficiency-buildings-2020-02-17_en.

[104] European Union, "Directive 2010/31/eu of the european parliament and of the council of 19 may 2010 on the energy performance of buildings (recast)," *Official Journal of the European Union*, 2021. https://eur-lex.europa.eu/legal-content/EN/TXT/?uri=CELEX%3A02010L0031-20210101.

[105] European Union, "Directive (eu) 2023/1791 of the european parliament and of the council of 13 september 2023 on energy efficiency and amending regulation (eu) 2023/955 (recast) (text with eea relevance)," *Official Journal of the European Union*, 2023. https://eur-lex.europa.eu/legal-content/EN/TXT/?uri=OJ%3AJOL_2023_231_R_0001&qid=1695186598766.

[106] J. H. Park, Y. U. Kim, J. Jeon, B. Y. Yun, Y. Kang, and S. Kim, "Analysis of biochar-mortar composite as a humidity control material to improve the building energy and hygrothermal performance," *Science of The Total Environment*, vol. 775, p. 145552, 2021.

[107] A. Danish, M. Ali Mosaberpanah, M. Usama Salim, N. Ahmad, F. Ahmad, and A. Ahmad, "Reusing biochar as a filler or cement replacement material in cementitious composites: A review," *Construction and Building Materials*, vol. 300, p. 124295, 2021.

[108] B. A. Akinyemi and A. Adesina, "Recent advancements in the use of biochar for cementitious applications: A review," *Journal of Building Engineering*, vol. 32, p. 101705, 2020.

[109] H. Maljaee, R. Madadi, H. Paiva, L. Tarelho, and V. M. Ferreira, "Incorporation of biochar in cementitious materials: A roadmap of biochar selection," *Construction and Building Materials*, vol. 283, p. 122757, 2021.

[110] D. Hermawan, I. Budiman, F. Febrianto, S. Subyakto, G. Pari, M. Ghozali, E. Bahtiar, J. Sutiawan, and A. Azevedo, "Enhancement of the mechanical, self-healing and pollutant adsorption properties of mortar reinforced with empty fruit bunches and shell chars of oil palm," *Polymers*, vol. 14, no. 3, p. 410, 2022.

[111] M. M. Santos, A. L. Marques Sierra, A. Amado Fierro, M. Suárez, F. Blanco, J. M. G. La Fuente, M. A. Diez, and T. A. Centeno, "Reducing cement consumption in mortars by waste-derived hydrochars," *Journal of Building Engineering*, vol. 75, p. 106987, 2023.

[112] D. Cuthbertson, U. Berardi, C. Briens, and F. Berruti, "Biochar from residual biomass as a concrete filler for improved thermal and acoustic properties," *Biomass and Bioenergy*, vol. 120, pp. 77–83, 2019.

[113] Y. Zhang, M. He, L. Wang, J. Yan, B. Ma, X. Zhu, Y. S. Ok, V. Mechtcherine, and D. C. W. Tsang, "Biochar as construction materials for achieving carbon neutrality," *Biochar*, vol. 4, no. 1, p. 59, 2022.

[114] R. Mota-Panizio, L. Carmo-Calado, A. C. Assis, V. Matos, M. J. Hermoso-Orzáez, P. Romano, M. Gonçalves, and P. Brito, "Properties and uses of biochars incorporated into mortars," *Environments*, vol. 10, no. 3, p. 47, 2023.

[115] C. Rojas, M. Cea, A. Iriarte, G. Valdés, R. Navia, and J. P. Cárdenas-R, "Thermal insulation materials based on agricultural residual wheat straw and corn husk biomass, for application in sustainable buildings," *Sustainable Materials and Technologies*, vol. 20, p. e00102, 2019.

[116] K. Deepak, S. Mohan, P. Dinesha, and R. Balasubramanian, "CO2 uptake by activated hydrochar derived from orange peel (citrus reticulata): Influence of carbonization temperature," *Journal of Environmental Management*, vol. 342, p. 118350, 2023.

[117] S. Gupta, A. Kashani, and A. H. Mahmood, "Carbon sequestration in engineered lightweight foamed mortar – effect on rheology, mechanical and durability properties," *Construction and Building Materials*, vol. 322, p. 126383, 2022.

[118] R. Roychand, J. Li, S. Kilmartin-Lynch, M. Saberian, J. Zhu, O. Youssf, and T. Ngo, "Carbon sequestration from waste and carbon dioxide mineralisation in concrete – a stronger, sustainable and eco-friendly solution to support circular economy," *Construction and Building Materials*, vol. 379, p. 131221, 2023.

Chapter 3

Material and Methods

3.1 Materials

Throughout the realization of the research work presented in this thesis, various materials were analyzed and applied. This section covers exclusively the materials directly obtained by local and national suppliers. Moreover, further information regarding additional materials selected through a thorough literature review is given.

3.1.1 Winery and distillery by-products

During this research work, winery and distillery by-products were used in Paper A, aimed at the optimization of HTC process parameters, to which I contributed, and to perform the pyrolysis and combustion kinetic analysis within Paper B. Moreover, the elaboration of Paper D relied on the utilization of the mass and energy balance derived from the HTC laboratory experiments conducted on these materials.

Vine pruning (VP) used for the experiments was obtained from a local farm in Umbria, located in the Center of Italy, while exhausted grape marc (EGM) and vinasse were collected from the Bonollo distillery (Italy) after ethanol and tartaric acid extraction by the distillation process. VP (moisture content as received of 42 wt%) and EGM (moisture content as received of 71 wt%) were dried at 105°C for 24 h to remove residual moisture. Subsequently, dried biomasses were milled to a final particle size smaller than 500 μm to obtain a uniform size distribution of the particles. Vinasse was also filtered with a 3 μm filter paper before its use in the HTC experiments.
Table 3.1 summarize the chemical and physical characterization of VP, EGM, and vinasse.

Table 3.1: *Physicochemical characteristics of winery and distillery by-products.*

	VP	**EGM**	**Vinasse**
Ultimate Analysis [wt%$_{daf}$]			
C	44.52	46.71	
H	6.97	6.84	
N	0.84	2.33	
S	0.05	0.12	
O	44.10	36.54	
Proximate Analysis [wt%$_{db}$]			
Volatile matter	76.07	71.03	
Ash	3.52	7.46	
Fixed carbon	20.41	21.51	
Lower Heating Value [MJ/kg,db]	17.59	19.20	
Compositional analysis [wt%$_{db}$]			
Cellulose	31.46	11.50	
Hemicellulose	12.37	7.31	
Lignin	30.29	43.14	
Extractives	6.27	11.83	
Liquid analysis			
pH			5.18
COD [mg/l]			23304
BOD [mg/l]			10440
TOC [mg/l]			9710
Total N [mg/l]			231
Total Phenols [mg_{GAE}/l]			781

Note: db: dry basis; daf: dry and ash-free bases

3.1.2 Municipal solid waste

Within Paper E, the stabilized organic fraction (SOF), the landfill leachate (LL), and the concentrate fraction (CF) of the reverse osmosis of LL were obtained from the same MSWs management plant located in Viterbo, Italy. The SOF was collected from the MBT and locally sieved down to a particle size of approximately 2.5 mm before the laboratory experiments to remove any inorganic residues, e.g. glass, metal, plastic, paper, etc. The LL was spilled from the MSW landfill while the CF came from the reverse osmosis plant, both located in the same area as the MBT plant. The LL and CF were gathered in plastic containers and stored at a temperature of +4°C.
The average values of the main chemical-physical parameters obtained for each substrate are listed in ***Table 3.2***.

Table 3.2: *Physicochemical characteristics of the SOF, LL, and CF.*

Fraction	**Substrate**	
Solid	*SOF*	
Ultimate Analysis [wt%$_{daf}$]		
C	22.40	
H	3.20	
N	1.37	
O	17.80	
Proximate Analysis [wt%$_{db}$]		
Ash	55.82	
Volatile matter	41.79	
Fixed carbon	2.39	
Liquid	*Landfill Leachate (LL)*	*Concentrate Fraction (CF)*
pH	7.9	6.8
BOD [mg/l]	2150	638
COD [mg/l]	8380	2490
Conductivity [mS/cm]	25.6	23.7
Total solids [%]	2.0	1.4

Note: db: dry basis; daf: dry and ash-free bases

3.1.3 Additional materials

Among the research activities, a focus was the study and retrieval of data concerning the state of the art of processes for the enhancement of biomass waste and residue. As already mentioned, attention was paid to the HTC. In detail, the hydrochar was considered to be eligible for metallurgical applications. In this context, for the elaboration of Paper C the use of the hydrochar was evaluated as a substitute to coal (anthracite) in the electric arc furnace as injected material and reducing agent, in comparison to other biochars obtained via pyrolysis and torrefaction.
The fuel properties and characteristics of the anthracite coal and each biochar sample were obtained from a thorough literature review [1–3], and listed in ***Table 3.3***. The biochar from torrefaction, slow pyrolysis, and HTC were named respectively "T300", "P500" and "H220" while the anthracite coal was "Ac".

Table 3.3: *Proximate and ultimate analysis of Ac [3], H220 [2], T300 and P500 [1].*

Materials	**Proximate Analysis [wt%$_{db}$]**			**Ultimate Analysis [wt%$_{daf}$]**			
	Ash	*VM*	*FC*	*C*	*H*	*N*	*O*
Ac	10.7	9.2	80.1	91.7	3.5	1.9	1.3
T300	36.6	42.2	21.2	67.6	5.3	1.8	24.9
P500	52.4	25.4	22.2	82.3	3.6	1.8	11.8
H220	6.7	72.5	18.3	51.9	4.8	0.04	43.2

Note: db: dry basis; daf: dry and ash-free bases

3.2 Characterization

3.2.1 Ultimate analysis

Ultimate analysis was performed by using a LECO Truspec C-H-N analyzer, in compliance with UNI EN 15104 standard method. The total content of sulfur was determined following the UNI EN 15289 (method A) by using the inductively coupled plasma emission spectrometer (Optima2000DV, Perkin Elmer). The oxygen content was calculated by difference as:

$$O[\%] = 100 - (C + N + H + S + Ash) \tag{3.1}$$

3.2.2 Proximate analysis

Proximate analysis was carried out following the standards EN 14774-2 for the moisture content, EN 15148 for the volatile matter (VM), and EN 14775 for the ash content, by using a thermogravimetric analyzer (TGA-701, LECO Co., USA). Fixed carbon (FC) was computed by difference according to ***Equation*** (3.2). Each analysis were conducted in triplicate.

$$FC[\%] = 100 - (Moisture + Volatiles + Ash) \tag{3.2}$$

3.2.3 Compositional analysis

Compositional analysis, in terms of hemicellulose, cellulose, lignin, and extractives contents was performed according to the National Renewable Energy Laboratory (NREL) protocols [4]. Non-structural materials in biomass often contribute significantly to mass closure and will interfere with the characterization of carbohydrates and lignin. The procedure described in [5] was followed to both remove and quantify the extractives in the biomass samples, using a two-step process sequentially with water and ethanol in a Soxhlet apparatus.
After the extraction process, the determination of structural carbohydrates and lignin content followed the procedure described in [6].
Structural carbohydrates and lignin make up the bulk of most feedstocks and often represent the most interesting portions. The structural carbohydrates are typically divided into two groups, cellulose and hemicellulose. The procedure used a two-step acid hydrolysis to fractionate the biomass. Briefly, after hydrolysis the solids were separated from the liquid and the fractions were analyzed separately. During hydrolysis, the polymeric carbohydrates are hydrolyzed into monomeric forms, which are soluble in the hydrolysis liquid. The liquid fraction hydrolyzed was analyzed via high-pressure liquid chromatography (HPLC). Acetyl groups were also quantified. The solid residue was processed by a gravimetric method in a muffle furnace, to determine the acid insoluble lignin content [7].

3.2.4 Heating value

The higher heating value (HHV) of the samples was measured according to the UNI EN ISO 18125:2018 by means of a isoperibolic calorimeter (AC-350, LECO

Corporation). Then, the lower heating value (LHV) was calculated as the difference between the HHV and the latent heat of vaporization of water (q_v = 2.26 MJ/kg) [8] as:

$$LHV[MJ/kg] = HHV - q_v(w + 9H) \tag{3.3}$$

where H is the hydrogen content, and w is the moisture content.

3.2.5 Specific surface area

In Paper E, the specific surface area of the hydrochar samples was examined with an ASAP 2460 surface area analyzer (Micromeritics, USA). Based on the Brunauer-Emmett-Teller (BET) method [9] the specific surface area was measured based on nitrogen adsorption isotherm curves at 77 K. The samples were degassed at 150°C before nitrogen adsorption. The instrument measures the amount of nitrogen gas adsorbed onto the surface of the hydrochar samples, producing an adsorption isotherm at each pressure point. These isotherms are then used to determine the specific surface area using the BET equation. The BET equation is a mathematical model that relates the amount of gas adsorbed to the equilibrium pressure, allowing for the calculation of the monolayer gas adsorption capacity. From this capacity, the specific surface area of the hydrochar samples can be determined.

3.2.6 Analysis of liquid samples

In Paper B, feedwater and aqueous phases were characterized in terms of pH, total organic carbon (TOC), total nitrogen (TN), chemical and biological oxygen demand (COD, BOD), and TPC. pH was determined using a pH meter (HI 2221-02, Hanna instruments). COD, BOD, and TOC were determined according to Standard Methods [10]. Total nitrogen is determined by a modified Kjeldahl method [11] through microwave digestion (CEM Mars Xpress, Matthews) with a mixture of 37% HCl and 30% H_2O_2 and the following spectrophotometric determination of ammonium using the nitroprusside method [7]. Total phenols content is determined by means of a spectrophotometer at 750 nm wavelength with Folin-Ciocalteu reagent [12]. The results are expressed as mg of gallic acid per L of liquid fraction.

3.3 Hydrothermal carbonization

A stainless-steel Parr 4560 mini-batch reactor with a volume of 600 ml was used for the hydrothermal carbonization treatment. The removable ceramic band heater was connected to the external control system (4848 reactor controller, Parr Instrument) which allowed the setting of both the temperature and the rotational speed of the stirrer. For each experimental run, the vessel was loaded with the solid and liquid substrate and purged with nitrogen to remove the air from the reactor. The reactor was heated up to the desired temperature with a heating rate of 3°C/min while the stirring rate was set to 200 rpm. The residence time refers to the holding time of the reactor after reaching the temperature set point. Then, the

internal cooling coil connected with an external chiller allowed for an immediate decrease in temperature by the coolant. The system is reported in ***Figure 3.1***. Thus, the liquor was separated by using a Büchner funnel with a vacuum pump and filter paper (Whatman filter paper, 8 μm). While the hydrochar was washed with distilled water several times and oven-dried at 105°C for 24 h to remove residual moisture, the liquid fraction was collected and maintained at +4°C for further analyses.
The mass yield (MY) of the HTC process was calculated as the ratio of the mass of hydrochar (M_f) to that of the initial feedstock (M_0) on a dry basis by using ***Equation*** (3.4).

$$MY = \frac{M_f}{M_0} * 100\ [\%] \tag{3.4}$$

Moreover, within the elaboration of Paper E the deashing efficiency (DE) of the HTC process was evaluated according to ***Equation*** (3.5),

$$DE = \frac{Ash_{feedstock} - (Ash_{Hydrochar,i} * MY_i)}{Ash_{feedstock}} * 100\ [\%] \tag{3.5}$$

where $\text{Ash}_{feedstock}$ is the ash content of the raw biomass before the HTC treatment, and $\text{Ash}_{Hydrochar,i}$ is the ash content of the hydrochar obtained from the HTC process regarding the i-th test with a mass yield of MY_i.

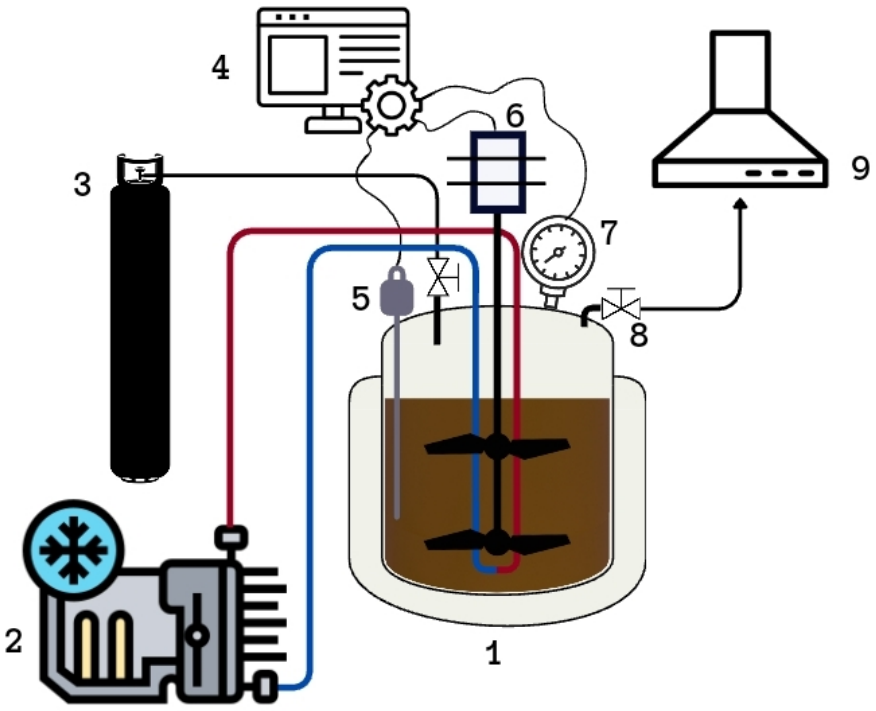

Figure 3.1: *HTC reactor system: 1) HTC reactor; 2) Cooling system; 3) N_2 gas inlet; 4) External control system; 5) Thermocouple; 6) Stirring system; 7) Pressure gauge; 8) Gas outlet; 9) Aspiration system*

3.4 Hydrodynamic cavitation

When the HTC process is scaled up to industrial size, the homogenization and viscosity of the solid and liquid substrate mixture become essential parameters affecting its pumpability. The pumpability of the slurry is limited by the type of pump, which generally has an upper limit of about 10–15% solids (dry basis) loading [13]. Thus, to further enhance the homogenization and viscosity of the solid and liquid substrate mixture before the HTC process, the application of hydrodynamic cavitation (HC) was investigated in this research work.

HC is a promising physicochemical process consisting of the phenomenon of formation, growth, and rapid collapse of vapor cavities due to the reduced local pressure [14]. The HC was performed by using single-step homogenization with a controlled cavitation approach patented by SOLDO Cavitators [15]. The cavitation unit, displayed in ***Figure 3.2***, is composed of a feed tank and a 5.5 kW electric motor which provides power to a stainless steel rotor (cavitator) working at 20 L/min, 3 bar, and 3600 rpm. The solid and liquid substrates were mixed at the desired solid-to-liquid ratio and pumped inside the cavitator in a closed loop until the flow temperature reached the desired temperature set point.

Figure 3.2: *Cavitation unit patented by SOLDO Cavitators [15].*

3.5 Statistical method

Statistical experiments were conducted to analyze the intricate interconnections between the key parameters and properties involved in the production of the hydrochar. Specifically,Box-Behnken experimental design (BBD), Central Composite Face-Centered Design (CCF-CD) and Response Surface Methodology (RSM) were utilized for this purpose. BBD and CCF-CD are a type of experimental design that allows for the exploration of a response variable by systematically varying the levels of input (or independent) variables. They are particularly useful when the relationship between the independent variables and the response variable is nonlinear or when there are interactions among the variables.

BBD consists of a replicated center point along with a collection of points situated at the midsection of every edge within the multidimensional cube delineated by the specified levels. On the other hand, CCF-CD involves setting up a design matrix that includes a combination of factorial points, axial points, and center points. The factorial points allow for the estimation of main effects, while the axial points enable the assessment of curvature and interaction effects. The center points are used for estimating experimental error and checking the model's adequacy.
A three-level, 3-factor BBD was employed in Paper A, while a three-level, 2-factor CCF-CD in Paper E. The independent variables were coded at three levels (-1, 0, and $+1$), corresponding to the minimum, medium and maximum levels. Each process factor level was carefully selected based on preliminary tests. Besides, three properties were chosen as responses.

By analyzing the response at different levels of the independent variables, the optimal conditions for achieving the desired response can be determined. RSM helps to pursue this aim by finding the relationship between the response variable and the independent variables, identifying significant factors, and optimizing the response within the experimental region. By using mathematical modeling and response surface analysis, RSM enables to understand the relationship between the input variables and the response variable, make predictions, and optimize the process to achieve desired outcomes. To find a suitable approximation for the relationship between the response and the set of factors, a second-order (quadratic) polynomial equation was used according to ***Equation*** (3.6),

$$Y_i = \beta_0 + \sum_{i=1}^{k} \beta_i X_i + \sum_{i=1}^{k} \beta_{ii} X_i^2 + \sum \sum_{j<i=2}^{k} \beta_{ij} X_i X_j \tag{3.6}$$

where Y_i is the predicted i-th response, β_0 is the intercept coefficient, β_i, β_{ii} and β_{ij} are interaction coefficients of linear, quadratic, and the second-order terms, k is the number of independent parameters, and X_i and X_j are the independent variables.
The software Minitab v17.1.0 (Minitab Ltd., Coventry, UK) was used to implement the statistical model. The statistical significance of the regression coefficients was examined by using analysis of variance (ANOVA) and regression analysis. This was accomplished by using the Fisher's F-test at a 95% confidence level. The coefficient of determination (R^2), the adjusted coefficient of determination (R^2_{adj}), the lack of fit (LOF) test, and the degrees of freedom (DF) were analyzed to evaluate the adequacy of the quadratic models. In detail, the accuracy of the experimental data is measured by R^2 while the R^2_{adj} values determine the deviation of data predicted from the models. High differences values between these coefficients are due to the non-significant model terms. Furthermore, the lack of fit test was carried out by comparing the variability of the actual model residuals to the variability between observations at replicate settings of the factors. A model is statistically significant at the 95% confidence level if the P-value of the lack of fit test is higher than 0.05. Furthermore, multi-response analysis, based on Derringer's desirability function, was used to concurrently optimize the response variables [16]. Each response (Y_i) is converted into an individual desirability function (d_i), ranging from 0 to 1, respectively the least and the most desirable case. It can be expressed by 3.7,

$$d_i = \begin{cases} 0 & Y_i \leq L_i \\ \left[\dfrac{Y_i - L_i}{U_i - L_i}\right]^r & L_i < Y_i \leq L_i \\ 1 & Y_i > U_i \end{cases} \tag{3.7}$$

where L_i, U_i denote the lowest and highest values of Y_i, while r is denoted as the shape function for desirability, which is assumed as 1 in the case of linear dependence.
According to the degree of optimization of the response Y_i, 0 and 1 are respectively the least and the most desirable cases.
The individual desirability are then combined into a composite desirability function (D) using the geometric mean, and when equal weightage are given and an importance parameter equal to 1 is assumed for all responses, can be determined as:

$$D = (d_l \times d_2 \times ... \times d_k)^{1/k} \tag{3.8}$$

This single value of D gives the overall assessment of the desirability of the combined response levels. D is a dimensionless function whose values fall in the interval [0, 1]. D increases as the balance of the properties becomes more favorable. Ence, when all the responses are on-target ($d_i = 1$ for every response), D is equal to 1. Also, if any $d_i = 0$ (that is, if one of the response variables is outside the specification limits) then D = 0 (that is, the overall product is unacceptable).

3.6 Thermogravimetric analysis

A TGA/DSC 3+ STARe System (Mettler Toledo, USA) was used to perform thermogravimetric analysis (TGA) included in Paper B. The samples were placed in a 70 μl Al_2O_3 pan and heated from room temperature (about 25°C) to 800°C at constant heating rates of 10, 20, 30, and 40°C/min, assuming that complete degradation of the sample is achieved at this temperature. Two gas atmospheres of nitrogen (N_2) and air (21%O_2/79%N_2) were used respectively to simulate pyrolysis and combustion conditions with a gas flow rate of 50 mL/min. To ensure reliable results, each test was replicated three times, and the averages were calculated to account for experimental reproducibility, which fell within the range of ±3%. Before each test, a blank run was performed using an empty pan to compensate for buoyancy effects. The weight loss (TG) curves and their respective first-order derivatives (differential thermogravimetric (DTG)) were recorded over time and temperature. Several parameters were directly computed by analyzing the results to identify the main pyrolysis and combustion characteristics, i.e. the initial temperature (T_i), the final temperature (T_f), and the peak temperature (T_p). T_i represents the temperature at which a conversion of 1% of the initial mass is obtained after the initial weight loss caused by the moisture. T_f is the temperature at which the degradation is almost complete and was defined as the temperature at which the conversion rate reaches 1%/min at the end of the DTG curve. The fuel reactivity was considered by accounting T_p which corresponds to the temperature of the maximum weight loss rate. Lower reactivity is determined by higher peak temperature [17].

3.7 Kinetic, reaction mechanism, and thermodynamic analysis

The integral iso-conversional methods of Starink (STK) [18], Kissinger-Akahira-Sunose (KAS) [19], and Ozawa-Flynn-Wall (OFW) [20, 21] were used for studying the decomposition kinetics by using data obtained from TGA within Paper B. According to the Arrhenius equation, the general equation of reaction rate can be expressed by ***Equation*** (3.9):

$$\frac{d\alpha}{dt} = k\left(T\right) f\left(\alpha\right) = Ae^{-\left(E_a/RT\right)} f\left(\alpha\right) \tag{3.9}$$

where t is the time, T is the absolute temperature (K), A is the pre-exponential factor (s^{-1}), E_a is the apparent activation energy (kJ/mol), and R is the gas constant (8.314 J/mol K), and f(α) is the reaction mechanism.
The conversion degree α during the reaction of the sample can be defined as:

$$\alpha = \frac{m_0 - m_t}{m_0 - m_f} \tag{3.10}$$

where m_0 and m_f represent the initial and final weights of the sample respectively, and m_t represents the weight of the sample at time t.
Rearranging ***Equation*** (3.9) by introducing the constant heating rate β=dT/dt the differential form of the non-isothermal rate law becomes:

$$\frac{d\alpha}{dT} = \frac{A}{\beta} e^{-\left(E_a/RT\right)} f(\alpha) \tag{3.11}$$

Since the differential form exhibits low accuracy, leading to scattered derivative curves, the integral form of ***Equation*** (3.11) is usually more suitable for determining activation energy values [22, 23], which brings to ***Equation*** (3.12).

$$g\left(\alpha\right) = \int_0^\alpha \frac{d\alpha}{f(\alpha)} = \frac{A}{\beta} \int_{T_0}^{T} e^{-\left(E_a/RT\right)} dT \tag{3.12}$$

As the integral form (***Equation*** (3.12)) does not have an analytical solution, the approximate solutions of STK (***Equation*** (3.13)), OFW (***Equation*** (3.14)), and KAS (***Equation*** (3.15)) were considered to determine the kinetic parameters, since iso-conversional methods can obtain reliable kinetics parameters by using multiple heating rates without requiring the reaction model [22].

$$\ln\left(\frac{\beta}{T^{1.92}}\right) = -1.0008\frac{E_a}{RT} + Const \tag{3.13}$$

$$\ln\left(\beta\right) = ln\left(\frac{AE_a}{Rg(\alpha)}\right) - 5.331 - 1.052\frac{E_a}{RT} \tag{3.14}$$

$$\ln\left(\frac{\beta}{T^2}\right) = ln\left(\frac{AR}{E_\alpha g(\alpha)}\right) - \frac{E_a}{RT} \tag{3.15}$$

For the STK method, the activation energy can be obtained from the slope of the fitted straight line by plotting $\ln(\beta/T^{1.92})$ vs. 1/T at the given conversion

degree α. Similarly, by using the OFW method, based on Doyle's approximation [24, 25], a linear relationship is established by plotting $\ln(\beta)$ against 1/T and the resulting slope is equal to $-1.052E_a/R$. Lastly, from the KAS method, the value of E_a can be determined from the slope of the fitted straight line formed by using $\ln(\beta/T^2)$ vs. 1/T.

While iso-conversional methods are highly accurate in determining E_a values, they do not provide information about the pre-exponential factor. Thus, the energy compensation effect (ECE) method was used to estimate the values of A. By taking the logarithm on both sides of ***Equation*** (3.11) and rearranging the terms, ln A_i and $E_{a,i}$ can be calculated from the intercept and the slope of the regression lines by plotting $\ln[\beta(d\alpha/dT)/f_i(\alpha)]$ vs. 1/T, where i refers to the mechanism function listed in ***Table A.1*** reported in Appendix (***Section A.1***). The linear relationship between $E_{a,i}$ and ln A_i, known as the compensation effect and described by ***Equation*** (3.16), allows to find the compensation parameters a and b [26].

$$lnA_i = aE_{a,i} + b \tag{3.16}$$

Once the compensation parameters are determined, the values of A are obtained with ***Equation*** (3.16) by using the E_a values beforehand determined by an iso-conversional method.

To complete the kinetic triplet is essential to determine the decomposition mechanism, which could be predicted by the master-plot method. By approximating to zero the lower limit (T_0) of the integral on the right side of ***Equation*** (3.12), as the rate of decomposition is extremely slow at ambient temperature [27, 28], the mentioned equation can be rewritten in ***Equation*** (3.17):

$$g(\alpha) = \frac{AE_a}{\beta R} p(u) \tag{3.17}$$

where $p(u) = \int_{\infty}^{u} -\left(\frac{e^{-u}}{u^2}\right) du$ is the temperature integral and $u=E_a/RT$. p(u) has no analytical solution and can be expressed by numerical approximation as Doyle's (***Equation*** (3.18)), which gives sufficiently reliable results [29].

$$p(u) = 0.0048e^{-1.0516u} \tag{3.18}$$

Using a reference at point α=0.5 and according to ***Equation*** (3.17), ***Equation*** (3.19) is obtained:

$$\frac{g(\alpha)}{g(0.5)} = \frac{p(u)}{p(u_{0.5})} \tag{3.19}$$

Thus, the experimental curves plotted as $p(u)/p(u_{0.5})$ for a given α, using data obtained at various heating rates, and the theoretical master plot represented as $g(\alpha)/g(0.5)$ are comparable when an appropriate kinetic model is employed.

Establishing thermodynamic parameters such as changes in enthalpy (ΔH), Gibbs free energy (ΔG), and entropy (ΔS) is a prerequisite for scaling up a process to industrial level, as it enables accurate energy calculations [30, 31]. These parameters were evaluated using kinetic data (E_a and A) and thermogravimetric data points according to ***Equations*** (3.20) to (3.22), where k_B is the Boltzmann constant (1.381×10^{-23} J/K), and $\hbar$ is the Plank constant (6.626×10^{-34} J/s).

$$\Delta H = E_a + RT \tag{3.20}$$

$$\Delta G = E_a + RT_p ln\left(\frac{k_b T_p}{\hbar A}\right) \tag{3.21}$$

$$\Delta S = \frac{\Delta H - \Delta G}{T_p} \tag{3.22}$$

3.8 Computational Fluid Dynamic Analysis (CFD)

Energy and resource efficiency are crucial factors for the economic production of industrial plant. Plant experiments, which would be required to assess the impact of various optimisation techniques, are costly and generally avoided for safety concerns. Trials, in general, should not disrupt existing operations, and there are not many pilot industrial facilities accessible for testing. An alternative is a numerical simulation. Computational Fluid Dynamics (CFD) resources can solve interpenetrating physical phenomena such as the solid particles combustion and also evaporation, likewise the turbulence and the radiation together. CFD is a sophisticated simulation tool with the potential to afford a comprehensive model for industrial applications like EAF [32–34].

Following are described the computational and numerical techniques applied to investigate biochar combustion and electrode radiation inside an EAF, formulated in Paper C.

3.8.1 Numerical model

Fluid and thermodynamic processes are described by the Navier-Stokes (NS) equations, balancing the fluxes of mass, momentum, energy, and species. The commercial software ANSYS Fluent was employed. To decrease the computational effort necessary to run numerous design simulations and obtain trustworthy findings, the steady-state Reynolds-Averaged Navier-Stokes (RANS) approach was adopted [32]. The pressure velocity coupling is achieved through the COUPLED algorithm. The Realizable k-ε model was applied in the model to solve the turbulence, which agrees well with experimental data of gas flows with coal particles combustion [35]. The proposed model includes different types of mathematical methods such as turbulent flows, multi-phase particle interaction, combustion reactions and radiation heat transfer. Hence, the following sub-models were applied. The discrete phase model (DPM) is a useful method to simulate the particle trajectory [36–38]. Since anthracite and each biomass sample were crushed and milled, the particles diameter distribution was considered uniform. The discrete random walk model was enabled for stochastic tracking of particles due to turbulence in the fluid phase. ANSYS Fluent can simulate chemical species mixing and transport by solving conservation equations that describe convection, diffusion, and reaction sources for each component species. The species transport model was chosen to solve these equations and the volumetric reaction option was enabled. Besides, the Eddy-Dissipation model (EDM) was applied, assuming the reaction rates to be controlled by turbulence [39, 40]. The P1 radiation model was adopted in the present model to efficiently solve the radiation arising from the electrodes and combustion processes [41–43].

3.8.2 Biomass combustion

A mathematical explanation of biomass combustion, on the other hand, is complicated. The proposed model contains heterogeneous surface reactions as well as gas-phase reactions and a global reduced chemistry mechanism, considered a practical compromise for modelling biomass combustion applied to industrial burner optimisation. The primary physical and chemical processes that occur during combustion when biomass particles are injected into the furnace are heating, devolatilization (volatile release), homogenous reactions of gaseous species (volatile combustion) and heterogeneous reaction (char oxidation) [44–46].

Particle transport

The Euler-Lagrange technique, commonly known as Discrete Phase, was used to solve the particle interaction. The fluid phase is handled as a continuum by solving the NS equations whereas the dispersed phase is addressed by tracking a large number of particles through the predicted flow field. The dispersed phase can exchange momentum, mass, and energy with the fluid phase [41]. A surface reaction occurs when the volatile components of the particle have fully changed phase, consuming the combustible fraction. Surface combustion consumes the particle's reactive content in the DPM. The types of oxidant and product species were defined in the injection properties tab in Fluent.

Particle heating and drying

During the initial stage of biomass fuel burning, water from the solid fuel particle is heated and evaporated. The vaporisation temperature of biomass volatiles is commonly thought to be significantly higher than that of water. Ansys Fluent's energy equation (***Equation*** (3.23)) depicts the conduction, convection, radiation heat transfer, and enthalpy of vaporisation during the drying process:

$$m_p c_p \frac{dT_p}{dt} = hA_p \left(T_\infty - T_p\right) + A_p \varepsilon_p \sigma(\theta_R^4 - T_p^4) - Q_v \tag{3.23}$$

where m_p, c_p, T_p, A_p, ε_p are the mass (kg), specific heat capacity (J/kg K), temperature (K), surface area (m^2) and emissivity of the particle, respectively. T_∞, h, σ, θ_R and Q_v are the continuous phase local temperature (K), convective heat transfer coefficient (W/m^2K), Stefan-Boltzmann constant ($5.67 \times 10^{-8} W/m^2K^4$), radiation temperature (K) and heat transfer due to vaporisation, respectively.

Devolatilization

The devolatilization of the particle material begins after the initial phase of heating and evaporation. Volatiles are commonly released during the pyrolysis of biomass at temperatures ranging from 160 to 300°C [47]. We assumed the devolatilization temperature of each biochar according to the literature results [1, 2], respectively 304°C, 366°C and 292°C for the biochar from torrefaction, slow pyrolysis and hydrothermal carbonization. The single kinetic rate and the constant rate devolatilization model are the most often used devolatilization models for biomass [48]. In the first model, the devolatilization rate is determined by the quantity of volatiles left in the biomass particle and the reaction rate, K, is defined

by the input of the pre-exponential factor, A, and the activation energy, Ea, in the single-step first-order Arrhenius reaction (***Equation*** (3.24)).

$$K = Ae^{-(E_a/RT)} \tag{3.24}$$

Instead, the constant rate model dictates that volatiles are released at a constant rate, defined as:

$$\frac{dm_{vol}}{dt} = -A_0 m_{vol,0} \tag{3.25}$$

where $m_{vol,0}$ is the initial mass of the volatiles in the fuel particle and A_0 is the rate constant (s^{-1}). The default value of A_0 is 12 s^{-1} for coal pyrolysis [49]. In Paper C, the constant rate model was adopted. It represents a compromise of processing power and precision, which explains its widespread usage in the industry [44]. Furthermore, the default value of 12 s^{-1} for A_0 was used since it offered enough biomass devolatilization forecasts while not being unduly sensitive to its value [48].

Homogeneous reactions

During devolatilization, the volatiles generated operate as a source for gaseous combustion. The majority of biomass volatiles are CO, CO_2, H_2O, CH_4, H_2 and other inorganic compounds [42, 50]. However, in CFD simulations, the volatile gases are combined into a single "artificial" specie, $C_zH_yO_x$ or a few artificial species [44]. The combustion of volatiles was simulated by using the development of a representative molecule with an atomic composition determined by proximate and ultimate analysis (***Table 3.3***) and an estimated molecular weight of 30 g/mol. For a more accurate approach, the oxidation of the hydrocarbon species was accomplished by employing the global two-step reaction mechanism, with carbon monoxide as the intermediate species. The resulting two-step stoichiometry is shown in ***Equations 3.26*** and ***3.27*** by using the species-transport technique in FLUENT and the built-in coal calculator.

$$C_zH_yO_xN_k + \left(\frac{z}{2} - \frac{x}{2}\right)O_2 \rightarrow zCO + \frac{y}{2}H_2O + \frac{k}{2}N_2 \tag{3.26}$$

$$CO + 0.5O_2 \rightarrow CO_2 \tag{3.27}$$

The EDM was used to achieve the chemistry-turbulence coupling for the homogeneous gas-phase reactions [41]. With this model, the net rate of generation of the species i due to reaction r, $R_{i,r}$, is provided by the smaller value calculated by ***Equation*** (3.28) or ***Equation*** (3.29). Parameters A and B are known as Magnussen constants, $v'_{i,r}$ and $v''_{i,r}$ corresponds to the stoichiometric coefficient for reactant and product respectively in reaction r, $M_{w,i}$ to the molecular weight, ε/k to the ratio of turbulent kinetic energy/dissipation rate, Y_R and Y_P to the mass fraction of any product species, P and particular reactant, R.

$$R_{i,r} = (v''_{i,r} - v\prime_{i,r})M_{w,i}A\rho\frac{\varepsilon}{k}min_R\left(\frac{Y_R}{v\prime_{R,r}M_{w,R}}\right) \tag{3.28}$$

$$R_{i,r} = (v''_{i,r} - v\prime_{i,r})M_{w,i}AB\rho\frac{\varepsilon}{k}\left(\frac{\sum_P Y_R}{\sum_j^N v\prime\prime_{j,r}M_{w,j}}\right) \tag{3.29}$$

The empirical default values of A and B by FLUENT are 4.0 and 0.5 respectively [41]. For biomass combustion, Magnussen constants A and B are recommended to be set as 0.6 and 0.5, respectively [51]. The simulations computed with these parameters are in good agreement with the observed data for CO concentration [52]. Because volatiles are gases, the models applied to homogeneous combustion are appropriate for both coal and biomass combustion.

Char combustion (heterogeneous surface reactions)

After the particle's volatile component has entirely developed, a surface reaction begins, which consumes the particle's combustible fraction (char). The combustion mechanism of the char may be described by the stoichiometry in ***Equation*** (3.30) by assuming the non-volatile fraction of the combustion particle is carbon.

$$C\,(s) + 0.5O_2 \rightarrow CO_2 \tag{3.30}$$

Surface reactions were solved by using the kinetic/diffusion-limited rate model, based on the model of Baum and Street [53] and Field [54]. The model assumes that the char surface reaction rate is defined either by reaction kinetics (ψ) or by a diffusion rate (D_0), ***Equations 3.31*** and ***3.32***, respectively and weighted to yield a char combustion rate represented in ***Equation*** (3.33).

$$D_0 = C_1 \frac{\left[\left(T_p + T_\infty\right)/2\right]^{0.75}}{d_p} \tag{3.31}$$

$$\psi = C_2 e 1^{-(E_a/RT_p)} \tag{3.32}$$

$$\frac{dm_p}{dt} = -A_p p_{ox} \frac{D_0 \psi}{D_0 + \psi} \tag{3.33}$$

The surface area (A_p), partial pressure of oxidant species (p_{ox}) in the gas around particles, diffusion rate coefficient and the kinetic rate all contribute to the weighting factor. The kinetic limited pre-exponential factor (C_2) and the kinetic limited activation energy (E_a) in ***Equations 3.32*** and ***3.33*** were acquired from the literature [1, 55] and listed in ***Table 3.4***, whereas the mass diffusion-limited rate constant (C_1) was set at the value of 5×10^{-12}.

Table 3.4: *Kinetic parameters of Ac [3], H220 [2], T300 and P500 [1].*

Materials	Ea [kJ/mol]	A [s^{-1}]
Ac	128.00	6.88×10^4
T300	97.30	1.15×10^6
P500	187.56	6.16×10^{12}
H220	171.73	1.30×10^{13}

3.9 Life Cycle Assessment (LCA)

Life cycle assessment (LCA) is a standardized framework for assessing the environmental impacts of a product or process at every stage of its life cycle, from manufacture to disposal. An LCA of a hypothetical but possible application of hydrochar as a replacement or partial substitute of fossil coal in the EAF steelmaking process was performed within Paper D.
The environmental analysis was conducted using the LCA methodology according to the ISO 14044 framework. Data were investigated through the use of the commercial software SimaPro v9.4.0.2 and the processes were mainly taken from the Ecoinvent database v3.8.

The proposed system (***Figure 3.3***) uses hydrochar instead of fossil-based carbonaceous material. The hydrochar- and anaerobic-digestion-based EAF route (base scenario) consists of the following steps:

- The milling of biomass to obtain an adequate particle size;
- Hydrothermal carbonization, where the biomass and the moisture source are converted into hydrochar, spent liquor, and gas;
- Anaerobic digestion of the spent liquor for bio-methane production;
- EAF steelmaking, where the steel scrap along with the carbon source (hydrochar) and fluxes are charged to the EAF to produce molten steel.

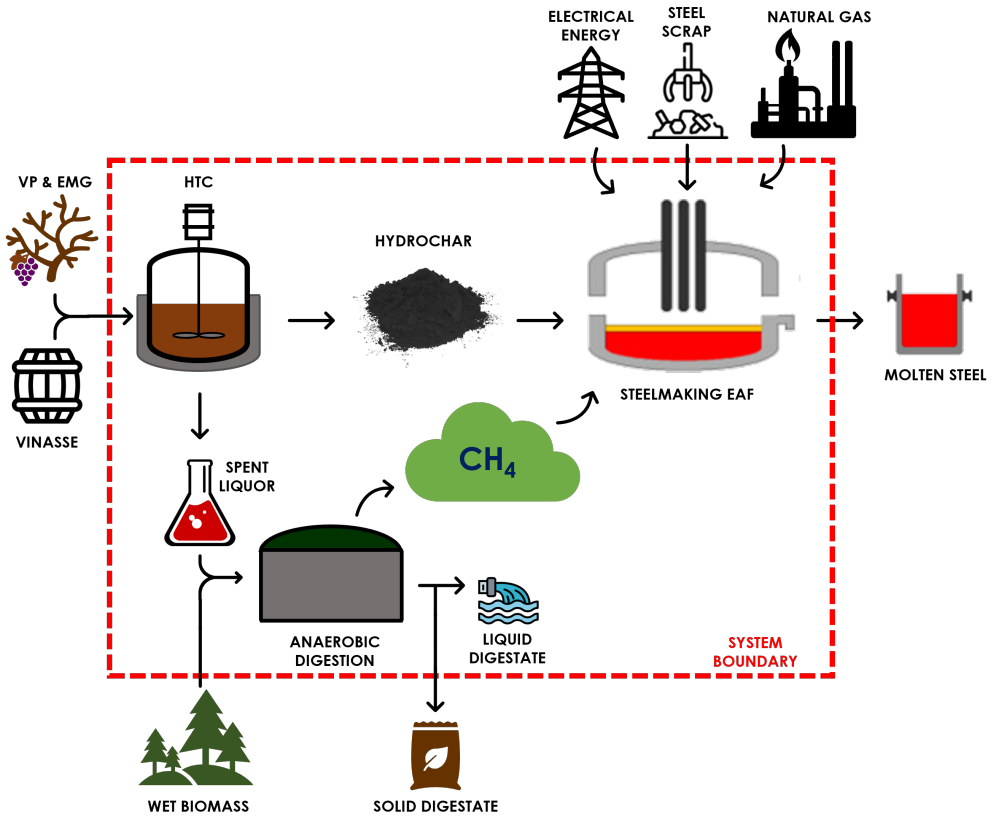

Figure 3.3: *System boundary considered in the LCA study case.*

Since the HTC process produces by-products, i.e., spent liquor and syngas, the system expansion approach was applied according to ISO 14044. Despite the possibility of recovering valuable organic chemicals from the spent liquor, with the absence of effective further treatment, no economic value would be provided by such a complex mixture [56]. In the research work discussed in Paper D, the spent liquor was chosen as a substrate for bio-methane production using the anaerobic digestion treatment. There are several studies in the literature on obtaining bio-methane using an anaerobic treatment of the wastewater from the HTC of oat husk [56], swine manure [57], sewage sludge [58], spent coffee grounds [59], agricultural and forestry waste [60], and olive pomace [61]. In the base scenario, the bio-methane was evaluated to be used as fuel for burners inside the EAF as a substitution for natural gas, thus the anaerobic digestion of the spent liquor from HTC was included in the boundary system. Furthermore, it is well known that CO_2 is the dominant gaseous species produced during the HTC process for biomass waste [62]. Hence, the gas phase discharged into the atmosphere from the HTC process was assumed to be biogenic CO_2 emission. The proposed system was compared with the traditional EAF process (traditional scenario), where the carbon source is provided directly from fossil-based carbonaceous material.
The methodology, which is described in detail in ***Section 5.2***, covers four main phases: definition of the goal and scope of the system, life cycle inventory (LCI), life cycle impact assessment (LCIA), and interpretation.

Nomenclature

Abbreviation		Y_i	predicted i-th response
VP	Vine Pruning	β_0	intercept coefficient
EGM	Exhausted Grape Marc	β_i	interaction coefficient of linear terms
HTC	Hydrothermal Carbonization	β_{ii}	interaction coefficients of quadratic terms
MBT	Mechanical Biological Treatment	β_{ij}	interaction coefficients of second-order terms
MSW	Municipal Solid Waste	R^2	coefficient of determination
SOF	Stabilized Organic Fraction	R^2_{adj}	adjusted coefficient of determination
LL	Landfill Leachate	di	individual desirability function
CF	Concentrate Fraction	D	desirability function
Ac	Anthracite coal	T_i	initial temperature (°C)
H220	biochar from HTC	T_f	final temperature (°C)
T300	biochar from torrefaction	T_p	peak temperature (°C)
P500	biochar from slow pyrolysis	t	time (s)
FC	Fixed Carbon	T	absolute temperature (K)
VM	Volatile Matter	A	pre-exponential factor (s^{-1})
HPLC	High-Pressure Liquid Chromatography	E_a	activation energy (kJ/mol)
COD	Chemical Oxygen Demand (mg/l)	R	gas constant (J/mol K)
BOD	Biochemical Oxygen Demand (mg/l)	$f(\alpha)$	reaction mechanism
TOC	Total Organic Carbon (mg/l)	α	conversion degree
TN	Total Nitrogen (mg/l)	m_0	initial weight sample
TPC	Total Phenolic Content (mg_{GAE}/l)	m_f	final weight sample
HHV	Higher Heating Value (MJ/kg)	β	heating rate (°C/min)
LHV	Lower Heating Value (MJ/kg)	a, b	compensation parameters
MY	Mass Yield (%)	ΔH	changes in enthalpy (kJ/mol)
DE	Deashing Efficiency (%)	ΔG	changes in Gibbs free energy (kJ/mol)
HC	Hydrodynamic Cavitation	ΔS	changes in entropy (J/mol K)
BBD	Box-Behnken Design	k_B	Boltzmann constant (J/K)
CCF-CD	Central Composite Face-Centered Design	$\hbar$	Plank constant (J/s)
LOF	Lack of Fit	k	turbolent kinetic energy
DF	Degrees of Freedom	ε	turbolent dissipation rate
TG	Thermogravimectric	m_p	particle mass (kg)
DTG	Differential Thermogravimetric	c_p	particle specific heat capacity (J/kg K)
STK	Starink method	A_p	particle surface area (m^2)
OFW	Ozawa-Flynn-Wall	ε_p	particle emissivity
KAS	Kissinger-Akahira-Sunose	T_∞	continuous phase local temperature (K)
ECE	Energy Compensation Effect	h	convective heat transfer coefficient (W/m^2K)
BF	blast furnace	θ_R	radiation temperature (K)
EAF	electric arc furnace	Q_v	heat transfer due to vaporisation
GHG	greenhouse gas emissions	$m_{vol,0}$	initial mass of the volatiles in the fuel particle
CFD	computational fluid dynamics	A, B	Magnussen constants
NS	Navier-Stokes	$\nu'_{i,r}$	stoichiometric coefficient for reactant
RANS	Reynolds-Averaged Navier-Stokes	$\nu''_{i,r}$	stoichiometric coefficient product
DPM	discrete phase model	r	reaction
EDM	Eddy-Dissipation model	$M_{w,i}$	molecular weight
3D	three-dimensional	Y_R	mass fraction of any product species
LCA	Life Cycle Assesment	Y_P	mass fraction of any particular reactant
Symbol		Ψ	reaction kinetics
q_v	latent heat of vaporization of water (MJ/kg)	D_0	diffusion rate
w	moisture content (%)	p_{ox}	partial pressure of oxidant species in the gas around particles
M_f	mass of hydrochar (g)	C_1	diffusion-limited rate constant
M_0	mass of the initial feedstock (g)	C_2	kinetic limited pre-exponential factor

Bibliography

[1] L. Chen, C. Wen, W. Wang, T. Liu, E. Liu, H. Liu, and Z. Li, "Combustion behaviour of biochars thermally pretreated via torrefaction, slow pyrolysis, or hydrothermal carbonisation and co-fired with pulverised coal," *Renewable Energy*, vol. 161, pp. 867–877, 2020.

[2] S. B. Kabakcı, "Pyrolysis and combustion characteristics and kinetics of wood sawdust and wood sawdust hydrochar," *Environmental Progress & Sustainable Energy*, vol. 39, no. 2, 2020.

[3] M. Gil, J. Riaza, L. Álvarez, C. Pevida, J. Pis, and F. Rubiera, "Kinetic models for the oxy-fuel combustion of coal and coal/biomass blend chars obtained in n2 and CO2 atmospheres," *Energy*, vol. 48, no. 1, pp. 510–518, 2012.

[4] National Renewable Energy Laboratory (NREL), "Biomass compositional analysis laboratory procedures," https://www.nrel.gov/bioenergy/biomass-compositional-analysis.html.

[5] A. Sluiter, R. Ruiz, C. Scarlata, J. Sluiter, and D. Templeton, "Determination of extractives in biomass. laboratory analytical procedure (lap). national renewable energy laboratory," *Golden, CO, USA*, pp. 1–9, 2008.

[6] A. Sluiter, B. Hames, R. Ruiz, C. Scarlata, J. Sluiter, D. Templeton, D. Crocker, *et al.*, "Determination of structural carbohydrates and lignin in biomass," *Laboratory analytical procedure*, vol. 1617, no. 1, pp. 1–16, 2008.

[7] M. Buratti, C. Lascaro, Elisa, and Barbanera, "Ethanol production from vineyard pruning residues with steam explosion pretreatment," *Environmental Progress & Sustainable Energy*, vol. 34, no. 3, pp. 802–809, 2014.

[8] A. Ruiz Celma, F. Cuadros, and F. López-Rodríguez, "Characterization of pellets from industrial tomato residues," *Food and Bioproducts Processing*, vol. 90, no. 4, pp. 700–706, 2012.

[9] S. Brunauer, P. H. Emmett, and E. Teller, "Adsorption of gases in multimolecular layers," *Journal of the American chemical society*, vol. 60, no. 2, pp. 309–319, 1938.

[10] American Public Health Association, American Water Works Association, Water Environment Federation, *Standard Methods for the Examination of Water and Wastewater*. APHA-AWWA-WEF, 2005.

[11] L. Domini, G. Cravotto, C. E. Canals, Antonio, and Vidal, "A simultaneous, direct microwave/ultrasound-assisted digestion procedure for the determination of total kjeldahl nitrogen," *Ultrasonics sonochemistry*, vol. 16, no. 4, pp. 564–569, 2008.

[12] T. Swain, W. E. and Hillis, "The phenolic constituents of prunus domestica. i. - the quantitative analysis of phenolic constituents," *Journal of the Science of Food and Agriculture*, vol. 10, no. 1, pp. 63–68, 1959.

[13] S. Nagarajan and V. V. Ranade, "Valorizing waste biomass via hydrodynamic cavitation and anaerobic digestion," *Industrial & Engineering Chemistry Research*, vol. 60, no. 46, pp. 16577–16598, 2021.

[14] A. Lanfranchi, G. Tassinato, F. Valentino, G. Martinez, E. Jones, C. Gioia, L. Bertin, and C. Cavinato, "Hydrodynamic cavitation pre-treatment of urban waste: Integration with acidogenic fermentation, PHAs synthesis and anaerobic digestion processes," *Chemosphere*, vol. 301, p. 134624, 2022.

[15] SoldoCavitators, "Emulsification with soldo cavitators technology," 2023. https://soldocavitators.com/omogeneizzazione-industriale/#.

[16] G. Derringer and R. Suich, "Simultaneous optimization of several response variables," *Journal of Quality Technology*, vol. 12, no. 4, pp. 214–219, 1980.

[17] J. Garcia Torrent, N. Fernandez Anez, L. Medic Pejic, and L. Montenegro Mateos, "Assessment of self-ignition risks of solid biofuels by thermal analysis," *Fuel*, vol. 143, pp. 484–491, 2015.

[18] M. Starink, "The determination of activation energy from linear heating rate experiments: a comparison of the accuracy of isoconversion methods," *Thermochimica Acta*, vol. 404, no. 1, pp. 163–176, 2003.

[19] T. Akahira and T. Sunose, "Method of determining activation deterioration constant of electrical insulating materials," *Res. Report Chiba Inst. Technol. (Sci. Technol.)*, vol. 16, pp. 22–31, 1971.

[20] T. Ozawa, "A new method of analyzing thermogravimetric data," *Bulletin of the Chemical Society of Japan*, vol. 38, no. 11, pp. 1881–1886, 1965.

[21] J. H. Flynn and L. A. Wall, "A quick, direct method for the determination of activation energy from thermogravimetric data," *Journal of Polymer Science Part B: Polymer Letters*, vol. 4, no. 5, pp. 323–328, 1966.

[22] S. Vyazovkin, A. K. Burnham, J. M. Criado, L. A. Pérez-Maqueda, C. Popescu, and N. Sbirrazzuoli, "ICTAC kinetics committee recommendations for performing kinetic computations on thermal analysis data," *Thermochimica Acta*, vol. 520, no. 1, pp. 1–19, 2011.

[23] G. D. Mumbach, J. L. F. Alves, J. C. G. Da Silva, M. Di Domenico, R. F. De Sena, C. Marangoni, R. A. F. Machado, and A. Bolzan, "Pyrolysis of cocoa shell and its bioenergy potential: evaluating the kinetic triplet, thermodynamic parameters, and evolved gas analysis using TGA-FTIR," *Biomass Conversion and Biorefinery*, vol. 12, no. 3, pp. 723–739, 2022.

[24] C. D. Doyle, "Kinetic analysis of thermogravimetric data," *Journal of Applied Polymer Science*, vol. 5, no. 15, pp. 285–292, 1961.

[25] S. Vyazovkin, A. K. Burnham, L. Favergeon, N. Koga, E. Moukhina, L. A. Pérez-Maqueda, and N. Sbirrazzuoli, "ICTAC kinetics committee recommendations for analysis of multi-step kinetics," *Thermochimica Acta*, vol. 689, p. 178597, 2020-07.

[26] H. Liu, C. Xiang, J. Mu, J. Yao, D. Ye, K. Jin, and Z. Lang, "Thermodynamic model and kinetic compensation effect of oil sludge pyrolysis based on thermogravimetric analysis," *Thermal Science*, vol. 26, no. 1, pp. 259–272, 2022.

[27] S. Singh, T. Patil, S. P. Tekade, M. B. Gawande, and A. N. Sawarkar, "Studies on individual pyrolysis and co-pyrolysis of corn cob and polyethylene: Thermal degradation behavior, possible synergism, kinetics, and thermodynamic analysis," *Science of The Total Environment*, vol. 783, p. 147004, 2021.

[28] K. Azizi, A. Moshfegh Haghighi, M. Keshavarz Moraveji, M. Olazar, and G. Lopez, "Co-pyrolysis of binary and ternary mixtures of microalgae, wood and waste tires through TGA," *Renewable Energy*, vol. 142, pp. 264–271, 2019.

[29] C. D. Doyle, "Estimating isothermal life from thermogravimetric data," *Journal of Applied Polymer Science*, vol. 6, no. 24, pp. 639–642, 1962.

[30] J. L. F. Alves, J. C. G. Da Silva, V. F. Da Silva Filho, R. F. Alves, M. S. Ahmad, M. S. Ahmad, W. V. D. A. Galdino, and R. F. De Sena, "Bioenergy potential of red macroalgae gelidium floridanum by pyrolysis: Evaluation of kinetic triplet and thermodynamics parameters," *Bioresource Technology*, vol. 291, p. 121892, 2019.

[31] A. Cardarelli, S. Pinzi, and M. Barbanera, "Effect of torrefaction temperature on spent coffee grounds thermal behaviour and kinetics," *Renewable Energy*, vol. 185, pp. 704–716, 2022.

[32] H.-J. Odenthal, A. Kemminger, F. Krause, L. Sankowski, N. Uebber, and N. Vogl, "Review on modeling and simulation of the electric arc furnace (EAF)," *steel research international*, vol. 89, no. 1, p. 1700098, 2018.

[33] E. Scheepers, Y. Yang, A. T. Adema, R. Boom, and M. A. Reuter, "Process modeling and optimization of a submerged arc furnace for phosphorus production," *Metallurgical and Materials Transactions B*, vol. 41, no. 5, pp. 990–1005, 2010.

[34] Y. Li and R. J. Fruehan, "Computational fluid-dynamics simulation of post-combustion in the electric-arc furnace," *Metallurgical and Materials Transactions B*, vol. 34, no. 3, pp. 333–343, 2003.

[35] J. Zhang, W. Prationo, L. Zhang, and Z. Zhang, "Computational fluid dynamics modeling on the air-firing and oxy-fuel combustion of dried victorian brown coal," *Energy & Fuels*, vol. 27, no. 8, pp. 4258–4269, 2013.

[36] Y. Wu, D. Liu, D. Zheng, J. Ma, L. Duan, and X. Chen, "Numerical simulation of circulating fluidized bed oxy-fuel combustion with dense discrete phase model," *Fuel Processing Technology*, vol. 195, p. 106129, 2019.

[37] A. Bhattad, J. Sarkar, and P. Ghosh, "Discrete phase numerical model and experimental study of hybrid nanofluid heat transfer and pressure drop in plate heat exchanger," *International Communications in Heat and Mass Transfer*, vol. 91, pp. 262–273, 2018.

[38] J. Broukal and J. Hájek, "Validation of an effervescent spray model with secondary atomization and its application to modeling of a large-scale furnace," *Applied Thermal Engineering*, vol. 31, no. 13, pp. 2153–2164, 2011.

[39] G. T. Marangwanda, D. M. Madyira, and T. O. Babarinde, "Coal combustion models: An overview," *Journal of Physics: Conference Series*, vol. 1378, no. 3, p. 032070, 2019.

[40] Z. Lyu, G. Li, X. Song, L. Cui, G. Ji, Z. Wang, X. Hu, and Z. Xu, "Comparative numerical analysis and optimization in downhole combustion chamber of thermal spallation drilling," *Applied Thermal Engineering*, vol. 119, pp. 481–489, 2017.

[41] T. Ahmad, S. L. Plee, and J. P. Myers, "Fluent theory guide," p. 814.

[42] L. Ma, J. Jones, M. Pourkashanian, and A. Williams, "Modelling the combustion of pulverized biomass in an industrial combustion test furnace," *Fuel*, vol. 86, no. 12, pp. 1959–1965, 2007.

[43] C. Yigit, G. Coskun, E. Buyukkaya, U. Durmaz, and H. R. Güven, "CFD modeling of carbon combustion and electrode radiation in an electric arc furnace," *Applied Thermal Engineering*, vol. 90, pp. 831–837, 2015.

[44] G. T. Marangwanda, D. M. Madyira, and T. O. Babarinde, "Combustion models for biomass: A review," *Energy Reports*, vol. 6, pp. 664–672, 2020.

[45] W. Wickramaarachchi and M. Narayana, "Pyrolysis of single biomass particle using three-dimensional computational fluid dynamics modelling," *Renewable Energy*, vol. 146, pp. 1153–1165, 2020.

[46] C. Zhang, G. Wang, X. Ning, J. Zhang, and C. Wang, "Numerical simulation of combustion behaviors of hydrochar derived from low-rank coal in the raceway of blast furnace," *Fuel*, vol. 278, p. 118267, 2020.

[47] T. P. Wampler, ed., *Applied pyrolysis handbook*. CRC Press/Taylor & Francis, 2nd ed., 2007.

[48] X. Ku, T. Li, and T. Løvås, "Effects of particle shrinkage and devolatilization models on high-temperature biomass pyrolysis and gasification," *Energy & Fuels*, vol. 29, no. 8, pp. 5127–5135, 2015.

[49] K. K. Pillai, *Influence of coal type on devolatilization and combustion in fluidized beds*, vol. 54:420. J. Inst. Energy; (United Kingdom), 1981.

[50] J. D. Smith, V. Sreedharan, M. Landon, and Z. P. Smith, "Advanced design optimization of combustion equipment for biomass combustion," *Renewable Energy*, vol. 145, pp. 1597–1607, 2020.

[51] F. A. Diaz-Mateus, H. C. Alvarez-Castro, and A. Chaves-Guerrero, "CFD simulation of sugarcane bagasse combustion in an industrial grate boiler," *DYNA*, vol. 85, no. 204, pp. 169–176, 2018.

[52] R. Scharler, T. Fleckl, and I. Obernberge, "Modification of a magnussen constant of the eddy dissipation model for biomass grate furnaces by means of hot gas in-situ FT-IR absorption spectroscopy," *Progress in Computational Fluid Dynamics, An International Journal*, vol. 3, no. 2, p. 102, 2003.

[53] M. M. Baum and P. J. Street, "Predicting the combustion behaviour of coal particles," *Combustion Science and Technology*, vol. 3, no. 5, pp. 231–243, 1971.

[54] M. A. Field, "Rate of combustion of size-graded fractions of char from a low-rank coal between 1 200°k and 2 000°k," *Combustion and Flame*, vol. 13, no. 3, pp. 237–252, 1969.

[55] L. Xinjie, S. Singh, H. Yang, C. Wu, and S. Zhang, "A thermogravimetric assessment of the tri-combustion process for coal, biomass and polyethylene," *Fuel*, vol. 287, p. 119355, 2021.

[56] H. A. Murillo, J. Pagés-Díaz, L. A. Díaz-Robles, F. Vallejo, and C. Huiliñir, "Valorization of oat husk by hydrothermal carbonization: Optimization of process parameters and anaerobic digestion of spent liquors," *Bioresource Technology*, vol. 343, p. 126112, 2022.

[57] R. Ferrentino, G. Sacchi, D. Scrinzi, G. Andreottola, and L. Fiori, "Valorization of swine manure for a circular approach through hydrothermal carbonization," *Biomass and Bioenergy*, vol. 168, p. 106689, 2023.

[58] U. K. Roy, T. Radu, and J. Wagner, "Hydrothermal carbonisation of anaerobic digestate for hydro-char production and nutrient recovery," *Journal of Environmental Chemical Engineering*, vol. 10, no. 1, p. 107027, 2022.

[59] B. Campbell, R. Thorpe, D. Peus, and J. Lee, "Anaerobic digestion of untreated and treated process water from the hydrothermal carbonisation of spent coffee grounds," *Chemosphere*, vol. 293, p. 133529, 2022.

[60] F. Deng, H. Jiang, Z. Xie, Y. Chen, P. Zhou, X. Liu, and D. Li, "Nutrient recovery from biogas slurry via hydrothermal carbonization with different agricultural and forestry residue," *Industrial Crops and Products*, vol. 189, p. 115891, 2022.

[61] J.-N. Semaan, V. Belandria, A. Missaoui, B. Sarh, I. Gökalp, and S. Bostyn, "Energy analysis of olive pomace valorization via hydrothermal carbonization," *Biomass and Bioenergy*, vol. 165, p. 106590, 2022.

[62] M. Heidari, A. Dutta, B. Acharya, and S. Mahmud, "A review of the current knowledge and challenges of hydrothermal carbonization for biomass conversion," *Journal of the Energy Institute*, vol. 92, no. 6, pp. 1779–1799, 2019.

Chapter 4

Energy application

In recent years, there has been growing interest in the utilization of agricultural residues and by-products for sustainable energy production and waste management. The research work provided in Paper A and Paper B made significant contributions in this field.
By linking the findings of Paper A with Paper B, a comprehensive understanding of the HTC process and its subsequent hydrochar utilization can be achieved. The optimization study in Paper A provides crucial insights into the most suitable HTC process conditions to obtain high-quality hydrochar. Paper B then extends the research by examining the pyrolysis and combustion kinetics of the hydrochar produced under these optimized conditions. The kinetic study in Paper B helps in assessing the thermal behavior and energy release characteristics of the hydrochar, which is essential for its efficient utilization in combustion or other energy conversion processes.

The integration of these findings paves the way for the practical implementation of HTC as a viable and sustainable waste management strategy for converting biomass residues into valuable energy resources.

4.1 Optimization of HTC process of VP and EGM – *Paper A*

Paper A, titled "*Valorization of winery and distillery by-products by hydrothermal carbonization*" [1] explores the HTC process as an efficient method for converting vine pruning and exhausted grape marc, by using vinasse as moisture source, into valuable hydrochar, recovering all the winery and distillery waste. The study investigates the optimal HTC process conditions, i.e. temperature, residence time, and solid-to-liquid ratio, that maximize the mass yield (MY), energy densification yield (EDY), phenols extraction yield (PEY), and the fuel ratio (FR), as well as minimize the energy consumption.
The optimal conditions were determined as being 246.3°C, 1.6 hours, and a liquid-to-solid ratio of 0.066. Under these conditions, the predicted values for PEY, EDY, FR, and MY were 21.88 mg_{GAE}/g, 1.21%, 0.60%, and 52.64%, respectively.
The findings of this study demonstrated a circular and environmentally sustainable approach to waste management in the winemaking industry, offering numerous advantages from economic, environmental, and social perspectives.

Economically, the proposed value chain presents opportunities for cost reduction in the management of winemaking and viticulture wastes, while also enabling their higher valorization in the energy and biochemical industries compared to the current practices. This has the potential to create new revenue streams and enhance the overall economic viability of the wine sector.
From an environmental standpoint, the implementation of this value chain has the potential to recover all wastes generated throughout the wine value chain. This holistic approach ensures that winemaking industries take responsibility for managing aspects such as pollutant emissions, resource consumption, and energy consumption. By minimizing waste and maximizing resource utilization, this approach contributes to the preservation of the environment and reduces the industry's ecological footprint.
Furthermore, the activation of this value chain has significant social implications. It can improve the quality of life and drive rural development by creating job opportunities in waste management, energy production, and the utilization of by-products. This not only ensures sustainable livelihoods but also fosters a sense of community engagement and participation. Additionally, it encourages the local population and authorities to prioritize environmental protection and the recovery of viticulture by-products, promoting a culture of sustainability and responsible waste management.

4.1.1 Experimental design and process parameters

The BBD experimental design included a total of 15 tests, with 3 replicates at the central point. Temperature (A), residence time (B), and S:L ratio (C) were assumed as independent variables, and reported in ***Table 4.1*** with their coded values. Besides, mass yield (MY), energy densification yield (EDY), fuel ratio (FR), phenols extraction yield (PEY), and energy input (EI) consumption as response variables.
As previously mentioned in ***Section 3.3***, MY was calculated according to ***Equation*** (3.4), while EDY, FR, and PEY are calculated as follow:

$$EDY = \frac{LHV_h}{LHV_f} \tag{4.1}$$

$$FR = \frac{FC}{VM} \tag{4.2}$$

$$PEY[mg_{GAE}/g] = \frac{((TPC * V_l) - (TPC_w * V_w))}{MF} \tag{4.3}$$

where:

- EDY was obtained by the ratio between lower heating value of hydrochar (LHV_h) and feedstock (LHV_f);
- FR by dividing fixed carbon content of the sample by its volatile matter content;
- PEY by considering the total phenols content (TPC) in the liquid fraction (expressed as mg of gallic acid equivalents (mg_{GAE}) per mL), the volume of

the liquid fraction (V_l, expressed in mL), the total phenols content (TPC_w) in the feedwater (expressed as mg of gallic acid equivalents per mL), and the volume of the feedwater (V_w, expressed in mL).

Table 4.1: *Independent variables, range values, and coded levels in experimental design.*

Independent variables	Symbols	Coded levels		
		−1	**0**	**1**
HTC temperature [°C]	A	180	220	260
Residence time [h]	B	1	4	7
S/L ratio	C	0.05	0.15	0.25

Moreover, a simplified calculation of the energy input for the thermal treatments was also performed considering the energy required to heat water and biomass in a closed batch system and the heat loss from the reactor.
The initial temperature in the reactor system was assumed to be 25 °C and heat released and absorbed by chemical reactions was neglected because HTC reactions are net exothermic based on external energy input to work at ideal temperatures [2]. The energy input (EI) at different operating conditions was calculated as follows:

$$\begin{aligned} EI[kJ] = [m_{water} * (H_{water,HTC} - H_{water,25})] \\ + [m_{feedstock} * c_{p,feedstock} * (T_{HTC} - 25)] \\ + \left[A_s * \frac{k}{s} * (T_{HTC} - 25) * t\right] \end{aligned} \quad (4.4)$$

being m_{water} (kg) and $m_{feedstock}$ (kg) the water and biomass weight of the mixture, respectively, while $H_{water,HTC}$ and $H_{water,25}$ the enthalpy of water at the HTC temperature and at 25°C. Moreover, A_s is the surface area of the reactor (0.041 m^2), k and s are the thermal conductivity of the insulation (0.042 W/mK) and the thickness of the insulation (0.075 m) material.
The specific heat capacity of the biomass, $c_{p,feedstock}$ (J/kgK), was calculated through ***Equation*** (4.5) by assuming a mean temperature between the HTC temperature and 25 °C.

$$c_{p,feedstock} = 2300 - 1150 * e^{-0.0055T} \quad (4.5)$$

Such a calculation does not account for water vaporization enthalpy because phase change is avoided in the HTC process and for drying the produced hydrochar.

4.1.2 Results discussion

Elemental analysis of hydrochars

Table 4.2 shows the elemental composition of the hydrochar obtained under different HTC conditions. It can be noted that the carbon content significantly

increases with increasing carbonization temperature while residence time and solid-to-liquid ratio do not have a prominent effect on the C content. In addition, the HTC conditions have no statistically significant effect on the hydrogen, nitrogen, and sulfur content of the hydrochar. Similar results are obtained by Tag et al. [3] during the hydrothermal carbonization of poultry litter, sunflower stalks, and algal biomass.
The increase in C content is mainly due to the degradation of organic constituents, hemicellulose and cellulose, and the deposition of dissolved compounds [4]. Furthermore, with the increase of the HTC temperature the dehydration and decarboxylation reactions of the coalification process are more intense, resulting in the decrease of H/C and O/C atomic ratios and, thus, in the increase of LHV and energy density of the hydrochar. In particular, the decomposition and cracking of biomass lead to the reduction of oxygen content in the hydrochar which is reduced by a maximum of 61.8% (for the sample 260-4-0.05) from the original feedstock (40.32 $wt\%_{db}$, calculated as the mean value of O content of vine pruning and EGM).
Furthermore, from the proximate analysis of hydrochars (***Table 4.2***) can be observed that the reaction temperature has the main effect on the volatile matter and fixed carbon contents. The increase in HTC temperature causes a reduction of the volatile matter and an accumulation of fixed carbon, confirming that dehydration, decarboxylation as well as carbonization reactions occur during HTC treatment.

Table 4.2: *Proximate analysis, ultimate analysis and heating value of hydrochars from BBD experimental design.*

Run order	1	2	3	4	5	6	7	8	9	10	11	12	13	14	15
Temperature [°C]	260	220	220	220	180	220	220	260	180	260	260	220	220	180	180
Time [h]	1	1	4	4	4	7	4	4	7	7	4	7	1	4	1
S/L ratio	0.15	0.05	0.15	0.15	0.25	0.05	0.15	0.25	0.15	0.15	0.05	0.25	0.25	0.05	0.15
Ultimate analysis $[wt\%_{daf}]$															
C	66.61	55.11	60.3	59.12	50.24	60.96	59.55	69.01	53.5	69.18	65.65	60.53	55.03	51.97	49.25
H	6.6	7.58	6.32	6.44	7.02	7.53	6.38	6.82	7.27	6.66	7.75	7.29	6.46	7.6	6.53
N	2.15	2.13	1.81	1.87	2.07	2.75	1.83	2.28	2.13	2.32	3.06	2.45	1.53	2.18	1.47
S	0.31	0.11	0.19	0.14	0.23	0.21	0.2	0.12	0.21	0.19	0.22	0.12	0.04	0.09	0.15
O	20.56	31.32	26.99	28.91	36.21	23.61	28.65	18.11	33.54	17.3	16.88	25.82	33.43	34.96	39.36
H/C	1.19	1.65	1.26	1.31	1.68	1.48	1.29	1.19	1.63	1.15	1.42	1.45	1.41	1.75	1.59
O/C	0.23	0.43	0.34	0.37	0.54	0.29	0.36	0.2	0.47	0.19	0.19	0.32	0.46	0.5	0.6
Proximate analysis $[wt\%_{db}]$															
VM	57.25	67.18	61.11	60.55	68.94	56.81	61.3	53.99	67.37	53.04	53.04	59.92	65.08	69.52	70.41
Ash	3.77	3.75	4.39	3.53	3.24	4.95	3.4	3.66	3.36	4.36	5.44	3.79	3.51	3.2	3.25
FC	38.98	29.08	34.5	35.93	27.63	38.25	35.31	42.36	29.28	42.39	41.52	36.3	31.42	27.29	26.45
LHV [MJ/kg,db]	23.36	19.88	21.16	21.17	18.21	22.44	21.34	23.73	20.05	24.84	24.47	21.71	19.87	18.95	18.03

Note: db: dry basis; daf: dry and ash-free bases

The Van Krevelen diagram (***Figure 4.1***) was used to analyze the coalification degree of the produced hydrochar during the HTC process. In this plot, the dashed lines represent the dehydration, decarboxylation, and demethanation processes, and other H/C–O/C atomic ratios [5] are reported for other feedstock (anthracite, lignite, sub-bituminous coal) in order to perform a comparison with the hydrochar samples. It is clear that the predominant reaction pathways are dehydration (production of water) and decarboxylation (formation of carbonyls including carboxylic acids) while demathanation (production of methane) has a negligible influence on the HTC process. When the coalification degree of the hydrochar is compared with other typical fossil fuels, it is observed that at higher temperatures the hydrochar shows greater carbonaceous similarity with coal and

lignite structure. In particular, lower atomic ratios of the hydrochars than the raw materials demonstrate the enhancement of the fuel properties of hydrochars because of the less smoke and water vapor released. The important upgrading of the fuel quality of the hydrochars is also confirmed by the LHV values which increase with increasing HTC temperature. In particular, the maximum values 23.36–24.84 MJ/kg obtained at 260°C are comparable to that of bituminous coal, demonstrating the effectiveness of the HTC treatment of the winery and distillery by-products to produce coal substitutes.

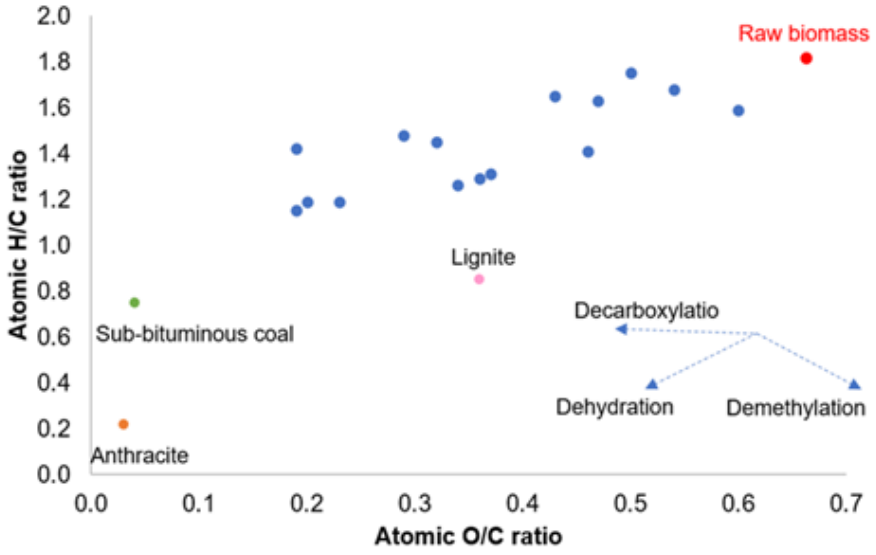

Figure 4.1: *Van Krevelen diagram for hydrochars under different conditions.*

Aqueous phase composition

HTC temperature, residence time, and S:L ratio have also an essential role in the physical-chemical properties of the liquid fraction product as shown in ***Table 4.3***. Also, in ***Figure A.1*** of the Appendix (***Section A.2***) are reported the main effects plots of the operating parameters on the spent liquor, indicating the relative strength of the effects of various factors.
The hydrothermal carbonization treatment involves a decrease in the pH value of the liquid phase at all conditions in the range of 3.69–4.49, mainly due to the production of organic acids (acetic, lactic, propionic, levulinic, and formic acids) from the thermal decomposition of hemicellulosic sugars [6]. As observed by Hoekman et al. [7] for the HTC liquor from HTC treatment of different woody and herbaceous biomass, the pH slightly decreases with increasing temperature. The same trend is obtained for the S:L ratio, due to the dilution effect of the water content, while the effect of residence time is not significant.
The analysis of the total organic carbon in the aqueous phase highlights that HTC treatment causes a significant increase from 9.71 g/L of the vinasse to the range of 12.05–22.93 g/L, with the highest value obtained at 260°C, 4h, and S:L ratio of 0.25. No strong effect of HTC temperature is observed with an initial decrease in TOC values up to about 220°C, followed by a gradual increase due to the degradation of intermediates, such as organic acids compounds and sugars, to gas products. On the other hand, the solid-to-liquid ratio has a strong impact on TOC

yield, with a clear increase of TOC values with increasing S:L ratio. Also, carbonization time plays a significant role in the TOC content of the spent liquor. The longer residence time gives slightly higher TOC results, demonstrating a higher concentration of intermediates. The comparison of the obtained results for TOC in spent liquor with Literature data is difficult because, as reported by Mihajlovic et al. [8], the trends of TOC values may differ depending on the type of biomass and operating conditions.
COD values show the same dependence of the TOC values on the HTC operating conditions. A linear relationship can be identified with COD values being much more than TOC, demonstrating the presence of inorganics in the spent liquor [9]. Moreover, the COD/TOC ratio shows high values, ranging from 1.91 to 2.72, indicating that the liquid phase at all HTC conditions contained a high concentration of oxidizable organics (sugars, organic acids) [10]. It is also interesting to note that the BOD/COD ratios are in the range of 0.37–0.54, suggesting that the dissolved organics in the spent liquors are adequately biodegradable to be treated and valorized by biological methods [11]. As regards the total nitrogen content in the liquid phase, a negligible effect of the residence time is observed, while the solid-to-liquid ratio and the temperature have a significant impact. In particular, it is interesting to analyze the effect of the HTC temperature; at the first temperature range (180-230°C), the nitrogen yield in the spent liquor showed a significant decrease, while during the second temperature range (230-260°C), the total N shows a slight increase, mostly due to the hydrothermal denitrification reaction and more inorganic nitrogen is produced [12].

Table 4.3: *Characterization of process waters at different HTC conditions.*

Run order	1	2	3	4	5	6	7	8	9	10	11	12	13	14	15
Temperature [°C]	260	220	220	220	180	220	220	260	180	260	260	220	220	180	180
Time [h]	1	1	4	4	4	7	4	4	7	7	4	7	1	4	1
S/L ratio	0.15	0.05	0.15	0.15	0.25	0.05	0.15	0.25	0.15	0.15	0.05	0.25	0.25	0.05	0.15
pH	4.52	4.08	4.13	4.03	3.47	4.09	4.33	4.40	3.83	4.24	3.96	4.28	3.83	4.10	3.80
Total N [mg/l]	452.65	368.36	331.42	356.58	549.53	394.36	350.07	323.73	455.90	374.79	681.47	366.35	603.54	339.39	352.27
TOC [g/l]	12.72	12.06	13.89	14.01	20.82	16.91	13.56	13.42	17.51	15.12	24.06	23.69	21.66	12.63	12.71
COD [g/l]	24.99	28.43	27.38	30.18	47.98	28.00	29.54	32.97	38.57	32.46	50.78	56.02	52.75	29.28	27.72
BOD [g/l]	15.41	8.87	6.31	7.55	21.61	14.77	7.34	13.92	19.42	13.48	23.43	11.99	22.33	11.96	14.91
COD/TOC	1.96	2.36	1.97	2.15	2.30	1.66	2.18	2.46	2.20	2.15	2.11	2.36	2.44	2.32	2.18
BOD/COD	0.62	0.31	0.23	0.25	0.45	0.53	0.25	0.42	0.50	0.42	0.46	0.21	0.42	0.41	0.54

Effects of HTC process parameters on mass yield

Table 4.4 lists the results of the 15 tests run, highlighting how the HTC process parameters influence the chosen response variables.

HTC operating conditions had a significant impact on the mass yield, dispersing widely from 45.33% (260°C – 4h – 0.05 S/L) to 75.73% (180°C – 4h – 0.25 S/L), which suggests that the hydrochar yield depended on the choice of hydrothermal conditions. In ***Figure 4.2*** are displayed the contour plots of MY, highlighting the interaction effects of the independent variables.
A decrease in the hydrochar yield from 70.59% to 48.41% was observed with the increase of the HTC temperature from 180°C to 260°C, keeping constant the other variables. Hence, the temperature has a high influence on hydrochar yield. This is in agreement with other studies available in the literature [13, 14], which show that a temperature rise increases the decomposition of biomass, mostly due to the degradation of cellulose and hemicellulose, and the potential for the release of

volatile matters. Furthermore, the decomposition of biomass could be facilitated at higher temperatures by decreasing the dielectric constant of water (i.e. by increasing the reaction temperature), making the water behave similarly to a polar organic solvent [15].

Table 4.4: *Result values of response variables from BBD experimental design.*

Run	Temperature [°C]	Time [h]	S:L ratio	MY [%]	EDY	FR	PEY [mg_{GAE}/g]	EI [kJ]
1	260	1	0.15	51.11	1.27	0.68	11.52	304.53
2	220	1	0.05	59.33	1.08	0.43	22.03	261.25
3	220	4	0.15	60.22	1.15	0.59	7.40	296.45
4	220	4	0.15	62.13	1.15	0.56	7.61	296.45
5	180	4	0.25	75.73	0.99	0.40	2.22	223.65
6	220	7	0.05	50.34	1.22	0.67	21.89	356.82
7	220	4	0.15	59.98	1.16	0.58	9.35	296.45
8	260	4	0.25	50.53	1.29	0.78	11.80	346.44
9	180	7	0.15	70.44	1.09	0.43	5.90	271.43
10	260	7	0.15	46.67	1.35	0.80	12.92	419.70
11	260	4	0.05	45.33	1.33	0.76	27.90	377.79
12	220	7	0.25	61.60	1.18	0.61	6.32	331.65
13	220	1	0.25	65.23	1.08	0.48	8.34	236.09
14	180	4	0.05	66.05	1.03	0.39	15.80	243.24
15	180	1	0.15	70.13	0.98	0.38	3.94	195.47

A negative correlation with the hydrochar yield was observed also for the residence time, although the effect was milder than that produced by the HTC temperature. This is probably ascribable to the slow heating rate which ensures sufficient time for biomass decomposition and for the cross-reaction of intermediate products, as also observed by Chen et al. [13]. Moreover, the further mass loss during the residence time, which is to say after heating up to the desired reaction temperature, may be related to the formation of lighter organic compounds and permanent gases. An opposite trend was observed for the S:L ratio, whose growth from 0.05 to 0.25 increases the mass yield from 55.26% to 63.27%, thanks to the greater ability of the liquid phase to dissolve and maintain solubilized chemical species deriving from biomass [16].
Based on the BBD results shown in ***Table 4.4***, the empirical relationship that relates the response (mass yield) and selected variables was obtained, as described by ***Equation*** (4.6).

$$\begin{aligned} MY\,[\%] = 86.2 - 0.071A + 1.470B + 1.112C \\ - 0.0003A^2 - 0.082B^2 - 0.009C^2 \\ - 0.010AB - 0.003AC + 0.045BC \end{aligned} \quad (4.6)$$

The significance and suitability of the quadratic model were evaluated by ANOVA at 95% confidence ($p < 0.05$), and the results are shown in ***Table A.2*** (Appendix ***Section A.2***). It is interesting to note that only the linear terms were found to be statistically significant ($p > 0.05$) meaning that the hydrochar yield depends more upon the individual change of the independent variables, rather than their interactions.vAccording to these results, the model F-value of 47.61 indicates that the model is statistically significant. The adequacy of the model was further

confirmed by an adjusted determination coefficient (R^2) of 0.9677 and a lack of fit (LOF) test of 2.62. The R^2 obtained for the regression model is 0.9885, meaning that the model explains 98.85% of the variation around the mean. However, R^2 is sensitive to the degree of freedom and, thus, adjusted R^2 is more reliable to be used for model evaluation, decreasing the number of insignificant terms in the model when the model factors increase. Its value higher than 0.95 proves the adequacy of the model. Furthermore, the good agreement between the predicted R^2 value of 0.8477 and the adjusted R^2 value of 0.9677 (being within 0.2 of each other) suggests that there is a linear relationship between the experimental and calculated mass yield [17]. In addition, the lack of fit test was carried out to determine the adequacy of the regression model in describing the observed data or if significant terms are excluded from the model. The lack-of-fit should be not significant (p-value $>$ 0.05) for a suitable fitting of response surface models. The "Lack of Fit F-value" of 2.62 implies there is a 28.9% chance that a "Lack of Fit F-value" this large could occur due to noise.

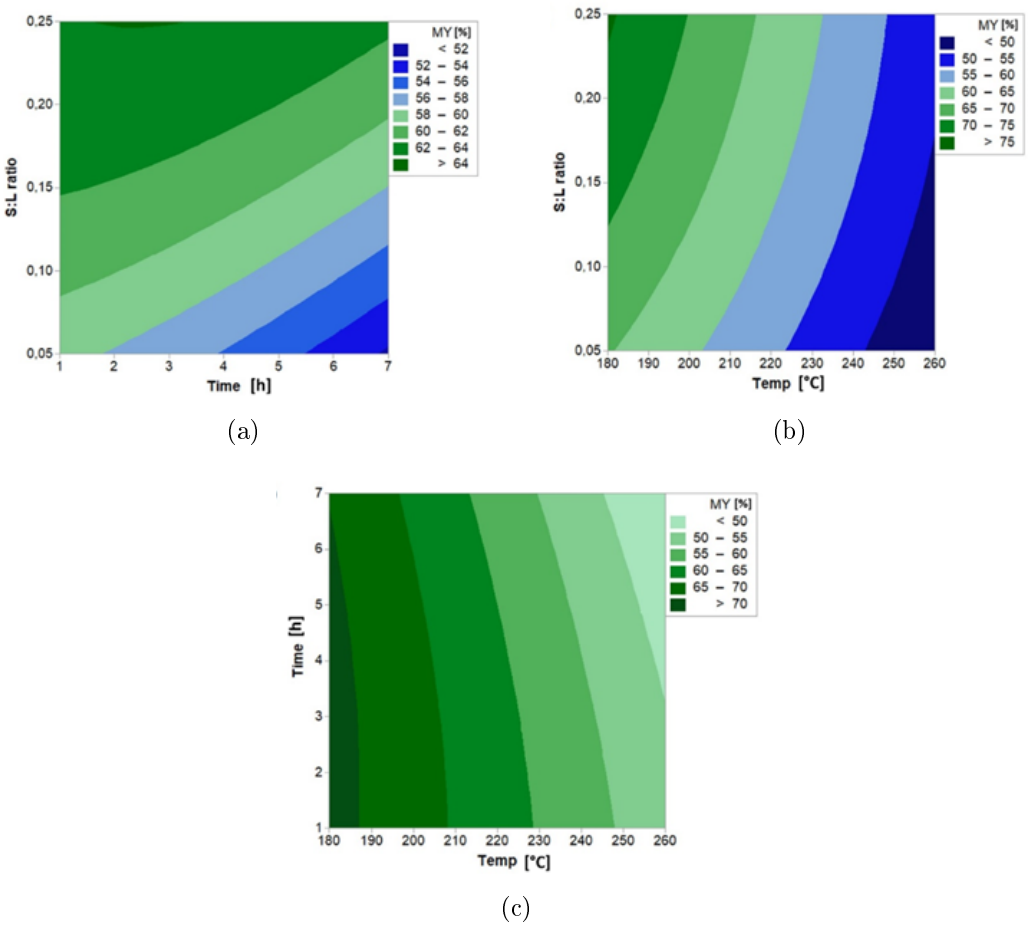

Figure 4.2: *Contour plot of MY with interaction between (a) S:L ratio vs time, (b) S:L ratio vs temperature, (c) time vs temperature.*

Effects of process parameters on energy densification yield

The observed EDY values (***Table 4.4***) higher than 1 indicated that the HTC treatment improves the energy density of the hydrochar. An increased calorific value of hydrochar was observed at all tested conditions, except for the hydrochar obtained at 180°C – 4h – 0.25 and 180°C – 1h – 0.05. Anyway, in these cases, the EDY reduction is always below 2%, thus confirming that good energy densification is obtained at most operating conditions. We also noted that EDY was strongly affected by the processing variables, with experimental values ranging from EDY=0.98, at 180°C – 1h – 0.05, to EDY=1.35, at 260°C – 7h – 0.15. Similar energy densification ratios are obtained for hydrochars produced from paper mill sludge residue (EDY = 1–1.6 [3]) and spent coffee grounds (EDY = 1.16–1.45 [11]). In contrast to the hydrochar yield trend, the energy densification yield of hydrochar grows by increasing the HTC temperature and the residence time.
The influence of the S:L ratio on EDY, shown in ***Figure 4.3***, was less significant with a slight EDY decrease detected at high and low S:L ratios for an HTC temperature below 210 °C and only at high S:L ratios in the rest of the temperature observation range.

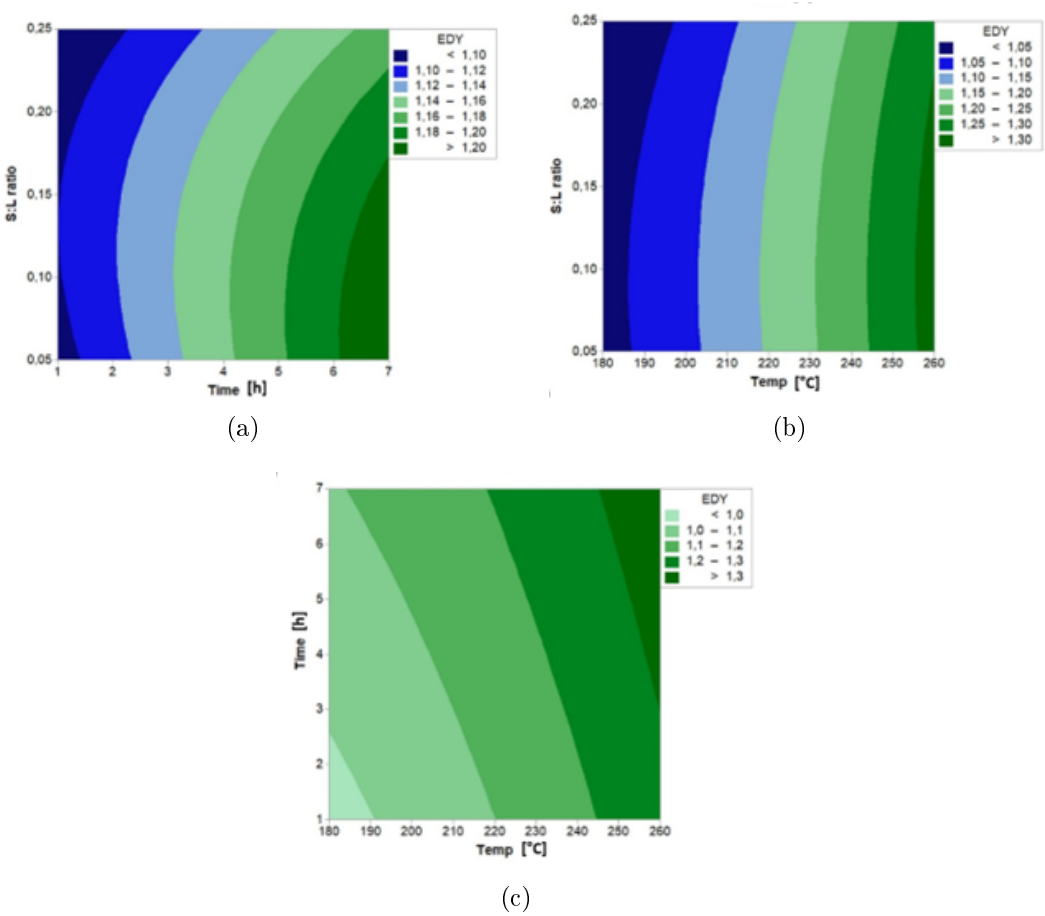

Figure 4.3: *Contour plot of EDY (Energy Densification Yield) with interaction between (a) S:L ratio vs time, (b) S:L ratio vs temperature, (c) time vs temperature.*

Similar effects of temperature and residence time upon energy densification yield were observed in literature with sunflower stalk [18], miscanthus [8], and

almond-tree pruning [19]. In fact, under severe conditions, the increase of EDY is mainly due to the decarboxylation of biomass components that causes a reduction of the oxygen content in the hydrochar [11].
The following equation represents the quadratic response surface regression model generated by ANOVA:

$$\begin{aligned} EDY = 0.873 - 0.002A + 0.042B + 0.004C \\ + 0.00001A^2 - 0.0004B^2 - 0.0001C^2 \\ - 0.00007AB - 0.000001AC - 0.0004BC \end{aligned} \quad (4.7)$$

Equation (4.7) allows to predict the EDY in terms of the actual factors. The F and p values, summarised in ***Table A.2*** (Appendix ***Section A.2***), demonstrated that the model is statistically significant as well as the linear coefficients (A, B, C) and a quadratic term coefficient (A^2), and indicating a nonlinear relationship between the hydrochar yield and the reaction temperature.
The high value of the regression coefficient (0.9959) suggests that the model could be accepted with satisfactory accuracy. The value of adjusted R^2 (0.9885) confirms that the model is highly significant. In addition, high predicted R^2 (0.9365) indicates that the model could be used to predict response for a given set of independent variables. The "Lack of Fit F-value" of 16.72 implies the Lack of Fit is not significant relative to the pure error. There is a 5.70% chance that a "Lack of Fit F-value" this large could occur due to noise.

Effects of process parameters on fuel ratio

The fuel ratio was used to understand the combustibility of the solid fuel. High values of the fuel ratio indicate a more stable combustion and a less violent flame, while low values suggest incomplete combustion with a higher smoke emission tendency [20].
Figure 4.4 shows the effect of temperature, residence time, and S:L ratio on the fuel ratio. The fuel ratio was influenced by the HTC temperature and the residence time while the effect of the S:L ratio was negligible. The fuel ratio was found to rise steeply with the temperature increasing from 0.40 to 0.76 (keeping constant the other variables), obtaining a maximum increase of about 121% when compared with raw feedstock. This result is mainly due to the rapid decrease of volatile matter content at a higher temperature, which accelerates the deoxygenation reaction of the biowaste. Similar trends and values have been observed for other biomass in previous studies [3, 14, 21] while slightly different values have been obtained for the HTC process of the single winery and distillery by-products using distilled water as process water. Petrovil et al. [22] obtained a fuel ratio of 0.41 from hydrothermal carbonization of grape pomace at 220 °C for 1 h, while Duman et al. [23] reported that FR varied from 0.68 (at 220 °C for 120 min) to 1.91 (at 260 °C for 30 min) for vine pruning. The effect of the holding time on the fuel ratio was less significant than the effect of temperature. However, it can be observed that the fuel ratio significantly increases (from 0.49 to 0.58) when the residence time rises from 1 h to 4 h, while, for a residence time up to 7 h, the fuel ratio slightly increases only up to 0.63.

The regression model for fuel ratio derived from ANOVA analysis is given below:

$$FR = -0.013 - 0.0003A + 0.028B + 0.004C + 0.000009A^2 - 0.002B^2 - 0.00009C^2 + 0.0001AB + 0.00001AC - 0.0009BC \quad (4.8)$$

ANOVA results, presented in ***Table A.2*** (Appendix ***Section A.2***), show that only the linear terms of reaction temperature and residence time of the regression model are significant. There is only a 0.1% chance that Model F-Value could occur due to noise, which confirms the validity of the predicted model. The lack of fit F-value of 8.86 implies the lack of fit is not significant, as there is a 10.3% chance that the lack of fit F-value occurs due to noise. The closeness of R^2 (0.9804) and adj-R^2 (0.9452) values shows also that there is a good relationship between the experimental and predicted values.

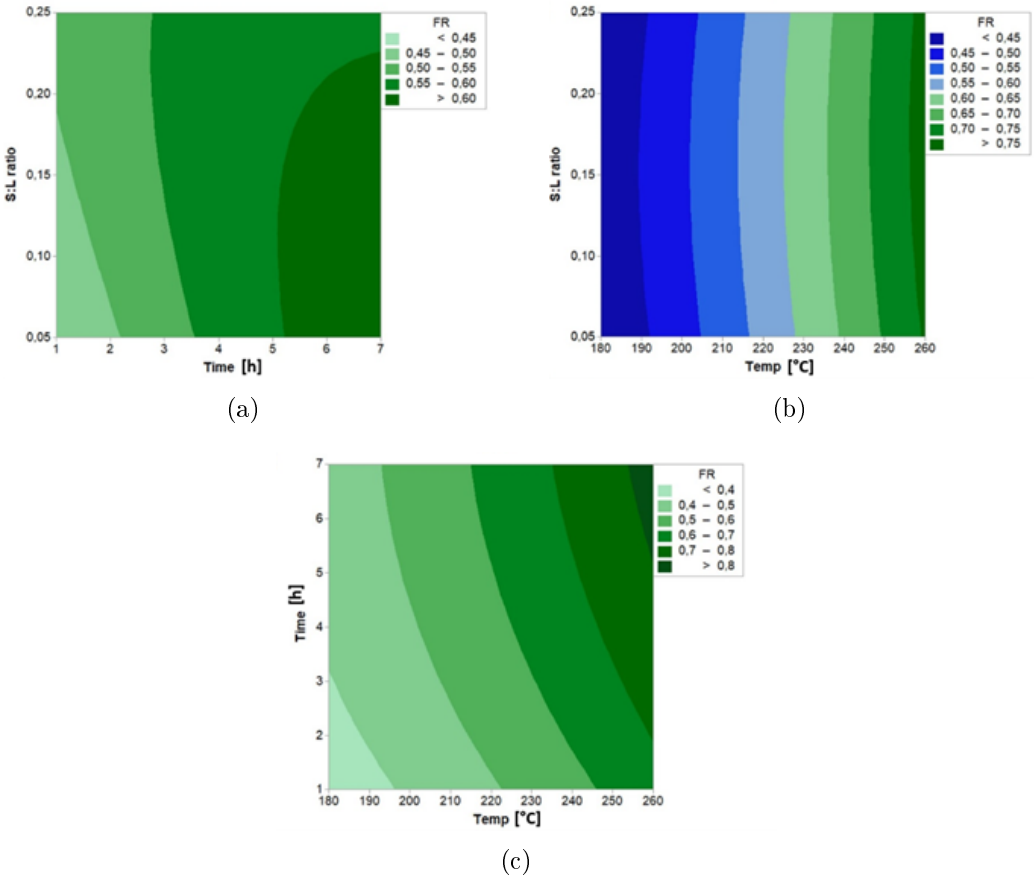

Figure 4.4: *Contour plot of FR (Fuel Ratio) with interaction between (a) S:L ratio vs time, (b) S:L ratio vs temperature, (c) time vs temperature.*

Effects of process parameters on phenols extraction yield

Vine pruning and EGM are composed of various non-volatile and volatile phenolic compounds that could be interesting to extract to be used in the pharmaceutical, cosmetics, and food industries. In particular, the high amount of phenolic

compounds in the grape pomace is due to their partial extraction during the wine-making process. However, the TPC content is significantly reduced in the exhausted grape marc due to the thermal degradation of polyphenols during the distillation process at high temperatures [24]. ***Figure 4.5*** shows that PEY is mostly influenced by S:L ratio and temperature while reaction time plays a negligible role in the polyphenols extraction. Atallah et al. [25] obtained the same result during the hydrothermal carbonization of olive mill wastewater. The biomass/water ratio had the main influence on the PEY, resulting in a steep reduction of the PEY, with the increase of ratio from 0.05 (21.91 mgGAE/g) to 0.15 (8.38 mgGAE/g), followed by a more gradual decrease (7.17 mgGAE/g, with 0.25 S/L ratio). On the other hand, HTC temperature had a more linear effect on the EPY, causing an increase of the phenols extraction from 6.96 mgGAE/g to 16.04 mg_{GAE}/g, when the temperature rose from 180°C to 260°C. This trend could be explained by considering that phenolic compounds in biomass are both present in a soluble form (free or conjugated to soluble carbohydrates by ester/ether bonds) or in an insoluble form bound by ester/ether bonds to lignin [26]. Thus, a high water content in the HTC process allows for ease of the solubilization of the free polyphenols, and under high temperatures, it plays the role of reactant hydrolyzing lignocellulosic structure. In fact, lignin starts to decompose at 200°C due to the dissociation of β-O-4 linkages by hydrolysis to produce phenol, aldehyde, and ketones, which are polar compounds diffusing into the liquid phase [27]. To obtain the maximum phenols extraction yield (27.78 mg_{GAE}/g), time and temperature should be kept at the maximum level while the solid-to-liquid ratio should be at the minimum value. This result is interesting if compared with the most common methods for recovery of polyphenols from grape pomace. Drevelegka and Goula [27] obtained a maximum yield of 33.88 mg_{GAE}/g by direct ultrasound-assisted extraction, Da Porto and Natolino [28] found an optimum value of 24.14 mg_{GAE}/g dry pomace by employing the solid-liquid extraction technique, while, according to Aliakbarian et al. [29] a yield of 31.69 mg_{GAE}/g dry pomace was obtained by subcritical water extraction.
The regression equation of the PEY response in terms of the actual variables is as follows:

$$\begin{aligned} PEY\,[mg_{GAE}/g] = 4.900 &+ 0.109A + 0.240B - 2.185C \\ &+ 0.00007A^2 + 0.037B^2 + 0.062C^2 \\ &- 0.001AB - 0.002AC - 0.016BC \end{aligned} \quad (4.9)$$

The analysis of variance confirmed the S:L ratio as having the most significant enhancement effect on phenols extraction given by its very large F value (436.116). The analysis revealed that the linear terms A, and C are significant model terms, as well as the squared term C^2. The statistical analysis of the response revealed that the regression coefficient (R^2) was 0.9836, whereas the predicted R^2 was 0.8898 and the adjusted R^2 was 0.9541.
The probability of the F function for the model term was less than 0.05 which confirmed the significance of the model, while the probability of the F function for the lack of fit was greater than 0.05 which proved the non-significance of error. Furthermore, the lack of fit F-value of 2.91 showed that the lack of fit was not significant relative to pure error.

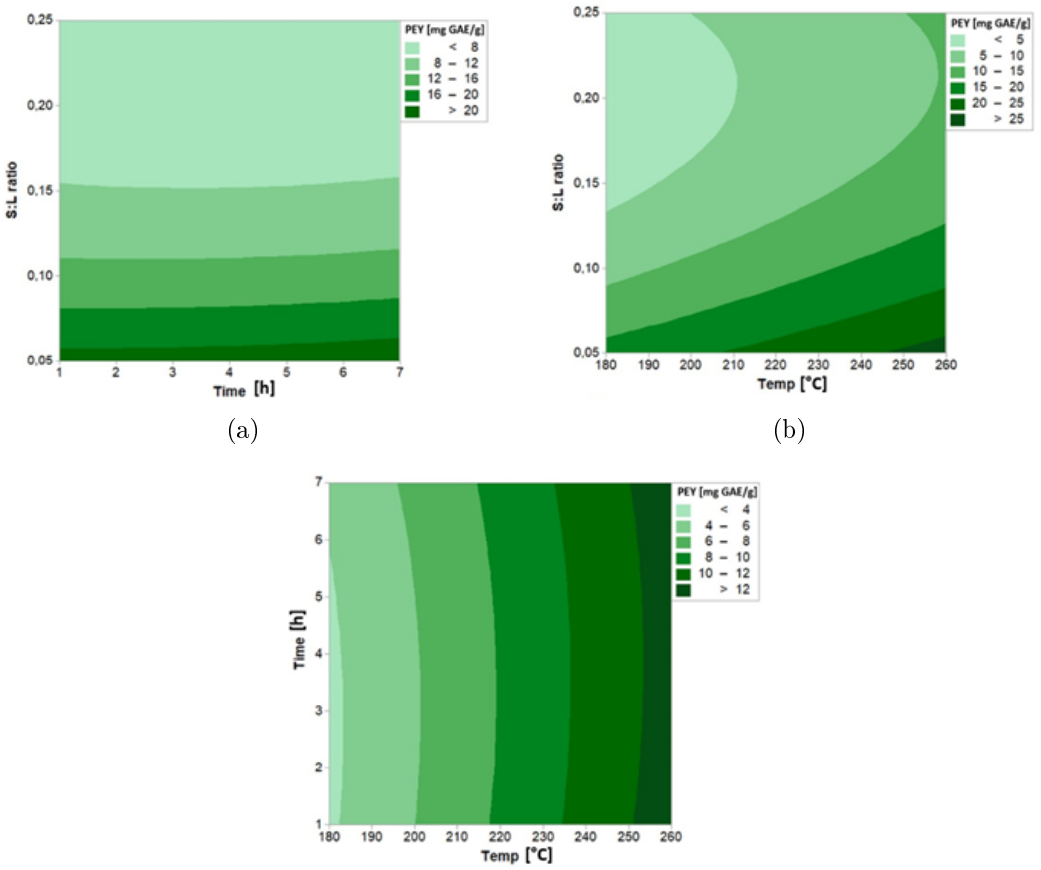

Figure 4.5: *Contour plot of PEY (Phenols Extraction Yield) with interaction between (a) S:L ratio vs time, (b) S:L ratio vs temperature, (c) time vs temperature.*

Process optimization and validation

The optimal process conditions of the co-hydrothermal carbonization of winery and and distillery by-products were determined through the desirability function approach. The optimization process aimed at finding the HTC temperature, residence time, and solid-to-liquid ratio that maximize the mass yield, energy densification yield, fuel ratio, and phenols extraction yield, as well as minimize the energy consumption, simultaneously.

It must be mentioned that the heating of water accounted for the majority of energy consumption during the HTC process, ranging from 57% to 91% of the total energy input. This finding confirms the critical role of water in the HTC treatment, while highlighting the energy-intensive nature of the heating process.

Figure A.2 (Appendix ***Section A.2***) shows the RSM optimizer generated results by the Minitab software. The low value of the maximum composite desirability (D=0.50) demonstrated that it is difficult to optimize all the response variables simultaneously. The values of individual desirability indicate that the optimum parameter settings are more effective for maximizing PEY, followed by EDY, FR, EI, and MY. The best-optimized conditions were found to be 246.3°C, 1.6 h, and a liquid-to-solid ratio of 0.066, while the predicted PEY, EDY, FR, and MY at these conditions were 21.88 mg_{GAE}/g, 1.21%, 0.60%, and 52.64%, respect-

ively.
Confirmation tests were also conducted at the optimal conditions by running three replicates to validate the accuracy of the predictive model. The results were PEY = 21.01±0.34 mg_{GAE}/g, EDY = 1.24±0.05, FR = 0.61±0.03, and MY = 50.77±0.43%. The results indicate that the developed models were in agreement with experimental test results and can predict the responses within a 5% error.

Furthermore, to evaluate the influence of vinasse as the moisture source for the HTC process of the winery and distillery by-products, an experimental test at optimal conditions was carried out by using deionized water as the reaction medium. Due to the increasing water scarcity, it is essential to find alternative carbonization liquid sources. The experiments were conducted in triplicate and the mean values of the response variables are shown in ***Table 4.5***.
It can be noted that hydrochar and spent liquor properties are substantially unaffected by carbonization in the presence of vinasse, according to the results obtained by Li et al. [30], using landfill leachate and activated sludge as liquid sources. The slight decrease in mass yield in the presence of vinasse, as compared to deionized water, could be attributed to the reactive constituents in the vinasse, such as organics, causing greater dissolution and hydrolysis of the biomass [31]. Therefore, the use of vinasse as a liquid source does not have any negative impacts on the HTC process of winery and and distillery by-products.

Table 4.5: *Physicochemical characterization of hydrochar and response variables at the optimal HTC conditions, obtained using vinasse or deionized water as the reaction media.*

	Vinasse	**Deionized water**
Ultimate analysis [wt%$_{daf}$]		
C	60.86	61.72
H	7.09	6.76
N	2.14	1.98
S	0.22	0.14
O	29.69	29.4
Proximate analysis [wt%$_{db}$]		
VM	59.21	59.4
Ash	3.58	3.33
FC	35.43	36.83
LHV [MJ/kg, db]	22.26	22.63
Response variables		
MY [%]	52.64	53.83
EDY	1.21	1.23
FR	0.6	0.62
PEY [mg_{GAE}/g]	21.88	22.06

Note: db: dry basis; daf: dry and ash-free bases

4.2 Pyrolysis and combustion kinetic of hydrochar – *Paper B*

Building upon the findings of Paper A, Paper B, titled "*Hydrochar from wine-making industry wastes as solid biofuel: A thermal and kinetic analysis of pyrolysis and combustion*", delves deeper into the hydrochar, named HY from now on, produced at the identified optimal HTC process conditions (246°C – 1h – 0.066 S/L). This study, currently under review for publication, focuses on understanding the pyrolysis and combustion kinetics of the hydrochar, which are crucial for evaluating its potential as a renewable energy source.
The kinetic parameters, i.e. activation energy (E_a), pre-exponential factor (A), and reaction mechanism (f(α)), collectively known as 'kinetic triplet', and thermodynamic parameters, enthalpy (ΔH), Gibbs free energy (ΔG), and entropy (ΔS) were determined through thermogravimetric analysis and mathematical modeling. Overall, this study aimed to gain a comprehensive understanding of the reaction mechanisms, rates, and influential factors involved in biomass conversion. This knowledge is essential for developing sustainable and efficient biomass utilization processes and advancing the field of biomass-based renewable energy.

The main outlines of this research work highlighted that even if HY exhibited a lower activation energy compared to EGM and VP during both pyrolysis and combustion, HTC has positive effects on the hydrochar's structure, which achieved a more thermodynamically stable, structurally ordered, and energetically favorable state. In detail, thermogravimetric analysis of pyrolysis and combustion highlighted that potentially co-HTC might reduce unstable biomass compounds, i.e. hemicellulose and cellulose, while increasing those with higher bond energy such as lignin. Also, modifying the resulting hydrochar's structure promotes its thermal stability and might grant a less turbulent combustion process, expressed by the reduced devolatilization and combustion index compared to the raw biomasses. Interestingly, the hydrochar from co-HTC of VP and EGM exhibited reduced activation energy for both pyrolysis and combustion processes. The diffusion-reaction mechanism dominated the pyrolysis' first stage of HY and EGM, while the reaction order model controlled both their second stage and that of the VP. Also, during combustion, stages I and II of EGM and VP were regulated by the reaction order model, however, HY by the diffusion model in the first stage and the geometrical contraction model in the second stage. Lastly, the analysis of thermodynamic parameters suggests that HY achieved a more stable thermodynamic state and favorable energy characteristics through the co-HTC process.
These outcomes highlight the potential value of HY as a solid bioenergy fuel.

4.2.1 Results discussion

Data about ultimate analysis, proximate analysis, and Lower Heating Value (LHV) of the raw biomasses (VP and EGM) and the hydrochar (HY) are reported in ***Table 3.1*** and ***4.5***. Also, thermogravimetric and kinetic analyses are extensively described in ***Sections 3.6*** and ***3.7***.

Pyrolysis behavior

The thermal degradation profiles of VP, EGM, and HY under a nitrogen atmosphere at a 10°C/min heating rate are shown in ***Figure 4.6***. The TG and DTG profiles at 20, 30, and 40°C/min are displayed in the Appendix ***Section A.2*** (***Figure A.3***) since no significant differences were revealed.

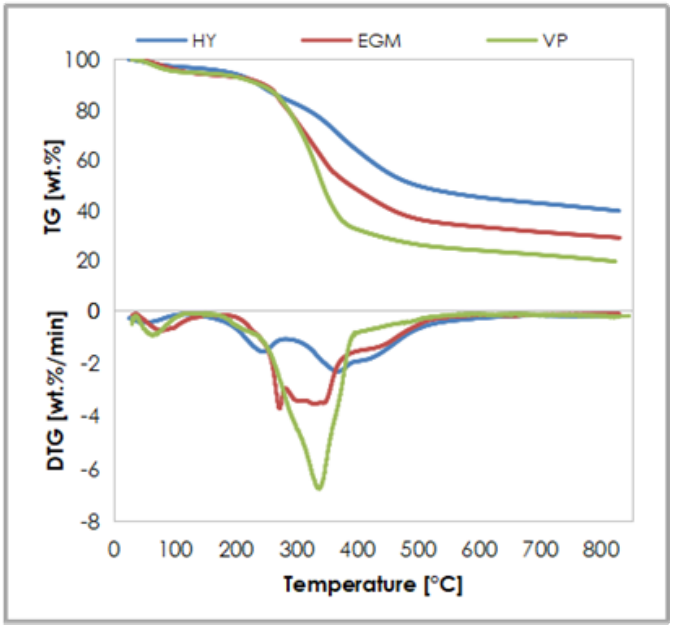

Figure 4.6: *Thermal degradation profiles of HY, EGM, and VP under N_2 atmosphere with a heating rate of 10°C/min.*

All the DTG (%/min) curves present the dehydration stage in which weakly bonded water molecules are released between 50–150°C. Then, the devolatilization and the decomposition of the major components of the biomass, i.e. hemicellulose, cellulose, and lignin, occur [32]. After the dehydration stage, EGM exhibited two main stages between 154–291°C (stage I), and 291–649°C (stage II). While stage I corresponds to the decomposition of non-polar extractives and hemicellulose, stage II comprises the degradation of cellulose and proteins (291–390°C), and the plateau (shoulder) between 390–520°C the decomposition of lignin as well as char formation and rearrangement [33, 34]. Instead, VP showed a single decomposition stage (123–657°C) with three small plateaus at around 200–280°C due to the depolymerization and volatilization of hemicellulose [35], 280–400°C attributable to the cellulose decomposition, and 400–490°C to lignin breakdown [36]. Compared to the EGM, VP exhibited high mass loss, which might be due to the lower ash and higher volatile content [1]. On the other hand, the area under the decomposition curve of HY considerably decreased in comparison with VP and EGM. Throughout the HTC process, water removes a portion of the loosely bonded amorphous cellulose, hemicellulose, and lignin, along with other water-soluble extractives and intermediate products [37]. As a result, the solid hydrochar is comprised of tightly bonded cellulose, hemicellulose, and lignin formed through recondensation reactions [38]. Consequently, the weight loss experienced by HY is lower compared to the VP and EGM. Interestingly, the HY displays a lack of decomposition peak within 280–360°C suggesting that hydrothermal treatment caused the degradation

of cellulose besides hemicellulose, fats, and proteins [39]. While the second degradation stage between 310 and 728°C (stage II) could be associated mainly with the degradation of lignin, the first one (stage I) between 114–310°C may be related to the degradation of repolymerized products, which formed during the HTC process [15, 40].

Effect of heating rate on pyrolysis behavior

From the TG and DTG results reported in ***Figure 4.7*** and ***Table 4.6***, it is remarkable that the heating rate affects the conversion and product distribution for each sample and results in an important parameter in possible commercial applications in determining the type of reactor to be used [41, 42].
When the samples are heated at higher β a slight shift is observed and the peak temperature of weight loss increases. This phenomenon, referred to as heat transfer limitation, caused the observed thermal lag.

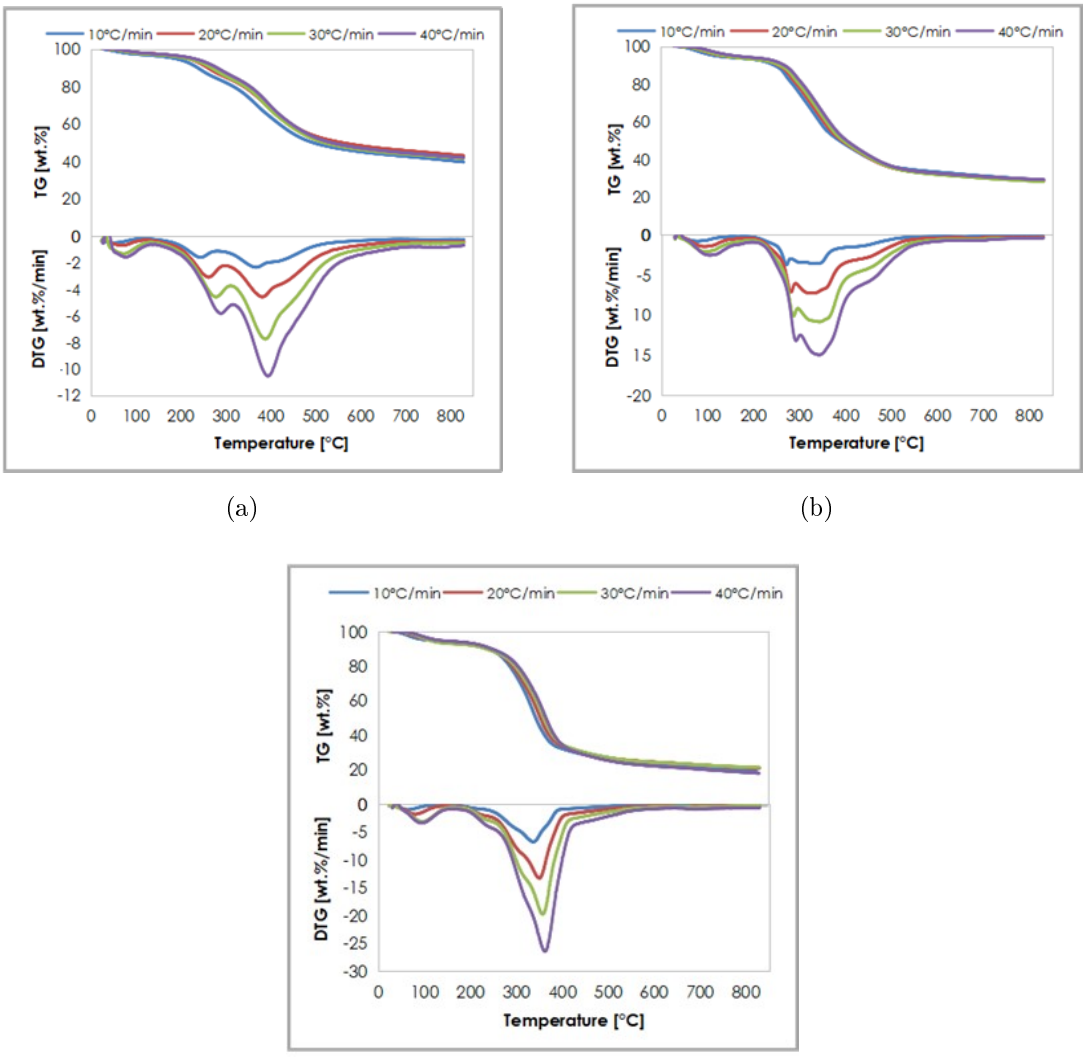

Figure 4.7: *TG and DTG profiles of (a) HY, (b) EGM, and (c) VP under the N_2 atmosphere at each heating rate.*

As the heating rate increases, the temperature gradient between the interior and exterior of the particles also increases. This leads to a lower degree of reaction occurring inside the particles compared to the outside, requiring higher temperatures to decompose the material [43, 44]. In contrast, when lower heating rates are employed, the particles experience a gradual and more efficient heat transfer towards the inner portions and among the particles [45, 46]. As a result, the peak of the weight loss rate shifts towards lower values. Furthermore, by considering the temperature of initial (T_i) and final (T_f) degradation, the pyrolysis of HY took place over a broader temperature range, spanning from 181 to 657°C, in comparison to VP, 186–565°C, and EGM, 181–571°C. Notably, the T_p significantly resulted higher for HY than raw biomass for each heating rate (***Table 4.6***), and the residue rate, by considering $\beta = 10$°C/min as a reference, rose from 19% of VP and 29% of EGM to 40% (***Figure 4.7***). These findings indicate that the feedstock exhibited improved thermal stability after undergoing hydrothermal carbonization [47].

Additionally, to assess the release performance of volatile components during the pyrolysis process, the devolatilization index (D_i) was determined according to ***Equation*** (4.10) [48], where DTG_{max} is the maximum weight loss rate and $\Delta T_{1/2}$ is the temperature range when the value of DTG/DTG_{max} is 1/2. Achieving a larger devolatilization index leads to higher yields of volatile products, making the devolatilization process easier.

$$D_i = \frac{DTG_{max}}{T_i T_p \Delta T_{1/2}} \tag{4.10}$$

From the results listed in ***Table 4.6***, the D_i of VP resulted higher than those of EGM for each heating rate. This could be related to the higher content of hemicellulose and cellulose in VP which are more reactive and easier to devolatilize.

Table 4.6: *Pyrolysis parameters of HY, EGM, and VP at each heating rate.*

β [°C/min]	T_i [°C]	T_f [°C]	T_p [°C]	$-DTG_{max}$ [%/min]	$-DTG_{mean}$ [%/min]	D_i [10^{-6}%min^{-1}C^{-3}]
HY						
10	213.54	476.66	367.27	2.33	2.61	0.12
20	200.80	542.01	381.16	4.56	4.62	0.25
30	189.13	597.54	387.69	7.75	6.22	0.52
40	180.70	657.33	393.52	10.55	7.40	1.58
EGM						
10	236.87	466.60	272.06	3.74	3.18	0.50
20	223.57	516.13	319.87	7.24	5.54	0.78
30	217.42	545.15	343.14	10.86	7.55	1.11
40	181.48	570.60	342.94	14.98	8.88	2.46
VP						
10	237.44	391.41	336.61	6.78	3.57	0.97
20	200.25	482.11	349.79	13.30	5.80	2.23
30	198.68	526.55	357.41	19.79	7.24	3.31
40	185.90	565.20	362.09	26.52	9.29	4.50

Nevertheless, compared to its precursors, the devolatilization index of HY at each β was considerably lower, indicating that HTC can increase the content of more thermal stable compounds such as lignin while reducing volatile matter, hemicellulose, extractives, and part of the cellulose. Thus, the HTC promotes the thermal stability of the hydrochar [49, 50]. Furthermore, for all the materials Di increased as the heating rate increased, indicating the devolatilization performance was improved 13 times for HY, and 5 times for EGM and VP as β went up from 10 to 40°C/min.

Combustion behavior

The TG and DTG results of hydrochar and its biomass precursors under the air environment are displayed in ***Figure 4.8*** performed at a heating rate of 10°C/min. The results for β equal to 20, 30, and 40°C/min are available in the Appendix ***Section A.2*** (***Figure A.4***) since no noteworthy differences were appreciated.

Overall, the mass loss curves for HY, EGM, and VP during combustion resulted in similar trends although with significant differences. The observed profiles align with the combustion patterns commonly observed for biomass fuels, mainly characterized by dehydration, devolatilization, and char oxidation stages [51, 52]. For all the samples, the initial mass loss between room temperature and around 130°C was due to moisture evaporation. Following, the devolatilization stage (stage I) occurred between 157–377°C and 156–377°C for EGM and VP, respectively. During stage I, VP exhibited the highest weight loss of 9%/min in comparison to 6%/min of EGM. This is mostly related to the release and combustion of volatile matter and connected to the thermal degradation of hemicellulose and cellulose, higher in VP than EGM. This agrees with the pyrolysis behavior previously discussed since the higher volatile matter, cellulose, and hemicellulose content in VP vs EGM produces higher reactivity in an oxidation atmosphere.

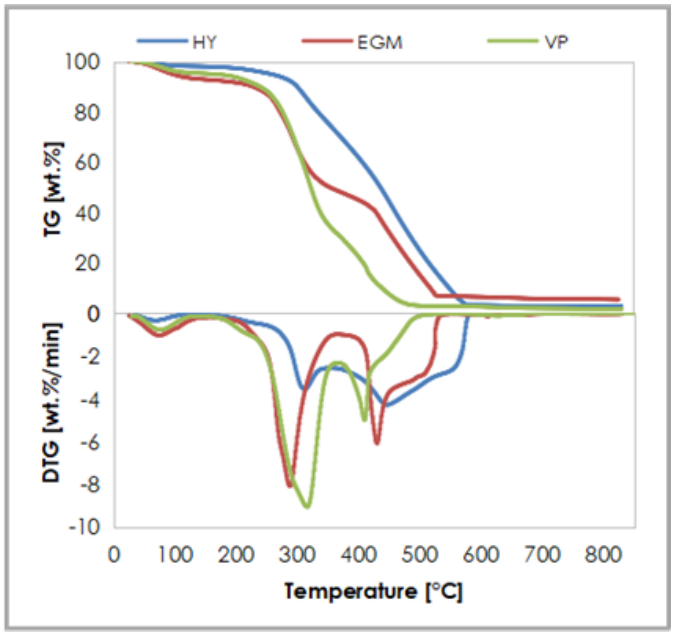

Figure 4.8: *Thermal degradation profiles of HY, EGM, and VP under air atmosphere with a heating rate of 10°C/min.*

Then, the combustion of fixed carbon (stage II), related to the decomposition of lignin, emerged between 377–708°C for EGM, and 377–650°C for VP [53]. Even if the fixed carbon content of EGM was comparable to VP, the temperature peak in this stage was more apparent and wider than VP, probably because of the slightly higher lignin content in EGM (around 13 wt% more) that promotes the thermal stability of the material. Co-HTC remarkably changed the combustion behavior. For the HY, stage I (135–374°C) was particularly weakened, whereas stage II (374–830°C), i. e. the char oxidation, leaned to be plentiful.
These results suggest that the HTC process is an effective thermal treatment aimed at reducing volatiles compounds while increasing fixed carbon [54–56].

Effect of heating rate on combustion behavior

Figure 4.9 presents the combustion TG-DTG profiles of all samples at different heating rates, while ***Table 4.7*** the combustion parameters. For each heating rate, the raw biomasses presented relatively lower T_i compared to HY. The lower content of thermally unstable VM, which releases the heat earlier and reduces the ignition temperature, makes the HY safer during handling, storage, and transportation operations [57]. The impact of increasing the heating rate was limited to causing a shift of the TG and DTG profiles to higher temperature ranges, while having only a minor effect on their overall patterns, primarily due to the influence of heat transfer limitations [58]. However, it is interesting to note that, for EGM and HY, the slower heating rate (10°C/min) allows for better access of oxygen to the char particles, facilitating the oxidation process and providing more time for the reactions to take place. In this case, the slower heating rate promotes more complete oxidation of the char, resulting in a higher mass loss rate during the char oxidation stage.
On the other hand, increasing the heating rate can cause the volatiles to be rapidly released before sufficient oxygen is available for their combustion. As a result, a larger proportion of the mass loss occurs during the devolatilization stage, rather than during the subsequent char oxidation stage [59]. After co-HTC, HY had higher FC and lower ash and volatile contents compared to EGM and VP, resulting in higher T_f. A higher burnout temperature indicates that the combustion process has been more thorough and complete. It implies that a larger proportion of the fuel has been combusted, resulting in improved combustion efficiency. This is desirable as it maximizes the utilization of the energy content and reduces slagging and fouling tendency during combustion, leading to higher energy conversion [60].

These findings were confirmed by the combustion index (S) calculated according to ***Equation*** (4.11) [61], where DTG_{mean} is the average conversion rate between ignition (T_i) and burnout temperatures (T_f) [62]. The higher value of S represents better combustion performance as the material is easier to ignite [63].

$$S = \frac{DTG_{max} DTG_{mean}}{T_i^2 T_f} \tag{4.11}$$

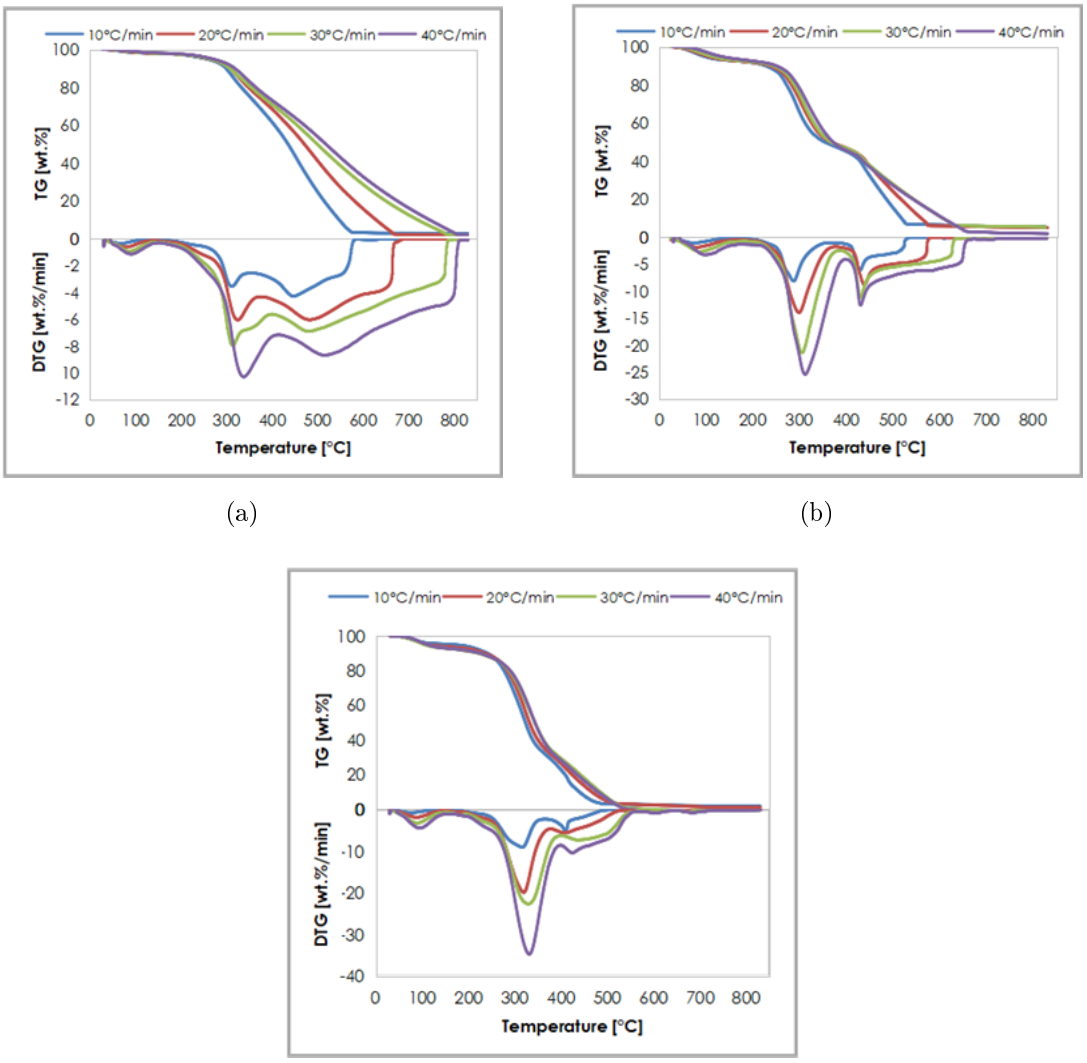

Figure 4.9: *TG and DTG profiles of (a) HY, (b) EGM, and (c) VP under air atmosphere at each heating rate.*

Overall, the combustion index of HY for each heating rate was lower than that of EGM and VP. S at 10°C/min was respectively 3.07×10^{-7}, 8.48×10^{-7}, and $14.24 \times 10^{-7} \%^2 min^{-2} C^{-3}$. The difference in S between the co-hydrothermal carbonized hydrochar and the raw biomasses increased with the heating rate, reaching respectively 18.15×10^{-7}, 100.05×10^{-7}, and $223.97 \times 10^{-7} \%^2 min^{-2} C^{-3}$ at 40°C/min for HY, EGM, and VP. HY showed a lower flammability compared to the original biomass material. The hydrothermal treatment may have induced structural changes in the biomass, resulting in the formation of a more condensed and stable carbonaceous structure in the hydrochar. Also, it was found that an unstable flame and large heat loss may result during the combustion of solid fuel with high VM content [64, 65].
Hence, although EGM and VP exhibited higher S values, their combustion performance may still be inadequate. In contrast, HY, characterized by lower VM and high FC content, might grant a combustion process that is less turbulent and features a more stable flame.

The decrease in the combustion index for HY can have both advantages and disadvantages depending on the application. While it may reduce the risk of uncontrolled combustion and self-heating, making it safer to handle, store, and transport, it may also impact the energy density of the material in certain applications, such as energy production or biofuel utilization [66–68]. However, lower combustion properties might be advantageous if used as a solid fuel or carbon source in steelmaking processes, e.g. electric arc furnace (EAF), as a substitute for fossil coal [69]. The reduced combustibility ensures the hydrochar may sustain the required high temperatures in the furnace without burning too quickly or uncontrollably. It provides a stable carbon feedstock for the metallurgic process, contributing to efficient and controlled heat generation and carbon dissolution [70].

Table 4.7: *Combustion parameters of HY, EGM, and VP at each heating rate.*

β [°C/min]	T_i [°C]	T_f [°C]	T_p [°C]	$-DTG_{max}$ [%/min]	$-DTG_{mean}$ [%/min]	S [10^{-7}%^{2}min^{-2}C^{-3}]
HY						
10	274.65	573.60	446.62	4.29	3.10	3.07
20	237.41	665.76	324.40	6.06	4.47	7.22
30	222.49	782.80	313.24	7.97	5.17	10.64
40	216.36	799.68	337.77	10.31	6.59	18.15
EGM						
10	227.20	519.65	436.23	7.48	3.04	8.48
20	220.00	618.42	299.28	14.67	4.56	22.34
30	215.32	629.77	305.36	21.43	6.51	47.82
40	171.79	655.36	312.07	25.43	7.61	100.05
VP						
10	220.29	469.05	315.82	9.07	3.57	14.24
20	202.06	510.31	319.43	19.90	5.80	55.39
30	170.38	541.42	329.34	22.65	7.24	104.31
40	161.98	548.57	331.59	34.71	9.29	223.97

Activation energy

As previously discussed, the main pyrolysis and combustion region of both the raw biomasses and the hydrochar exhibited distinct weight loss stages. Thus, to evaluate the kinetic accurately, the kinetic triplets were obtained by stages.

Figure 4.10 and ***4.11*** present the changes in the apparent activation energies at each conversion degree obtained with the STK method during pyrolysis and combustion, respectively. No significant differences in E_a values between the iso-conversional methods were appreciated. The numerical results from the STK, OFW, and KAS methods, regarding both atmospheres, were reported in the Appendix ***Section A.2*** (***Table A.3*** to ***A.8***).
According to ***Table A.3*** to ***A.8***, the coefficient of determination (R^2) was above 0.9 for all the samples indicating that the apparent activation energy obtained for α between 0.1–0.9 had a high degree of consistency. Also, the fitting results based on the iso-conversional methods from the pyrolysis and combustion tests

are reported in Appendix ***Section A.2*** and displayed in ***Figure A.5*** and ***A.6***, respectively.

As shown in ***Figure 4.10***, in the full pyrolysis decomposition stage of VP and the first stage of HY and EGM, the apparent activation energy did not change significantly with α, mainly because of the rapid degradation of weakly bonded amorphous cellulose and hemicellulose. In the second stage, as α increased, the activation energy of HY and EGM gradually rose until reaching a certain limit and then decreased.

Once the weak bonds were degraded, the degradation of all-crystalline cellulose began, with lignin contributing to a further increase in activation energy [71]. The higher lignin content than cellulose in HY and EGM samples indicates that the pyrolysis process was primarily controlled by lignin and its intermediate products during the second decomposition stage. However, as the temperature increased beyond 300°C, the degradation of lignin led to the formation of stable higher molecular mass reaction products through self-condensation reactions [38]. These reaction products had higher activation energy and were not easily decomposed under moderate temperatures. Nevertheless, they gradually decomposed within the temperature range of 680°C to 845°C. Furthermore, regarding the average activation energy values, HY exhibited a lower value (82 kJ/mol) compared with EGM (171 kJ/mol) and VP (156 kJ/mol), in the first stage of pyrolysis. In the second stage, Ea of HY increased up to 160 kJ/mol, remaining lower than EGM (197 kJ/mol) and slightly higher than VP. This was related with the HTC process that alters the structure of the hydrochar by degrading hemicellulose and cellulose, which makes the HY require less energy during the first stage of pyrolysis while increasing lignin content that provides thermal stability and present higher bond energy [72, 73]. The pyrolysis results are in good agreement with previous studies [35, 59, 74, 75].
During combustion (***Figure 4.11***), E_a slightly increased with α between 0.1–0.2 for all the samples because of the volatiles release and their combustion [76], then began to decrease as it continued into the second stage because the active char reacts continuously with the available oxygen and undergoes thermal cracking to form lower compounds [77]. During both the first and second stage of combustion, the average activation energy value of HY (116 and 47 kJ/mol respectively) remained lower than EGM (158 kJ/mol and 114 kJ/mol) and VP (149 kJ/mol and 103 kJ/mol). This remark highlighted that HY has a greater porous structure and higher surface area, which contribute to the surface combustion reactions [54, 72, 76].

Pre-exponential factor

The energy compensation effect method was used to estimate the values of A. ***Table A.9*** and ***A.10*** list the values of A during pyrolysis and combustion at each conversion rate calculated according to ***Equation*** (3.16), where the values of the activation energy used came from the STK method since no significative variations of E_a values were highlighted between the iso-conversional methods. The corresponding plots are given in ***Figure A.7*** and ***A.8***, reported in Appendix ***Section A.2***. The high coefficients of determination ($R^2 > 0.99$) demonstrate the applicability of ECE, which is the linear correlation between $E_{a,i}$, and $\ln[A_i]$. During the first stage of pyrolysis, the pre-exponential values of EGM ranged in

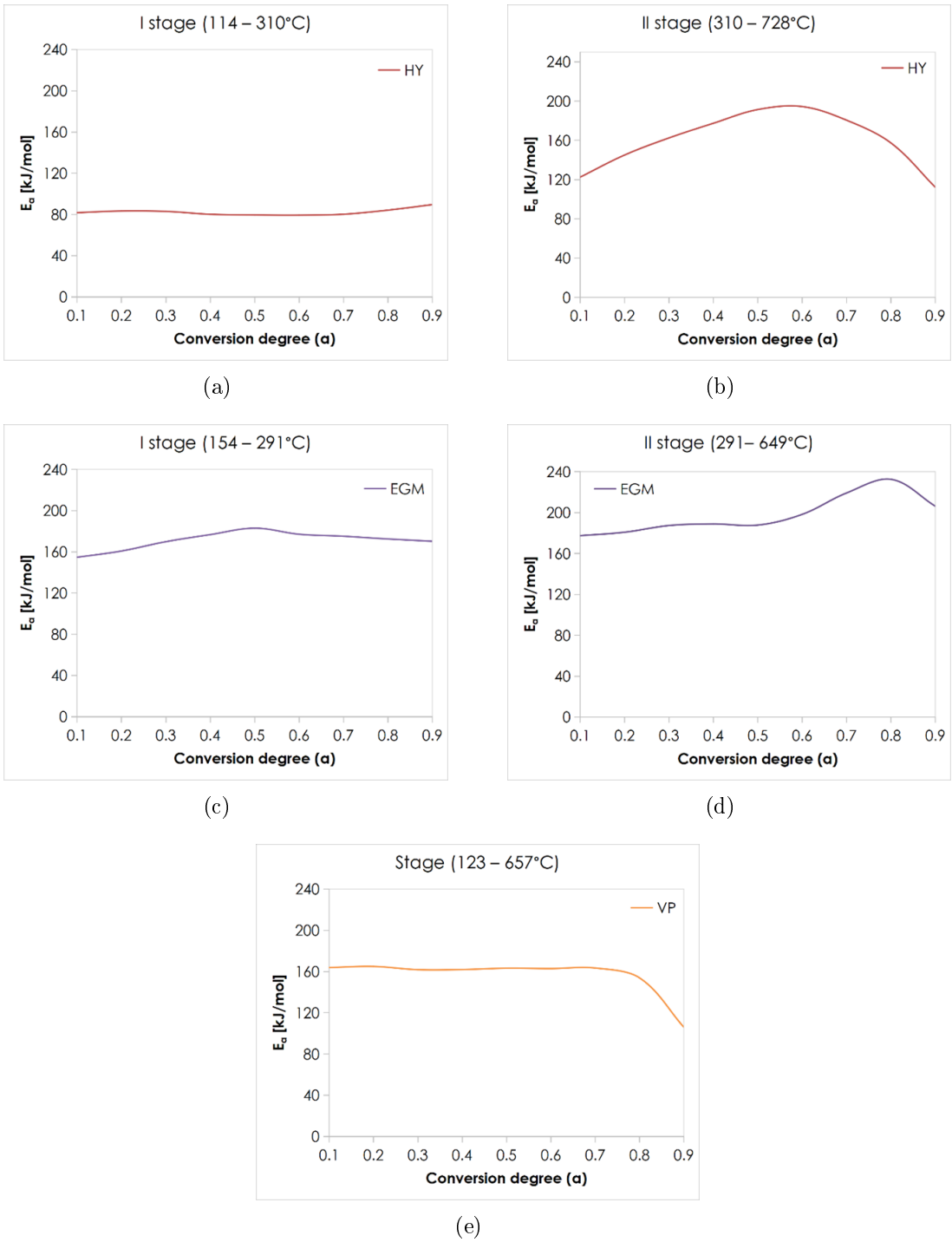

Figure 4.10: *Trend of apparent activation energy of HY a–b, EGM c–d, and VP e, during pyrolysis obtained by STK method.*

the order of 10^{13} to 10^{16} s^{-1} with the highest value at $\alpha = 0.5$, while those of VP remained constant at 10^{12} s^{-1} with α between 0.1 and 0.7 then decreasing up to 10^{6} s^{-1} at $\alpha = 0.9$. Instead, the overall values of HY were lower than those of EGM and VP, remaining prettily constant with α in the order of 10^{5}–10^{6} s^{-1}. However, a slight variance of A with α was revealed in the second stage for EGM and HY, indicating more complex chemical reactions. The pre-exponential factors of EGM

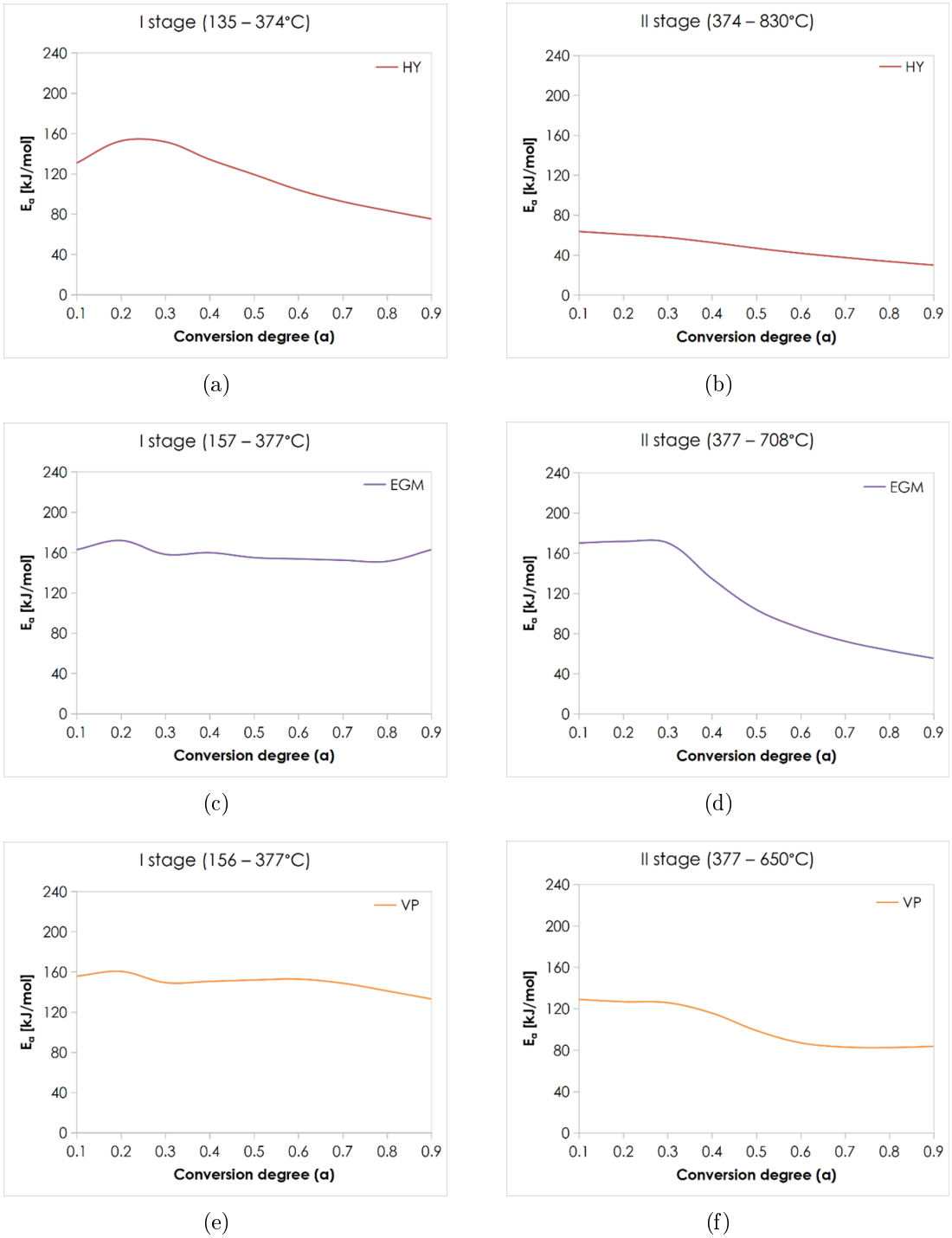

Figure 4.11: *Trend of apparent activation energy of HY a–b, EGM c–d, and VP e–f, during combustion obtained by STK method.*

and HY increased from an order of 10^{13} and 10^{7} s^{-1} up to 10^{18} and 10^{13} s^{-1} at a conversion rate of 0.8 and 0.6, respectively, then decreased to 10^{14} and 10^{6} s^{-1} at $\alpha = 0.9$. A higher pre-exponential value implicates an increased frequency of molecular collisions, thereby necessitating a greater amount of heat transfer [78]. Furthermore, while values of A less than 10^{9} s^{-1} typically indicate poor reactivity related mainly to surface reactions, or tight complex if not dependant on the surface

area, A values greater than 10^9 s^{-1} represent simple complex inbound reactions, which demand larger activation energies [79, 80].
During the first stage of combustion, the pre-exponential values of EGM and VP were higher than 10^9 s^{-1}, with a slight decrement trend in the order of 10^{11}–10^{13} and 10^9–10^{12}, respectively. Instead, HY showed a small increase of A from 10^9 to 10^{11} s^{-1} between $\alpha = 0.1$ and 0.2, then decreased up to 10^4 s^{-1} at $\alpha = 0.9$. In the second stage, all the samples provided a pre-exponential value $\leq 10^9$ s^{-1}, decreasing from 10^1 and 10^{-1} s^{-1}, from 10^9 to 10^1 s^{-1}, and from 10^7 to 10^3 s^{-1}, respectively for HY, EGM, and VP. Generally, A values below $10^4 s^{-1}$, are primarily associated with the combustion of porous carbon characterized by a lower E_a value [81]. These findings suggest that a broad range of pre-exponential values implies a more complex composition of the sample, requiring multiple energy levels at different conversion degrees during the combustion process [72, 78].

Reaction mechanism

The kinetic mechanism function was determined by using the master-plot method based on the activation energy from the STK method. According to ***Equation*** (3.19), the best fit between the experimental and theoretical curves of the master plot revealed the most appropriate reaction model. The results are reported in Appendix ***Section A.2*** and displayed in ***Figure A.9*** and ***A.10***.
Different reaction mechanisms were identified for each step of pyrolysis and combustion of HY, EGM, and VP. During the first stage of pyrolysis, HY and EGM are dominated by the one-dimensional diffusion-reaction mechanism (D1), migrating respectively to the reaction order model F4 and F6 in the second stage. This was mostly ascribed to the ongoing release of volatiles and the creation of more porous structures, which improved the diffusion mechanism [82]. Instead, VP was characterized by reaction order model F3, thus was assumed that the rate of reaction was mainly proportional to the concentration of the reactants. Also, during the first and second stages of combustion of EGM and VP the experimental master plot revealed the best fit with the theoretical curves of the reaction order model F3–F1 and F2–F1, respectively. However, HY was best described with the two-dimensional diffusion mechanism (D2) in the first stage, approaching the second-order geometrical contraction model (R2) in the second stage. This behavior suggests that after volatile release, combustion processes began at the outside of the char particles and moved inside toward the central core. This model assumed that the reaction rate was controlled by the decomposition occurring on the surface, thus resulting in the contraction of area [80, 83].
Combining the reaction model with ***Equation*** (3.11), the kinetic equations describing the pyrolysis and combustion of HY, EGM, and VP can be obtained, as reported in ***Table 4.8*** and ***4.9***.

Table 4.8: *Pyrolysis rate equations of HY, EGM, and VP at 10°C/min.*

Sample	Reaction rate equation	Stage [°C]
HY	$\frac{d\alpha}{dt} = 1.97 \times 10^{6} e^{-(82.19/RT)} 0.5\alpha$	114–310
	$\frac{d\alpha}{dt} = 9.68 \times 10^{12} e^{-(160.19/RT)} (1-\alpha)^{4}$	310–728
EGM	$\frac{d\alpha}{dt} = 2.53 \times 10^{15} e^{-(170.93/RT)} 0.5\alpha$	154–291
	$\frac{d\alpha}{dt} = 2.07 \times 10^{17} e^{-(197.50/RT)} (1-\alpha)^{6}$	291–649
VP	$\frac{d\alpha}{dt} = 2.30 \times 10^{12} e^{-(155.66/RT)} (1-\alpha)^{3}$	123–657

Table 4.9: *Combustion rate equations of HY, EGM, and VP at 10°C/min.*

Sample	Reaction rate equation	Stage [°C]
HY	$\frac{d\alpha}{dt} = 8.28 \times 10^{10} e^{-(115.92/RT)} [-ln(1-\alpha)]^{-1}$	135–374
	$\frac{d\alpha}{dt} = 12.41\ e^{-(47.08/RT)} 2 (1-\alpha)^{1/2}$	374–830
EGM	$\frac{d\alpha}{dt} = 1.33 \times 10^{13} e^{-(158.61/RT)} (1-\alpha)^{3}$	157–377
	$\frac{d\alpha}{dt} = 2.59 \times 10^{9} e^{-(114.02/RT)} (1-\alpha)$	377–708
VP	$\frac{d\alpha}{dt} = 6.92 \times 10^{11} e^{-(149.27/RT)} (1-\alpha)^{2}$	156–377
	$\frac{d\alpha}{dt} = 6.73 \times 10^{6} e^{-(103.51/RT)} (1-\alpha)$	377–650

Thermodynamic parameters

By replacing the corresponding value of E_a obtained from the STK method (***Table A.3*** and ***A.6***) in the ***Equations*** (3.20) to (3.22), the value of Gibbs free energy, ΔG, change of enthalpy, ΔH, and change of entropy, ΔS, were obtained. The corresponding values at each conversion degree for both the pyrolysis and combustion are listed in ***Table A.11*** and ***A.12*** reported in Appendix (***Section A.2***).

Enthalpy is the total energy consumed by biomass samples during pyrolysis or combustion reactions predicting the bond strength [54]. The results demonstrate a similar shifting pattern between the change of ΔH and E_a for all the samples during both pyrolysis and combustion. Moreover, the positive values of ΔH revealed that pyrolysis and combustion of HY, EGM, and VP were based on endothermic reactions, meaning that molecules absorbed heat energy to break and establish new chemical bonds [84]. Also, the average difference between E_a and ΔH, for each material and in both the case of pyrolysis and combustion, was less than 6 kJ/mol, meaning that HY, EGM, and VP are prone to reaction since the potential energy barrier is low [78].
The Gibbs free energy provides information about the spontaneity and direction of reactions in both pyrolysis and combustion processes. Higher values of ΔG imply lower favorability of the reactions [54]. Overall, EGM and VP HY showed a larger average value of ΔG compared with HY in both the case of pyrolysis and combustion, showing that the reactions of HY's precursors require an input of more energy.
The ΔS value reflects the degree of disorder in a system. The higher ΔS, the less the system is near to its own thermodynamic equilibrium, demonstrating more reactivity [58]. The lower value of ΔS for HY indicates that the hydrochar is more structurally ordered compared to the original biomasses. This could be the result of the removal of volatile components and the restructuring of carbonaceous materials after HTC, leading to a more stable and structured product. Furthermore, only EGM revealed positive values of entropy under a nitrogen atmosphere, demonstrating high reactivity and a shorter reaction time for the formation of the activated complex through the release of volatiles and molecular rearrangement [36, 78].

Considering all available data, including kinetic and thermodynamic characteristics, as well as combustion and pyrolysis indexes, might be inferred that the hydrochar achieved a more thermodynamically stable, structurally ordered, and energetically favorable state through the co-HTC process, thus resulting in a potentially valuable product.

4.3 Pyrolysis kinetic of biomass and plastics mixture

During the course of my PhD, I had the opportunity to spend three months as a Visiting PhD Fellow at the prestigious Universidad de Córdoba, Spain. Throughout this time, I worked at the Department of Physical Chemistry and Applied Thermodynamics, focusing on the significant research area of biomass waste valorization into value-added products. Specifically, my contribution centered on the development of kinetic analysis for the co-pyrolysis of olive pomace and thermoplastic waste, utilizing thermogravimetric analysis as the primary investigative technique. This collaboration allowed me to delve deep into the intricacies of biomass conversion, uncovering valuable insights that will undoubtedly contribute to the advancement of sustainable and efficient waste management strategies. Based on this work, there is a forthcoming publication entitled "*Kinetic and thermodynamic behavior of co-pyrolysis of olive pomace and thermoplastic waste via*

thermogravimetric analysis".

Briefly, kinetic and thermodynamic parameters, as well as the reaction mechanism during the co-pyrolysis of olive pomace (OP) biomass and several waste plastic materials (WPMs) were investigated by thermogravimetric (TG) and differential thermogravimetric (DTG) techniques. Among WPMs, polypropylene (PP), polystyrene (PS), high-density polypropylene (HDPE), polyvinyl chloride (PVC) and polyethylene terephthalate glycol (PETG) were selected. Non-isothermal TG experiments were carried out under inert conditions at four heating rates (5, 10, 20, and 40 °C/min) testing both the raw biomass and the waste plastic materials singularly, and their blends (1:1 ratio).

The main results demonstrated that co-pyrolysis of PWMs with OP is an excellent alternative to individual material pyrolysis. The addition of olive pomace to plastic waste materials decreased the activation energy in a range from 50-25% for all the blends except for PVC/OP. Nevertheless, the complexity of the reactions that occur during the co-pyrolysis of biomass and plastic materials makes the reaction mechanism not straightforwardly defined.

The synergistic analysis showed that PETG-OP and PVC-OP were the blends with a positive synergistic effect during co-pyrolysis meaning accelerated degradation of the mixtures. However, the thermodynamic parameters showed the feasibility, spontaneity, and constant formation of stable products in the co-pyrolysis of WPMs with OP.

Overall, this research presents a viable solution to reduce the enormous volumes of WPMs and, at the same time, generate new value-added products. Further, experiments in a pyrolysis reactor for a comprehensive analysis would allow a better understanding of the process, to ensure optimal implementation in the reactor and progress towards its commercialization.

Nomenclature

Abbreviation		*Symbol*	
VP	Vine Pruning	m_{water}	water weight of the mixture (kg)
EGM	Exhausted Grape Marc	$m_{feedstock}$	biomass weight of the mixture (kg)
HTC	Hydrothermal Carbonization	$H_{water,HTC}$	enthalpy of water at the HTC temperature
MY	Mass Yield (%)	$H_{water,25}$	enthalpy of water at 25°C
EDY	Energy Densification Yield	A_s	Surface area of the HTC reactor (m^2
PEY	Phenols Extraction Yield (mgGAE/g)	k	thermal conductivity of the insulation (W/mK)
FR	Fuel Ratio	s	thickness of the insulation (m)
BBD	Box-Behnken Design	$c_{p,feedstock}$	heat capacity of the biomass (J/kgK)
EI	Enegy Input (kJ)	E_a	activation energy (kJ/mol)
GAE	Gallic Acid Equivalents	A	pre-exponential factor (s^{-1})
TPC	Total Phenolic Content	ΔH	changes in enthalpy (kJ/mol)
TG	Thermogravimectric	ΔG	changes in Gibbs free energy (kJ/mol)
DTG	Differential Thermogravimetric	ΔS	changes in entropy (J/mol K)
STK	Starink method	β	heating rate (°C/min)
OFW	Ozawa-Flynn-Wall	D_i	devolatilization index ($\%min^{-1}C^{-3}3$)
KAS	Kissinger-Akahira-Sunose	DTG_{max}	maximum weight loss rate
OP	Olive Pomace	T_i	initial temperature (°C)
WPMs	Waste Plastic Materials	T_f	final temperature (°C)
PP	Polypropylene	T_p	peak temperature (°C)
PS	Polystyrene	S	combustion index ($\%^2min^{-2}C^{-3}3$)
HDPE	High-Density Polypropylene	α	conversion degree
PVC	Polyvinyl Chloride		
PETG	Polyethylene Terephthalate Glycol		

Bibliography

[1] M. Barbanera, A. Cardarelli, E. Carota, M. Castellini, T. Giannoni, and S. Ubertini, "Valorization of winery and distillery by-products by hydrothermal carbonization," *Scientific Reports*, vol. 11, no. 1, p. 23973, 2021.

[2] V. Belete, R. Y. Spitzer, R. Posmanik, D. Jassby, A. Iddya, N. Kassem, J. W. Tester, Y. Z. Gross, Amit, and Mau, "Hydrothermal carbonization of anaerobic digestate and manure from a dairy farm on energy recovery and the fate of nutrients," *Bioresource technology*, vol. 333, pp. 125164–125164, 2021.

[3] G. Tag, A. T. Yanik, Jale, and Duman, "Influences of feedstock type and process variables on hydrochar properties.," *Bioresource technology*, vol. 250, pp. 337–344, 2017.

[4] D. Lee, K. Lee, J. Park, Ki Young, and Sohn, "Solid fuel production through hydrothermal carbonization of sewage sludge and microalgae chlorella sp. from wastewater treatment plant.," *Chemosphere*, vol. 230, pp. 157–163, 2019.

[5] S. Missaoui, V. Belandria, B. Cagnon, B. Sarh, A. Gökalp, Iskender, and Bostyn, "Hydrothermal carbonization of dried olive pomace: Energy potential and process performances," *Journal of Analytical and Applied Pyrolysis*, vol. 128, pp. 281–290, 2017.

[6] B. Nakason, V. Kanokkantapong, N. Viriya-empikul, W. Kraithong, K. Pavasant, Prasert, and Panyapinyopol, "Hydrothermal carbonization of unwanted biomass materials: Effect of process temperature and retention time on hydrochar and liquid fraction," *Journal of the Energy Institute*, vol. 91, no. 5, pp. 786–796, 2018.

[7] A. Hoekman, C. Robbins, B. Zielinska, S. K. Felix, Larry G., and Broch, "Hydrothermal carbonization (HTC) of selected woody and herbaceous biomass feedstocks," *Biomass Conversion and Biorefinery*, vol. 3, no. 2, pp. 113–126, 2012.

[8] J. Mihajlović, S. Maletić, M. K. Isakovski, M. Stojanović, Z. Lopičić, M. Trifunović, Snežana, and Petrović, "Hydrothermal carbonization of miscanthus × giganteus: Structural and fuel properties of hydrochars and organic profile with the ecotoxicological assessment of the liquid phase," *Energy Conversion and Management*, vol. 159, pp. 254–263, 2018.

[9] P. J. Lu, J. R. Flora, X. Berge, Nicole D., and Pellechia, "Influence of reaction time and temperature on product formation and characteristics associated with the hydrothermal carbonization of cellulose.," *Bioresource technology*, vol. 138, pp. 180–190, 2013.

[10] B. Wang, Z. Gong, Y. Zhai, M. Cao, T. Peng, Chuan, and Si, "Co-hydrothermal carbonization of food waste-woody sawdust blend: Interaction effects on the hydrochar properties and nutrients characteristics.," *Bioresource technology*, vol. 316, pp. 123900–NA, 2020.

[11] M. Afolabi, O. O. Cheng, Yu-Ling, and Sohail, "Optimisation and characterisation of hydrochar production from spent coffee grounds by hydrothermal carbonisation," *Renewable Energy*, vol. 147, pp. 1380–1391, 2020.

[12] S. M. Z. Sultana, M. E. Mohammed, M. F. Irfan, B. Haq, M. O. Faruque, A. Razzak, N. Hossain, Mohammad M., and Hossain, "Experimental study and parameters optimization of microalgae based heavy metals removal process using a hybrid response surface methodology-crow search algorithm.," *Scientific reports*, vol. 10, no. 1, pp. 15068–15068, 2020.

[13] X. Chen, X. Peng, Y. Lin, X. Yao, Zhongliang, and Ma, "Conversion of sweet potato waste to solid fuel via hydrothermal carbonization," *Bioresource technology*, vol. 249, pp. 900–907, 2017.

[14] A. K. Sharma, H. B. Dubey, Brajesh, and Sarmah, "Hydrothermal carbonization of renewable waste biomass for solid biofuel production: A discussion on process mechanism, the influence of process parameters, environmental performance and fuel properties of hydrochar," *Renewable and Sustainable Energy Reviews*, vol. 123, p. 109761, 2020.

[15] M. Volpe and L. Fiori, "From olive waste to solid biofuel through hydrothermal carbonisation: The role of temperature and solid load on secondary char formation and hydrochar energy properties," *Journal of Analytical and Applied Pyrolysis*, vol. 124, pp. 63–72, 2017.

[16] M. Buratti, E. Lascaro, C. Cotana, Franco, and Barbanera, "Optimization of torrefaction conditions of coffee industry residues using desirability function approach.," *Waste management (New York, N.Y.)*, vol. 73, pp. 523–534, 2017.

[17] V. Mäkelä, M. Fullana, Andres, and Benavente, "Hydrothermal carbonization of lignocellulosic biomass: Effect of process conditions on hydrochar properties," *Applied Energy*, vol. 155, pp. 576–584, 2015.

[18] H. S. Kambo, Animesh and Dutta, "Comparative evaluation of torrefaction and hydrothermal carbonization of lignocellulosic biomass for the production of solid biofuel," *Energy Conversion and Management*, vol. 105, pp. 746–755, 2015.

[19] M. Aguado, L. Pérez-Villarejo, M. L. Martínez-Cartas, R. Sánchez, Sebastián, and Cuevas, "Upgrading almond-tree pruning as a biofuel via wet torrefaction," *Renewable Energy*, vol. 145, pp. 2091–2100, 2020.

[20] A. Singh, R. K. Chakraborty, Jyoti Prasad, and Sarkar, "Effect of torrefaction on the physicochemical properties of eucalyptus derived biofuels: estimation of kinetic parameters and optimizing torrefaction using response surface methodology (RSM)," *Energy*, vol. 198, p. 117369, 2020.

[21] M. Wilk, M. Gajek, Marcin, and Śliz, "The effects of hydrothermal carbonization operating parameters on high-value hydrochar derived from beet pulp," *Renewable Energy*, vol. 177, pp. 216–228, 2021.

[22] N. Petrovil, J. D. Maksimovil, V. Maksimovil, M. Kragovil, M. Stojanovil, M. Lauševil, J. Mihajlovil, Marija, and Perišil, "Hydrothermal conversion of grape pomace: Detailed characterization of obtained hydrochar and liquid phase," *Journal of Analytical and Applied Pyrolysis*, vol. 118, pp. 267–277, 2016.

[23] G. Duman, H. Cay, I. C. Kantarli, G. Yanik, Jale, and Balmuk, "Comparative evaluation of torrefaction and hydrothermal carbonization: Effect on fuel properties and combustion behavior of agricultural wastes," *Energy & Fuels*, vol. 34, no. 9, pp. 11175–11185, 2020.

[24] A. Natolino, Carla and D. Porto, "Kinetic models for conventional and ultrasound assistant extraction of polyphenols from defatted fresh and distilled grape marc and its main components skins and seeds," *Chemical Engineering Research and Design*, vol. 156, pp. 1–12, 2020.

[25] J. Atallah, M. N. Ahmad, J. J. Leahy, E. Kwapinski, Witold, and Zeaiter, "Hydrothermal carbonization of spent mushroom compost waste compared against torrefaction and pyrolysis," *Fuel Processing Technology*, vol. 216, p. 106795, 2021.

[26] P. Arigò, P. Šilarová, C. Ml, A. Česlová, Lenka, and Česla, "Development of extraction method for characterization of free and bonded polyphenols in barley (hordeum vulgare l.) grown in czech republic using liquid chromatography-tandem mass spectrometry.," *Food chemistry*, vol. 245, pp. 829–837, 2017.

[27] I. Drevelegka, Athanasia M. and Goula, "Recovery of grape pomace phenolic compounds through optimized extraction and adsorption processes," *Chemical Engineering and Processing - Process Intensification*, vol. 149, p. 107845, 2020.

[28] C. Da Porto, Andrea and Natolino, "Optimization of the extraction of phenolic compounds from red grape marc (vitis vinifera l.) using response surface methodology," *Journal of Wine Research*, vol. 29, no. 1, pp. 26–36, 2018.

[29] A. Aliakbarian, P. Perego, B. Dehghani, Fariba, and Fathi, "Extraction of antioxidants from winery wastes using subcritical water," *The Journal of Supercritical Fluids*, vol. 65, pp. 18–24, 2012.

[30] M. Li, P. Olsen, L. Berge, Nicole D., and Hale, "Using liquid waste streams as the moisture source during the hydrothermal carbonization of municipal solid wastes," *Waste management (New York, N.Y.)*, vol. 34, no. 11, pp. 2185–2195, 2014.

[31] H. B. Venna, P. H. P. Reddy, S. Chowdhury, S. Dubey, Brajesh, and Sharma, "Landfill leachate as an alternative moisture source for hydrothermal carbonization of municipal solid wastes to solid biofuels.," *Bioresource technology*, vol. 320, p. 124410, 2020.

[32] S. Wang, G. Dai, H. Yang, and Z. Luo, "Lignocellulosic biomass pyrolysis mechanism: A state-of-the-art review," *Progress in Energy and Combustion Science*, vol. 62, pp. 33–86, 2017.

[33] B. Khiari and M. Jeguirim, "Pyrolysis of grape marc from tunisian wine industry: Feedstock characterization, thermal degradation and kinetic analysis," *Energies*, vol. 11, no. 4, p. 730, 2018.

[34] M. Salgado-Ramos, F. J. Martí-Quijal, A. J. Huertas-Alonso, M. P. Sánchez-Verdú, A. Moreno, and F. J. Barba, "Winemaking-derived by-products: In-depth characterization and sustainable, advanced pulsed electric field (PEF) processing to a zero-waste-based approach," *Journal of Environmental Chemical Engineering*, vol. 11, no. 5, p. 110535, 2023.

[35] R. Torres, B. Valdez, M. T. Beleño, M. A. Coronado, M. Stoytcheva, C. García, B. A. Rojano, and G. Montero, "Char production with high-energy value and standardized properties from two types of biomass," *Biomass Conversion and Biorefinery*, vol. 13, no. 6, pp. 4831–4847, 2023.

[36] G. D. Mumbach, J. L. F. Alves, J. C. G. Da Silva, M. Di Domenico, R. F. De Sena, C. Marangoni, R. A. F. Machado, and A. Bolzan, "Pyrolysis of cocoa shell and its bioenergy potential: evaluating the kinetic triplet, thermodynamic parameters, and evolved gas analysis using TGA-FTIR," *Biomass Conversion and Biorefinery*, vol. 12, no. 3, pp. 723–739, 2022.

[37] J. A. Libra, K. S. Ro, C. Kammann, A. Funke, N. D. Berge, Y. Neubauer, M.-M. Titirici, C. Fühner, O. Bens, J. Kern, and K.-H. Emmerich, "Hydrothermal carbonization of biomass residuals: a comparative review of the chemistry, processes and applications of wet and dry pyrolysis," *Biofuels*, vol. 2, no. 1, pp. 71–106, 2011.

[38] M. A. Islam, M. Asif, and B. Hameed, "Pyrolysis kinetics of raw and hydrothermally carbonized karanj (pongamia pinnata) fruit hulls via thermogravimetric analysis," *Bioresource Technology*, vol. 179, pp. 227–233, 2015.

[39] M. Mäkelä, C. W. Kwong, M. Broström, and K. Yoshikawa, "Hydrothermal treatment of grape marc for solid fuel applications," *Energy Conversion and Management*, vol. 145, pp. 371–377, 2017.

[40] M. Pala, I. C. Kantarli, H. B. Buyukisik, and J. Yanik, "Hydrothermal carbonization and torrefaction of grape pomace: A comparative evaluation," *Bioresource Technology*, vol. 161, pp. 255–262, 2014.

[41] A. M. Mastral, R. Murillo, M. S. Callén, T. García, and C. E. Snape, "Influence of process variables on oils from tire pyrolysis and hydropyrolysis in a swept fixed bed reactor," *Energy & Fuels*, vol. 14, no. 4, pp. 739–744, 2000.

[42] A. Mishra, S. Nanda, M. Ranjan Parida, P. K. Jena, S. K. Dwibedi, S. Manjari Samantaray, D. Samantaray, M. K. Mohanty, and M. Dash, "A comparative study on pyrolysis kinetics and thermodynamic parameters of little millet and sunflower stems biomass using thermogravimetric analysis," *Bioresource Technology*, vol. 367, p. 128231, 2023.

[43] S. Singh, T. Patil, S. P. Tekade, M. B. Gawande, and A. N. Sawarkar, "Studies on individual pyrolysis and co-pyrolysis of corn cob and polyethylene:

Thermal degradation behavior, possible synergism, kinetics, and thermodynamic analysis," *Science of The Total Environment*, vol. 783, p. 147004, 2021.

[44] A. K. Sakhiya, A. Anand, V. K. Vijay, and P. Kaushal, "Thermal decomposition of rice straw from rice basin of india to improve energy-pollution nexus: Kinetic modeling and thermodynamic analysis," *Energy Nexus*, vol. 4, p. 100026, 2021.

[45] Z. Lei, S. Wang, H. Fu, W. Gao, B. Wang, J. Zeng, and J. Xu, "Thermal pyrolysis characteristics and kinetics of hemicellulose isolated from camellia oleifera shell," *Bioresource Technology*, vol. 282, pp. 228–235, 2019.

[46] S.-S. Kim, H. V. Ly, J. Kim, J. H. Choi, and H. C. Woo, "Thermogravimetric characteristics and pyrolysis kinetics of alga sagarssum sp. biomass," *Bioresource Technology*, vol. 139, pp. 242–248, 2013.

[47] Y. Li, H. Liu, K. Xiao, M. Jin, H. Xiao, and H. Yao, "Combustion and pyrolysis characteristics of hydrochar prepared by hydrothermal carbonization of typical food waste: Influence of carbohydrates, proteins, and lipids," *Energy & Fuels*, vol. 34, no. 1, pp. 430–439, 2020.

[48] Q. He, L. Ding, Y. Gong, W. Li, J. Wei, and G. Yu, "Effect of torrefaction on pinewood pyrolysis kinetics and thermal behavior using thermogravimetric analysis," *Bioresource Technology*, vol. 280, pp. 104–111, 2019.

[49] Q. He, C. Cheng, A. Raheem, L. Ding, S. Shiung Lam, and G. Yu, "Effect of hydrothermal carbonization on woody biomass: From structure to reactivity," *Fuel*, vol. 330, p. 125586, 2022.

[50] Y. Yu, A. Lau, and S. Sokhansanj, "Hydrothermal carbonization and pelletization of moistened wheat straw," *Renewable Energy*, vol. 190, pp. 1018–1028, 2022.

[51] E. Cárdenas-Aguiar, G. Gascó, J. Paz-Ferreiro, and A. Méndez, "Thermogravimetric analysis and carbon stability of chars produced from slow pyrolysis and hydrothermal carbonization of manure waste," *Journal of Analytical and Applied Pyrolysis*, vol. 140, pp. 434–443, 2019.

[52] D. Mortari, D. Perondi, G. Rossi, J. Bonato, M. Godinho, and F. Pereira, "The influence of water-soluble inorganic matter on combustion of grape pomace and its chars produced by slow and fast pyrolysis," *Fuel*, vol. 284, p. 118880, 2021.

[53] W. Cao, J. Li, T. Martí-Rosselló, and X. Zhang, "Experimental study on the ignition characteristics of cellulose, hemicellulose, lignin and their mixtures," *Journal of the Energy Institute*, vol. 92, no. 5, pp. 1303–1312, 2019.

[54] Q. Lang, B. Zhang, Z. Liu, Z. Chen, Y. Xia, D. Li, J. Ma, and C. Gai, "Co-hydrothermal carbonization of corn stalk and swine manure: Combustion behavior of hydrochar by thermogravimetric analysis," *Bioresource Technology*, vol. 271, pp. 75–83, 2019.

[55] T. Zhang, K. Kang, S. Nanda, A. K. Dalai, T. Xie, and Y. Zhao, "Comparative study on fuel characteristics and pyrolysis kinetics of corn residue-based hydrochar produced via microwave hydrothermal carbonization," *Chemosphere*, vol. 291, p. 132787, 2022.

[56] M. Ebrahim Malool, M. Keshavarz Moraveji, and J. Shayegan, "Co-hydrothermal carbonization of digested sewage sludge and sugarcane bagasse: Integrated approach for waste management, optimized production, characterization and pb(II) adsorption," *Alexandria Engineering Journal*, vol. 74, pp. 79–105, 2023.

[57] X. Zhuang, H. Zhan, Y. Huang, Y. Song, X. Yin, and C. Wu, "Conversion of industrial biowastes to clean solid fuels via hydrothermal carbonization (HTC): Upgrading mechanism in relation to coalification process and combustion behavior," *Bioresource Technology*, vol. 267, pp. 17–29, 2018-11.

[58] J. Ma, H. Luo, Y. Li, Z. Liu, D. Li, C. Gai, and W. Jiao, "Pyrolysis kinetics and thermodynamic parameters of the hydrochars derived from co-hydrothermal carbonization of sawdust and sewage sludge using thermogravimetric analysis," *Bioresource Technology*, vol. 282, pp. 133–141, 2019.

[59] A. F. Ferreira, J. P. Ribau, and M. Costa, "A decision support method for biochars characterization from carbonization of grape pomace," *Biomass and Bioenergy*, vol. 145, p. 105946, 2021.

[60] Y. Niu, H. Tan, and S. Hui, "Ash-related issues during biomass combustion: Alkali-induced slagging, silicate melt-induced slagging (ash fusion), agglomeration, corrosion, ash utilization, and related countermeasures," *Progress in Energy and Combustion Science*, vol. 52, pp. 1–61, 2016.

[61] D. Vamvuka and S. Sfakiotakis, "Combustion behaviour of biomass fuels and their blends with lignite," *Thermochimica Acta*, vol. 526, no. 1, pp. 192–199, 2011.

[62] A. Cardarelli, S. Pinzi, and M. Barbanera, "Effect of torrefaction temperature on spent coffee grounds thermal behaviour and kinetics," *Renewable Energy*, vol. 185, pp. 704–716, 2022.

[63] Z.-X. Xu, H. Song, S. Zhang, S.-Q. Tong, Z.-X. He, Q. Wang, B. Li, and X. Hu, "Co-hydrothermal carbonization of digested sewage sludge and cow dung biogas residue: Investigation of the reaction characteristics," *Energy*, vol. 187, p. 115972, 2019.

[64] Y. Liu, Y. Song, J. Fu, W. Ao, A. Ali Siyal, C. Zhou, C. Liu, M. Yu, Y. Zhang, J. Dai, and X. Bi, "Co-pyrolysis of sewage sludge and lignocellulosic biomass: Synergistic effects on products characteristics and kinetics," *Energy Conversion and Management*, vol. 268, p. 116061, 2022.

[65] X. Chen, X. Ma, X. Peng, Y. Lin, and Z. Yao, "Conversion of sweet potato waste to solid fuel via hydrothermal carbonization," *Bioresource Technology*, vol. 249, pp. 900–907, 2018.

[66] G. K. Parshetti, A. Quek, R. Betha, and R. Balasubramanian, "TGA–FTIR investigation of co-combustion characteristics of blends of hydrothermally carbonized oil palm biomass (EFB) and coal," *Fuel Processing Technology*, vol. 118, pp. 228–234, 2014-02.

[67] J. L. F. Alves, J. C. G. Da Silva, G. D. Mumbach, M. D. Domenico, R. F. De Sena, R. A. F. Machado, and C. Marangoni, "Demonstrating the suitability of tamarind residues to bioenergy exploitation via combustion through physicochemical properties, performance indexes, and emission characteristics," *BioEnergy Research*, vol. 13, no. 4, pp. 1308–1320, 2020.

[68] L. Riva, A. Cardarelli, G. J. Andersen, T. V. Buø, M. Barbanera, P. Bartocci, F. Fantozzi, and H. K. Nielsen, "On the self-heating behavior of upgraded biochar pellets blended with pyrolysis oil: Effects of process parameters," *Fuel*, vol. 278, p. 118395, 2020.

[69] Y. Lu, H. Yang, A. V. Karasev, C. Wang, and P. G. Jönsson, "Applications of hydrochar and charcoal in the iron and steelmaking industry—part 1: Characterization of carbonaceous materials," *Sustainability*, vol. 14, no. 15, p. 9488, 2022.

[70] X. Huang, K. W. Ng, L. Giroux, M. Duchesne, D. Li, and T. Todoschuk, "Interaction behavior of biogenic material with electric arc furnace slag," *Fuels*, vol. 2, no. 4, pp. 420–436, 2021.

[71] M. Lopez-Velazquez, V. Santes, J. Balmaseda, and E. Torres-Garcia, "Pyrolysis of orange waste: A thermo-kinetic study," *Journal of Analytical and Applied Pyrolysis*, vol. 99, pp. 170–177, 2013.

[72] Q. Lang, Z. Liu, Y. Li, J. Xu, J. Li, B. Liu, and Q. Sun, "Combustion characteristics, kinetic and thermodynamic analyses of hydrochars derived from hydrothermal carbonization of cattle manure," *Journal of Environmental Chemical Engineering*, vol. 10, no. 1, p. 106938, 2022.

[73] X. Dong, S. Guo, M. Ma, H. Zheng, X. Gao, S. Wang, and H. Zhang, "Hydrothermal carbonization of millet stalk and dilute-acid-impregnated millet stalk: combustion behaviors of hydrochars by thermogravimetric analysis and a novel mixed-function fitting method," *Fuel*, vol. 273, p. 117734, 2020.

[74] A. Vasileiadou, "Sustainable energy production from grape marc: from thermo-analytical and chemical analysis to kinetic modeling and environmental impact assessment," *Energy, Ecology and Environment*, vol. 8, no. 5, pp. 471–484, 2023.

[75] P. Rantuch, J. Ondruška, and I. Wachter, "A comparison of thermal decomposition of vineyard pruning waste in the flow of air and nitrogen," *International Journal of Global Warming*, vol. 13, no. 2, p. 138, 2017.

[76] S. B. Kabakcı, "Pyrolysis and combustion characteristics and kinetics of wood sawdust and wood sawdust hydrochar," *Environmental Progress & Sustainable Energy*, vol. 39, no. 2, p. e13315, 2020.

[77] R. Tariq, Y. Mohd Zaifullizan, A. A. Salema, A. Abdulatif, and L. S. Ken, "Co-pyrolysis and co-combustion of orange peel and biomass blends: Kinetics, thermodynamic, and ANN application," *Renewable Energy*, vol. 198, pp. 399–414, 2022.

[78] C. T. Chong, G. R. Mong, J.-H. Ng, W. W. F. Chong, F. N. Ani, S. S. Lam, and H. C. Ong, "Pyrolysis characteristics and kinetic studies of horse manure using thermogravimetric analysis," *Energy Conversion and Management*, vol. 180, pp. 1260–1267, 2019.

[79] S. C. Turmanova, S. D. Genieva, A. S. Dimitrova, and L. T. Vlaev, "Non-isothermal degradation kinetics of filled with rise husk ash polypropene composites," *Express Polymer Letters*, vol. 2, no. 2, pp. 133–146, 2008.

[80] N. Thejaswini, P. K. R. Annapureddy, D. Rammohan, and N. Kishore, "Kinetics and thermodynamics of non-isothermal pyrolysis of *Terminalia chebula* branches at different heating rates," *International Journal of Chemical Kinetics*, vol. 55, no. 11, pp. 673–687, 2023-11.

[81] M. Barbanera, F. Cotana, and U. Di Matteo, "Co-combustion performance and kinetic study of solid digestate with gasification biochar," *Renewable Energy*, vol. 121, pp. 597–605, 2018.

[82] S. A. El-Sayed and M. E. Mostafa, "Pyrolysis and co-pyrolysis of egyptian olive pomace, sawdust, and their blends: Thermal decomposition, kinetics, synergistic effect, and thermodynamic analysis," *Journal of Cleaner Production*, vol. 401, p. 136772, 2023.

[83] J. Zhang, H. Zou, J. Liu, F. Evrendilek, W. Xie, Y. He, and M. Buyukada, "Comparative (co-)pyrolytic performances and by-products of textile dyeing sludge and cattle manure: Deeper insights from py-GC/MS, TG-FTIR, 2d-COS and PCA analyses," *Journal of Hazardous Materials*, vol. 401, p. 123276, 2021.

[84] Z. Boubacar Laougé and H. Merdun, "Pyrolysis and combustion kinetics of sida cordifolia l. using thermogravimetric analysis," *Bioresource Technology*, vol. 299, p. 122602, 2020.

Chapter 5

Industrial application

Replacing the use of fossil fuels with biogenic materials in the industrial sector is one of the main challenges that researchers are facing nowadays. Biochars, which are coal-like carbon-rich materials obtained from the thermochemical conversion of biomass, have gained significant attention due to their potential to reduce CO_2 emissions and enhance the sustainability of industrial processes. As previously mentioned in ***Subsection 2.3.2***, the steelmaking industry is one of the branches of the industrial sector which largely contributes to the global CO_2 emissions. Even if there is a shift from the high energy and CO_2-intensive dominant BF-BOF production route towards the scrap-based EAF steelmaking, the decarbonization pathway remains a

Thus, Paper C and Paper D want to provide a boost to the research on the possible (and reasonable) use of biochars in the EAF steelmaking processes.
Overall, the integration of computational fluid dynamics simulations (Paper C) and life cycle analysis (Paper D) provides a powerful framework for understanding and optimizing the application of biochars in the industrial sector, facilitating sustainable practices, and reducing the environmental impact of steel production.

5.1 CFD analysis of biochars in electric arc furnace steelmaking process – *Paper C*

Computational fluid dynamics (CFD) is a powerful tool that plays a crucial role in understanding and optimizing the application of biochar derived from biomass in the steelmaking industry.

Within Paper C, titled "*Computational fluid dynamics analysis of biochar combustion in a simulated ironmaking electric arc furnace*" [1], a three-dimensional CFD model for biochar combustion and electrode radiation inside an EAF was developed by assuming particle surface and gas-phase reactions to predict injected biochar particles combustion. The use of biochar from torrefaction (T300), slow pyrolysis (P500), and hydrothermal carbonization (H220) of biomass as a substitute for fossil coal in EAF was investigated.
One among the important targets was to research the combustion phenomenon of injected biochar particles, electric arc radiation, temperature distribution, and the influence of intermediate gas release. The accuracy of simulations and the combustion efficiency of T300, P500, and H220 as an alternative to anthracite (Ac)

were analyzed and verified.
Overall, the CFD model offered extensive information on the spatial distribution of the jet velocity, temperature profile, reaction heat release, and distributions of combustion species.
The main findings emphasized that for all biochars the high-temperature difference inside the furnace revealed the rapid and strong exothermicity of the combustion reactions. The higher volatile matter and the lower fixed carbon content of T300, P500, and H220 than anthracite caused the reactions to be fast, and the exothermic heat released was more concentrated. The results showed that T300 and H220 behaved more as burners, producing a sharper heat release than P500. Also, extensive gas generation of CO was observed from biochars while anthracite showed slightly lower levels of gas generation. P500 provided a slower rate of gas generation than T300 and H220, making it easier for the slag to trap gases and generate sustained levels of slag foaming.
Even if the combustion behavior of the biochars was quite different from that of anthracite coal and far from their application in EAF steelmaking processes, P500 would seem more prone to be employed as a slag foaming promoter than T300 and H220. To enhance the biochar combustion properties for EAF applications e.g., by reducing volatiles, increasing fixed carbon, or reducing the porosity, it might be useful to operate on the pretreatment process parameters, such as reaction temperature, residence time, heating rate, particle size, etc. In this sense, the combustion behavior of pyrolyzed cottonwood (W400) with higher FC content and lower VM and ash content was also modeled. As expected, the results showed that W400 exhibited less CO generation, thus a higher concentration of C might be available for iron oxide reduction. Consequently, W400 could be a more suitable candidate for iron carburization instead of a foaming agent promoter. Carbon sources for EAF steelmaking are mainly employed as a fuel, to provide heat, as a slag foaming agent, which protects the equipment by covering the arcs with electricity conservation, and as an iron carburizer, to modify the carbon content in the steel. This research aimed to highlight the potential advantages of using biomass in EAF steelmaking. By undergoing biomass to thermal pretreatments, e.g., torrefaction, pyrolysis, and hydrothermal carbonization, it is possible to enhance its chemical-physical characteristics to be used for a specific purpose. The faster heat release of very reactive biochars promotes the rising of higher temperatures inside the EAF. This might reduce the energy demand from the electrodes and electrical consumption. Biochar that generates reducing gases at higher temperatures might be suitable as a reducing agent and foaming slag promoter. Moreover, biochar with higher fixed carbon and lower ash and volatile matter would be more prone to be used as an iron carburizer. However, it may be essential to test the mixing of coal and biochar to produce both a rise in temperatures, a decrease in electrical load, and, as a result, an increase in the carbon injected into the foamy slag. The use of pretreated biomass via torrefaction, pyrolysis, and hydrothermal carbonization instead of fossil coal (anthracite) in the EAF steelmaking process does not affect the typical metallurgy of the EAF process and can help steelmakers to operate in an expected carbon-neutral production scenario.

5.1.1 Computational domain

Geometry

The common EAF geometry parameters were determined based on the literature [2, 3] and reported in ***Table 5.1***. The 3D domain is displayed in ***Figure 5.1***. The injectors, as shown in ***Figure 5.1***, were used to insert biochar particles and O_2 into the furnace. Instead of modeling the total melt volume, the bottom surface of the computational domain was adopted as a slag surface to simplify the model and reduce the computational effort. The inner surfaces of the furnace walls, as well as the top and sidewalls of the chimney, form part of the computational domain borders. The exhaust surface of the EAF allows combustion products and other unburned gases to depart the computational domain. The electric arc and radiated energy are generated by the bottom surfaces of three electrodes with constant heat flux.

Table 5.1: *Common electric arc furnace geometry parameters*

Parameter	Value
Internal height [mm]	3505.25
Internal furnace radius [mm]	3600
Internal slag surface radius [mm]	3080
Electrode radius [mm]	305
Coal injector diameter [mm]	25.4
Oxygen injector diameter inner e outer [mm]	68.14–45.4
Injector angle	45° downwards
Oxygen flow rate [kg/s/injector]	1.2955
Coal flow rate [kg/s/injector]	0.333

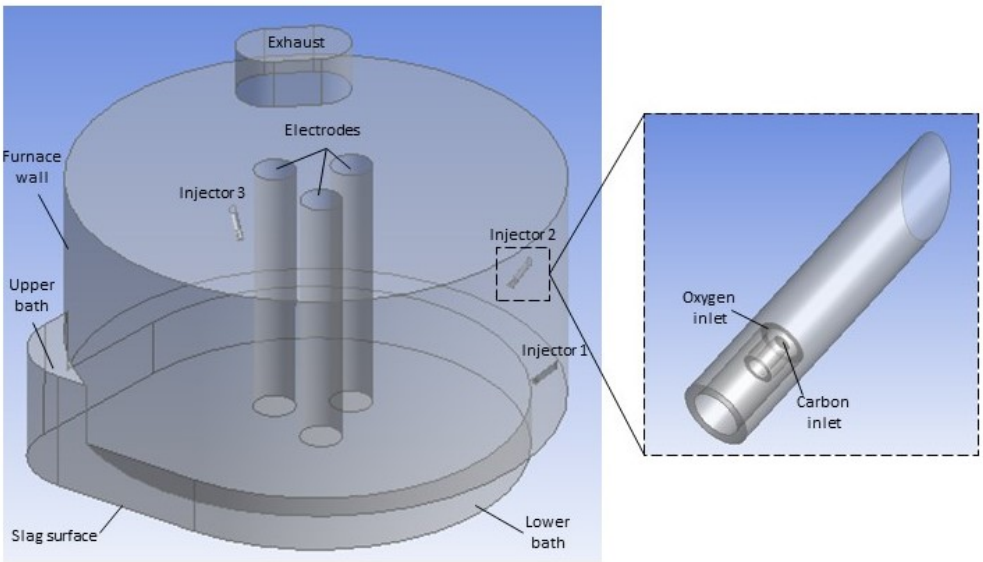

Figure 5.1: *3D geometry of the electric arc furnace, and injector detail.*

Computational mesh

The quality of the mesh has a considerable impact on the accuracy and stability of the numerical calculation, as well as the outcomes of the analysis. The quality and amount of the mesh elements or grids affect the computational time, convergence, and accuracy of the solution. Small computational regions in the model were created using tetrahedral mesh structures.

To capture surface interactions and guarantee computational stability, sufficient grid refinement at the electrode and injector surfaces is required. The final mesh structure of the EAF domain included 225726 cells, with an orthogonal quality of 0.756 and skewness of 0.24. Skewness and orthogonal quality are crucial factors for mesh quality tests. To avoid the solution readily diverging, the maximum skewness should be less than 0.98 [4]. Skewness and orthogonal quality values vary from 0 to 1, with zero being the best and one being the worst. The lower the number for orthogonal quality, which runs from 0 to 1, the poorer the mesh quality. The simplified geometry allowed the generation of a mesh with very good quality.

Boundary conditions

The standard wall function was applied to each wall boundary. Given the water-cooling operation, the static temperature applied to the furnace wall was 393 K [2, 5]. 873 K and 773 K static temperatures were applied for the lower and the upper bath walls, respectively [3]. For modeling 100 MW electricity, a heat flux of $1.15b \times 810^8 W/m^2$ was applied at the bottom surface of each electrode. The surface temperature resulted from the thermal conditions (conduction, convection, radiation). Convection to the outside ambient and conduction on the melt layer were incorporated in the model including convection and conduction heat transfer equations at the slag surface boundary to achieve more realistic thermal boundary conditions.

The convection heat transfer coefficient was 30 W/m^2K, while the thermal conductivity was 0.5 W/mK. The effective radiation was computed as a function of the electrode surfaces' emissivity, irradiation, and radiation energy, as well as the upper and lower bath surfaces, slag surface, and furnace wall. The radiating surfaces operate as a black body (ε=1) and are transparent with regard to absorption of radiation. The other defined walls were considered as grey bodies. The slag surface had an internal emissivity of 0.7, while the lower and upper bath walls and the granite electrode walls had an internal emissivity of 0.85 [3]. As shown in ***Figure 5.1***, the outer tube of the injector feeds the oxygen-enriched air, which was specified as a velocity inlet boundary condition with a constant velocity of 480 m/s. The initial temperature of the air was set to 1500 K to activate the combustion reactions. The inner tube of the injectors was defined as an injection model that feeds the coal particles. The velocity and temperature of the coal particles were set to 0.76 m/s and 300 K, respectively.

5.1.2 Results and discussion

The model aimed to study and compare the performance of the different pretreated biomass (T300, P500, and H220) with the anthracite coal in the electric arc furnace. The air and fuel injection was simulated considering their release from

the three injectors. In this study, the possible interaction between injections was not considered since the results showed no significant differences among them.

Velocity and temperature profile

Figure 5.2 shows the velocity profiles on a plane intersecting the center of injector 1 for H220. Because the contours do not provide significant differences, the velocity profiles for the other materials (Ac, P500, and T300) were reported in the Appendix ***Section A.3*** (***Figure A.11***). Velocity data plotted in ***Figure 5.2*****b** was obtained from a straight line, corresponding to the axis of the lance, from the slag surface to the injector. Values record a maximum peak of 228.6, 205.2, 208.3, and 210.0 m/s, respectively at a distance from the slag of 2.12 m for anthracite, T300, P500, and H220. The speed of the jet decreased as it expanded and mixed with the coal particles and gases. The velocity gradients were increased to greater volumes due to swirls and high-temperature combustion effects. Jet reached the melt surface at about 42.9, 42.2, 43.6, and 43.2 m/s respectively for anthracite, T300, P500, and H220. It was evident that the velocity profile was approximately the same for each material. This was due to the same inlet conditions and the same particle size that did not give any further contribution. Furthermore, the fastest velocity particles occurred in the middle zone just out of the injector and the lowest at the devolatilization zone. This was reasonable, as the middle area just out of the injector had a higher particle conversion through the combustion leading to a higher velocity.

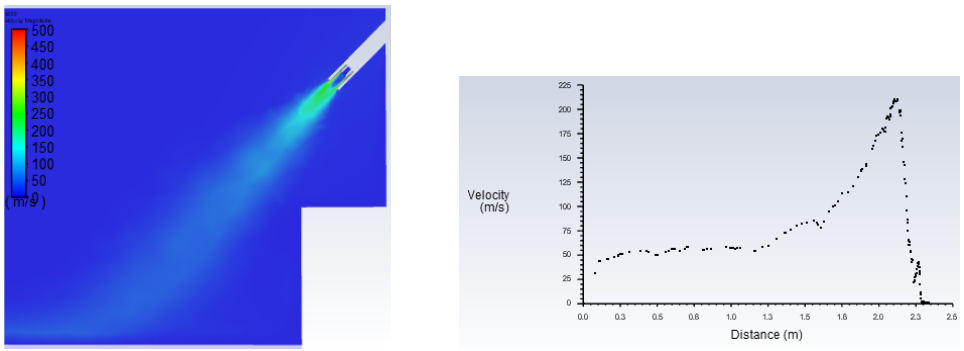

(a) (b)

Figure 5.2: *Velocity magnitude (a) and velocity distribution profile vs distance (b) for H220.*

As for the velocity magnitude, the temperature profiles inside the EAF are presented for a plane intersecting from the center of the injectors 1. The static temperature profiles of each material are shown in ***Figure 5.3***.
In the core of the cone jet flow, the temperature was distributed between 1968 and 3234 K for each material. The average static temperature difference was around 422 K. This high-temperature difference means that the reactions were fast and strongly exothermic. This affected the temperature profile inside the furnace. Indeed, the radiation temperature near the lance ranged from 1868 and 2956 K and the average radiation temperature difference was 272 K (***Figure 5.4***). Thus, the combustion reactions provided a significant contribution to increasing the temperature inside the furnace. Because the radiation temperature profile was

the same for each material, without loss of generality, it was reported only for T300. The radiation temperature contours of anthracite, P500, and H220, can be found in the Appendix ***Section A.3*** (***Figure A.12***).

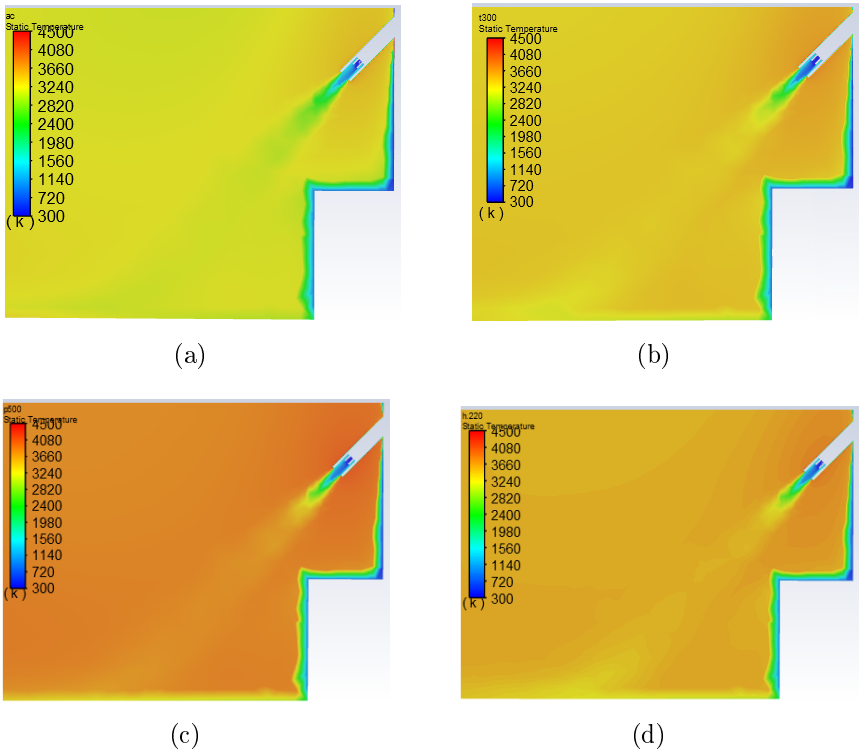

Figure 5.3: *Temperature profile for anthracite (a), T300 (b), P500 (c), and H220 (d).*

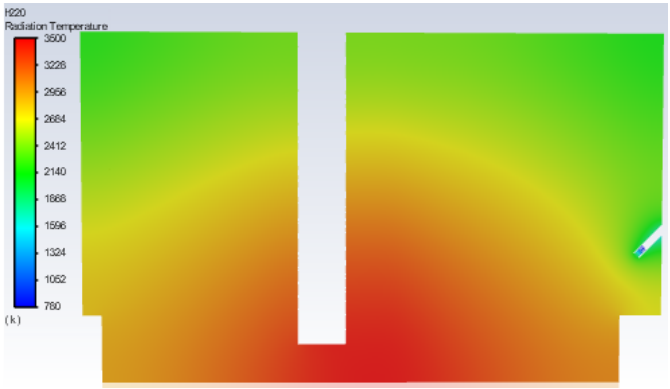

Figure 5.4: *Radiation temperature profile for H220.*

Heat of reaction

Gas-phase reactions include extremely complex mechanisms. The gas-phase processes may occur in different phases or concurrently, depending on the furnace type, carbonaceous material and its composition, particle size, heating rates, decomposition, and oxygen transfer. Every carbonaceous material is classified and rated according to its chemical composition, which includes volatile matter, ash,

and carbon content. The carbon content of a fuel defines its calorific value as well as the temperature of the flame. The flame stability is determined by the volatile matter content (VM). With the decrease of VM, the ignition of the carbonaceous materials is delayed and the combustion is slow. At high temperatures, the formation of pores in the residue is strongly related to the release of volatile matter in the carbonaceous material [6]. The gases released will be affected by the rates of devolatilization of the carbonaceous materials investigated in this study, affecting the interactions of the carbon with the slag. Medium rates of volatile matter evolution will result in steady gas releases that may be accessible during the subsequent contact with the EAF slag, allowing the gas to be entrapped over a longer period of time. On the other hand, a faster passage through the slag will occur with higher gas production rates, which results in poor gas entrapment [7].

This can be seen in the heat of reaction displayed in ***Figure 5.5***. The heat of reaction is defined as the heat that is generated or withdrawn as a result of chemical processes. The heat of reaction and the values represented in the plots refer to the sum of the heat for all the reactions. The heat of reaction is indicated as a positive quantity in exothermic reactions and as a negative quantity in endothermic reactions. This source of energy resulting from chemical reactions might yield valuable information regarding the spatial locations and severity of combustion reactions.
Furthermore, fixed carbon (FC) is defined as the amount of combustible material remaining in the sample after the removal of moisture, volatile matter, and ash. Thus, the lower the FC, the lower the combustible fraction of material that can penetrate the slag surface and reduce the metallurgical melting properties. From ***Figure 5.5*** it is evident how the volatile content and the fixed carbon in the material influence the reactions. In detail, as reported in ***Table 3.3***, the highest volatile content is found for H220 (72.5 $wt\%_{db}$), decreasing up to 42.2 $wt\%_{db}$ and 25.4 $wt\%_{db}$, respectively for T300 and P500 and reaching the lowest value for anthracite (9.2 $wt\%_{db}$). Because of the high reactivity of volatile matter, biomass combustion is usually completed within a small temperature range, and the majority of the weight is lost in a shorter time.

The heat of reaction profile and the plot of the heat of reaction vs the distance from the slag surface on a straight line, corresponding to the axis of the lance, were shown in ***Figure 5.5***. For H220 (***Figure 5.5*****g** and **h**), the higher VM content made the reactions to be fast and the heat release was concentrated in the upper zone of the lower bath. It reached the highest value of 4645 W at 1.5 m from the slag surface. A similar trend was recorded for T300 (***Figure 5.5*****c** and **d**) but with a maximum value of heat release of around 3079 W at the same distance of 1.5 m. For P500 (***Figure 5.5*****e** and **f**) the reactions seemed to be slower and the heat release was shifted closer to the slag surface (1 m distanced), reaching a maximum value of 1774 W.
On the other hand, anthracite was characterized by a production of heat more concentrated on the slag surface, with a peak value of 128 W (***Figure 5.5*****a** and **b**). It can be noted that the behavior of all biomasses was the opposite of anthracite. The higher FC and the lowest VM content for Ac provided a delay in the devolatilization reactions that were concentrated on the slag surface.

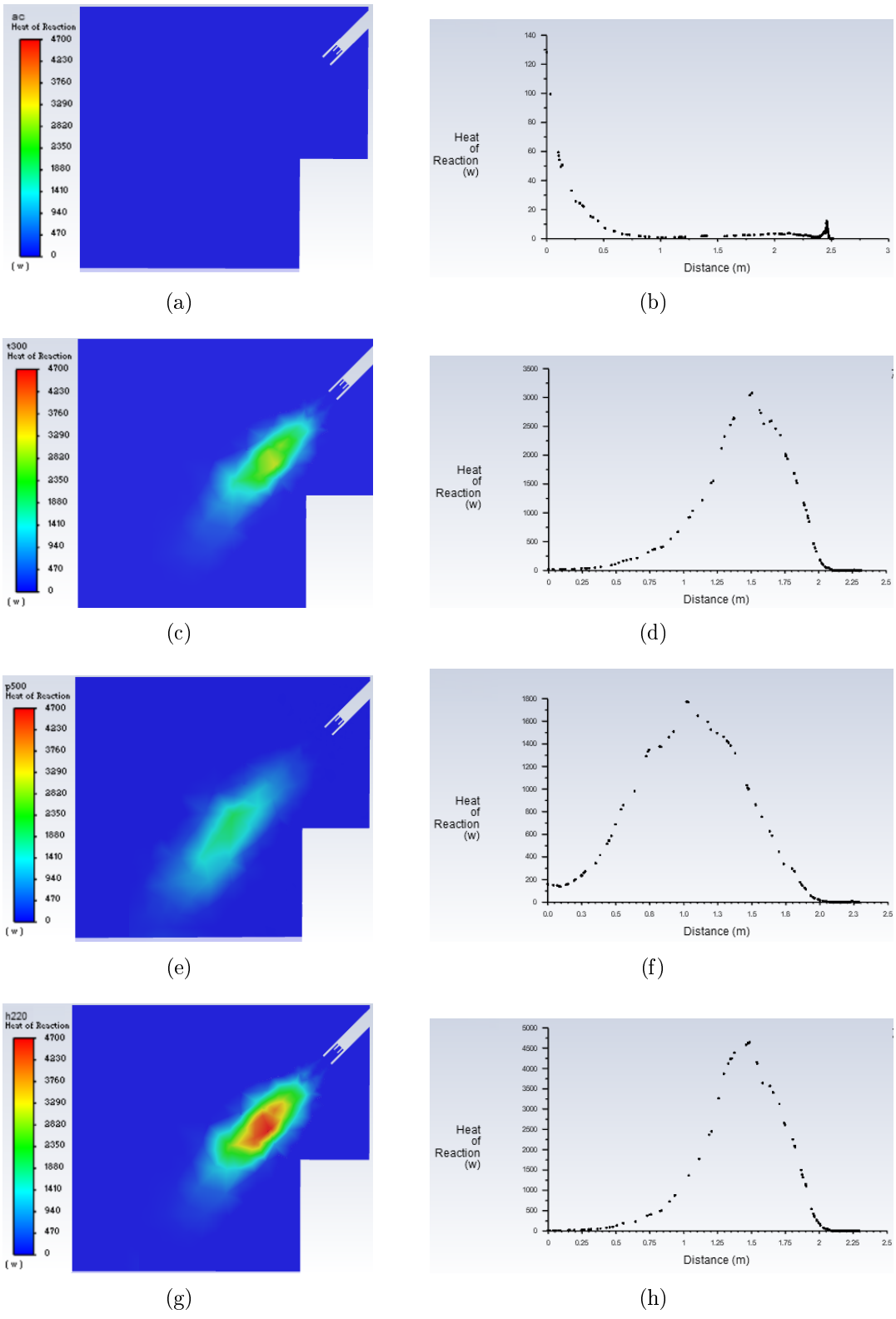

Figure 5.5: *Heat of reactions for anthracite (a,b), T300 (c,d), P500 (e,f), and H220 (g,h).*

On the other hand, T300, P500, and H220 started to react and combust as soon as they left the lance, while near the slag surface the reactions ended. Here, the heat release was near zero for T300 and H220 (20 W and 11.7 W, respectively) while for P500 the combustion reactions were spread over a wider distance, producing

158.5 W on the slag surface. These considerations were confirmed by the trend of the kinetic parameters reported in ***Table 3.4***. With a larger pre-exponential factor (A), the molecules are more activated and the reactions are easier. Concurrently, with larger activation energy (E_a), the reactions have more difficulties to proceed. The highest value of A was recorded for H220 ($1.3 \times 10^{13} s^{-1}$), decreasing up to 6.16×10^{12} and $1.15 \times 10^{6} s^{-1}$ for P500 and T300, respectively, and reaching the lowest value of $6.88 \times 10^{4} s^{-1}$ for anthracite. Furthermore, the highest value of Ea for P500 (187.56 kJ/mol) explained the lower and slower heat release in comparison to T300, which had the lowest value of Ea (97.3 kJ/mol). It can be deduced that T300 and H220 behave more as burners, producing a sharper heat release with respect to P500, which promotes the delay of heat release closer to the slag surface. Biochar from biomass outperformed anthracite coal in terms of combustion and gasification reactivity. A similar result was found for grape seed and pumpkin seed char [8]. The medium rates of combustion evolution of P500 will lead to steady gas releases which might be available during subsequent contact with the EAF slag, allowing the entrapment of gases over a longer time, while the higher rates of gas generation of T300 and H220 might lead to poor gas entrapment, allowing a fast passage through the slag.

Mass fraction of CO inside the EAF

In EAF slag foaming is a well-consolidated and commonly used technology for improving energy transfer efficiency in the furnace. The shielding of electric arcs by foamy slag decreases the energy losses via the water-cooled furnace walls and roof, allowing for a better energy transfer from the arc into the melt. The foaming of the slag is generated by the CO/CO_2 gas bubbles in the EAF process caused by the oxidation of carbon dissolved in the molten steel by oxides in the slag. The addition of carbon to the slag enhances and maintains the foaming process. As a result, the injected carbon can either directly react with the iron oxide as described in ***Equation*** (5.1), or indirectly reduce the iron oxide as described in ***Equation*** (5.2) via an intermediate gasification stage [9].

$$FeO + \ C_s \rightarrow Fe + CO \tag{5.1}$$

$$FeO + \ CO \rightarrow Fe + CO_2 \tag{5.2}$$

Figure 5.6 shows the CO mass fraction distribution of each material along the straight line corresponding to the axis of the lance from the slag surface to the injector 1. The mass fraction is defined as the mass of a species per unit mass of the mixture [10]. All materials showed a first peak of CO mass fraction as soon as the particles started mixing with the oxidizer. This may be caused by the high contact temperature of oxygen (1500 K) and the high turbulent kinetic energy inside the injector. Thus, as the mixture of fuel and oxidizer leaves the injector, the turbulent kinetic energy decreases and the rate of the reactions decelerates. Extensive gas generation of CO was observed from pretreated biomass chars. Metallurgical anthracite showed slightly lower levels of gas generation. The CO gas concentration from T300 and H220 (***Figure 5.6*****b** and **d**) showed a sharp rise, attaining the value of 4.2×10^{-3} and 5.7×10^{-3} respectively, and a subsequent fast decrease which was attributed to the fast volatile combustion. A different distribution was recorded for P500 (***Figure 5.6*****c**) where the curve of CO mass

fraction was smoother, reaching a value of 2.9×10^{-3}. The anthracite coal showed a slower CO release (***Figure 5.6*****a**), concentrating on the slag surface with a value of 1.2×10^{-4}. These different concentrations were reasonable because the biochars contain higher oxygen levels than anthracite. Moreover, a lower CO mass fraction means that fewer intermediate products are generated and more concentration of C is available for iron oxide reduction (***Equation*** (5.1)). However, a greater mass fraction of CO as an intermediate product can contribute to the FeO reduction according to ***Equation*** (5.2). Furthermore, slower gas production rates made it easier for the slag to trap gases and maintain high levels of slag foaming. This gas production rate was in accordance with the literature [11], where specific amounts of produced gas and gas production rates for several materials (palm kernel shells, wood chip pellets, walnut shells, olive kernels, pyrolyzed wood char, torrefied biomass pellets, and hydrothermally carbonized green waste pellets) were determined. Moreover, Yunos et al. [7] reported that the higher the CO concentration, the more violent carbon-slag interactions occurred when palm shell-derived biochar was used in EAF steelmaking.
From these results, it is recognizable that P500 would seem more prone to be employed as a slag foaming agent promoter than T300 and H220.

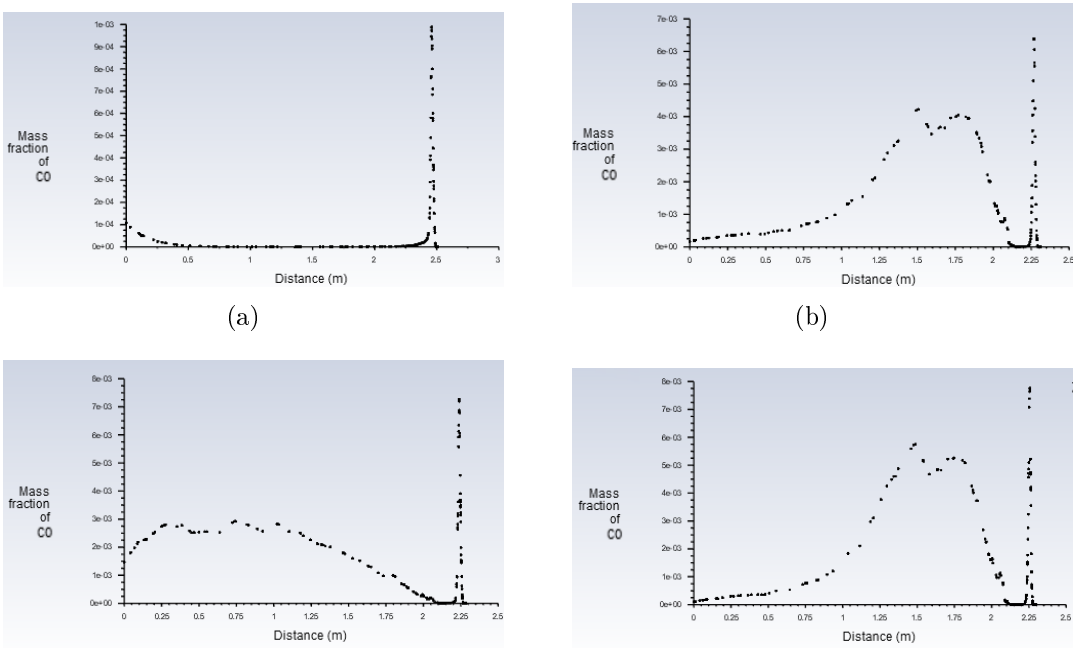

Figure 5.6: *CO mass fraction vs distance from the slag surface for anthracite (a), T300 (b), P500 (c), and H220 (d).*

Validation

The model validation was carried out by comparing the results with experimental data from the literature. In this work, the coal combustion was simulated by using the same reactions as Zhang et al. [12] which was validated by their experimental results. They provided a CFD modeling of the coal combustion and verified their results through experimental observations in a lab-scale drop-tube

furnace. To compare these two studies, proportional gas temperature differences were obtained from the core of the combustion cone. For the model validation, anthracite coal was taken as reference material. Totally five different data points were selected along the straight line corresponding to the axis of the lance of injector 1 (***Figure 5.7*****a**). The temperatures recorded were 1109, 1273 1601 1909, and 2053 K, respectively from points 1 to 5. Each data point was divided by the maximum temperature value in order to obtain proportional gas temperature differences. The same procedure was applied to Figure 17 in the work of Zhang et al. [12]. The graphical comparison consisting of proportional gas temperature differences from the simulation results was given in ***Figure 5.7*****b**. The simulation results were found to fall in the error range (10%) of the experimental measurements. The good qualitative consistencies between the two sets of results confirm the basic reliability of the numerical model.

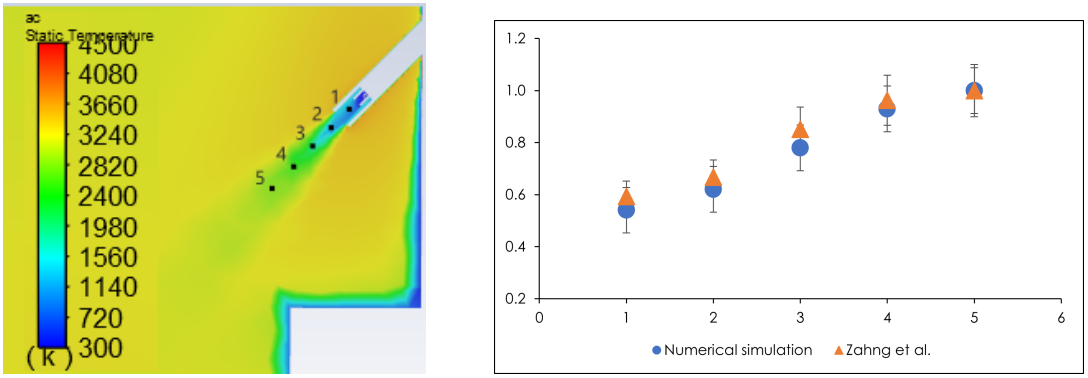

(a) (b)

Figure 5.7: *Proportional gas temperature differences for each data point. Data points of the temperature profile of anthracite a); comparison of the data points of current simulation with Zhang et al. [12] b).*

Discussion about chemical-physical properties of biochar

The characteristics of char from biomass might be tailored to meet the requirements for their use in EAF. In order to highlight the combustion differences between biomasses with different chemical-physical characteristics, cottonwood pyrolyzed biochar, named W400, was also tested. The fuel properties of the W400 sample were obtained from the literature [13] and summarized in ***Table 5.2***. The same inlet conditions, boundary conditions, and the same particle size did not provide significant differences regarding the velocity profile (***Figure A.13***), static temperature and radiation temperature profile (***Figure A.14***) of W400 in comparison with the other materials (anthracite, T300, P500, and H220), and are reported in Appendix ***Section A.3***. In detail, the highest velocity value of 200.1 m/s was recorded at a distance from the slag of 2.12 m and reached the melt surface at about 40.1 m/s; the burning cone generated by the reactions was comparable in temperature and area with all the other materials. As mentioned before, the volatile content and the fixed carbon in the material influence the reactions. Cottonwood pyrolyzed biochar is characterized by a higher value of FC content (68.6 $wt\%_{db}$), in comparison to T300 (21.2 $wt\%_{db}$), P500 (22.2 $wt\%_{db}$) and H220 (18.3

$wt\%_{db}$), but lower than that of anthracite (80.1 $wt\%_{db}$). Instead, the VM content of W400 (25.3 $wt\%_{db}$) is close to that of P500 (25.4 $wt\%_{db}$), lower than that of T300 (42.2 $wt\%_{db}$) and H200 (72.5 $wt\%_{db}$) and higher than anthracite (9.2 $wt\%_{db}$). The heat of reaction profile and the plot of the heat of reaction vs the distance from the slag surface are shown in ***Figure A.15*** of Appendix (***Section A.3***). The comparable chemical characteristics of W400 and P500 make the combustion behavior to be resemblant. In detail, the heat of reaction of W400 appears to have the same distribution of P500 because of approximately the same volatile matter content. However, the higher combustible fraction of W400 shifts the heat release at the same distance from the slag surface of P500 (1 m distanced) but reaches a maximum value of 2230 W, higher than that of P500 (1774 W). ***Figure 5.8*** shows the CO mass fraction distribution of W400 along the straight line corresponding to the axis of the lance from the slag surface to the injector 1. As for the other materials, W400 showed a first peak of CO mass fraction as soon as the particles started mixing with the oxidizer. After the first peak, CO followed the same distribution recorded for P500 (***Figure 5.6c***), reaching a value of 1.55 $\times 10^{-3}$. This value of CO mass fraction for W400, recorded nearby the slag surface, was between the value of P500 (2.9 $\times 10^{-3}$) and that of anthracite (1.2 $\times 10^{-4}$). This result is in accordance with the values of FC content (***Table 3.3*** and ***Table 5.2***). The higher the FC, the more concentration of C is available for iron oxide reduction, the fewer intermediate products are generated and a lower CO mass fraction is recorded. Thus, W400 is more prone to be indicated as a candidate for iron carburization instead of as a foaming agent promoter.
This agrees with the work of Murakami et al. [14] which demonstrated that the iron carburization is accelerated using charcoal from cedar in comparison to coal and graphite. Furthermore, the ash content and its composition might influence the slag phase by changing variables such as slag viscosity, surface tension, composition, and the final steel produced. In this sense, the lower ash content of W400 (5.8 $wt\%_{db}$) in comparison to the other materials (***Table 3.3***) might have a positive influence.

Table 5.2: *Proximate and ultimate analysis and kinetic parameters of W400 [13].*

Materials	Proximate Analysis [wt%$_{db}$]			Ultimate Analysis [wt%$_{daf}$]				Kinetic parameters	
	Ash	VM	FC	C	H	N	O	Ea [kJ/mol]	A [s^{-1}]
W400	5.8	25.3	68.6	74.9	4.0	0.3	15.0	141.2	6.25 $\times 10^5$

Note: db: dry basis; daf: dry and ash-free bases

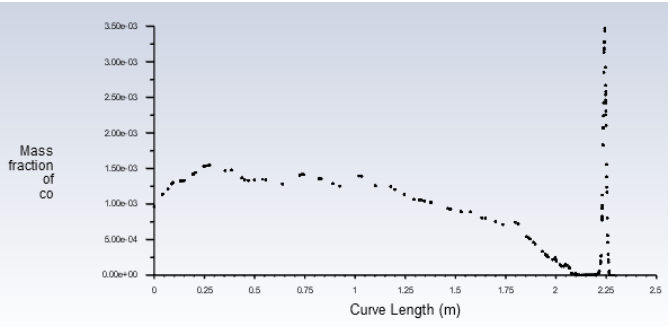

Figure 5.8: *CO mass fraction vs distance from the slag surface for W400.*

5.2 Substitution of fossil coal with hydrochar in electric arc furnace: A comprehensive LCA – *Paper D*

By quantifying the environmental impacts and energy consumption associated with biomass-derived biochar implementation, decision-makers can make informed choices that promote sustainability and minimize the carbon footprint of the steelmaking industry. Pushing toward recycling, circular economy, and the use of renewable materials might help the decarbonization pathway.
Despite the several studies dealing with the environmental impact of steel production [15–17], there is a lack of LCA studies on the use of biocarbon in the EAF steelmaking process [18–20]. The research work discussed in Paper D titled "*Substitution of Fossil Coal with Hydrochar from Agricultural Waste in the Electric Arc Furnace Steel Industry: A Comprehensive Life Cycle Analysis*" [21], aimed at providing a comprehensive assessment of the environmental impacts of steel produced using electric arc furnaces that employ pulverized hydrochar as charged and injected material as a substitute for fossil coal.

Within this work, two different outlines were evaluated: the use of fossil coal and its replacement with hydrochar from the winemaking industry as a carbon source in the EAF steelmaking process. The environmental impacts from the manufacturing of hydrochar were calculated. This included the novel industrial way to use vinasse as a moisture source for the co-hydrothermal carbonization of vine pruning and exhausted grape marc discussed in Paper A [22], and the production of bio-methane from the anaerobic digestion of the spent liquor (liquid fraction) of the HTC process. An industrial layout of the novel hydrochar- and anaerobic-digestion-based EAF (base scenario) was proposed. The life cycle analysis of the hydrochar manufacturing was achieved through the inventory of the mass and energy balance of the HTC process performed in the laboratory reactor of the University of Tuscia site in Viterbo, Italy. Laboratory-scale data were then upscaled using the methods presented in the literature [23].
The environmental impacts per unit of molten steel were reported as a function of the ratio between the fixed carbon of the injected material and the material amount itself. Moreover, the impact related to the production and use of the carbonaceous material was assessed and some improvements and technological upgrading were proposed. Finally, since electricity plays a central role in the decarbonization transition, further scenarios considering the national electricity mix based on the 2030 and 2050 projections were analyzed.

The results of the LCA analysis showed that the base scenario outperforms the traditional EAF route in most of the impact categories, i.e., positively affecting the environment. Furthermore, the comparison of the environmental impact characterization of the production and use of each carbon source was also evaluated. It was found that even though the manufacture of hydrochar was associated with some environmental burden, its use was advantageous since it was related to biogenic CO_2 emissions, contrary to the use of fossil coal. It was found that by replacing fossil coal with hydrochar in EAF steelmaking, the GWP impact can be reduced by around 2%. Moreover, natural gas and electricity consumption were the main contributors to the environmental impacts. Thus, by increasing

the production of bio-methane and its collection efficiency to substitute higher quantities of natural gas, the proposed base scenario may become environmentally more suitable. However, it may be interesting to analyze the production and use of different green fuels as alternatives to natural gas in the steelmaking industry, e.g., hydrogen. Moreover, the LCA of additional scenarios was performed by applying the electricity mix based on the 2030 INECP and the EU Green Deal 2050 previsions. The simultaneous use of higher renewable energies and reduced fossil resources percentages for the national electricity production globally led to a reduction in the environmental burden, confirming that the substitution of fossil coal with a biogenic carbon source (i.e., the hydrochar) is a promising way toward decarbonization process in the EAF steelmaking industry.

5.2.1 Goal and Scope

The objective of this work was to compare the environmental performance of fossil-based and renewable injecting materials employed as carbon sources in the EAF steelmaking process. As the functional unit, 1 ton of molten steel produced was selected. Since the study was based on laboratory-scale data, all involved steps of the HTC process were scaled up singularly according to the methodology presented in the literature [23]. The cradle-to-gate perspective of steel production was adopted, where gate refers to molten steel. The commercial software SimaPro v9.2.0.2 and the Ecoinvent v3.8 database were used to model and carry out the LCA. The system boundary of this study has been described in ***Chapter 3*** and illustrated in ***Figure 3.3***. The upstream activities include the raw materials supply chain, i.e., biomass transport from the collecting site to the processing site, as well as the steel scrap. In detail, the biomass feedstock considered was derived from the winery (vine pruning (VP) and exhausted grape marc (EGM)) and distillery (vinasse) industry. Furthermore, in the base scenario, the system boundary is defined to exclude plantation and management activities, as the wine residue and EGM are treated as waste products resulting from the pruning and distillery processes. Therefore, these waste products do not contribute to the environmental burden.

5.2.2 HTC mass and energy balance calculations

The energy and mass balance of the HTC process was crucial for conducting accurate and robust life cycle inventory analysis. It provides the necessary data to quantify inflows and outflows of materials and energy of the process ensuring that the conservation laws of mass and energy are upheld. This information is essential for conducting a thorough and accurate inventory analysis, which forms the basis for assessing the environmental impacts of the HTC process.
Mass balance on the HTC process has been carried out on gas, solid, and liquid phase. The inventory of the mass and energy balance of the HTC process on laboratory-scale was based on the results from Paper A.
Table 5.3 lists the average data used for the HTC process scale-up based on literature values [23].

Table 5.3: *Reference data for the HTC scale-up process [23]*

Parameter	Symbol	Unit	Value
Heating			
Reactor volume	$V_{reactor}$	m^3	1
Surface area	Ar	m^2	5.899
Thermal conductivity of insulation	λ	W/m K	0.042
Insulation thickness	s	m	0.075
Efficiency of the heating element	η_{heat}	%	74
Starting and outside temperature	$T_0 = T_{out}$	°C	25
Stirring			
Impeller diameter	d	m	0.373
Type of impeller	Np	/	0.79
Rotational speed	N	1/s	1.417
Efficiency of stirring	η_{stirr}	%	90
Filtration			
Filtration energy consumption	E_{filt}	kWh/t	10
Drying			
Specific heat capacity of water	$c_{p,liq}$	kJ/kg K	4.186
Drier efficiency	η_{dryer}	%	80
Boiling temperature	T_{boil}	°C	100
Starting temperature	T_0	°C	25
Enthalpy of evaporation	ΔH_{vap}	kJ/kg	2571
Milling			
Milling energy consumption	E_{mill}	kWh/t	16
Pumping			
Gravitational acceleration	g	m/s^2	9.81
Height different	Δh	m	4.2
Milling efficiency	η_{mill}	%	75

Milling energy consumption

The raw feedstock is generally ground to an adequate particle size before being sent to the reactor. The energy consumption of a mill mainly depends on the size of the final particles, the material to be ground and the type of grinding. A value of 16 kWh/ton of ground material was chosen as energy consumption for milling ($E_{milling}$), according to the literature [23]:

$$E_{milling} = 16 * m_{biomass,HTC}\ [kWh] \tag{5.3}$$

where $m_{biomass,HTC}$ is the sum of the mass of VP and EGM. In detail, $m_{biomass,HTC}$ was determined as a function of the carbon content in 12 kg of coal, which is used per ton of steel produced in the EAF [24, 25]. Thus, to substitute 12 kg of metallurgical coal with a carbon content of 85%, 16.8 kg of hydrochar with a carbon content of 60.86% on a dry basis is needed. By considering the mass yield on a dry basis of the hydrochar equal to 52.64% [22], the total solid content of the biomass feedstock ($m_{biomass,HTC,db}$) results in 31.8 kg, which is a blend of 50%wt of VP and EGM. With a moisture content of 42% and 71% [22] respectively for VP and EGM, the total $m_{biomass,HTC}$ was 82.3 kg/ton of molten steel.

Thermal energy for HTC

The thermal energy required during the reaction stage was calculated as the energy to raise the reaction mixture to the set temperature and to keep it for the duration of the reaction (E_{react}).

$$E_{react} = \frac{E_{heat} + E_{loss}}{\eta_{heat}} \; [kWh] \tag{5.4}$$

E_{heat} is the energy for raising the temperature and calculated as:

$$E_{heat} = (c_{p\ biomass,HTC} * m_{biomass,HTC,db} * (T_r - T_0) + m_{vinasse} * (H_{vinasse,Tr} - H_{vinasse,T0})) * 0.000278 \; [kWh] \tag{5.5}$$

where:

- $c_{p\ biomass,HTC}$ = 2.18 kJ/kg K is the specific heat capacity of dry biomass (VP+EMG) [22];
- $m_{biomass,HTC,db}$ is the mass of dry biomass in the inlet of the HTC reactor ($m_{VP,db} + m_{EGM,db}$) [kg];
- T_r is the reaction temperature (246.6°C);
- T_o is the entering temperature of the feedstock reached after the regenerative heat exchanger (HE) (T_o = 109.8°C);
- $m_{vinasse}$ is the mass of vinasse entering the reactor (400.1 kg);
- $H_{vinasse,Tr}$: is the enthalpy of vinasse at 246.6°C (before phase transition to steam) ($H_{vinasse,Tr}$ = 1009.3 kJ/kg);
- $H_{vinasse,T0}$: is the enthalpy of vinasse at 109.8°C (reached after the regenerative heat exchanger (HE), $H_{vinasse,T0}$ = 457.1 kJ/kg);
- 0.000278 is the conversion factor kWh/kJ.

E_{loss} the energy related to the heat lost on the reactor surface and η_{heat} the efficiency of the heating device, calculated as

$$E_{loss} = A * \frac{\lambda}{s} * (T_r - T_{out}) * t/1000 \; [kWh] \tag{5.6}$$

where:

- A_r: surface area of the reactor [m^2];
- λ: thermal conductivity of the insulation material [W/m K]
- s: the thickness of the insulation [m]
- T_r: the reaction temperature (246.6°C);
- T_o: the temperature of the external environment (25°C);
- t: the residence time (2.6 h);

Finally, η_{heat} the efficiency of the heating device [23].
The thermal energy required for HTC heating is partly recovered by the heat exchanger and the remaining contribution is provided by an external heating source.

Electric energy HTC

Electrical energy is considered the energy required for stirring and pumping. During the reaction stirring energy is consumed depending on the type (Np) and diameter (d) of the impeller, the stirring rate (N), the density of the reaction mixture (ρ_{mix}) as well as the reaction time (t) and the impeller system efficiency (η_{stirr}). The following equation was used:

$$E_{stirr} = \frac{(N_p * \rho_{mix} * N^3 * d_{rotor}^5) * t}{\eta_{stirring} * 1000} \; [kWh] \tag{5.7}$$

In this work, an axial flow impeller (hydrofoil type) is assessed as stirrer type and turbulent flow is considered to be generated during stirring, leaving the power number constant for the calculations [26]. Moreover, the density of the reaction mixture was assumed equal to 1000 kg/m^3.
Since the slurry (m_{slurry}) is transferred to the filtration stage through the pumping system, as well as the vinasse ($m_{vinasse}$) from the heat exchanger to the HTC reactor, the electrical energy was calculated by considering the efficiency of the pump η_{pump}, the mass to be transferred m ($m_{slurry} + m_{vinasse}$), the gravitational acceleration g, and a height different Δ h [23], the energy consumption in turbulent flow as follows:

$$E_{pump} = \frac{m * g * \Delta h}{\eta_{pump}} * 0.000278 \; [kWh] \tag{5.8}$$

A safety factor of 10% was considered.

Electric energy for slurry filtration (solid-liquid separation)

One of the main influencing factors on energy consumption during filtration is the particle size of the slurry. Since during the experimental laboratory procedure the particle size of the solid fraction was lower than 500 μm, within the elaboration of Paper D, the filtration process was supposed to be energy intensive. For this reason, the energy consumption during the filtration stage ($E_{filtration}$) was estimated 10 kWh/ton [23].

$$E_{filtration} = 10 * m_{slurry} [kWh] \tag{5.9}$$

The dry content of hydrochar after the filter press was assumed equal to 60 wt% [27].

Dryer

Drying was applied to remove the residual hydrochar moisture. After the filter press, wet hydrochar (relative humidity = 40 wt%) was assumed to be dried up to a solid content equal to 8 wt%, according to the literature [28, 29]. Thus, the amount of water to be removed was obtained as the difference of the water between wet and dried hydrochar.

Thermal energy to evaporate water

The thermal energy required to remove water was calculated as follows:

$$E_{dryer} = \frac{c_{p,liq} * m_{liq} * (T_{boil} - T_0) + \Delta \mathrm{H}_{steam} * m_{steam}}{3600 * \eta_{dryer}} \; [kWh] \tag{5.10}$$

Where:

- $c_{p,liq}$ is the specific heat capacity of water at 25°C (4.186 kJ/kg K);
- m_{liq} is the amount of water to be evaporated [kg];
- T_{boil} is 100°C;
- T_0 is the room temperature (25°C);
- ΔH_{steam} is the latent heat of water 2571 kJ/kg;
- m_{steam} is the amount of steam to be produced equal to m_{liq} [kg];
- η_{dryer} is the efficiency factor of the dryer [23];

The total amount of steam ($m_{steam} = m_{liq}$= 9.7 kg) was calculated assuming an 8 wt% of moisture after drying.

Heat exchanger

Energy from the slurry exiting the HTC is recovered to preheat the liquid feedstock (vinasse) entering into the HTC reactor, in a regenerative heat exchanger operating in continuous mode.
A temperature of 35°C was established for the spent liquor leaving the heat exchanger in order to satisfy the mesophilic conditions for anaerobic digestion [30]. The temperature of the vinasse entering the HTC reactor ($T_{vinasse,OUT}$) was determined according to the following relation:

$$m_{vinasse} * c_{p,vinasse} * (T_{vinasse,OUT} - T_{vinasse,IN}) = m_{SL} * (H_{SL,OUT} - H_{SL,IN}) \quad (5.11)$$

where:

- $c_{p,vinasse}$ is the specific heat capacity of vinasse assumed equal to 4.186 kJ/kg K);
- $m_{vinasse}$ is the mass of vinasse in the inlet of the HTC reactor [kg];
- $T_{vinasse,OUT}$ is the initial temperature of the vinasse (15°C);
- m_{SL} is the mass of the hot spent liquor leaving the HTC reactor [kg];
- $H_{SL,OUT}$ is the enthalpy of the spent liquor at 35°C in non-saturated conditions (146.56 kJ/kg);
- $H_{SL,IN}$ is the enthalpy of the spent liquor at 246.6°C in non-saturated conditions (1009.28 kJ/kg);

The temperature of the slurry out of the heat exchanger was determined (102.1°C).

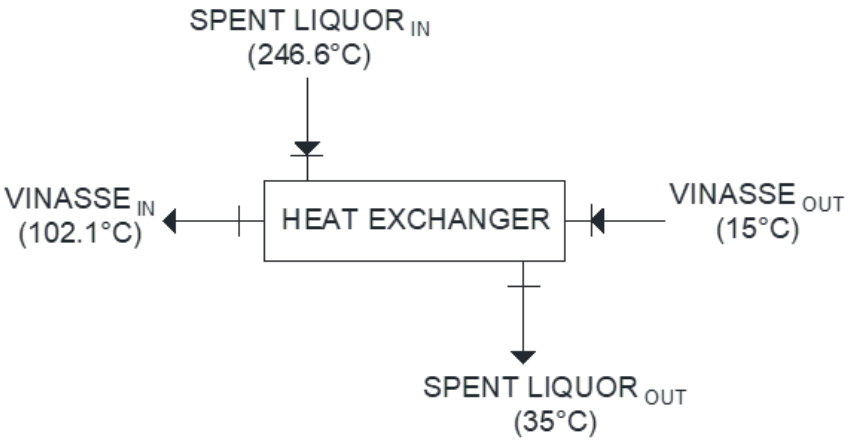

Figure 5.9: *HTC reactor system.*

Gas balance calculations

Carbon (C) yields were applied to carry out the balance for gas. The hydrochar yield in terms of C was calculated as follows:

$$\mathrm{HY}_C = \frac{\%C_{HC} * m_{HC,db}}{(\%C_{VP} * m_{VP,db}) + (\%C_{EGM} * m_{EGM,db}) + \left(\frac{\mathrm{TOC}_{vinasse} * L_{vinasse}}{1000}\right)} * 100\ [\%] \quad (5.12)$$

where $L_{vinasse} = m_{vinasse}/\rho_{vinasse}$, and $\rho_{vinasse}$ was considered equal to 1000 kg/m^3. Thus, HY_C resulted equal to 60.23 wt%.

The liquid (spent liquor) yield in terms of C was calculated as follows:

$$LY_C = \frac{TOC_{spent\ liquor} * m_{spent\ liquor}}{(\%C_{VP} * m_{VP,db}) + (\%C_{EGM} * m_{EGM,db}) + \left(\frac{TOC_{vinasse} * L_{vinasse}}{1000}\right)} * 100\ [\%] \quad (5.13)$$

and LY_C resulted equal to 11.08 wt %.

The gas yield in terms of C was calculated as follows:

$$GY_C\ (\%) = 100 - LY_C - HY_C \quad (5.14)$$

where all the terms were already defined previously. Thus, GY_C (%) resulted equal to 28.69 wt%.

Then, the mass flow of carbon in the gas was calculated as:

$$m_{C\ gas} = GY_C\,(\%) * \left[(\%C_{VP} * m_{VP,db}) + (\%C_{EGM} * m_{EGM,db}) + \left(\frac{\mathrm{TOC}_{vinasse} * L_{\ vinasse}}{1000}\right)\right] \quad (5.15)$$

where all the terms were already known.

Further, the carbon converted into the gas phase was assumed to be a mixture of CO_2 and CO according to the literature [31]:

$$m_{gas} = \frac{x_{CO_2} * \ \mathrm{PM}_{\mathrm{CO_2}} + \ x_{CO} * \ \mathrm{PM}_{CO}}{\mathrm{PM}_C} * m_{C\ gas}\ [kg] \quad (5.16)$$

where:

- x_{CO_2} is the percentage of CO_2 in gas (92 vol%) [31];
- x_{CO} is the percentage of CO in gas (8 vol%) [31];

- PM_{CO_2} is the molecular weight of CO_2 (44 g/mol);
- PM_{CO} is the molecular weight of CO (28 g/mol);
- PM_C is the molecular weight of C (12 g/mol);

This gas mixture has been directly emitted into the atmosphere, so the emissions of biogenic CO_2 can be calculated.

Gas density has been calculated using the ideal gas law (0°C, and 1 atm):

$$\rho_{gas} = \frac{P}{RT} * (x_{CO_2} * \ \mathrm{PM}_{\mathrm{CO_2}} + \ x_{CO} * \ \mathrm{PM}_{CO}) \ [kg/m^3] \tag{5.17}$$

where P is equal to 101 325 Pa, T is the temperature of 0°C (273.15 K), R is the universal gas constant (8.314 J/mol K), and all the other terms were already defined above.

The gas volume was calculated as:

$$V_{gas} = \frac{m_{gas}}{\rho_{gas}} \ [m^3] \tag{5.18}$$

Lastly, CO_2 and CO emissions were calculated using the following equations:

$$m_{CO_2} = x_{CO_2} * \ V_{gas} * \ \frac{P * \ \mathrm{PM}_{\mathrm{CO_2}}}{R * T} \ [kg \ \mathrm{CO_2}] \tag{5.19}$$

$$m_{CO} = x_{CO} * \ V_{gas} * \ \frac{P * \ \mathrm{PM}_{CO}}{R * T} \ [kg \ CO] \tag{5.20}$$

Resulting in 17.82 kg CO_2 and 0.99 kg CO.

5.2.3 Life Cycle Inventory (LCI)

Electric energy is used to melt ferrous scrap, which is used as the primary raw material in the EAF steelmaking process. Additional inputs include natural gas as chemical energy and carbonaceous material. LCI data were obtained from different sources, such as laboratory data, scientific literature, industrial reports, and the Ecoinvent v3.8 database. All the material flow and energy data in the system boundary refer to 1 ton of molten steel produced using an EAF.

Biomass Feedstock for HTC

For the HTC treatment of the biomass, laboratory experiments were used as the primary source to model the scale-up plant. The biomass that underwent HTC consisted of VP and EGM as feedstock and vinasse as the moisture source, as described in ***Subsection 3.1.1***. The first step in the biomass supply chain is the collection and transport of raw materials. The solid and liquid feedstock was assumed to be transported 50 km [32] to the HTC plant. In this study, all road transport to and from the transformation facility was modeled using the process "Transport, freight, lorry 7.5-16 metric ton, euro6 RER|market for transport, freight, lorry 7.5-16 metric ton, EURO6|Cut-off, U" from the Ecoinvent v3.8 database.

Hydrochar Production

The HTC process has been described in ***Section 3.3*** while its optimal process conditions (246.3°C – 1.6h – 6.6% solid-to-liquid ratio) has been discussed within the findings of the Paper A (***Section 4.1***).
To evaluate the environmental impact of the HTC process, including its by-products (spent liquor and gases) and the anaerobic treatment of the spent liquor, a scale-up of the entire process is needed. To the best of our knowledge, industrial-scale HTC technology does not exist for the winemaking industry. Thus, the methodology presented in the literature [23] was used for scaling up the laboratory procedure. The hypothetical industrial plant flow chart is reported in ***Figure 5.10***. According to laboratory data, a mixture composed of a 50 wt% blend of VP and EGM was used. The blend was mixed with vinasse with a solid-to-liquid ratio of 6.6%. In the hypothetical industrial layout, vinasse was pre-heated up to around 102°C before being pumped into the continuous HTC reactor. This was achieved by passing the vinasse through a heat exchanger (HE) in which the hot spent liquor out of HTC was recirculated. Thus, the mixture of VP, EMG, and vinasse is further heated to the operational temperature (246.6°C) in the HTC reactor. Hence, the exiting slurry is sent to a filter press for the solid fraction (SF) and spent liquor (SL) separation. SF is dried to remove the residual moisture, while SL is supposed to be recirculated into an anaerobic digestion (AD) plant for methane production. A total of 0.48 tons of wet biomass (VP and EGM) and vinasse were considered per ton of molten steel produced. The inventory data of the HTC process are reported in ***Table 5.4***, where:

- E_{react} is the thermal energy required during the reaction stage;
- E_{stirr} is the energy required for stirring;
- $E_{filtration}$ is the electric energy for the filtration of the slurry (solid-liquid separation);
- E_{dryer} is the thermal energy required to remove the residual hydrochar moisture;
- E_{mill} is the electric energy required to grind the biomass feedstock to an adequate particle size before being sent to the reactor;
- E_{pump} is the energy required for transfer the blend through the pumping system.

The energy and mass balance of the HTC process was calculated based on laboratory experimental results discussed in ***Section 4.1***. The electric energy (EE) and thermal energy (TE) consumptions of the system were calculated as reported in detail in ***Subsection 5.2.2***.

Table 5.4: *Inventory data of the HTC process (values per ton of molten steel).*

Input from Technosphere						Emission to Air	
E_{react} $[kWh/t]$	E_{stirr} $[kWh/t]$	$E_{filtration}$ $[kWh/t]$	E_{dryer} $[kWh/t]$	E_{mill} $[kWh/t]$	E_{pump} $[kWh/t]$	m_{CO2} $[kg/t]$	m_{CO} $[kg/t]$
105.84	0.05	1.97	9.73	1.32	0.09	17.82	0.99

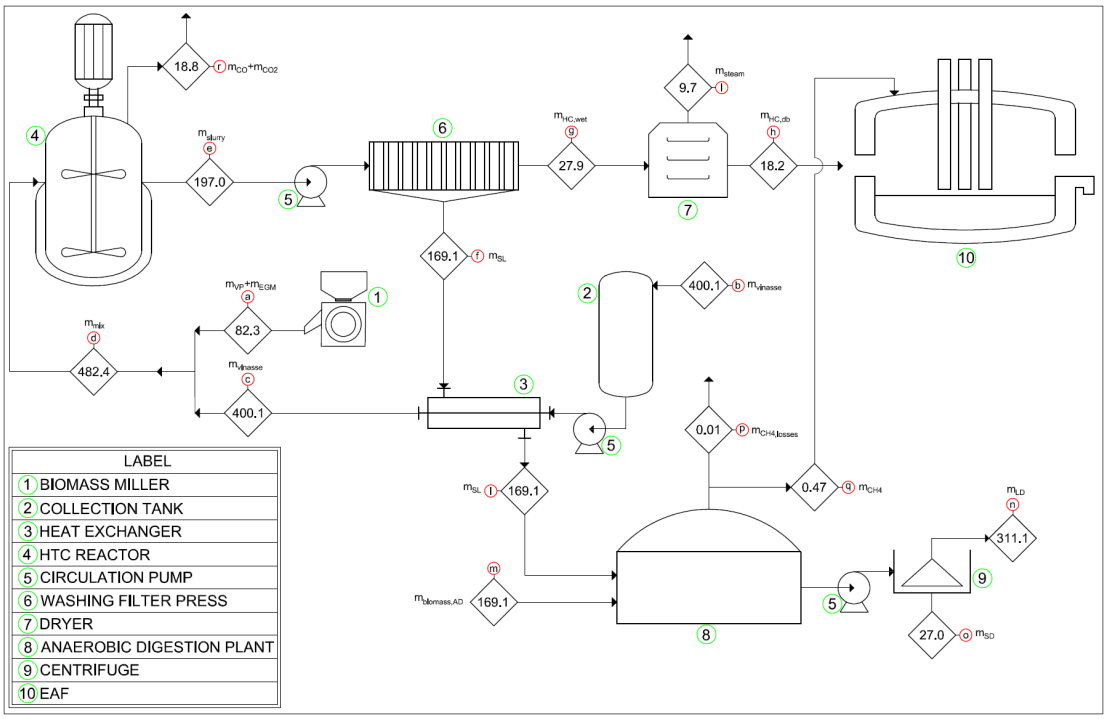

Figure 5.10: *Simple plant flow chart and mass balance of the reaction process.*

Bio-Methane Production

Besides hydrochar, from the filtration step of the slurry, process water (spent liquor) is also obtained during HTC. One option for managing the HTC liquor is feeding it to the anaerobic digestion process [33], to substitute a fraction of dilution tap water used in centralized biogas plants to correct the feedstock moisture before anaerobic digestion. Moreover, since spent liquor contains a high content of organic matter [34], its anaerobic digestion could also yield some additional methane, avoiding additional wastewater treatment units. The characteristics of spent liquor at the HTC operational conditions have been analyzed in ***Section 4.1*** and summarized ***Table 5.5***. The specific methane production of spent liquor was assumed to equal 150 $mL_{CH4}/g_{COD,SL}$ in mesophilic conditions (35°C) [30]. Since, spent liquor out of the HTC reactor has a temperature higher than 35°C, no further heating of anaerobic digestion feedstock was considered. In this way, the thermal energy calculations were made considering only the losses through the anaerobic digestion reactor according to ***Equation*** (5.21):

$$E_{loss,AD} = R_{tot} * Ar * \frac{(T_{reaction} - T_o)}{1000} * 24 \; [kWh/d] \tag{5.21}$$

where

- R_{tot}: total thermal resistance (W/m^2K);
- Ar: reactor area (m^2);
- $T_{reaction}$: the operational temperature (35°C);
- T_o: the temperature of the external environment (15°C).

R_{tot} was calculated assuming that the reactor surface was made of a layer of reinforced concrete with 1% of steel (0.25 m) (concrete = 2.3 W/m K) and a coat of extruded polyurethane foam (0.05 m) (polyurethane = 0.034 W/m K) [29]. The volume of the anaerobic digestion reactor (3000 m^3) was calculated assuming an industrial-sized plant (***Equation*** (5.22)):

$$V = \dot{m}_{in,AD} * t \ [m^3] \tag{5.22}$$

where $\dot{m}_{in,AD}$ is the flow in the AD reactor (100 m^3/d) and t is the residence time (30 days). Considering a cylindrical reactor (in which the diameter of 16 m was equal to the height), the value of the reactor area was equal to 804 m^2. Since we considered that spent liquor was used as dilution water, by starting from a biomass feedstock ($m_{biomass,AD}$) with a solid content of 30% and in order to reach the requirements of wet anaerobic digestion (total solid content of 15%), it was assumed that 50% of the overall heating loss could be allocated to added spent liquor.
The electric energy for pumping and stirring was calculated using the equations reported in ***Subsection 5.2.2***, while the electricity consumption for centrifugation was assumed to be 5 kWh/t [35]. Finally, the digested liquid stream (m_{LD}) was sent to wastewater treatment.
Table 5.6 presents the inventory data for the anaerobic digestion stage, considering that CH_4 fugitive emissions in the anaerobic digestion stage account for 2.5% of the produced biogas [36]. The TE and EE consumptions required for the integrated HTC-AD industrial plant proposed are in line with those found in the literature [37–39].

Table 5.5: *Characterization of the liquid fraction obtained at optimal HTC conditions*

Parameter	Unit	Spent Liquor
pH		4.08
Total N	mg/L	368.36
TOC	g/L	12.06
COD	g/L	28.43
BOD	g/L	8.87

Table 5.6: *Main inventory data of the anaerobic digestion stage of process water (values per ton of molten steel).*

Input from Technosphere				Emission to Air	Emission to Water
$E_{loss,AD}$	E_{stirr}	$E_{centrifugation}$	E_{pump}	$m_{CH4,losses}$	m_{LD}
$[kWh/t]$	$[kWh/t]$	$[kWh/t]$	$[kWh/t]$	$[kg/t]$	$[kg/t]$
0.26	0.43	1.69	0.05	0.01	311.1

EAF Steelmaking Process

An electric arc furnace is one of the main technologies used for recycling metal scrap and producing molten steel, through which the scraps and additives are melted using high-power electric arcs generated between the electrode and the charged material. Oxygen is also injected to reduce the carbon content of the steel to the desired level, while lime is added to the metal bath to regulate its composition [40]. Graphite electrodes are used to generate the arc on the scrap, which creates the necessary thermal energy for its melting. The specific consumption of electrodes has a significant impact on the economic efficiency of steel production in EAFs. Furthermore, the melting of the scrap is assisted by the injection of natural gas, which acts as chemical energy that also enhances the productivity of the furnace.

As this study was focused on evaluating the environmental impact of substituting fossil-based carbonaceous materials used in the EAF process, the coal dataset considered the entire supply chain, from mining to processing and transportation. Suitable grades of feed and injection coal were assumed based on industry data and literature, with an average usage of approximately 12 kg of coal per ton of steel produced in the EAF [24, 25]. The process of "Steel, low-alloyed Europe without Switzerland and Austria|steel production, electric, low-alloyed|Cut-off, U" from the Ecoinvent v3.8 database, using the Italian electricity mix and natural gas, was used to model molten steel.

5.2.4 Results

Life Cycle Impact Assessment (LCIA) of the Steelmaking Process

In this study, the impact assessment method adopted the ReCiPe 2016 v1.1 Midpoint method and the results are shown and discussed per functional unit. The substitution of fossil coal with hydrochar was performed on an equal carbon content basis. Thus, the emissions factor for converting the molar mass of carbon to CO_2 was 3.583 kg CO_2/kg C [25].

The characterization impact results of the base and traditional scenario are listed in ***Table 5.7***. The impacts on stratospheric ozone depletion, ionizing radiation, ozone formation (terrestrial ecosystem), marine eutrophication, terrestrial ecotoxicity, human non-carcinogenic toxicity, mineral resource scarcity, and fossil resource scarcity for the base scenario were higher than those of the traditional route, indicating that the hydro-char injection had a destructive effect on these environmental impacts. On the other hand, the EAF steelmaking process with hydrochar injection outperformed the fossil-based EAF process in the global warm-

ing, terrestrial acidification, freshwater eutrophication, and water consumption impact categories. The impacts of both routes on ozone formation (human health), fine particulate matter formation, freshwater ecotoxicity, marine ecotoxicity, human carcinogenic toxicity, and land use were not significantly different ($\leq \pm 0.5\%$). Since the EAF steelmaking processes for both routes analyzed were composed of the same metallurgical operations, except for the production and use of the carbon source, an in-depth analysis of hydrochar and fossil coal production and use was performed.

Table 5.7: *Characterization impact results of the base and traditional electric arc furnace scenarios.*

Impact Category	Unit	Traditional Scenario	Base Scenario
Global warming	kg CO_2 eq	526.56	514.94
Stratospheric ozone depletion	kg CFC11 eq	2.16×10^{-4}	2.26×10^{-4}
Ionizing radiation	kBq Co-60 eq	3.58	3.66
Ozone formation (human health)	kg NO_x eq	1.14	1.14
Fine particulate matter formation	kg $PM_{2.5}$ eq	7.02×10^{-1}	7.00×10^{-1}
Ozone formation (terrestrial ecosystems)	kg NO_x eq	1.17	1.17
Terrestrial acidification	kg SO_2 eq	1.5	1.49
Freshwater eutrophication	kg P eq	2.84×10^{-2}	2.79×10^{-2}
Marine eutrophication	kg N eq	1.11×10^{-3}	2.10×10^{-3}
Terrestrial ecotoxicity	kg 1.4-DCB	2183.61	2263.78
Freshwater ecotoxicity	kg 1.4-DCB	$2.29 \times 10^{+1}$	$2.29 \times 10^{+1}$
Marine ecotoxicity	kg 1.4-DCB	$3.53 \times 10^{+1}$	$3.55 \times 10^{+1}$
Human carcinogenic toxicity	kg 1.4-DCB	$1.81 \times 10^{+3}$	$1.81 \times 10^{+3}$
Human non-carcinogenic toxicity	kg 1.4-DCB	$3.32 \times 10^{+2}$	$3.34 \times 10^{+2}$
Land use	m^2a crop eq	$1.52 \times 10^{+1}$	$1.52 \times 10^{+1}$
Mineral resource scarcity	kg Cu eq	1.38	1.4
Fossil resource scarcity	kg oil eq	130.56	137.59
Water consumption	m^3	9.85	9.74

Life Cycle Impact Assessment (LCIA) of the Carbon Sources Production

The comparison of the environmental characterization of the production and use of hydrochar and fossil coal is reported in ***Table 5.8*** per ton of molten steel.

Since the characterization impact results cannot be directly compared with each other, in order to define the most relevant impact categories, the normalization impact analysis was performed (***Figure 5.11***). The results showed that the most affected categories were:

- global warming;
- ozone formation (human health and terrestrial ecosystems);
- terrestrial acidification;
- freshwater eutrophication;
- terrestrial ecotoxicity;
- marine ecotoxicity;

- human carcinogenic toxicity;
- fossil resource scarcity.

Table 5.8: *Characterization impact results of the production and use of hydrochar and fossil coal.*

Impact Category	Unit	Fossil Coal	Hydrochar
Global warming	kg CO_2 eq	49.64	38.47
Stratospheric ozone depletion	kg CFC11 eq	1.47×10^{-6}	1.19×10^{-5}
Ionizing radiation	kBq Co-60 eq	1.43×10^{-2}	8.92×10^{-2}
Ozone formation (human health)	kg NO_x eq	2.45×10^{-2}	3.07×10^{-2}
Fine particulate matter formation	kg $PM_{2.5}$ eq	1.32×10^{-2}	1.23×10^{-2}
Ozone formation (terrestrial ecosystems)	kg NO_x eq	2.47×10^{-2}	3.20×10^{-2}
Terrestrial acidification	kg SO_2 eq	4.11×10^{-2}	3.31×10^{-2}
Freshwater eutrophication	kg P eq	1.60×10^{-3}	1.10×10^{-3}
Marine eutrophication	kg N eq	2.22×10^{-5}	1.01×10^{-3}
Terrestrial ecotoxicity	kg 1.4-DCB	5.25	85.53
Freshwater ecotoxicity	kg 1.4-DCB	2.45×10^{-3}	1.65×10^{-2}
Marine ecotoxicity	kg 1.4-DCB	6.69×10^{-3}	1.25×10^{-1}
Human carcinogenic toxicity	kg 1.4-DCB	3.91×10^{-2}	1.52×10^{-1}
Human non-carcinogenic toxicity	kg 1.4-DCB	2.98×10^{-1}	2.61
Land use	m^2a crop eq	3.33×10^{-1}	3.98×10^{-1}
Mineral resource scarcity	kg Cu eq	6.43×10^{-3}	2.60×10^{-2}
Fossil resource scarcity	kg oil eq	6.94	14.68
Water consumption	m^3	1.07×10^{-2}	-9.26×10^{-2}

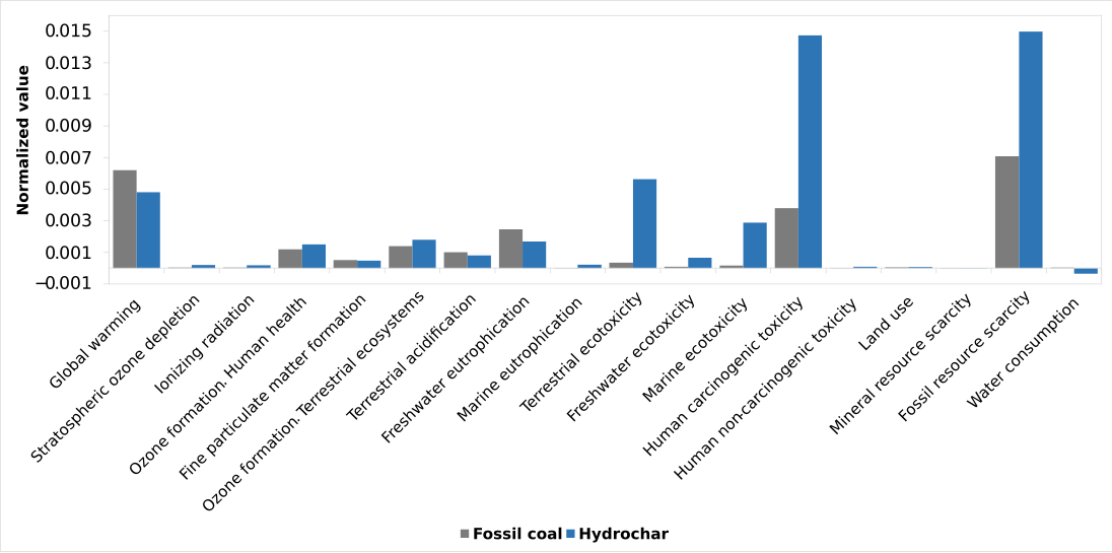

Figure 5.11: *Normalization impact analysis of the carbonaceous materials production.*

Global Warming

Table 5.7 shows that the hydrochar- and anaerobic-digestion-based EAF route results in a reduction of approximately –2.2% in the GWP impact in comparison

with the fossil-based EAF route. By analyzing the GWP of the hydrochar and fossil coal production, around 2.15 and 0.46 kg CO_2 eq/kg of carbonaceous material were produced, respectively. The hydrochar had a GWP in good agreement with that of charcoal, which was recorded in the Ecoinvent 3.8 database as "Charcoal GLO|market for|Cut-off, U," with an impact of 1.74 kg CO_2 eq/kg. Therefore, the hydrochar produced through the HTC process had a slightly higher impact than the charcoal produced using traditional reactors, primarily due to the combustion of natural gas for heating the hydrothermal reactor (77%). On the other hand, the impact of fossil coal was lower than that of hydrochar. Therefore, although the production of hydrochar was linked to some environmental burden, it was its usage that was found to be convenient because it was related to biogenic CO_2 emissions, unlike the use of fossil coal. From the impact assessment of the production and usage of these carbonaceous materials in steelmaking (***Table A.13*** and ***A.14*** of the Appendix ***Section A.3***), it can be inferred that by replacing fossil coal in EAF steelmaking, the GWP impact can be reduced by at least around 9%. In this context, 38 and 50 kg CO_2 eq/t of molten steel were produced by using hydrochar and coal in EAF steelmaking, respectively. This means that the usage of renewable carbon material in EAF steelmaking can reduce the EAF process GWP by 2% (***Figure 5.12***).

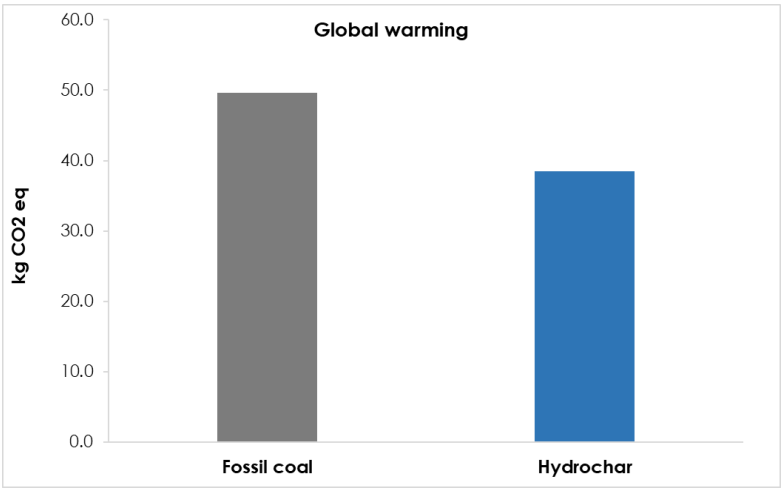

Figure 5.12: *Normalization impact analysis of the carbonaceous materials production.*

Ozone Formation (Human Health and Terrestrial Ecosystems)

Anthropogenic activities are the main cause of increased levels of nitrous oxide (NO_x) in the atmosphere. Most of the NO_x is formed in combustion processes, mainly originating from the transport and the industrial sector. When NO_x is emitted into the atmosphere, it undergoes a photochemical reaction with volatile organic compounds, resulting in the creation of tropospheric ozone. This can cause harm to both human health and terrestrial ecosystems [41].
While transport is the main cause of ozone formation during the production of fossil coal (66.8%), the combustion of natural gas for the heating needed for the hydrothermal carbonization reaction is the main contributor (56.5%) of the NO_x emissions of hydrochar production. For both human health (***Figure 5.13*****a**) and

terrestrial ecosystems (***Figure 5.13*b**), fossil coal production and usage present a higher NO_x concentration.

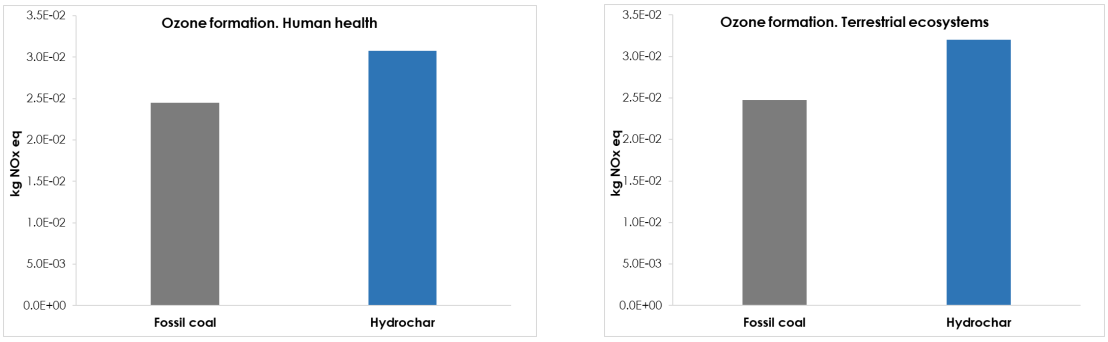

(a) (b)

Figure 5.13: *Ozone formation (human health (a) and terrestrial ecosystem (b)) impacts of the production of hydrochar vs. fossil coal.*

Freshwater Eutrophication

Phosphorus is the nutrient that restricts growth in freshwater ecosystems, and the impacts are measured in terms of kg P eq. Fossil coal has the most adverse effects on freshwater eutrophication (***Figure 5.14***), mainly due to the spoil from hard coal mining (90.4%). The production and use of hydrochar reduce the freshwater eutrophication impact by 2%, even if the wastewater produced by the anaerobic digestion of the spent liquor was responsible for 31.1%, while the transport of the biomass feedstock was responsible for 57.9%.

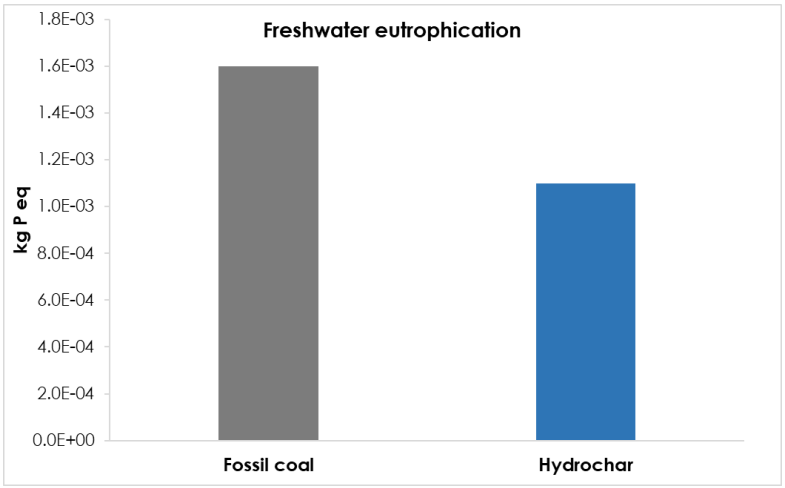

Figure 5.14: *Freshwater eutrophication impact of the production of hydrochar vs. fossil coal.*

Terrestrial Ecotoxicity

Hydrochar production and usage presented a higher terrestrial ecotoxicity impact than fossil coal (***Figure 5.15***). Feedstock transportation accounted for 89%

of the impact, which was the main contribution. The impact of fossil coal was less significant. It mostly belonged to transport, shared by train (20%), road (21%), and sea shipping (50%).

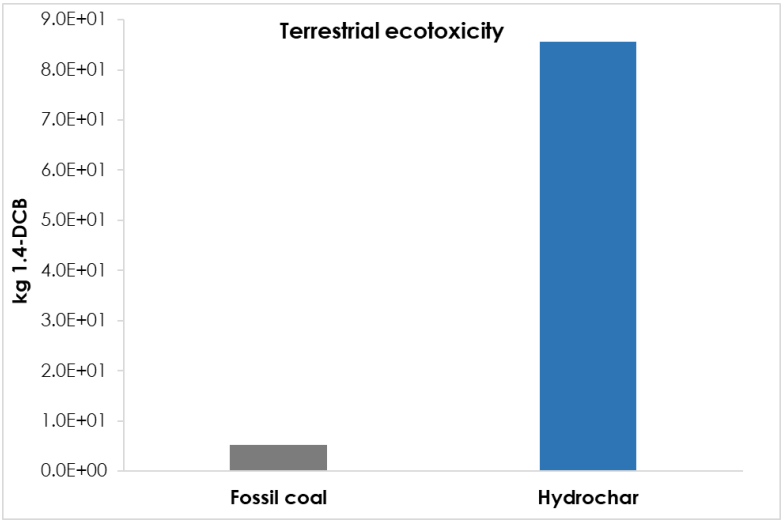

Figure 5.15: *Freshwater eutrophication impact of the production of hydrochar vs. fossil coal.*

Marine Ecotoxicity

As seen for the terrestrial ecotoxicity impact category, hydrochar had a higher marine ecotoxicity impact than fossil coal (***Figure 5.16***). The major emissions came from transport (46.4%) and from the background process of the offshore well oil/gas production (46.3%). The impact associated with fossil coal was less relevant since it was mainly shared between coal mine operations (38.2%) and transport by sea (37.5%).

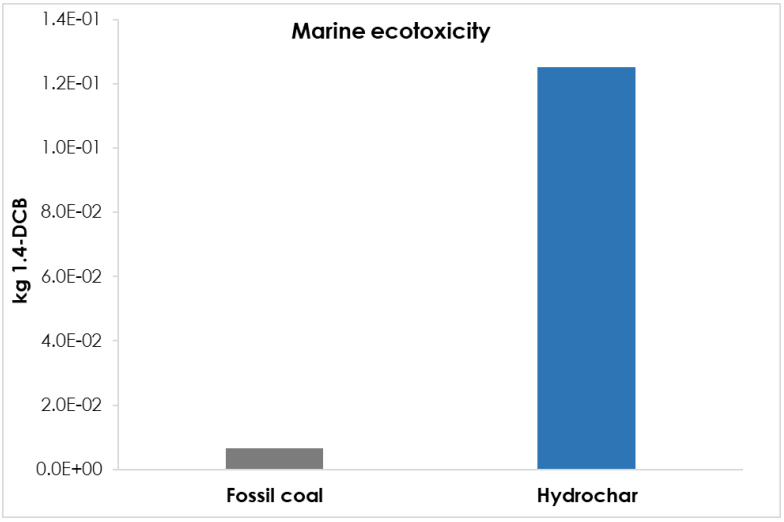

Figure 5.16: *Freshwater eutrophication impact of the production of hydrochar vs. fossil coal.*

Human Carcinogenic Toxicity

Similarly to the marine ecotoxicity impact category, fossil coal generated the least burden of human carcinogenic toxicity (***Figure 5.17***). The latter showed the highest contribution in transport (71%) and mine operation (27%), while natural gas (31.2%), electricity consumption (18.3%), and transport (41%) played the most important roles in hydrochar production.

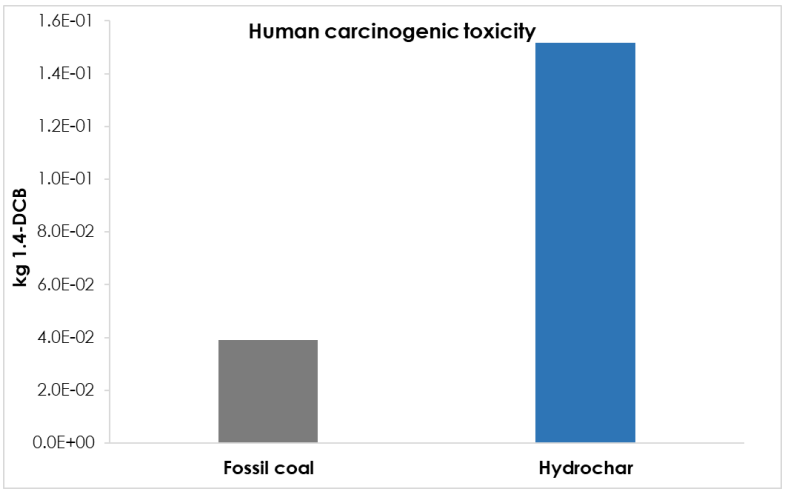

Figure 5.17: *Freshwater eutrophication impact of the production of hydrochar vs. fossil coal.*

Fossil Resource Scarcity

As displayed in ***Figure 5.18***, the extraction of 15 kg of oil equivalent caused the hydrochar production and usage to have a 6% higher impact on the fossil resource scarcity category than that of fossil coal (7 kg oil eq). These impacts were mainly related to the use of natural gas (83.6%) and hard coal mine operation and preparation (94.2%) for hydrochar and fossil coal scenarios, respectively.

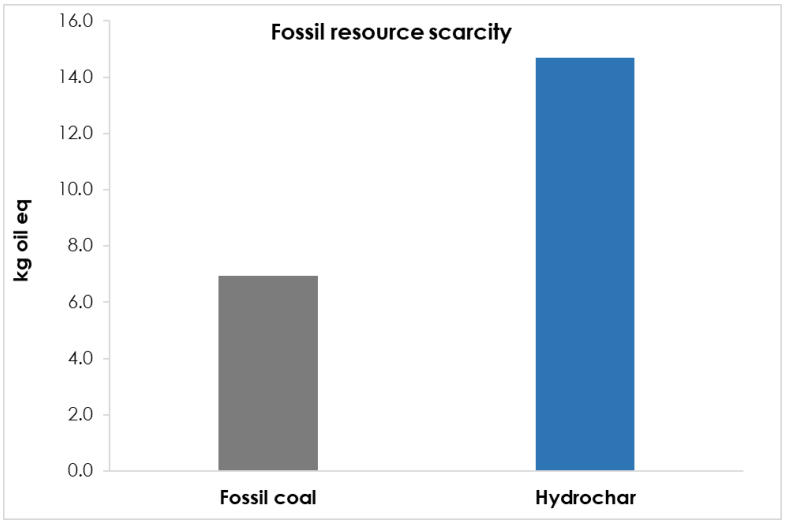

Figure 5.18: *Freshwater eutrophication impact of the production of hydrochar vs. fossil coal.*

5.2.5 Discussion

Overall, the outcomes of this research aligned with previous studies [24, 37, 42–44]. Nevertheless, differences in the selection of background data and system boundaries, significant variations in production amounts, and the utilization of different technologies in various steel plants can result in differences in the findings. The results regarding hydrochar production and use indicated that the use of natural gas was the dominant contributor to global warming, ozone formation, marine ecotoxicity, human carcinogenic toxicity, and fossil resource scarcity. Meanwhile, freshwater eutrophication was primarily influenced by the wastewater produced by the anaerobic digestion and terrestrial ecotoxicity by the feedstock transport. Thus, improving the efficiency of resources is essential for green development in hydrochar production. CO_2 and NO_x emissions from fossil resources (natural gas and coal) combustion are highly variable depending on the engine type and efficiency, the technology adopted, and the operating conditions [45]. The implementation of technologies for emissions abatement may dramatically reduce global warming and ozone formation impacts. It is worth noting that only the fossil resource scarcity impact category produced higher values for the base scenario in both the overall characterization impact results and the normalization analysis of hydrochar versus fossil coal production. In general, the majority of the environmental influences in this category were caused by the use of fossil fuels to produce the electricity required for the process. Thus, by increasing the production of bio-methane and its collection efficiency, not only the fossil resource scarcity impact could be reduced but also the environmental burden caused by the combustion for heating the hydrothermal reactor might be further reduced by replacing natural gas with bio-methane. Furthermore, the HTC reactor might be considered to run with electricity, supported by a solar photovoltaic system in order to positively affect the environment.

Particular attention must be given to the global warming category since it is largely used to inform international climate agreements and policies on the relative impacts of different greenhouse gases on climate change. From the overall results exposed, it was evident that electricity had important impacts on total global warming of around 42 and 44% for the traditional and base scenarios, respectively. The Italian system for the generation of electricity currently consists of a mix of traditional thermal power plants that primarily consume fossil fuels (mostly gas and coal) and renewable sources, such as hydro, solar PV, wind, geothermal, and bioenergy [46]. Despite the EU's pledge (EU Green Deal) to achieve carbon neutrality by 2050 [47], Italy's power system continues to rely heavily on non-renewable fossil fuels.

Additional Scenarios for the Steelmaking Process

To evaluate the effect of the national electricity mix on the environmental impact of the EAF steelmaking process, alternative scenarios were analyzed. For the alternative scenario 1 (AS1) and 2 (AS2), the composition of the Italian electricity mix was based on the Integrated National Energy and Climate Plan (INECP) objectives by 2030 [48, 49] and the complete decarbonization strategy by 2050 (EU Green Deal) [47, 50], respectively. Also, the possibility of heating the HTC reactor with an electrical source instead of natural gas in order to promote the use of re-

newable resources according to each decarbonizing pathway (2030–2050) was taken into consideration. Thus, alternative scenarios 3 (AS3) and 4 (AS4) were based on providing E_{react} by an electrical source considering the electrical mix of 2030 and 2050, respectively. The current Italian electricity mix was modeled by using the process in the Ecoinvent v3.8 database "Electricity, high voltage IT|market for|Cut-off, U", while the national electricity mix compositions based on the 2030 INECP and the EU Green Deal 2050 can be found in the literature [49, 50]. The comparison of the environmental impact between the base scenario (set as the zero reference) and each alternative scenario is displayed in ***Figure 5.19***.

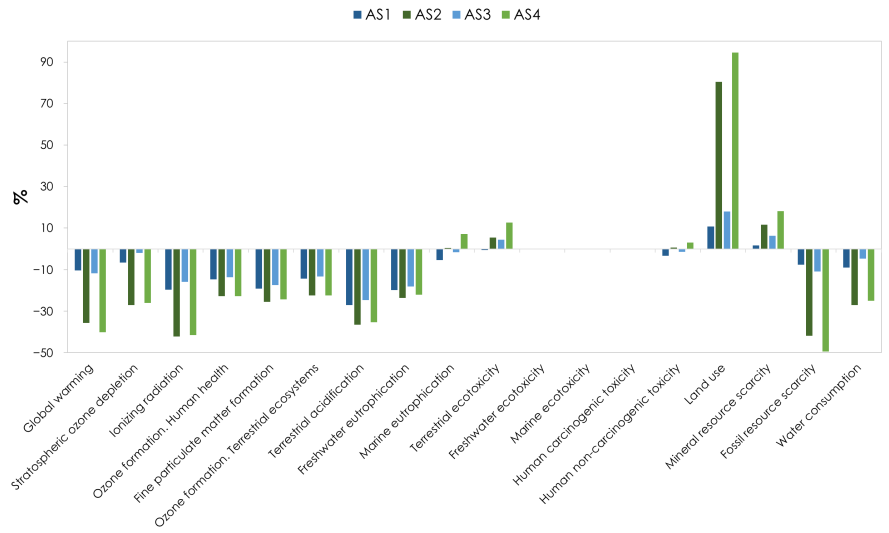

Figure 5.19: *Characterization impact comparison of the alternative scenarios with the base scenario.*

The importance of the substitution of fossil coal with hydrochar in EAF steelmaking assumed more relevance for the alternative scenarios since the share of electricity production from coal was reduced from around 10% to zero. The results showed that most of the contributions to the impact assessment for all the alternative scenarios were negative, i.e., they positively affected the environment.

Global warming potential was significantly reduced by considering AS1 and AS2 (–10 and –36%); additionally, the implementation of AS3 and AS4 led to further reductions by –12% and –40%, respectively. Furthermore, since the use of renewable energies will be increasing by 2030 and 2050, fossil resource scarcity was also reduced by –8%, –42%, –11%, and –50% for alternative scenarios 1, 2, 3, and 4, respectively. On the other hand, the land use impact category results in an aggravation by 2030 for AS1 and AS3 (+11 and +80%), while by 2050, the increase is more prominent (+18 and +95%). This was mainly related to the increase of biomass-derived electricity production of +1% by 2030 and +4% by 2050.

Additional Scenarios for the Hydrochar Production and Use

The effect of the additional scenarios was also evaluated on the production and use of the hydrochar (***Figure 5.20***). The normalization analysis displayed in ***Figure 5.20*****a** highlighted that the most affected categories of each alternative scenario were global warming, terrestrial ecotoxicity, marine ecotoxicity, human

carcinogenic toxicity, and fossil resource scarcity. The impact characterization presented in ***Figure 5.20b*** shows that the substitution of natural gas with electricity for providing the heat necessary for the HTC reaction greatly increased the environmental impacts in the terrestrial ecotoxicity, marine ecotoxicity, and human carcinogenic toxicity categories for AS3 and AS4. This reduced the effect of global warming and fossil resource scarcity up to –64% and –75%, respectively, by 2050. The increase in the cited categories was primarily due to the transport of biomass feedstock to the HTC plant. The related impact might be reduced by changing the heavy-duty transport technologies based on traditional combustion engines and fuels into more renewable alternatives, such as electric (battery electric, hybrid electric, plug-in hybrid) [51], biogas [52, 53], biofuels [54, 55], and hydrogen-based [56] vehicles.

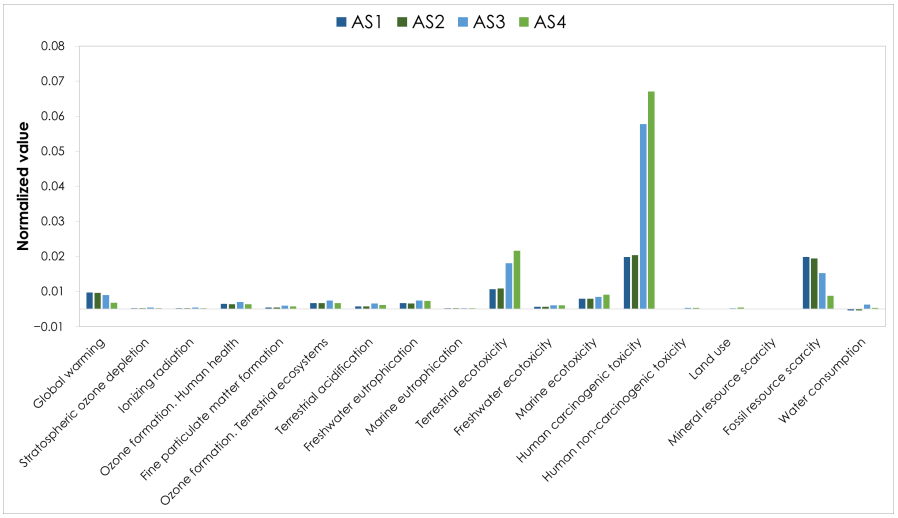

(a)

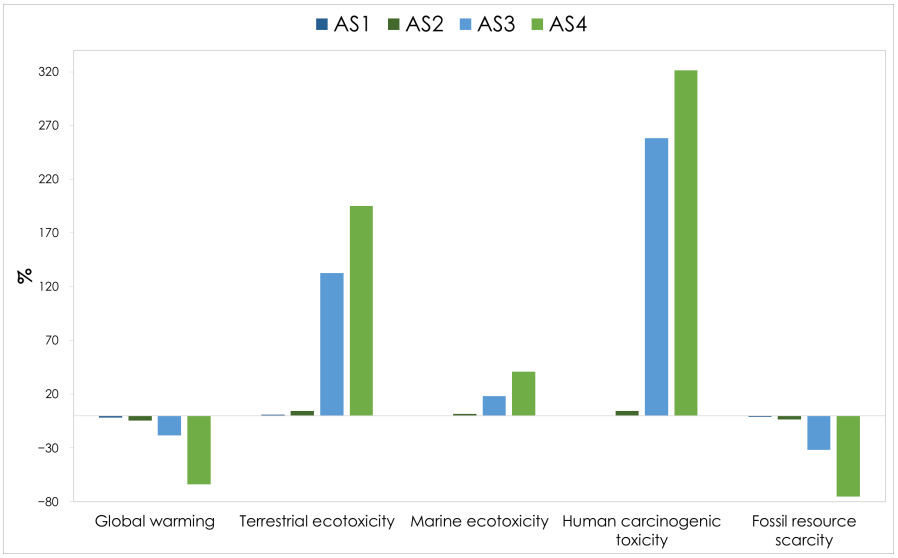

(b)

Figure 5.20: *Normalization analysis (a) and characterization impact (b) of hydrochar production and use for each alternative scenario.*

Challenges and future prospects of the study

LCA involves subjective decisions, such as choosing the functional unit, system boundaries, and impact categories, which can affect the results. Furthermore, it requires a large amount of data, which may not be readily available or of sufficient quality. However, the study helped to identify the hotspots of the life cycle that mostly contribute to the environmental impact and allows for targeted improvements.
The following recommendations are put forth for the future advancement of hydrochar applications:

1. Assessing the environmental impact of transportation in an LCA analysis can be challenging due to the high degree of variability, as factors such as distance, mode of transportation, and vehicle efficiency can vary widely between different products and processes. Thus, the transport of the raw biomass from the collection site to the processing site could be further assessed for the specific application, i.e., EAF steelmaking, since was found to contribute to the environmental impact of the hydrochar production.

2. Despite the properties of the hydrochar produced being in line with metallurgical applications [57], improving the mechanical characteristics will be beneficial for both the transportation and handling operations in the furnace. Through pelletizing both the logistics costs and safety risks might be reduced while the furnace efficiency enhanced [58–61]. Thus, it will be beneficial to include this stage in the system boundaries of future LCA analyses to grow stakeholders' understanding of the potential hydrochar applications.

3. Although some HTC pilot plants and industrial-scale reactors exist [62, 63], no detailed data on the reactor configuration, optimization and energy recovery systems, and energy and mass balance calculations are available. However, time-consuming, labor-intensive, and costly multiple trial-and-error experiments are required to obtain exhaustive information. Thus, to overcome the lack of data without incurring these issues will be interesting to make use of both a chemical process simulator (e.g., Aspen Plus®) to predict balances and performances of an industrial-scale HTC process [64] and numerical simulation to foresee the hydrochar behavior in the specific metallurgic application [1].

4. Further investigations on the techno-economic feasibility of the HTC process are required before moving toward the industrial scale-up. Whether biomass waste is converted into value-added products (hydrochar) largely depends on these biofuels' cost competitiveness compared with fossil-based fuels. Therefore, will be crucial to gain a thorough understanding of the techno-economic assessments (TEAs) of the HTC process for biomass, especially for large-scale production, together with the environmental performances (LCA) [65].

Nomenclature

Abbreviation			
BF-BOF	Blast Furnace-Basic Oxygen Furnace	η_{dryer}	Drier efficiency (%)
EAF	Electric Arc Furnace	T_{boil}	Boiling temperature (°C)
CFD	computational fluid dynamics	T_0	Starting temperature (°C)
Ac	Anthracite coal	ΔH_{vap}	Enthalpy of evaporation (kJ/kg)
H220	biochar from HTC	E_{mill}	Milling energy consumption (kWh/t)
T300	biochar from torrefaction	g	Gravitational acceleration (m/s^2)
P500	biochar from slow pyrolysis	Δh	Height different (m)
W400	cottonwood pyrolyzed biochar	η_{mill}	Milling efficiency (%)
FC	Fixed Carbon	$m_{biomass,HTC}$	sum of the mass of VP and EGM (kg)
VM	Volatile Matter	E_{react}	Thermal energy for HTC reaction (kWh)
VP	Vine Pruning	E_{heat}	energy for raising the temperature
EGM	Exhausted Grape Marc	E_{loss}	energy related to the heat lost on the reactor surface
HTC	Hydrothermal Carbonization	$c_{p\ biomass,HTC}$	specific heat capacity of dry biomass (kJ/kg K)
LCA	Life Cycle Assesment	T_r	reaction temperature (°C)
LCI	Life Cycle Inventory	T_o	entering temperature of the feedstock (°C)
AS	Alternative Scenario	$m_{vinasse}$	mass of vinasse entering the reactor (kg)
Symbol		$H_{vinasse,Tr}$	enthalpy of vinasse at 246.6°C (kJ/kg)
$V_{reactor}$	Reactor volume (m^3)	$H_{vinasse,T0}$	enthalpy of vinasse at 109.8°C (kJ/kg)
Ar	Surface area (m^2)	m_{liq}	amount of water to be evaporated (kg)
λ	Thermal conductivity of insulation (W/m K)	ΔH_{steam}	latent heat of water (kJ/kg)
s	Insulation thickness (m)	m_{steam}	amount of steam to be produced equal to m_{liq} (kg)
η_{heat}	Efficiency of the heating element (%)	$T_{vinasse,OUT}$	initial temperature of the vinasse (°C)
$c_{p,liq}$	Specific heat capacity of water (kJ/kg K)	m_{SL}	mass of the hot spent liquor leaving the HTC reactor (kg)
d	Impeller diameter (m)	$H_{SL,OUT}$	enthalpy of the spent liquor at 35°C in non-saturated conditions (kJ/kg)
Np	Type of impeller (/)	$H_{SL,IN}$	enthalpy of the spent liquor at 246.6°C in non-saturated conditions (kJ/kg)
N	Rotational speed (1/s)	HY_C	hydrochar yield in terms of carbon (C) content
η_{stirr}	Efficiency of stirring (%)	LY_C	spent liquor yield in terms of carbon (C) content
E_{filt}	Filtration energy consumption (kWh/t)	GY_C	gas yield in terms of carbon (C) content
		$E_{loss,AD}$	themal energy losses through the anaerobic digestion reactor

Bibliography

[1] A. Cardarelli, M. De Santis, F. Cirilli, and M. Barbanera, "Computational fluid dynamics analysis of biochar combustion in a simulated ironmaking electric arc furnace," *Fuel*, vol. 328, p. 125267, 2022.

[2] H.-J. Odenthal, A. Kemminger, F. Krause, L. Sankowski, N. Uebber, and N. Vogl, "Review on modeling and simulation of the electric arc furnace (EAF)," *steel research international*, vol. 89, no. 1, p. 1700098, 2018.

[3] C. Yigit, G. Coskun, E. Buyukkaya, U. Durmaz, and H. R. Güven, "CFD modeling of carbon combustion and electrode radiation in an electric arc furnace," *Applied Thermal Engineering*, vol. 90, pp. 831–837, 2015.

[4] M. M. Noor, A. P. Wandel, and T. Yusaf, "The simulation of biogas combustion in a mild burner," *Journal of Mechanical Engineering and Sciences*, vol. 6, pp. 995–1013, 2014.

[5] A. A. Ahmadi and M. Bahiraei, "Thermohydraulic performance optimization of cooling system of an electric arc furnace operated with nanofluid: A CFD study," *Journal of Cleaner Production*, vol. 310, p. 127451, 2021.

[6] L. Leng, Q. Xiong, L. Yang, H. Li, Y. Zhou, W. Zhang, S. Jiang, H. Li, and H. Huang, "An overview on engineering the surface area and porosity of biochar," *Science of The Total Environment*, vol. 763, p. 144204, 2021.

[7] N. F. M. Yunos, M. Zaharia, M. A. Idris, D. Nath, R. Khanna, and V. Sahajwalla, "Recycling agricultural waste from palm shells during electric arc furnace steelmaking," *Energy & Fuels*, vol. 26, no. 1, pp. 278–286, 2012.

[8] B. Fidalgo, C. Berrueco, and M. Millan, "Chars from agricultural wastes as greener fuels for electric arc furnaces," *Journal of Analytical and Applied Pyrolysis*, 2015.

[9] B. Bhoi, A. K. Jouhari, H. S. Ray, and V. N. Misra, "Smelting reduction reactions by solid carbon using induction furnace: foaming behaviour and kinetics of FeO reduction in CaO–SiO_2–FeO slag," *Ironmaking & Steelmaking*, vol. 33, no. 3, pp. 245–252, 2006.

[10] T. Ahmad, S. L. Plee, and J. P. Myers, "Fluent theory guide," p. 814.

[11] A. Kalde, T. Demus, T. Echterhof, and H. Pfeifer, "Determining the reactivity of biochar-agglomerates to replace fossil coal in electric arc furnace steelmaking," *Proceedings of the 23rd European Biomass Conference and Exhibition*, vol. 1-4 June 2015, p. 11 Pages, 2015.

[12] J. Zhang, W. Prationo, L. Zhang, and Z. Zhang, "Computational fluid dynamics modeling on the air-firing and oxy-fuel combustion of dried victorian brown coal," *Energy & Fuels*, vol. 27, no. 8, pp. 4258–4269, 2013.

[13] S. Sadaka, H. Liechty, M. Pelkki, and M. Blazier, "Pyrolysis and combustion kinetics of raw and carbonized cottonwood and switchgrass agroforests," *BioResources*, vol. 10, no. 3, pp. 4498–4518, 2015.

[14] T. Murakami, M. Ohno, K. Suzuki, K. Owaki, and E. Kasai, "Acceleration of carburization and melting of reduced iron in iron ore–carbon composite using different types of carbonaceous materials," *ISIJ International*, vol. 57, no. 11, pp. 1928–1936, 2017.

[15] J. Suer, M. Traverso, and N. Jäger, "Review of life cycle assessments for steel and environmental analysis of future steel production scenarios," *Sustainability*, vol. 14, no. 21, p. 14131, 2022.

[16] J. M. Terrones-Saeta, J. Suárez-Macías, E. R. Moreno-López, and F. A. Corpas-Iglesias, "Determination of the chemical, physical and mechanical characteristics of electric arc furnace slags and environmental evaluation of the process for their utilization as an aggregate in bituminous mixtures," *Materials*, vol. 14, no. 4, p. 782, 2021.

[17] C. Harpprecht, T. Naegler, B. Steubing, A. Tukker, and S. Simon, "Decarbonization scenarios for the iron and steel industry in context of a sectoral carbon budget: Germany as a case study," *Journal of Cleaner Production*, vol. 380, p. 134846, 2022.

[18] G. Surup, H. Kaffash, Y. Ma, A. Trubetskaya, J. Pettersen, and M. Tangstad, "Life cycle based climate emissions of charcoal conditioning routes for the use in the ferro-alloy production," *Energies*, vol. 15, no. 11, p. 3933, 2022.

[19] L. Kieush, J. Rieger, J. Schenk, C. Brondi, D. Rovelli, T. Echterhof, F. Cirilli, C. Thaler, N. Jaeger, D. Snaet, K. Peters, and V. Colla, "A comprehensive review of secondary carbon bio-carriers for application in metallurgical processes: Utilization of torrefied biomass in steel production," *Metals*, vol. 12, no. 12, p. 2005, 2022.

[20] E. Gul, L. Riva, H. K. Nielsen, H. Yang, H. Zhou, Q. Yang, O. Skreiberg, L. Wang, M. Barbanera, M. Zampilli, P. Bartocci, and F. Fantozzi, "Substitution of coke with pelletized biocarbon in the european and chinese steel industries: An LCA analysis," *Applied Energy*, vol. 304, p. 117644, 2021.

[21] A. Cardarelli and M. Barbanera, "Substitution of fossil coal with hydrochar from agricultural waste in the electric arc furnace steel industry: A comprehensive life cycle analysis," *Energies*, vol. 16, no. 15, p. 5686, 2023.

[22] M. Barbanera, A. Cardarelli, E. Carota, M. Castellini, T. Giannoni, and S. Ubertini, "Valorization of winery and distillery by-products by hydrothermal carbonization," *Scientific Reports*, vol. 11, no. 1, p. 23973, 2021.

[23] F. Piccinno, R. Hischier, S. Seeger, and C. Som, "From laboratory to industrial scale: a scale-up framework for chemical processes in life cycle assessment studies," *Journal of Cleaner Production*, vol. 135, pp. 1085–1097, 2016.

[24] T. Norgate and D. Langberg, "Environmental and economic aspects of charcoal use in steelmaking," *ISIJ International*, vol. 49, no. 4, pp. 587–595, 2009.

[25] T. Echterhof, "Review on the use of alternative carbon sources in EAF steelmaking," *Metals*, vol. 11, no. 2, p. 222, 2021.

[26] L. Albright, ed., *Albright's Chemical Engineering Handbook*. CRC Press, 0 ed., 2008.

[27] M. Lucian, M. Volpe, F. Merzari, D. Wüst, A. Kruse, G. Andreottola, and L. Fiori, "Hydrothermal carbonization coupled with anaerobic digestion for the valorization of the organic fraction of municipal solid waste," *Bioresource Technology*, vol. 314, p. 123734, 2020.

[28] B. Mendecka, L. Lombardi, F. Micali, and A. De Risi, "Energy recovery from olive pomace by hydrothermal carbonization on hypothetical industrial scale: a LCA perspective," *Waste and Biomass Valorization*, vol. 11, no. 10, pp. 5503–5519, 2020.

[29] G. Mannarino, S. Caffaz, R. Gori, and L. Lombardi, "Environmental life cycle assessment of hydrothermal carbonization of sewage sludge and its products valorization pathways," *Waste and Biomass Valorization*, vol. 13, no. 9, pp. 3845–3864, 2022.

[30] G. Mannarino, A. Sarrion, E. Diaz, R. Gori, M. A. De La Rubia, and A. F. Mohedano, "Improved energy recovery from food waste through hydrothermal carbonization and anaerobic digestion," *Waste Management*, vol. 142, pp. 9–18, 2022.

[31] D. Basso, "Hydrothermal carbonization of waste biomass," pp. 1–227, 2016.

[32] E. Medina-Martos, I.-R. Istrate, J. A. Villamil, J.-L. Gálvez-Martos, J. Dufour, and A. F. Mohedano, "Techno-economic and life cycle assessment of an integrated hydrothermal carbonization system for sewage sludge," *Journal of Cleaner Production*, vol. 277, p. 122930, 2020.

[33] F. Merzari, M. Langone, G. Andreottola, and L. Fiori, "Methane production from process water of sewage sludge hydrothermal carbonization. a review. valorising sludge through hydrothermal carbonization," *Critical Reviews in Environmental Science and Technology*, vol. 49, no. 11, pp. 947–988, 2019.

[34] M. Heidari, A. Dutta, B. Acharya, and S. Mahmud, "A review of the current knowledge and challenges of hydrothermal carbonization for biomass conversion," *Journal of the Energy Institute*, vol. 92, no. 6, pp. 1779–1799, 2019.

[35] L. Lombardi, C. Nocita, E. Bettazzi, D. Fibbi, and E. Carnevale, "Environmental comparison of alternative treatments for sewage sludge: An italian case study," *Waste Management*, vol. 69, pp. 365–376, 2017-11.

[36] V. Parravicini, P. H. Nielsen, D. Thornberg, and A. Pistocchi, "Evaluation of greenhouse gas emissions from the european urban wastewater sector, and options for their reduction," *Science of The Total Environment*, vol. 838, p. 156322, 2022.

[37] A. S. Erses Yay, B. Birinci, S. Açıkalın, and K. Yay, "Hydrothermal carbonization of olive pomace and determining the environmental impacts of post-process products," *Journal of Cleaner Production*, vol. 315, p. 128087, 2021.

[38] L. Lombardi, F. Tuci, M. Śliz, K. Czerwińska, S. Fabrizi, and M. Wilk, "Life cycle assessment of the hydrothermal carbonization process applied to the wet fraction mechanically separated from municipal mixed waste," *Waste Management*, vol. 166, pp. 181–193, 2023.

[39] M. Śliz, F. Tuci, K. Czerwińska, S. Fabrizi, L. Lombardi, and M. Wilk, "Hydrothermal carbonization of the wet fraction from mixed municipal solid waste: Hydrochar characteristics and energy balance," *Waste Management*, vol. 151, pp. 39–48, 2022.

[40] M. Karbowniczek, *Electric Arc Furnace Steelmaking*. CRC Press, 1 ed., 2021.

[41] G. Vinci, R. Ruggieri, A. Billi, C. Pagnozzi, M. V. Di Loreto, and M. Ruggeri, "Sustainable management of organic waste and recycling for bioplastics: A LCA approach for the italian case study," *Sustainability*, vol. 13, no. 11, p. 6385, 2021.

[42] A. Nurdiawati, I. N. Zaini, W. Wei, R. Gyllenram, W. Yang, and P. Samuelsson, "Towards fossil-free steel: Life cycle assessment of biosyngas-based direct reduced iron (DRI) production process," *Journal of Cleaner Production*, vol. 393, p. 136262, 2023.

[43] D. Burchart-Korol, "Life cycle assessment of steel production in poland: a case study," *Journal of Cleaner Production*, vol. 54, pp. 235–243, 2013.

[44] L. Yang, H. Hu, S. Yang, S. Wang, F. Chen, and Y. Guo, "Life cycle carbon footprint of electric arc furnace steelmaking processes under different smelting modes in china," *Sustainable Materials and Technologies*, vol. 35, p. e00564, 2023.

[45] F. Battini, A. Agostini, A. Boulamanti, J. Giuntoli, and S. Amaducci, "Mitigating the environmental impacts of milk production via anaerobic digestion of manure: Case study of a dairy farm in the po valley," *Science of The Total Environment*, vol. 481, pp. 196–208, 2014.

[46] J. Bastos, M. G. Prina, and R. Garcia, "Life-cycle assessment of current and future electricity supply addressing average and marginal hourly demand: An application to italy," *Journal of Cleaner Production*, vol. 399, p. 136563, 2023.

[47] European Commission, "European green deal.," https://climate.ec.europa.eu/eu-action/european-green-deal_en.

[48] Ministry of Economic Development,Ministry of the Environment {and} Protection of Natural Resources {and} the Sea, Ministry of Infrastructure {and} Transport, "Integrated national energy and climate plan (2019)," 2019. https://energy.ec.europa.eu/system/files/2020-02/it_final_necp_main_en_0.pdf.

[49] A. Gargiulo, M. L. Carvalho, and P. Girardi, "Life cycle assessment of italian electricity scenarios to 2030," *Energies*, vol. 13, no. 15, p. 3852, 2020.

[50] F. Lanati and M. Gaeta, "How to achieve a complete decarbonization of the italian energy system by 2050?," in *2020 17th International Conference on the European Energy Market (EEM)*, pp. 1–5, IEEE, 2020.

[51] L. L. P. De Souza, E. E. S. Lora, J. C. E. Palacio, M. H. Rocha, M. L. G. Renó, and O. J. Venturini, "Comparative environmental life cycle assessment of conventional vehicles with different fuel options, plug-in hybrid and electric vehicles for a sustainable transportation system in brazil," *Journal of Cleaner Production*, vol. 203, pp. 444–468, 2018.

[52] J. Van Mierlo, M. Messagie, and S. Rangaraju, "Comparative environmental assessment of alternative fueled vehicles using a life cycle assessment," *Transportation Research Procedia*, vol. 25, pp. 3435–3445, 2017.

[53] P. Tratzi, M. Torre, V. Paolini, L. Tomassetti, C. Montiroli, E. Manzo, and F. Petracchini, "Liquefied biomethane for heavy-duty transport in italy: A well-to-wheels approach," *Transportation Research Part D: Transport and Environment*, vol. 107, p. 103288, 2022.

[54] A. Sonthalia and N. Kumar, "Hydroprocessed vegetable oil as a fuel for transportation sector: A review," *Journal of the Energy Institute*, vol. 92, no. 1, pp. 1–17, 2019.

[55] A. Singh Verma, S. Chhabra, A. Karnwal, A. Gupta, and R. Kumar, "A review on performance, combustion and emissions utilizing alternative fuels," *Materials Today: Proceedings*, vol. 64, pp. 1459–1464, 2022.

[56] M. M. Mohideen, B. Subramanian, J. Sun, J. Ge, H. Guo, A. V. Radhamani, S. Ramakrishna, and Y. Liu, "Techno-economic analysis of different shades of renewable and non-renewable energy-based hydrogen for fuel cell electric vehicles," *Renewable and Sustainable Energy Reviews*, vol. 174, p. 113153, 2023.

[57] L. Kieush, J. Schenk, A. Koveria, G. Rantitsch, A. Hrubiak, and H. Hopfinger, "Utilization of renewable carbon in electric arc furnace-based steel production: Comparative evaluation of properties of conventional and non-conventional carbon-bearing sources," *Metals*, vol. 13, no. 4, p. 722, 2023.

[58] C. Wang, Y.-C. Lu, L. Brabie, and G. Wang, *A Pilot Trial Investigation of Using Hydrochar Derived from Biomass Residues for EAF Process*. Springer Nature Switzerland, 2023.

[59] L. Riva, A. Cardarelli, G. J. Andersen, T. V. Buø, M. Barbanera, P. Bartocci, F. Fantozzi, and H. K. Nielsen, "On the self-heating behavior of upgraded biochar pellets blended with pyrolysis oil: Effects of process parameters," *Fuel*, vol. 278, p. 118395, 2020.

[60] Y. Lu, H. Yang, A. V. Karasev, C. Wang, and P. G. Jönsson, "Applications of hydrochar and charcoal in the iron and steelmaking industry—part 1: Characterization of carbonaceous materials," *Sustainability*, vol. 14, no. 15, p. 9488, 2022.

[61] Y.-C. Lu, L. Brabie, A. V. Karasev, and C. Wang, "Applications of hydrochar and charcoal in the iron and steelmaking industry—part 2: Carburization of liquid iron by addition of iron–carbon briquettes," *Sustainability*, vol. 14, no. 9, p. 5383, 2022.

[62] Lucian Michela, Merzari Fabio, Messineo Antonio, and Volpe Maurizio, "Hydrothermal carbonization of sludge residues via carborem c700 industrial scale continuous operating plant," *Chemical Engineering Transactions*, vol. 92, pp. 19–24, 2022-06.

[63] N. U. Saqib, H. B. Sharma, S. Baroutian, B. Dubey, and A. K. Sarmah, "Valorisation of food waste via hydrothermal carbonisation and techno-economic feasibility assessment," *Science of The Total Environment*, vol. 690, pp. 261–276, 2019.

[64] A. Sarrion, E. Medina-Martos, D. Iribarren, E. Diaz, A. F. Mohedano, and J. Dufour, "Life cycle assessment of a novel strategy based on hydrothermal carbonization for nutrient and energy recovery from food waste," *Science of The Total Environment*, vol. 878, p. 163104, 2023.

[65] F. Hussin, N. N. Hazani, M. Khalil, and M. K. Aroua, "Environmental life cycle assessment of biomass conversion using hydrothermal technology: A review," *Fuel Processing Technology*, vol. 246, p. 107747, 2023.

Chapter 6

Building application

In recent years, the exploration of alternative materials for building construction has gained significant momentum due to the growing concern for environmental sustainability and the need for a circular economy. One such promising material that has emerged is hydrochar from hydrothermal carbonization (HTC) which holds great potential as a building admixture derived from waste biomass. The utilization of hydrochar not only presents a pathway for large-scale waste recycling but also contributes to the realization of an eco-sustainable society. By harnessing the virtuosic waste-to-resource approach, hydrochar applications can significantly enhance environmental sustainability, public health, and the overall viability of the building industry.

This chapter delves into the application of hydrochar from HTC in the building sector and emphasizes how it can provide a sustainable solution to the challenges associated with municipal solid waste (MSW) management. By diverting waste biomass from landfills and converting it into a valuable resource, hydrochar applications pave the way for a more efficient and circular waste management system.

6.1 Hydrochar from MSW as admixture for sustainable plasters – *Paper E*

The elaboration of Paper E titled "*Co-Hydrothermal Carbonization of Cavitated Stabilized Organic Fraction and Landfill Leachate: Optimization of Hydrochar Characteristics*" [1] arises from the project "ECOPLASTER - Biostabilized for Ecosustainable Building" co-funded in 2022 by the Ministry of Environment and Energetic Security.

The project intends to use the outputs of the municipal solid waste management chain, i.e. SOF, LL, and the CF as input for the hydrothermal carbonization (HTC) process. The hydrochar (solid fraction) of the HTC process will be used for the production of an eco-sustainable plaster to be used in the building sector, while the spent liquor (liquid fraction) will be employed for the growth of microorganisms aimed at the production of bioplastics. A schematic outline of the project process is reported in ***Figure 6.1***.

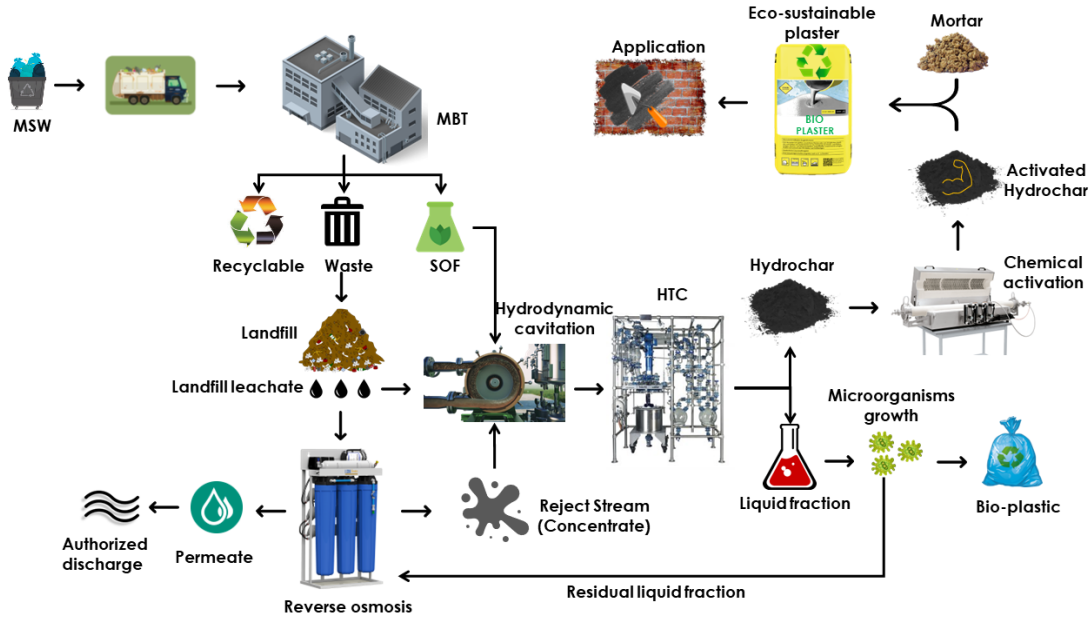

Figure 6.1: *Schematic outline of the ECOPLASTER project process*

The first section of this chapter provides the preliminary results on evaluating the efficacy of landfill leachate and concentrate fraction as reaction media for the hydrothermal conversion of SOF derived from MSWs to hydrochar. Moreover, to further enhance the homogenization and viscosity of the solid and liquid substrate mixture before the HTC process, the application of hydrodynamic cavitation (HC) was investigated.
Next, the chapter delves into the research project and examines any potential relationships between the hydrochar production parameters (temperature and residence time) and the impacts on the fixed carbon content, deashing, and mass yield, by using the Central Composite Face-Centered Design (CCF-CD) and Response Surface Methodology (RSM) methodology.

The preliminary results showed that the hydrochar from HTC of the stabilized organic fraction blended with landfill leachate is a valid mixture for the production of eco-sustainable plasters to be used in the building sector in a circular economy approach. Moreover, the hydrodynamic cavitation was confirmed as a valid pretreatment to enhance both the homogenization of the slurry, avoiding incurring pumpability problems at an industrial scale, and the hydrochar characteristics.
In detail, the CCF-CD together with the RSM proved to be very useful in determining the influence of independent variables on the response variables. HTC temperature had the most influence on the physicochemical properties of hydrochar while the effects of residence time were less significant. Besides, the BET analysis performed on the hydrochar from the experimental CCF-CD design highlighted that up to 250°C and 3 hours, the HTC may increase the hydrochar's surface area by 41.6% in comparison to the raw SOF.
The optimum conditions for the HTC process were found at 232°C and 2.65 h resulting in a fixed carbon content of 6.17%, a deashing efficiency of 53.87%, and a mass yield of 54.26%. Under the optimized conditions obtained from Derringer's desired function methodology, the experimental values were in close agreement with the predicted ones.

Overall, the results demonstrated the efficiency of the HTC process in enhancing the hydrochar properties to be used as admixture material in plasters in the building sector.

6.1.1 Preliminary tests and experimental design

Firstly, preliminary tests of HTC were conducted to understand the influence of the liquid substrate (landfill leachate and concentrate fraction) on the chemical properties of the hydrochar. The HTC was performed at different process temperatures (200, 250, and 270°C) and residence times (1, 3, and 6 h), while the solid-to-liquid ratio was maintained at 1/10. Then, the effect of the hydrodynamic cavitation on the chemical characteristics of the hydrochar was evaluated by considering a temperature set point of 60°C. A schematic overview of the experimental process is displayed in ***Figure 6.2***.

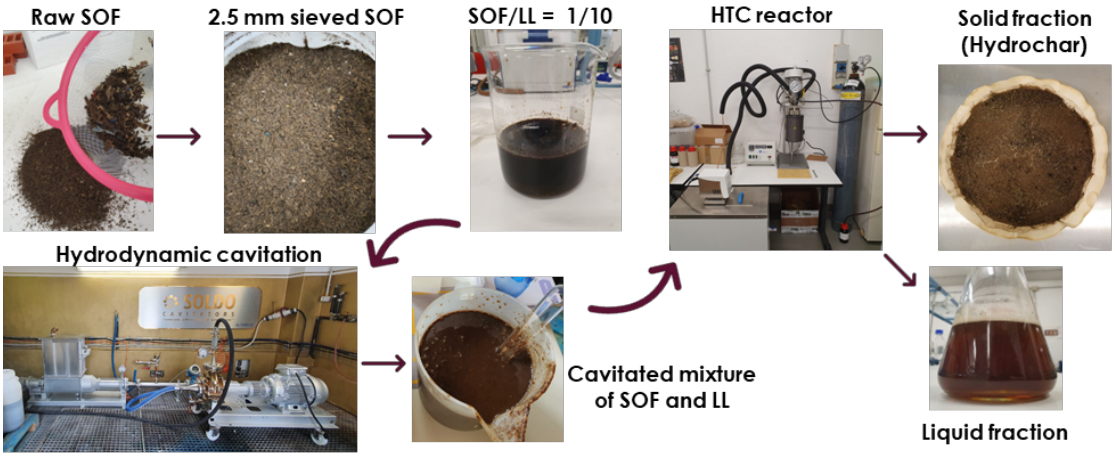

Figure 6.2: *Schematic overview of the experimental process.*

RSM and CCF-CD were used to examine any potential relationships between the hydrochar production parameters (temperature and residence time) and the impacts on the fixed carbon content, deashing, and mass yield. A three-level, 2-factor CCF-CD was employed. HTC process temperature (X_1) and residence time (X_2) were assumed as independent variables and coded at three levels (–1, 0, and +1), corresponding to the minimum, medium and maximum levels. Each process factor level was carefully selected based on preliminary tests. For the hydrochars, the chosen responses were fixed carbon content (Y_1), deashing efficiency (Y_2), and mass yield (Y_3) of the HTC process. The software Minitab v17.1.0 (Minitab Ltd., Coventry, UK) was used to implement the statistical model. The statistical significance of the regression coefficients was examined by using analysis of variance (ANOVA) and regression analysis. This was accomplished by using the Fisher's F-test at a 95% confidence level, previously describe in ***Section 3.5***. Multi-response analysis, based on Derringer's desirability function, was used to concurrently optimize the response variables. The desired response of FC content, DE, and MY was the maximum of the target goal. The same importance was assumed for each response during the optimization analysis. Three replications of experiments under optimum conditions were conducted to validate the optimized models by comparing the experimental data to the expected values.

6.1.2 Results and discussion

Characterization of preliminary tests

The characteristics of biomass before and after the HTC process in terms of proximate and ultimate analysis, mass yield, and deashing efficiency are shown in ***Table 6.1***.
Preliminary results indicate that tests performed at 250°C and a residence time of 3 h with LL rather than CF produce hydrochar with improved characteristics. Dehydration, decarboxylation, hydrolysis, and condensation are the main reactions that occur during the hydrothermal carbonization process [2, 3]. The balance between these different reactions determines the carbon content of the resulting hydrochar. At moderate temperatures (250°C) and residence times (3 hours), the HTC process primarily involves dehydration and decarboxylation reactions, which lead to an increase in the carbon content [4], resulting in about +22% and 23% by using LL and CF respectively.

Table 6.1: *Characteristics of raw SOF and hydrochars from preliminary tests.*

Liquid substrate		LL	CF	LL	CF	LL	CF
HTC temperature [°C]		200	200	250	250	270	270
Residence time [h]		1	1	3	3	6	6
Material	**Raw SOF**	**Hydrochars**					
Ultimate Analysis [wt%$_{daf}$]							
C	22.40	23.60	22.60	30.40	29.20	28.97	24.12
H	3.20	4.42	2.87	2.79	2.36	1.87	2.42
N	1.37	0.88	0.83	1.17	1.27	1.67	1.84
O	17.80	23.56	17.55	11.79	9.15	12.82	14.05
Proximate Analysis [wt%$_{db}$]							
Ash	55.82	47.54	56.15	53.85	58.02	47.54	57.57
VM	41.79	46.77	36.73	41.72	36.82	46.77	39.38
FC	2.39	5.69	7.12	4.43	5.16	5.69	3.05
DE [%]	-	38.04	11.32	24.48	16.14	28.45	22.11
MY [%]	-	72.75	88.16	78.28	80.68	72.28	74.72

Note: db: dry basis; daf: dry and ash-free bases

However, as the reaction temperature and residence time increase (270°C and 6 hours), hydrolysis and condensation reactions become more prevalent, leading to a decrease in the carbon content [5] of about –5% and –21% by using LL and CF respectively. Thus, at lower temperatures and residence times, the increase in carbon content due to dehydration and decarboxylation reactions outweighs the decrease due to hydrolysis and condensation reactions. However, at higher temperatures and longer residence times, the decrease in carbon content due to hydrolysis and condensation reactions outperforms the increase due to dehydration and decarboxylation reactions, resulting in a net decrease in carbon content. Furthermore, for both the hydrochar obtained with LL and CF the ash content increased first and then lightly decreased as the temperature and residence time increased. A similar trend was found in literature [6]. The reason might be attributed to the decrease of the organic compounds while the ash increased with the increment of the reaction temperature and residence time from 220°C and

1 hour to 250°C and 3 hours. However, with the further increase of the HTC process parameters (270°C and 6 hours), the degradation of organic components promotes the decomposition of inorganics into the liquid fraction. Thus, despite a higher carbon content (+14.15%), the HTC of SOF with concentrate fraction promotes the formation of ashes (+7.19%) in comparison to using landfill leachate. Furthermore, by using the CF the deashing efficiency of the process resulted in a reduction of –51.69%. Higher ash content in hydrochar reduces its porosity as the inorganic materials can fill up the pore spaces. Additionally, ash could also coat the surface of hydrochar particles and reduce their specific area available for reactions or adsorption [7]. Thus, the reduction in porosity and specific area of the produced hydrochar might be unsuitable for the application as an admixture for plaster production. For this reason, the hydrodynamic cavitation was performed only on the mixture of SOF and LL. The mixture cavitated at a temperature set point of 60°C was submitted to the HTC at a process temperature of 250°C and a residence time of 3 hours to evaluate the effect of the HC on the hydrochar properties. The characteristics of the hydrochars from the HTC process of the mixture of SOF and LL before and after undergoing HC are reported in ***Table 6.2***.
The hydrodynamic cavitation performed at a temperature set point of 60°C showed significant advantages in terms of hydrochar properties. In detail, HC as pretreatment of HTC provided higher disintegration and homogenization of the solid/liquid mixture leading to higher carbon and fixed carbon content (+11.37% and +33.68% respectively), lower ash formation (–12.33%) and upgraded DE (+63.91%), lending support for producing hydrochar with raised porosity.

Table 6.2: *Characteristics of raw SOF and hydrochars from preliminary tests.*

Mixture	**Not cavitated**	**Cavitated**
HTC temperature [°C]	250	250
Residence time [h]	3	3
Ultimate Analysis [wt%$_{daf}$]		
C	30.40	34.3
H	2.79	3.77
N	1.17	1.44
O	11.79	12.55
Proximate Analysis [wt%$_{db}$]		
Ash	53.85	47.94
VM	41.72	45.86
FC	4.43	6.68
DE [%]	24.48	67.86
MY [%]	78.28	37.45

Note: db: dry basis; daf: dry and ash-free bases

Central Composite Face-Centered Design

The CCF-CD experimental design was established from the results of the preliminary analysis. In detail, the HTC process was performed by using the mixture of SOF and LL cavitated at a temperature set point of 60°C. The factors and their coded values are shown in ***Table 6.3***. A total number of 13 tests were carried out, including 4 runs of factorial points, 4 runs of face-centered points, and 5 replicates at the central point useful to evaluate the pure error.

Table 6.3: *Independent process variables, range values, and coded levels in experimental design*

Independent variables	**Symbols**	**Coded levels**		
		-1	0	1
HTC temperature [°C]	X_1	220	250	280
Residence time [h]	X_2	1.5	3	4.5

Elemental analysis of hydrochars from CCF-CD experimental design

Table 6.4 displays the results of the proximate analysis of hydrochars from the CCF-CD experimental design. The trials were performed in random order for minimising the effects of unexpected variability on the observed responses.
The changes in the elemental composition of raw SOF and the obtained hydrochars are also given in the Van Krevelen diagram (***Figure 6.3***), which is a plot of the atomic H/C ratio versus the atomic O/C ratio. The hydrochars had significantly lower H/C and O/C atomic ratios than the raw SOF. This mainly results from the dehydration and decarboxylation reactions occurring during HTC [8, 9]. The dehydration and decarboxylation reactions, which reduce the amount of H and O elements and increase the presence of C, were caused by the rise in HTC temperature [10]. Likewise, the increase in residence time only influenced the O/C ratios, which decreased. While dehydration and decarboxylation are the predominant reaction pathways, demethanation has a negligible influence on the HTC process.

Table 6.4: *Ultimate analysis of hydrochars from CCF-CD experimental design.*

Run order	**1**	**2**	**3**	**4**	**5**	**6**	**7**	**8**	**9**	**10**	**11**	**12**	**13**
X_1 [°C]	250	250	250	220	250	250	280	220	220	250	280	250	280
X_2 [h]	1.5	3	4.5	3	3	3	4.5	1.5	4.5	3	1.5	3	3
Ultimate Analysis [wt%$_{daf}$]													
C	34.70	36.60	37.68	30.13	34.40	35.00	35.13	30.43	33.40	33.20	34.18	33.00	34.85
H	4.03	3.98	4.11	3.61	3.68	4.13	3.48	3.81	3.93	3.67	3.45	3.83	3.40
N	1.32	1.38	1.75	1.04	1.50	1.46	1.24	0.89	0.98	0.89	1.28	1.52	1.15
O	14.19	10.15	12.38	17.58	11.41	12.53	7.76	21.03	15.28	11.65	10.67	12.93	9.70

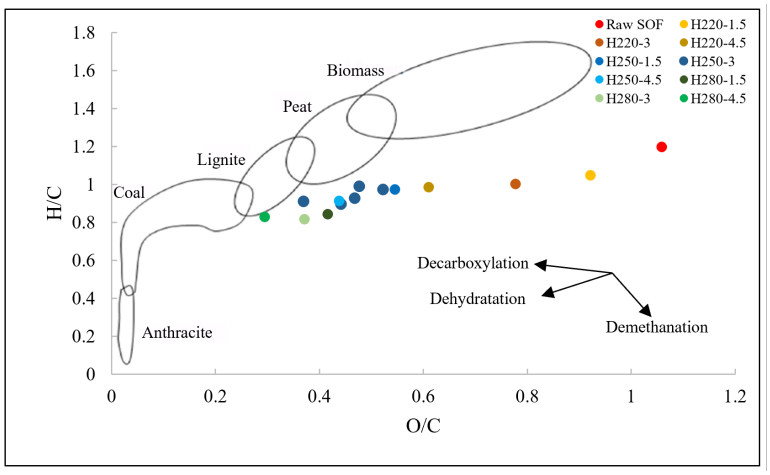

Figure 6.3: *Van Krevelen diagram for hydrochars under different conditions.*

BET analysis of hydrochars

As shown in ***Figure 6.4***, the specific surface area of all hydrochars was larger than that of the raw SOF. As the HTC temperature increased from 220°C to 250°C, the surface area gradually increased. This might be due to the release of gases from the decomposition of unstable components and the removal of VM during the hydrothermal process, resulting in the formation of open pores and cracks on the surface of the hydrochar [11–13]. However, at higher HTC temperatures and long residence times, the surface area decreased, which might be due to the secondary polymerization of soluble intermediates produced during the hydrolysis phase led to the blocking of pores [14, 15]. Even though the values for the surface area were generally low for raw SOF and hydrochars produced at all conditions, ranging from around 7 to 12 m^2/g, they are consistent with previous studies on biomass-derived hydrochars. Low surface area values for hydrochars derived from municipal solid waste, sewage sludge, livestock manure, spent coffee grounds, and macroalgae, have been reported in the literature [11, 13, 15–18]. Nevertheless, the combination of thermal and chemical or physical activation might explain the surface area increase [19–21].

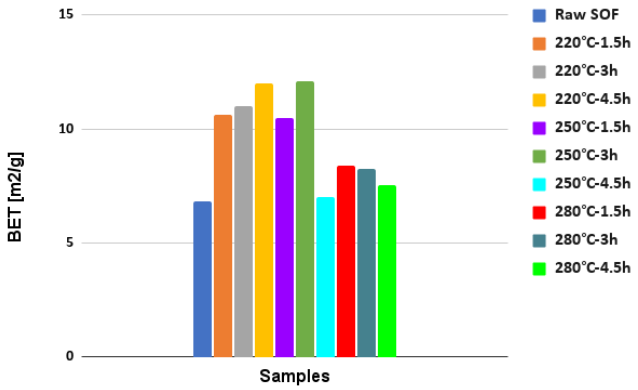

Figure 6.4: *BET surface area of the hydrochars from CCF-CD experimental design.*

Effect of independent variables

The proximate analysis of hydrochars from the CCF-CD experimental design, together with their respective experimental responses are listed in ***Table 6.5***.

Table 6.5: *Proximate analysis of hydrochars from CCF-CD experimental design.*

Run order	**1**	**2**	**3**	**4**	**5**	**6**	**7**	**8**	**9**	**10**	**11**	**12**	**13**
X_1 [°C]	250	250	250	220	250	250	280	220	220	250	280	250	280
X_2 [h]	1.5	3	4.5	3	3	3	4.5	1.5	4.5	3	1.5	3	3
Proximate Analysis [wt%$_{db}$]													
Ash	45.76	47.89	44.09	47.64	49.01	46.88	52.39	43.84	46.41	50.58	50.44	48.71	50.90
VM	48.78	45.59	50.08	46.95	44.12	46.17	43.13	51.47	48.91	42.60	46.06	44.34	44.49
FC (Y_1)	5.46	6.52	5.83	5.41	6.87	6.95	4.48	4.69	4.68	6.82	3.50	6.95	4.61
DE (Y_2) [%]	60.45	67.51	70.17	37.86	65.63	67.98	49.78	35.10	38.77	67.68	45.06	66.88	47.56
MY (Y_3) [%]	47.73	37.47	37.37	72.04	38.73	37.72	52.94	81.76	72.87	35.29	60.16	37.55	56.90

By applying multiple regression analysis to the experimental data, the relationship between the response variables, fixed carbon content (Y_1), deashing efficiency (Y_2), and mass yield (Y_3) of the HTC process, and the input variables, HTC process temperature (X_1) and residence time (X_2), was expressed by second-order polynomial equations with interaction terms. The final models generated in coded factors are shown as:

$$Y_1 = -99.18 + 0.8427X_1 + 1.263X_2 - 0.001743X_1X_1 - 0.4149X_2X_2 + 0.00550X_1X_2 \quad (6.1)$$

$$Y_2 = -1635.0 + 13.376X_1 + 3.76X_2 - 0.026446X_1X_1 - 0.534X_2X_2 + 0.0058X_1X_2 \quad (6.2)$$

$$Y_3 = 1939.2 - 14.675X_1 - 15.60X_2 + 0.02866X_1X_1 + 1.723X_2X_2 + 0.0093X_1X_2 \quad (6.3)$$

Analysis of variance (ANOVA) was performed for the adequacy and fitness of predicted models and the results are presented in ***Table 6.6***. The calculated F-values of 70.97, 197.38, and 182.08 for Y_1, Y_2, and Y_3 respectively, demonstrated that the regression models are highly significant ($p < 0.0001$). There is only a 0.01% chance that these large F-values could occur due to noise, confirming the validity of the predicted model. Furthermore, the adequacy of the model was analyzed by the evaluation of the determination coefficient ($R^2 > 0.95$) and the lack of fit (LOF) test. An R^2 value of 0.9807, 0.9930, and 0.9924 for Y_1, Y_2, and Y_3 respectively, ensured that only 1.93%, 0.7%, and 0.76% of the total variations are not explained by the regression models, validating the precision of the deduced models. Moreover, the values of R^2_{adj} (0.9668, 0.9879, 0.9869) were very high and in reasonable agreement with the R^2 values, confirming that the regression models were highly significant. The acceptability of the quadratic models was also verified by the lack of fit (LOF) test. A p-value higher than 0.05 means that LOF is insignificant due to relative pure error. Thus, the lack of fit p-values (0.265, 0.093, and 0.120 for each model) confirms that the models can be effectively employed for the prediction.

Effect on fixed carbon content

The influence of the independent variables on the responses and their interactions were evaluated by plotting response surface graphs and contour plots. ***Figure 6.5*** shows the effects of process temperature and residence time on fixed carbon content. The FC content increased with the increase in process temperature from 220 to 250°C and then decreased at the higher process temperature of 280°C. This result is in agreement with previous studies [22]. Moreover, according to the F-values and p-values of ***Table 6.6***, it can be noted that for the FC content X_1, X_2, X_1X_1, and X_2X_2 are significant model terms because their p-values were higher than 0.05. From the F-values, the process temperature (X_1) had a slightly greater effect on the FC content rather than residence time (X_2).

Table 6.6: *ANOVA of response surface quadratic models.*

Source	DF	F-Value	Prob > F
Fixed carbon content			
Model	5	70.97	< 0.0001
X_1	1	18.06	0.004
X_2	1	6.76	0.035
X_1X_1	1	153.47	< 0.0001
X_2X_2	1	54.36	< 0.0001
X_1X_2	1	5.53	0.051
Lack-of-Fit	3	1.94	0.265
$R^2 = 0.9807$; $R^2_{adj} = 0.9668$			
Deashing efficiency			
Model	5	197.38	< 0.0001
X_1	1	73.08	< 0.0001
X_2	1	25.48	0.001
X_1X_1	1	729.38	< 0.0001
X_2X_2	1	1.86	0.215
X_1X_2	1	0.13	0.731
Lack-of-Fit	3	4.42	0.093
$R^2 = 0.9807$; $R^2_{adj} = 0.9668$			
Mass yield			
Model	5	182.08	< 0.0001
X_1	1	157.31	< 0.0001
X_2	1	34.32	0.001
X_1X_1	1	540.20	< 0.0001
X_2X_2	1	12.20	0.010
X_1X_2	1	0.20	0.664
Lack-of-Fit	3	3.68	0.120
$R^2 = 0.9807$; $R^2_{adj} = 0.9668$			

Therefore, the positive signs of X_1 and X_2 in the ***Equation*** (6.1) indicate synergistic effects on the FC. However, the negative signs of X_1X_1 and X_2X_2 provide antagonistic effects on the response which make the FC increase up to a certain threshold with increasing HTC temperature and residence time after which it decreases.

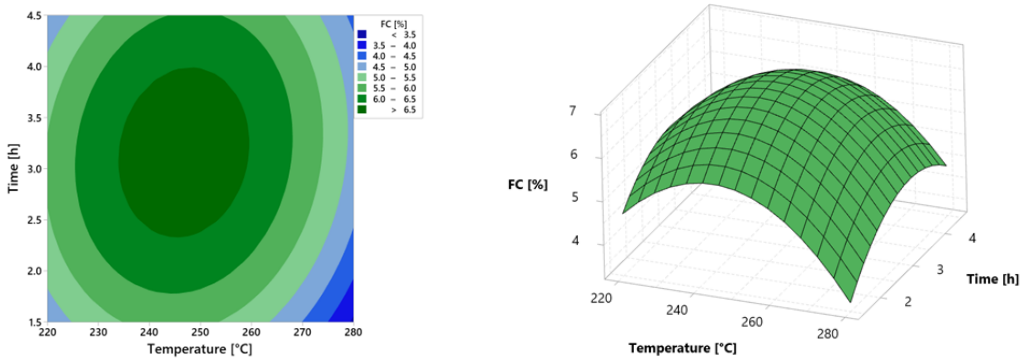

(a) (b)

Figure 6.5: *Contour and surface plots of the fixed carbon content vs the independent variables (temperature and time)*

Effect on dashing efficiency

A similar trend obtained for the FC was found for the deashing efficiency (***Figure 6.6***). The proximate analysis of ***Table 6.5*** shows that the DE increased from 35.10% up to 70.17% with the increase of process temperature and residence time from 220°C and 1.5h to 250°C and 4.5h and then decreasing up to 45.06% at 280°C and 1.5h. Similar findings were observed in literature studies [23–25]. This was expected to be due to the fact that the ash can be leached into the liquid fraction during HTC and its increase may be caused by the condensation and reprecipitation of some inorganics on the hydrochar surface after a long residence time at high temperatures. Furthermore, the F-values and p-values of ***Table 6.6*** highlighted how X_1, X_2, and X_1X_1 are significant model terms. Likewise for FC content, the F-values of process temperature (X_1) had a slightly greater effect on the DE rather than residence time (X_2), while the quadratic effect of process temperature (X_1X_1) showed a higher impact. However, an important result from the ANOVA analysis is that the residence time had no significant quadratic and interactive effects on the deashing efficiency.

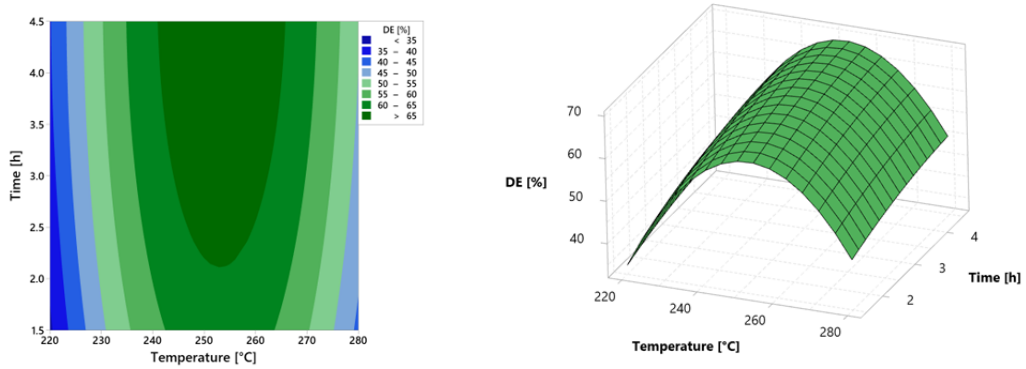

(a) (b)

Figure 6.6: *Contour and surface plots of deashing efficiency vs the independent variables (temperature and time)*

Effect on mass yield

The effect of the independent variables on hydrochars mass yield is shown in ***Figure 6.7***. By considering each process temperature, the increase in residence time determined a slight decrease in MY. On the other hand, the hydrochar yield decreased by a mean of 46% points from 220°C to 250°C and increased again by a mean of 40% points from 250°C to 280°C. The decrease in the yield as a function of temperature and residence time might be due to the higher carbonization degree, which led to a higher degree of material decomposition, fragmentation, and solubilization [26–28]. Furthermore, by raising the HTC temperature from 250°C to 280°C the formation of secondary char by polymerization reactions of small molecules in the liquid phase and recondensation into the char phase made the mass yield increase [29]. The influence of the independent variables is confirmed by the ANOVA analysis, as reported in ***Table 6.6***. All linear and quadratic terms were significant. In detail, having the highest F-value for both linear and quadratic coefficients, the process temperature affected most significantly the MY and might be considered the main controlling factor of the HTC process. Furthermore, the positive coefficients of the quadratic terms X_1X_1 and X_2X_2 denoted that there is a possible point of deflexion after which the independent variables have a negative or positive effect on the MY.

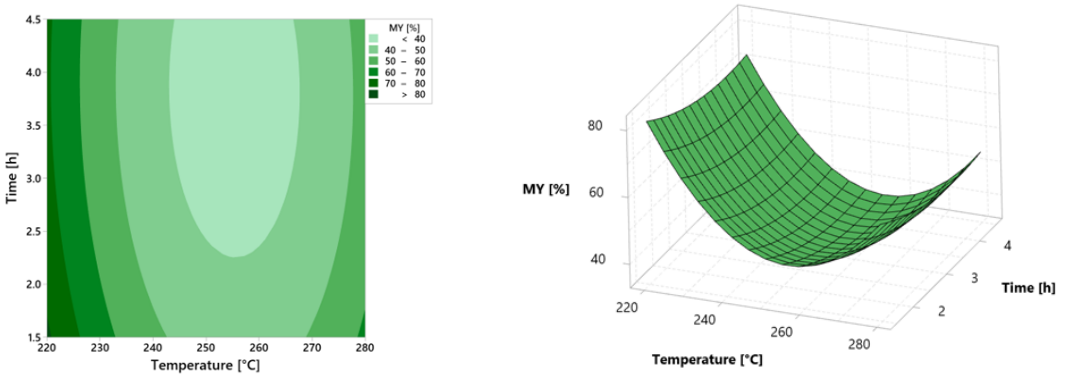

(a) (b)

Figure 6.7: *Contour and surface plots of mass yield vs the independent variables (temperature and time)*

Determination and validation of optimum conditions

Since the aim of this work was the preliminary investigation of the possible use of hydrochar as an admixture for the production of a sustainable plaster as carbon-capture, thermal insulation, moisture absorption, and acoustic insulation material, the FC, DE, and MY were chosen as response variables to obtain the optimum HTC process conditions at which they are maximized. The high ash content in the SOF may clog the pores, resulting in a decrease in specific surface area during the hydrothermal carbonization process [30]. On the other hand, with the increase of FC the surface area of hydrochar generally shows a regular increase [31, 32]. This is because of the dehydration, decarboxylation, and devolatilization

reactions, which increase the carbon content and open these clogged pores [3]. Furthermore, a higher MY could lead to greater efficiency in the production process, reducing production costs and increasing the economic viability of hydrochar in large-scale industrial production [33, 34]. Thus, the deashing effect of the HTC process, the fixed carbon and the mass yield, should be maximised to enhance the characteristics of the plaster. However, the optimization of all responses under the same operative conditions is difficult because their intervals of variation are different. For this reason, the multi-response optimization was carried out by the desirability function approach. In this study, equal weightage was given for all responses (FC, DE and MY) and an importance parameter equal to 1 were assumed. As can be noted in ***Figure 6.8*** the composite desirability (D) of the optimization was 56.87%, indicating that it is challenging to optimize all the response variables simultaneously. In particular, the maximum fixed carbon content, deashing efficiency and mass yield was found to be 6.34%, 54.73% and 53.81% respectively at an optimal parametric combination of a process temperature of 232°C and a residence time of 2.65h.

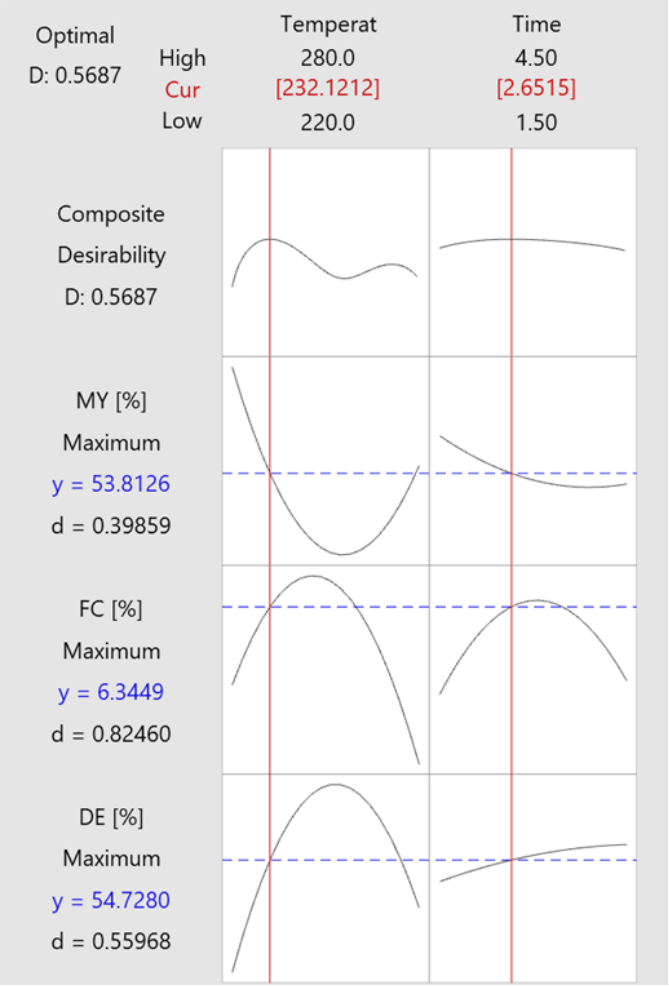

Figure 6.8: *BET surface area of the hydrochars from CCF-CD experimental design.*

To consolidate the results of the model, a hydrothermal carbonization treatment of the cavitated mixture of SOF and LL was performed under the optimized

conditions. Experiments were performed in triplicate and the values of the response variables are reported in ***Table 6.7***. Results confirm the suitability of the developed quadratic models because the experimental findings are in close agreement with the predicted values within a <3% error (***Table 6.7***).

Table 6.7: *Physicochemical characterization of hydrochar and response variables at the optimal HTC conditions.*

Analysis	**Measured**	**Predicted**	**Deviation [%]**
FC (Y_1) [%]	6.17	6.34	−2.64
DE (Y_2) [%]	53.87	54.73	−1.58
MY (Y_3) [%]	54.26	53.81	0.84

Note: db: dry basis; daf: dry and ash-free bases

Nomenclature

Abbreviation			
HTC	Hydrothermal Carbonization	MY	Mass Yield (%)
MBT	Mechanical Biological Treatment	DE	Deashing Efficiency (%)
MSW	Municipal Solid Waste	FC	Fixed Carbon
SOF	Stabilized Organic Fraction	VM	Volatile Matter
LL	Landfill Leachate	LOF	Lack of Fit
CF	Concentrate Fraction	*Symbol*	
CCF-CD	Central Composite Face-Centered Design	$X_{1,2}$	indipendent variables
RSM	Response Surface Methodology	$Y_{1,2,3}$	response variables
HC	Hydrodynamic Cavitation	R^2	coefficient of determination
		R^2_{adj}	adjusted coefficient of determination

Bibliography

[1] A. Cardarelli, P. Lombardi, A. Nicolini, and M. Barbanera, "Co-hydrothermal carbonization of cavitated stabilized organic fraction and landfill leachate: Optimization of hydrochar characteristics," *Environmental Engineering and Management Journal*, vol. 22, no. 10, pp. 1689–1702, 2023.

[2] A. Nawaz and P. Kumar, "Impact of temperature severity on hydrothermal carbonization: Fuel properties, kinetic and thermodynamic parameters," *Fuel*, vol. 336, p. 127166, 2023.

[3] Q. Wang, S. Wu, D. Cui, H. Zhou, D. Wu, S. Pan, F. Xu, and Z. Wang, "Co-hydrothermal carbonization of organic solid wastes to hydrochar as potential fuel: A review," *Science of The Total Environment*, vol. 850, p. 158034, 2022.

[4] O. S. Djandja, R. K. Liew, C. Liu, J. Liang, H. Yuan, W. He, Y. Feng, B. G. Lougou, P.-G. Duan, X. Lu, and S. Kang, "Catalytic hydrothermal carbonization of wet organic solid waste: A review," *Science of The Total Environment*, vol. 873, p. 162119, 2023.

[5] E. Danso-Boateng, A. B. Ross, T. Mariner, J. Hammerton, and M. Fitzsimmons, "Hydrochars produced by hydrothermal carbonisation of seaweed, coconut shell and oak: effect of processing temperature on physicochemical adsorbent characteristics," *SN Applied Sciences*, vol. 4, no. 8, p. 203, 2022.

[6] C. Chen, W. Liang, F. Fan, and C. Wang, "The effect of temperature on the properties of hydrochars obtained by hydrothermal carbonization of waste *Camellia oleifera* shells," *ACS Omega*, vol. 6, no. 25, pp. 16546–16552, 2021.

[7] S. Masoumi and A. K. Dalai, "Optimized production and characterization of highly porous activated carbon from algal-derived hydrochar," *Journal of Cleaner Production*, vol. 263, p. 121427, 2020.

[8] H. Si, C. Zhao, B. Wang, X. Liang, M. Gao, Z. Jiang, H. Yu, Y. Yang, Z. Gu, K. Ogino, and X. Chen, "Liquid-solid ratio during hydrothermal carbonization affects hydrochar application potential in soil: Based on characteristics comparison and economic benefit analysis," *Journal of Environmental Management*, vol. 335, p. 117567, 2023.

[9] S. Venna, H. B. Sharma, P. H. P. Reddy, S. Chowdhury, and B. K. Dubey, "Landfill leachate as an alternative moisture source for hydrothermal carbonization of municipal solid wastes to solid biofuels," *Bioresource Technology*, vol. 320, p. 124410, 2021.

[10] I. Budiman, Subyakto, U. D. Syafitri, B. A. Widyaningrum, R. Marlina, Triastuti, and E. Widodo, "Characteristics optimization of empty fruit bunches chars using central composite design," *Biomass Conversion and Biorefinery*, 2022.

[11] H. Fu, B. Wang, H. Wang, H. Liu, H. Xie, L. Han, N. Wang, X. Sun, Y. Feng, and L. Xue, "Assessment of livestock manure-derived hydrochar as cleaner products: Insights into basic properties, nutrient composition, and heavy metal content," *Journal of Cleaner Production*, vol. 330, p. 129820, 2022.

[12] S. Wu, Q. Wang, D. Cui, D. Wu, J. Bai, H. Qin, F. Xu, and Z. Wang, "Insights into the chemical structure evolution and carbonisation mechanism of biomass during hydrothermal treatment," *Journal of the Energy Institute*, vol. 108, p. 101257, 2023.

[13] X. Yang, B. Wang, Y. Guo, F. Yang, and F. Cheng, "Insights into the structure evolution of sewage sludge during hydrothermal carbonization under different temperatures," *Journal of Analytical and Applied Pyrolysis*, vol. 169, p. 105839, 2023.

[14] A. Magdziarz, A. Mlonka-Mędrala, M. Sieradzka, C. Aragon-Briceño, A. Pożarlik, E. A. Bramer, G. Brem, L. Niedzwiecki, and H. Pawlak-Kruczek, "Multiphase analysis of hydrochars obtained by anaerobic digestion of municipal solid waste organic fraction," *Renewable Energy*, vol. 175, pp. 108–118, 2021.

[15] Q. Xu, Q. Qian, A. Quek, N. Ai, G. Zeng, and J. Wang, "Hydrothermal carbonization of macroalgae and the effects of experimental parameters on the properties of hydrochars," *ACS Sustainable Chemistry & Engineering*, vol. 1, no. 9, pp. 1092–1101, 2013.

[16] A. Mlonka-Mędrala, M. Sieradzka, and A. Magdziarz, "Thermal upgrading of hydrochar from anaerobic digestion of municipal solid waste organic fraction," *Fuel*, vol. 324, p. 124435, 2022.

[17] S. Venkatesan, H. A. Baloch, I. A. Jamro, and N. Rafique, "Evaluation of the production of hydrochar from spent coffee grounds under different operating conditions," *Journal of Water Process Engineering*, vol. 49, p. 103037, 2022.

[18] M. Wilk, K. Czerwińska, M. Śliz, and M. Imbierowicz, "Hydrothermal carbonization of sewage sludge: Hydrochar properties and processing water treatment by distillation and wet oxidation," *Energy Reports*, vol. 9, pp. 39–58, 2023.

[19] F. M. Jais, C. Y. Chee, Z. Ismail, and S. Ibrahim, "Experimental design via NaOH activation process and statistical analysis for activated sugarcane bagasse hydrochar for removal of dye and antibiotic," *Journal of Environmental Chemical Engineering*, vol. 9, no. 1, p. 104829, 2021.

[20] A. E. Ogungbenro, D. V. Quang, K. Al-Ali, and M. R. Abu-Zahra, "Activated carbon from year seeds for CO2 capture applications," *Energy Procedia*, vol. 114, pp. 2313–2321, 2017.

[21] Z. Zhang, Y. Li, L. Ding, J. Yu, Q. Zhou, Y. Kong, and J. Ma, "Novel sodium bicarbonate activation of cassava ethanol sludge derived biochar for removing tetracycline from aqueous solution: Performance assessment and mechanism insight," *Bioresource Technology*, vol. 330, p. 124949, 2021.

[22] S. Zhang, T. Chen, W. Li, Q. Dong, and Y. Xiong, "Physicochemical properties and combustion behavior of duckweed during wet torrefaction," *Bioresource Technology*, vol. 218, pp. 1157–1162, 2016.

[23] I. S. Mohammed, R. Na, K. Kushima, and N. Shimizu, "Investigating the effect of processing parameters on the products of hydrothermal carbonization of corn stover," *Sustainability*, vol. 12, no. 12, p. 5100, 2020.

[24] K. Nakason, B. Panyapinyopol, V. Kanokkantapong, N. Viriya-empikul, W. Kraithong, and P. Pavasant, "Characteristics of hydrochar and liquid fraction from hydrothermal carbonization of cassava rhizome," *Journal of the Energy Institute*, vol. 91, no. 2, pp. 184–193, 2018.

[25] M. Tahmid Islam, J. L. Klinger, and M. Toufiq Reza, "Evaluating combustion characteristics and combustion kinetics of corn stover-derived hydrochars by cone calorimeter," *Chemical Engineering Journal*, vol. 452, p. 139419, 2023-01.

[26] C. A. Melo, F. H. S. Junior, M. C. Bisinoti, A. B. Moreira, and O. P. Ferreira, "Transforming sugarcane bagasse and vinasse wastes into hydrochar in the presence of phosphoric acid: An evaluation of nutrient contents and structural properties," *Waste and Biomass Valorization*, vol. 8, no. 4, pp. 1139–1151, 2017.

[27] S. Z. Roslan, S. F. Zainudin, A. Mohd Aris, K. B. Chin, M. Musa, A. R. Mohamad Daud, and S. S. A. Syed Hassan, "Hydrothermal carbonization of sewage sludge into solid biofuel: Influences of process conditions on the energetic properties of hydrochar," *Energies*, vol. 16, no. 5, p. 2483, 2023.

[28] M. Wilk, M. Śliz, and M. Gajek, "The effects of hydrothermal carbonization operating parameters on high-value hydrochar derived from beet pulp," *Renewable Energy*, vol. 177, pp. 216–228, 2021-11.

[29] G. R. Surup, J. J. Leahy, M. T. Timko, and A. Trubetskaya, "Hydrothermal carbonization of olive wastes to produce renewable, binder-free pellets for use as metallurgical reducing agents," *Renewable Energy*, vol. 155, pp. 347–357, 2020.

[30] Q. Gao, L. Ni, Y. He, Y. Hou, W. Hu, and Z. Liu, "Effect of hydrothermal pretreatment on deashing and pyrolysis characteristics of bamboo shoot shells," *Energy*, vol. 247, p. 123510, 2022.

[31] K. Kahandawa Arachchi, A. Selvaratnam, J. Gamage, and G. De Silva, "Green composite plaster with modified morphology for enhanced thermal comfort in buildings," *Case Studies in Construction Materials*, vol. 15, p. e00611, 2021.

[32] R. Tu, Y. Sun, Y. Wu, X. Fan, S. Cheng, E. Jiang, and X. Xu, "A new index for hydrochar based on fixed carbon content to predict its structural properties and thermal behavior," *Energy*, vol. 229, p. 120572, 2021.

[33] F. Hussin, N. N. Hazani, M. Khalil, and M. K. Aroua, "Environmental life cycle assessment of biomass conversion using hydrothermal technology: A review," *Fuel Processing Technology*, vol. 246, p. 107747, 2023.

[34] F. Yao, G. Ye, W. Peng, G. Zhao, X. Wang, Y. Wang, W. Zhu, Y. Jiao, H. Huang, and D. Ye, "Preparation of activated biochar with adjustable pore structure by hydrothermal carbonization for efficient adsorption of VOCs and its practical application prospects," *Journal of Environmental Chemical Engineering*, vol. 11, no. 2, p. 109611, 2023-04.

Chapter 7

Conclusions

7.1 Remarkable outcomes

The scope of this thesis was the study of alternative valorization routes concerning the biomass waste supply chain driven by a circular economy approach. Hydrothermal carbonization was selected as a suitable process for the conversion of raw biomass waste into carbonaceous products (hydrochar). The main outcomes of this research project aimed to demonstrate the valuable and sustainable application of hydrochar in several fields, energy, industrial, and building.

The first step in the research work was to address concerns regarding biomass waste management and select the main industrial supply chains that generate waste streams suitable for the HTC valorization process. Thus, prioritizing the valorization of winemaking industry residues and municipal solid waste was a strategic decision driven by the recognition of their abundance, the environmental burden of their disposal, the presence of valuable components, the significant potential for resource recovery, and the promotion of a circular economy.
It was demonstrated that by optimizing the main HTC process conditions (temperature, residence time, and solid-to-liquid ratio) the obtained hydrochars from winemaking by-products and municipal solid waste supply chain resulted in high potential application in the energy, industrial, and building sectors.

The study on the valorization of winery and distillery by-products by hydrothermal carbonization offered a comprehensive and integrated solution to the challenges of waste management in the winemaking industry. From the experimental design on co-HTC of vine pruning and exhausted grape marc, by using vinasse as wet catalytic vector, the optimal HTC conditions that maximized the mass yield, energy densification yield, phenols extraction yield, and the fuel ratio, as well as minimized the energy consumption, were determined as being 246.3°C, 1.6 hours, and a liquid-to-solid ratio of 6.6%. The produced hydrochar resulted in a sustainable and resourceful solution and contributed to the transition towards a more circular and sustainable economy by effectively closing the loop and turning winemaking industry waste into a valuable resource.

Furthermore, by investigating the pyrolysis and combustion kinetics of the hydrochar produced under optimal HTC conditions reported above, valuable insights have been gained into its thermal decomposition, combustion characteristics, and energy release potential. Kinetic analysis plays a crucial role in understanding, optimizing, and commercializing the production and utilization of hydrochar. The

kinetic results highlighted that even if the hydrochar exhibited a lower activation energy compared to its biomass precursors (vine pruning and exhausted grape marc) during both pyrolysis and combustion, HTC had positive effects on the hydrochar's structure, which achieved a more thermodynamically stable, structurally ordered, and energetically favorable state. This knowledge is crucial for the efficient utilization of hydrochar as a biofuel source, enabling its integration into existing energy systems and facilitating a transition towards cleaner and more sustainable energy production.

Besides, the integration of kinetic analysis with computational fluid dynamics enables a comprehensive understanding and modeling of the fluid flow, heat transfer, and chemical reactions within hydrochar energy systems. It facilitates system optimization, design, and parameter estimation, leading to improved efficiency and performance in hydrochar-based energy applications. The study conducted on the computational fluid dynamics analysis of biochar combustion in a simulated iron-making electric arc furnace laid the foundations for providing information on the potential (and possible) use of biochar from torrefaction, slow pyrolysis, and hydrothermal carbonization of biomass as a substitute for fossil coal in EAF. Overall, the three-dimensional CFD model offered extensive information on the spatial distribution of the jet velocity, temperature profile, reaction heat release, and distributions of combustion species inside the furnace. The higher volatile matter and the lower fixed carbon content of the biochar, from the thermal treatments cited above, than anthracite caused the reactions to be fast, and the exothermic heat released was more concentrated. The findings highlighted the need to tailor the biochar properties aimed for EAF applications e.g., by reducing volatiles, increasing fixed carbon, or reducing the porosity, by operating on the pretreatment process parameters.

Concurrently, by quantifying the environmental impacts and energy consumption associated with biomass-derived biochar implementation, decision-makers can make informed choices that promote sustainability and minimize the carbon footprint of the steelmaking industry. For this purpose, a comprehensive assessment of the environmental impacts of steel produced using EAFs that employ pulverized hydrochar from HTC of winery and distillery by-products as charged and injected material as a substitute for fossil coal was achieved. An industrial layout of a novel hydrochar- and anaerobic-digestion-based EAF was proposed. It was drawn that even though the manufacture of hydrochar was associated with some environmental burden, its use was advantageous since it was related to biogenic CO_2 emissions, contrary to the use of fossil coal. It was demonstrated that by replacing fossil coal with hydrochar in EAF steelmaking, the GWP impact can be reduced by around 2%. Furthermore, the LCA of the hydrochar- and anaerobic-digestion-based EAF, considering the 2030 INECP and the EU Green Deal 2050 projections for Italian electricity production, revealed a significant reduction in the environmental impact. The results confirmed that substituting fossil coal with a biogenic carbon source, such as hydrochar, holds great promise for advancing the decarbonization efforts within the EAF steelmaking industry. This finding underscores the potential of hydrochar as a sustainable alternative, paving the way for a greener and cleaner future in steel production.

This thesis work demonstrated the valuable application of the hydrochar in several fields. Besides the energy and industrial sectors, already discussed, the po-

tential use of hydrochar as an admixture material for plaster in the building sector was exploited. Overall, the results confirmed the efficiency of the HTC process in enhancing the hydrochar properties for the production of a sustainable plaster to be used as carbon-capture, thermal insulation, moisture absorption, and acoustic insulation material.
The experimental tests conducted revealed the remarkable efficiency of landfill leachate as a liquid substrate for the HTC of the stabilized organic fraction of municipal solid waste. Furthermore, the significance of hydrodynamic cavitation pretreatment was demonstrated, as it effectively improved both the homogenization of the slurry and the resulting hydrochar characteristics. Also, at mild conditions of temperature and residence time (250°C – 3 h) the specific surface area of the hydrochar was shown to increase up to around 42%. Finally, the optimum conditions for the HTC process were found at 232°C and 2.65 h resulting in a fixed carbon content of 6.17%, a deashing efficiency of 53.87%, and a mass yield of 54.26%.

In conclusion, this research thesis highlights the potential of hydrochar applications as a sustainable solution to address the challenges related to winemaking industry residues and municipal solid waste management. By diverting waste biomass from landfills and transforming it into a value-added product through the HTC process, a more efficient and circular waste management system can be established. This approach not only mitigates the environmental impact of waste disposal but also paves the way to the realization of a more sustainable and resourceful future. The utilization of hydrochar represents a pathway for large-scale waste recycling, as well as contributes to the realization of an eco-sustainable society. By harnessing the virtuosic waste-to-resource approach, hydrochar applications can significantly enhance environmental sustainability, public health, and the overall viability of the energy, industrial, and building industries.

7.2 Techno-economic considerations

As highlighted in this thesis, the attractiveness of hydrochar as a renewable energy source and substitute for conventional fossil coal to mitigate environmental burdens is undoubtedly significant. Also, the advantages of the HTC technology and its flexibility in handling a wide range of wastes have been proven. However, its economic competitiveness should be addressed to evaluate industrial feasibility. Economic feasibility encompasses a wide range of factors, including feedstock procurement, capital investment, operating costs, waste management, logistics costs, revenue potential, market dynamics, and financial viability.
Within this section, techno-economic considerations based on a thorough literature review are provided.

It should be mentioned that only a limited number of studies have provided thorough economic evaluations of the entire HTC process. Achieving consistency among them is challenging due to varying factors such as plant capacities, the amount of biomass waste processed, and the intended final use, which significantly impact the economic outcomes. Sangaré et al. (2024) focused on the energy balance and techno-economic analysis of the conversion of avocado stone into hydrochar pellets [1]. They considered the hydrochar pellets' breakeven selling prices

economically viable in the range of 250 $/ton and 379 $/ton (230–349 €/ton). For Lucian and Fiori (2017) the selling price of the hydrochar from off-specification compost and grape marc would be between 157 €/ton and 200 €/ton [2]. Besides, Saba et al. (2019) revealed that breakeven prices could decrease to 113–118 $/ton (104–108 €/ton) of hydrochar obtained from co-HTC of biomass (miscanthus) and coal [3]. Furthermore, the importance of the plant size was evaluated González-Arias et al. (2021) [4]. They found that increasing the HTC plant capacity from 312.5 to 1250 kg/h of olive tree pruning might reduce the price of hydrochar from 590 to 390 €/ton.
Considering the price trends observed over the past decade for wood pellets and traditional coal, which typically fall within the range of 170 €/ton to 200 €/ton and from 50 €/ton to 150 €/ton [5, 6], respectively, could be inferred that achieving profitable production of hydrochar at a price that is competitive for energy purposes or as a substitute for fossil coal is a highly challenging endeavor. However, the recent global energy crisis created significant oscillations in the wood pellet and coal market, making them reach peaks of 600 €/ton and 450 €/ton, respectively in 2022 [7, 8]. Hence, this apparent uncertainty may turn into an opportunity for HTC business. Moreover, the economic and environmental benefits of hydrochar highly depend on its applications. Recently, Nadarajah et al. (2024) provided a techno-economic analysis of hydrochar production from rice straw for contaminants adsorption in water [9]. They estimated the minimum selling price of the hydrochar to be almost half compared to the market price for other similar carbon-based sorbent materials (76 $/t vs. 136 $/t). Furthermore, the use of hydrochar as an admixture in mortars would reduce the consumption of cement without increasing the price of mortar (222 $/m^3 admixtured mortar vs. 225 $/m^3 of traditional mortar) [10–12].
Finally, the economic efficiency of hydrochar production could be improved by optimizing process, time, temperature, logistics, plant capacity, and feedstock choices. Moreover, pushing the energy transition towards the use of higher renewable energy sources for the production of the national electricity mix would reduce the hydrochar production costs [4, 13].

Overall, the foreseen increase in fossil fuel prices, the worldwide policies for renewable fuel sources, and climate change mitigation along with the rising cost of CO_2 emission rights and waste management burden could make hydrochar competitive in the near future.

7.3 Challenges and future perspectives

The study of alternative valorization routes for biomass waste within a circular economy framework, as explored in this thesis, presents both challenges and future perspectives.
While the valuable and sustainable application of hydrochar has been demonstrated in the energy, industrial, and building sectors, there is still a need for further research and development to explore its full potential. In this regard, it is deemed appropriate to acknowledge the significant challenges and limitations encountered in this research. The author hopes that these obstacles will be thoroughly investigated and overcome through the contributions of future research. Below is a concise list highlighting some of these challenges and perspectives:

⇒ Scaling up and commercialization: One of the primary challenges is the scale-up of hydrothermal carbonization processes for industrial implementation. The research demonstrates the potential of hydrochar in various sectors, but the transition from laboratory-scale experiments to large-scale production requires further optimization, process engineering, and economic viability assessment.

⇒ Technological improvements: The efficiency and effectiveness of the HTC process can be further improved through technological advancements. This might include advancements in reactor design and catalyst utilization can enhance the process efficiency quality of hydrochar.

⇒ Feedstock availability and variability: The availability and composition of biomass waste feedstocks can vary geographically and seasonally. It is essential to develop robust and flexible HTC processes that can handle different types of biomass feedstocks with varying characteristics, including moisture content, particle size, and chemical composition.

⇒ Techno-economic assessments: Evaluating the economic feasibility and viability of hydrochar production and its application in various sectors plays a crucial role. They involve analyzing the costs and benefits associated with the entire value chain, including feedstock collection, preprocessing, hydrothermal carbonization, post-processing, and end-use applications.

⇒ Integration with existing systems: This includes investigating the compatibility of hydrochar with existing energy systems, optimizing its use as a fuel source, and developing innovative technologies for its integration into industrial processes.

⇒ Industrial-scale chemical and fluid dynamic process simulations: Chemical process simulations are valuable tools for predicting the balances and performances of an industrial-scale HTC process. These simulations provide insights into mass and energy balances, reaction kinetics, process optimization, and product characterization without incurring costly multiple trial-and-error experiments. Moreover, integrating a time-dependent and multiphase CFD model can enhance the understanding of the process behavior (e.g. combustion, pyrolysis, etc.) and interactions between different phases, leading to improved process understanding.

⇒ Pilot plant design: Despite HTC being an emerging technology, there are relatively few industrial-scale or pilot-scale plants dedicated to HTC at the national level. Designing and establishing a flexible HTC pilot plant can serve as a testing ground to evaluate the technical feasibility, economic viability, and environmental performance of HTC processes using different feedstocks. The data and insights gained from pilot-scale operations can inform stakeholders for future industrial-scale plants, paving the way for broader adoption of HTC technology. Also, might be crucial for research institutions for funding opportunities, fostering the development of projects and collaboration for biomass waste valorization within a circular economy framework.

Bibliography

[1] D. Sangaré, M. Moscosa-Santillan, A. Aragón Piña, S. Bostyn, V. Belandria, and I. Gökalp, "Hydrothermal carbonization of biomass: experimental study, energy balance, process simulation, design, and techno-economic analysis," *Biomass Conversion and Biorefinery*, vol. 14, no. 2, pp. 2561–2576, 2024-01.

[2] M. Lucian and L. Fiori, "Hydrothermal carbonization of waste biomass: Process design, modeling, energy efficiency and cost analysis," *Energies*, vol. 10, no. 2, p. 211, 2017-02-13.

[3] A. Saba, K. McGaughy, and M. Reza, "Techno-economic assessment of co-hydrothermal carbonization of a coal-miscanthus blend," *Energies*, vol. 12, no. 4, p. 630, 2019-02-15.

[4] J. González-Arias, F. M. Baena-Moreno, M. E. Sánchez, and J. Cara-Jiménez, "Optimizing hydrothermal carbonization of olive tree pruning: A techno-economic analysis based on experimental results," *Science of The Total Environment*, vol. 784, p. 147169, 2021-08.

[5] European Biomass Industry Association, "Share of renewable energy in gross final energy consumption by sector," https://www.eubia.org/cms/wiki-biomass/biomass-pelleting/economics-applications-and-standards/.

[6] Statista Research Department, "Price of thermal coal from 2013 to 2022," 2023. https://www.statista.com/statistics/214236/thermal-coal-prices-since-2003/.

[7] Rinnovabili.it, "Pellet, cippato, legna: continua il calo dei prezzi dei biocombustibili legnosi," 2023. https://www.rinnovabili.it/le-aziende-informano/prezzi-dei-biocombustibili-legnosi-calo-pellet-cippato-legna/.

[8] P. Romano, N. Stampone, and G. Di Giacomo, "Evolution and prospects of hydrothermal carbonization," *Energies*, vol. 16, no. 7, p. 3125, 2023-03-29.

[9] K. Nadarajah, O. M. Rodriguez-Narvaez, J. Ramirez, E. R. Bandala, and A. Goonetilleke, "Lab-scale engineered hydrochar production and techno-economic scaling-up analysis," *Waste Management*, vol. 174, pp. 568–574, 2024-02.

[10] S. Allende, R. Tuladhar, and M. V. Jacob, "Sugarcane bagasse-derived carbon for partial replacement of cementitious material in concrete," *Materials Circular Economy*, vol. 6, no. 1, p. 3, 2024-12.

[11] S. Gupta, H. W. Kua, and S. D. Pang, "Biochar-mortar composite: Manufacturing, evaluation of physical properties and economic viability," *Construction and Building Materials*, vol. 167, pp. 874–889, 2018-04.

[12] M. M. Santos, A. L. Marques Sierra, A. Amado-Fierro, M. Suàrez, F. Blanco, J. M. G. La Fuente, M. A. Diez, and T. A. Centeno, "Reducing cement consumption in mortars by waste-derived hydrochars," *Journal of Building Engineering*, vol. 75, p. 106987, 2023-09.

[13] A. Gargiulo, M. L. Carvalho, and P. Girardi, "Life cycle assessment of italian electricity scenarios to 2030," *Energies*, vol. 13, no. 15, p. 3852, 2020-07-28.

Appendix A

Appendices

A.1 Supplementary material Chapter 3

Table A.1: *Most frequently mechanism functions of solid-state processes.*

Serial No.	Mechanism	Symbol	f (α)	g(α)
Order of reaction				
1	First-order	F1	$1-\alpha$	$-ln(1-\alpha)$
2	Second-order	F2	$(1-\alpha)^2$	$(1-\alpha)^{-1}-1$
3	Third-order	F3	$(1-\alpha)^3$	$[(1-\alpha)^{-2}-1]/2$
n	n-order	Fn	$(1-\alpha)^n$	$[(1-\alpha)^{-(n-1)}-1]/(n-1)$
Diffusion				
4	One-way transport	D1	0.5α	α^2
5	Two-way transport	D2	$[-ln(1-\alpha)]^{-1}$	$(1-\alpha)ln(1-\alpha)+\alpha$
6	Three-way transport	D3	$1.5(1-\alpha)^{2/3}[1-(1-\alpha)^{1/3}]^{-1}$	$[1-(1-\alpha)^{1/3}]^2$
7	Ginstling-Brounshtein equation	D4	$1.5[(1-\alpha)^{-1/3}-1]^{-1}$	$(1-2\alpha/3)-(1-\alpha)^{2/3}$
Limiting surface reaction between both phases				
8	One dimension	R1	1	α
9	Two dimensions	R2	$2(1-\alpha)^{1/2}$	$1-(1-\alpha)^{1/2}$
10	Three dimensions	R3	$3(1-\alpha)^{2/3}$	$1-(1-\alpha)^{1/3}$
Random nucleation and nuclei growth				
11	Two-dimensional	A2	$2(1-\alpha)[-ln(1-\alpha)]^{1/2}$	$[-ln(1-\alpha)]^{1/2}$
12	Three-dimensional	A3	$3(1-\alpha)[-ln(1-\alpha)]^{2/3}$	$[-ln(1-\alpha)]^{1/3}$
Exponential nucleation				
13	Power law. $n=1/2$	P2	$2\alpha^{1/2}$	$\alpha^{1/2}$
14	Power law. $n=1/3$	P3	$3\alpha^{2/3}$	$\alpha^{1/3}$
15	Power law. $n=1/4$	P4	$4\alpha^{3/4}$	$\alpha^{1/4}$

A.2 Supplementary material Chapter 4

Supplementary material *Section 4.1*

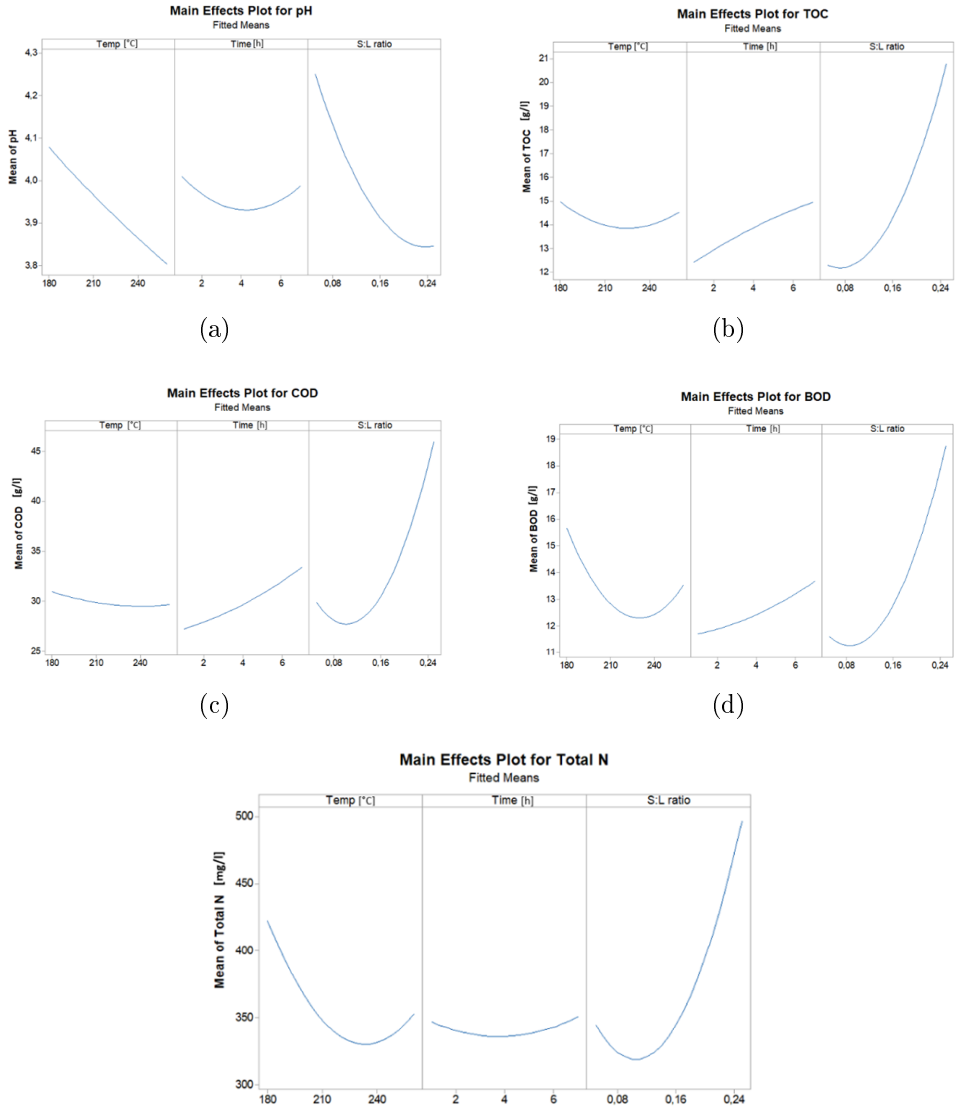

(a) (b) (c) (d) (e)

Figure A.1: *Effects of the HTC operating parameters on the spent liquor characteristics*

Table A.2: *ANOVA of response surface quadratic models.*

Source	F-value	p-value
MY [%]		
Model	47.61	<0.0001
A	360.26	<0.0001
B	12.85	0.016
C	46.99	0.001
A^2	0.28	0.622
B^2	0.74	0.430
C^2	1.13	0.337
AB	2.07	0.209
AC	1.84	0.233
BC	2.63	0.166
Lack of fit	2.62	0.289
R^2=0.9885, R^2_{adj}=0.9677, R^2_{pred}=0.8477		
EDY		
Model	134.72	<0.0001
A	1035.54	<0.0001
B	143.81	<0.0001
C	10.42	0.023
A^2	11.65	0.019
B^2	0.28	0.620
C^2	4.25	0.094
AB	1.64	0.256
AC	0.02	0.991
BC	3.57	0.118
Lack of fit	16.72	0.057
R^2=0.9959, R^2_{adj}=0.9885, R^2_{pred}=0.9365		
FR		
Model	27.81	0.001
A	213.66	<0.0001
B	30.55	0.003
C	0.01	0.998
A^2	0.69	0.443
B^2	1.29	0.308
C^2	0.24	0.643
AB	0.74	0.430
AC	0.07	0.808
BC	2.87	0.151
Lack of fit	8.86	0.103
R^2=0.9804, R^2_{adj}=0.9452, R^2_{pred}=0.8809		
PEY [$\mathbf{mg_{GAE}/g}$]		
Model	33.34	0.001
A	66.44	<0.0001
B	0.07	0.798
C	175.16	<0.0001
A^2	0.02	0.892
B^2	0.17	0.701
C^2	57.16	0.001
AB	0.03	0.867
AC	0.64	0.459
BC	0.36	0.576
Lack of fit	2.91	0.266
R^2=0.9836, R^2_{adj} 0.9541, R^2_{pred}=0.8898		

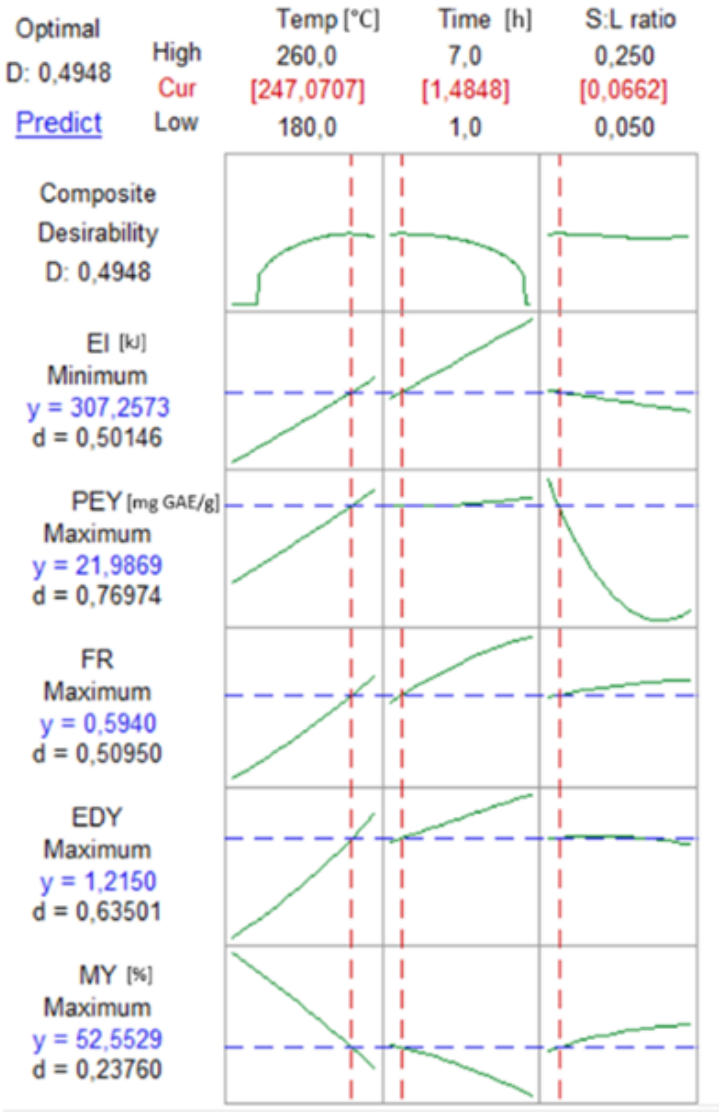

Figure A.2: *RSM optimizer plot of (MY) Hydrochar Yield; (EDY) Energy Densification Yield; (FR) Fuel Ratio; (PEY) Phenols Extraction Yield; (EI) Energy Input.*

Supplementary material *Section 4.2*

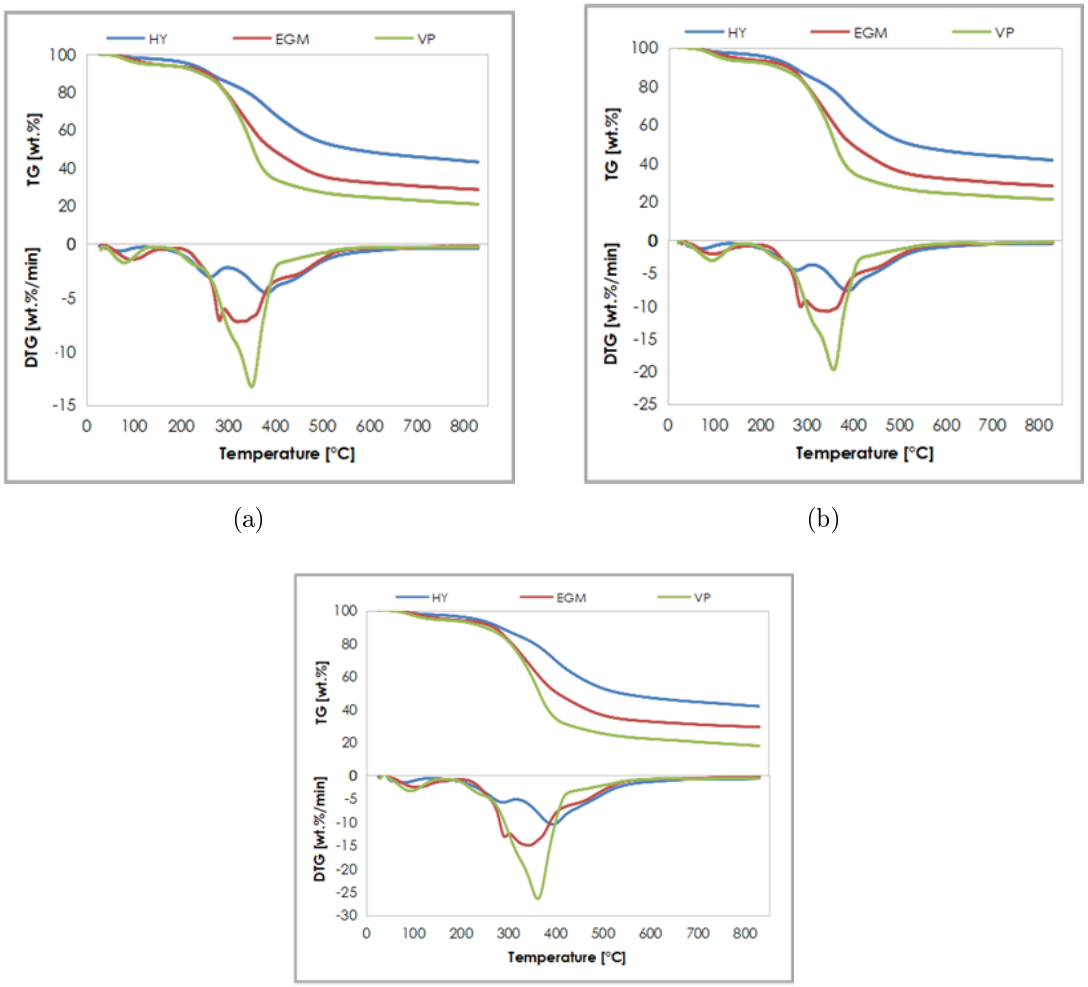

(a) (b)

(c)

Figure A.3: *Thermal degradation profiles of HY, EGM, and VP under N_2 atmosphere with a heating rate of a) 20°C/min, b) 30°C/min, and c) 40°C/min.*

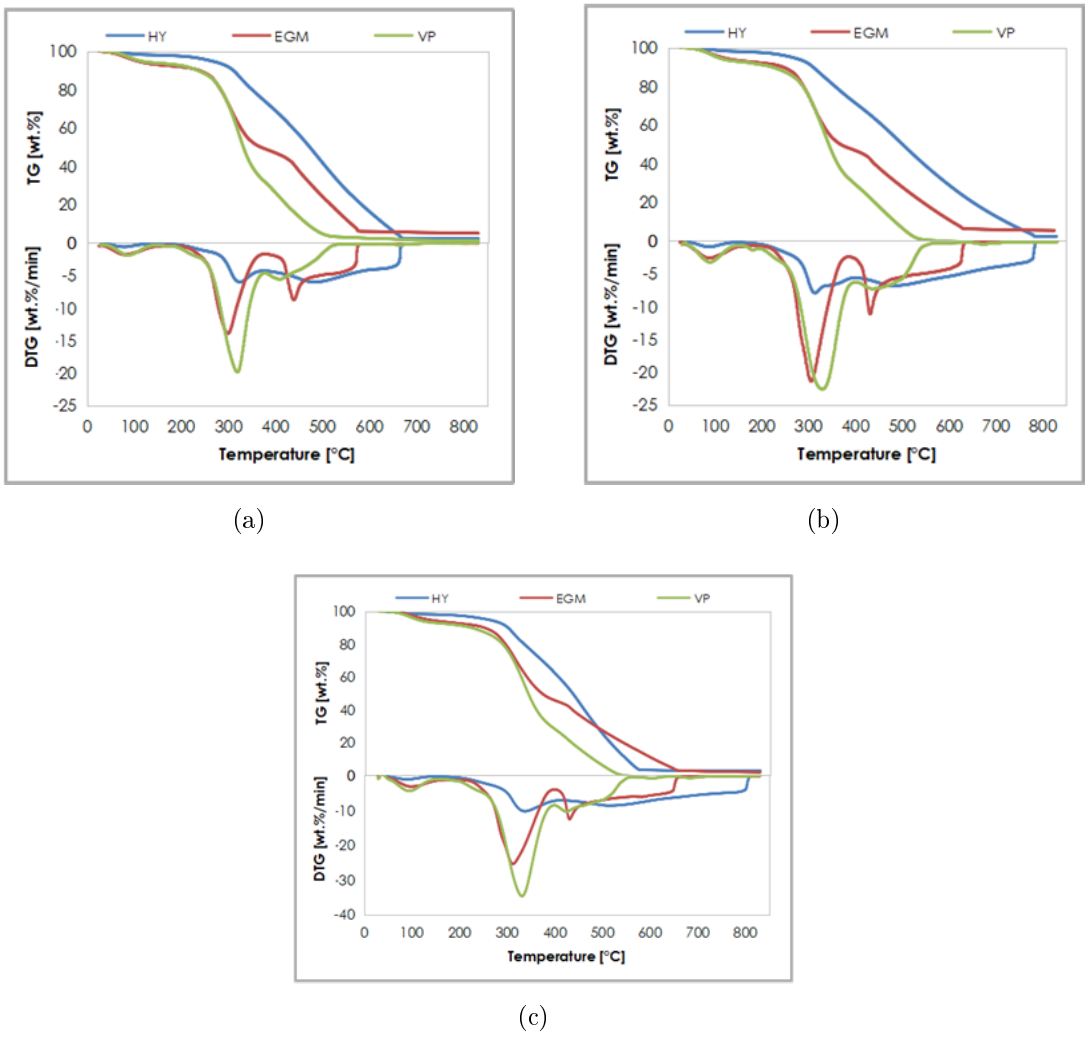

Figure A.4: *Thermal degradation profiles of HY, EGM, and VP under air atmosphere with a heating rate of a) 20°C/min, b) 30°C/min, and c) 40°C/min.*

Table A.3: *Apparent activation energy of HY, EGM, and VP during pyrolysis obtained by STK method.*

Sample	α	$\mathbf{E_a}$ **[kJ/mol]**	$\mathbf{R^2}$	$\mathbf{E_a}$ **[kJ/mol]**	$\mathbf{R^2}$
HY		*Stage I (114–310°C)*		*Stage II (310–728°C)*	
	0.1	81.55	0.990	122.34	0.996
	0.2	83.21	0.995	144.86	0.996
	0.3	82.80	0.996	162.29	0.996
	0.4	80.05	0.995	177.23	0.987
	0.5	79.38	0.996	191.19	0.974
	0.6	79.18	0.996	194.25	0.971
	0.7	80.08	0.996	180.39	0.967
	0.8	84.05	0.995	157.18	0.971
	0.9	89.39	0.995	112.03	0.968
	Avg.	82.19		160.19	
EGM		*Stage I (154–291°C)*		*Stage II (291–649°C)*	
	0.1	154.52	0.967	177.34	0.997
	0.2	160.60	0.984	180.68	0.998
	0.3	169.66	0.994	187.21	0.998
	0.4	176.52	0.997	188.82	0.998
	0.5	182.79	0.998	187.66	0.996
	0.6	176.92	0.997	198.15	0.993
	0.7	174.97	0.998	219.06	0.986
	0.8	172.30	0.998	232.45	0.977
	0.9	170.08	0.998	206.16	0.961
	Avg.	170.93		197.50	
VP		*Stage (123–657°C)*			
	0.1	163.72	0.969		
	0.2	164.80	0.967		
	0.3	161.70	0.971		
	0.4	161.81	0.979		
	0.5	163.09	0.989		
	0.6	162.76	0.990		
	0.7	163.29	0.985		
	0.8	153.76	0.986		
	0.9	105.96	0.998		
	Avg.	155.66			

Table A.4: *Apparent activation energy of HY, EGM, and VP during pyrolysis obtained by OFW method.*

Sample	α	$\mathbf{E_a}$ **[kJ/mol]**	$\mathbf{R^2}$	$\mathbf{E_a}$ **[kJ/mol]**	$\mathbf{R^2}$
HY		*Stage I (114–310°C)*		*Stage II (310–728°C)*	
	0.1	84.52	0.991	125.58	0.997
	0.2	86.53	0.996	147.37	0.997
	0.3	86.40	0.996	164.24	0.996
	0.4	83.98	0.996	178.71	0.988
	0.5	83.50	0.997	192.29	0.977
	0.6	83.45	0.997	195.51	0.974
	0.7	84.44	0.997	182.69	0.971
	0.8	88.34	0.996	161.08	0.975
	0.9	93.58	0.996	118.96	0.974
	Avg.	86.08		162.94	
EGM		*Stage I (154–291°C)*		*Stage II (291–649°C)*	
	0.1	154.49	0.970	177.57	0.999
	0.2	160.62	0.985	180.96	0.999
	0.3	169.43	0.995	187.39	0.999
	0.4	176.12	0.998	189.13	0.999
	0.5	182.18	0.999	188.24	0.997
	0.6	176.68	0.997	198.51	0.994
	0.7	174.89	0.999	218.83	0.987
	0.8	172.41	0.998	232.06	0.979
	0.9	170.36	0.999	207.68	0.965
	Avg.	170.80		197.82	
VP		*Stage (123–657°C)*			
	0.1	163.98	0.972		
	0.2	165.46	0.970		
	0.3	162.78	0.974		
	0.4	163.12	0.981		
	0.5	164.53	0.990		
	0.6	164.38	0.992		
	0.7	165.06	0.986		
	0.8	156.25	0.988		
	0.9	111.46	0.999		
	Avg.	157.45			

Table A.5: *Apparent activation energy of HY, EGM, and VP during pyrolysis obtained by KAS method.*

Sample	α	$\mathbf{E_a}$ **[kJ/mol]**	$\mathbf{R^2}$	$\mathbf{E_a}$ **[kJ/mol]**	$\mathbf{R^2}$
HY		*Stage I (114–310°C)*		*Stage II (310–728°C)*	
	0.1	81.31	0.990	122.03	0.996
	0.2	82.96	0.995	144.56	0.996
	0.3	82.53	0.996	161.99	0.996
	0.4	79.77	0.995	176.93	0.987
	0.5	79.10	0.996	190.89	0.974
	0.6	78.89	0.996	193.94	0.971
	0.7	79.78	0.996	180.05	0.967
	0.8	83.75	0.995	156.80	0.971
	0.9	89.09	0.995	111.58	0.968
	Avg.	81.91		159.86	
EGM		*Stage I (154–291°C)*		*Stage II (291–649°C)*	
	0.1	154.31	0.967	177.10	0.999
	0.2	160.39	0.984	180.43	0.999
	0.3	169.44	0.994	186.95	0.999
	0.4	176.31	0.997	188.55	0.999
	0.5	182.57	0.998	187.38	0.996
	0.6	176.69	0.997	197.87	0.993
	0.7	174.74	0.999	218.78	0.986
	0.8	172.07	0.998	232.16	0.977
	0.9	169.84	0.998	205.82	0.961
	Avg.	170.71		197.23	
VP		*Stage (123–657°C)*			
	0.1	163.49	0.969		
	0.2	164.56	0.967		
	0.3	161.44	0.971		
	0.4	161.54	0.979		
	0.5	162.81	0.989		
	0.6	162.48	0.990		
	0.7	163.00	0.984		
	0.8	153.45	0.986		
	0.9	105.58	0.999		
	Avg.	155.37			

Table A.6: *Apparent activation energy of HY, EGM, and VP during combustion obtained by STK method.*

Sample	α	$\mathbf{E_a}$ **[kJ/mol]**	$\mathbf{R^2}$	$\mathbf{E_a}$ **[kJ/mol]**	$\mathbf{R^2}$
HY		*Stage I (135–374°C)*		*Stage II (374–830°C)*	
	0.1	130.70	0.969	63.52	0.977
	0.2	152.56	0.983	60.68	0.983
	0.3	151.64	0.972	57.56	0.986
	0.4	134.17	0.966	52.52	0.986
	0.5	119.24	0.970	46.81	0.983
	0.6	104.00	0.978	41.77	0.981
	0.7	92.38	0.976	37.45	0.978
	0.8	83.48	0.971	33.49	0.974
	0.9	75.15	0.967	29.90	0.965
	Avg.	115.92		47.08	
EGM		*Stage I (157–377°C)*		*Stage II (377–708°C)*	
	0.1	162.83	0.990	170.08	0.968
	0.2	171.87	0.990	171.65	0.970
	0.3	158.15	0.973	170.19	0.965
	0.4	159.76	0.975	134.48	0.987
	0.5	154.93	0.977	103.75	0.996
	0.6	153.63	0.968	85.34	1.000
	0.7	152.34	0.970	72.29	0.999
	0.8	151.22	0.965	63.10	0.997
	0.9	162.76	0.967	55.27	0.994
	Avg.	158.61		114.02	
VP		*Stage I (156–377°C)*		*Stage II (377–650°C)*	
	0.1	155.73	0.981	128.89	0.970
	0.2	160.42	0.965	126.66	0.968
	0.3	149.32	0.985	125.71	0.978
	0.4	150.52	0.984	115.63	0.974
	0.5	151.90	0.981	98.79	0.967
	0.6	152.79	0.976	86.98	0.967
	0.7	148.68	0.967	82.92	0.971
	0.8	141.04	0.969	82.44	0.975
	0.9	133.02	0.980	83.57	0.983
	Avg.	149.27		103.51	

Table A.7: *Apparent activation energy of HY, EGM, and VP during combustion obtained by OFW method.*

Sample	α	$\mathbf{E_a}$ **[kJ/mol]**	$\mathbf{R^2}$	$\mathbf{E_a}$ **[kJ/mol]**	$\mathbf{R^2}$
HY		*Stage I (135–374°C)*		*Stage II (374–830°C)*	
	0.1	132.37	0.973	70.89	0.983
	0.2	153.72	0.985	68.64	0.989
	0.3	153.12	0.975	66.06	0.991
	0.4	136.67	0.971	61.64	0.991
	0.5	122.62	0.974	56.58	0.990
	0.6	108.26	0.981	52.18	0.989
	0.7	97.36	0.980	48.51	0.989
	0.8	89.06	0.977	45.23	0.988
	0.9	81.30	0.975	42.36	0.985
	Avg.	119.39		56.90	
EGM		*Stage I (157–377°C)*		*Stage II (377–708°C)*	
	0.1	162.93	0.991	172.33	0.972
	0.2	171.87	0.991	174.10	0.974
	0.3	158.98	0.976	172.96	0.969
	0.4	160.68	0.977	139.24	0.989
	0.5	156.23	0.980	110.26	0.997
	0.6	155.14	0.972	93.03	1.000
	0.7	154.08	0.974	80.91	1.000
	0.8	153.21	0.969	72.47	0.998
	0.9	164.42	0.971	65.34	0.997
	Avg.	159.73		120.07	
VP		*Stage I (156–377°C)*		*Stage II (377–650°C)*	
	0.1	156.25	0.983	132.79	0.974
	0.2	161.06	0.969	130.86	0.973
	0.3	150.73	0.986	130.11	0.982
	0.4	152.03	0.986	120.69	0.979
	0.5	153.50	0.983	104.83	0.974
	0.6	154.49	0.978	93.74	0.974
	0.7	150.72	0.970	90.07	0.978
	0.8	143.60	0.973	89.83	0.981
	0.9	136.18	0.983	91.16	0.987
	Avg.	150.95		109.34	

Table A.8: *Apparent activation energy of HY, EGM, and VP during combustion obtained by KAS method.*

Sample	α	$\mathbf{E_a}$ **[kJ/mol]**	$\mathbf{R^2}$	$\mathbf{E_a}$ **[kJ/mol]**	$\mathbf{R^2}$
HY		*Stage I (135–374°C)*		*Stage II (374–830°C)*	
	0.1	132.37	0.973	70.89	0.983
	0.2	153.72	0.985	68.64	0.989
	0.3	153.12	0.975	66.06	0.991
	0.4	136.67	0.971	61.64	0.991
	0.5	122.62	0.974	56.58	0.990
	0.6	108.26	0.981	52.18	0.989
	0.7	97.36	0.980	48.51	0.989
	0.8	89.06	0.977	45.23	0.988
	0.9	81.30	0.975	42.36	0.985
	Avg.	119.39		56.90	
EGM		*Stage I (157–377°C)*		*Stage II (377–708°C)*	
	0.1	162.93	0.991	172.33	0.972
	0.2	171.87	0.991	174.10	0.974
	0.3	158.98	0.976	172.96	0.969
	0.4	160.68	0.977	139.24	0.989
	0.5	156.23	0.980	110.26	0.997
	0.6	155.14	0.972	93.03	1.000
	0.7	154.08	0.974	80.91	1.000
	0.8	153.21	0.969	72.47	0.998
	0.9	164.42	0.971	65.34	0.997
	Avg.	159.73		120.07	
VP		*Stage I (156–377°C)*		*Stage II (377–650°C)*	
	0.1	156.25	0.983	132.79	0.974
	0.2	161.06	0.969	130.86	0.973
	0.3	150.73	0.986	130.11	0.982
	0.4	152.03	0.986	120.69	0.979
	0.5	153.50	0.983	104.83	0.974
	0.6	154.49	0.978	93.74	0.974
	0.7	150.72	0.970	90.07	0.978
	0.8	143.60	0.973	89.83	0.981
	0.9	136.18	0.983	91.16	0.987
	Avg.	150.95		109.34	

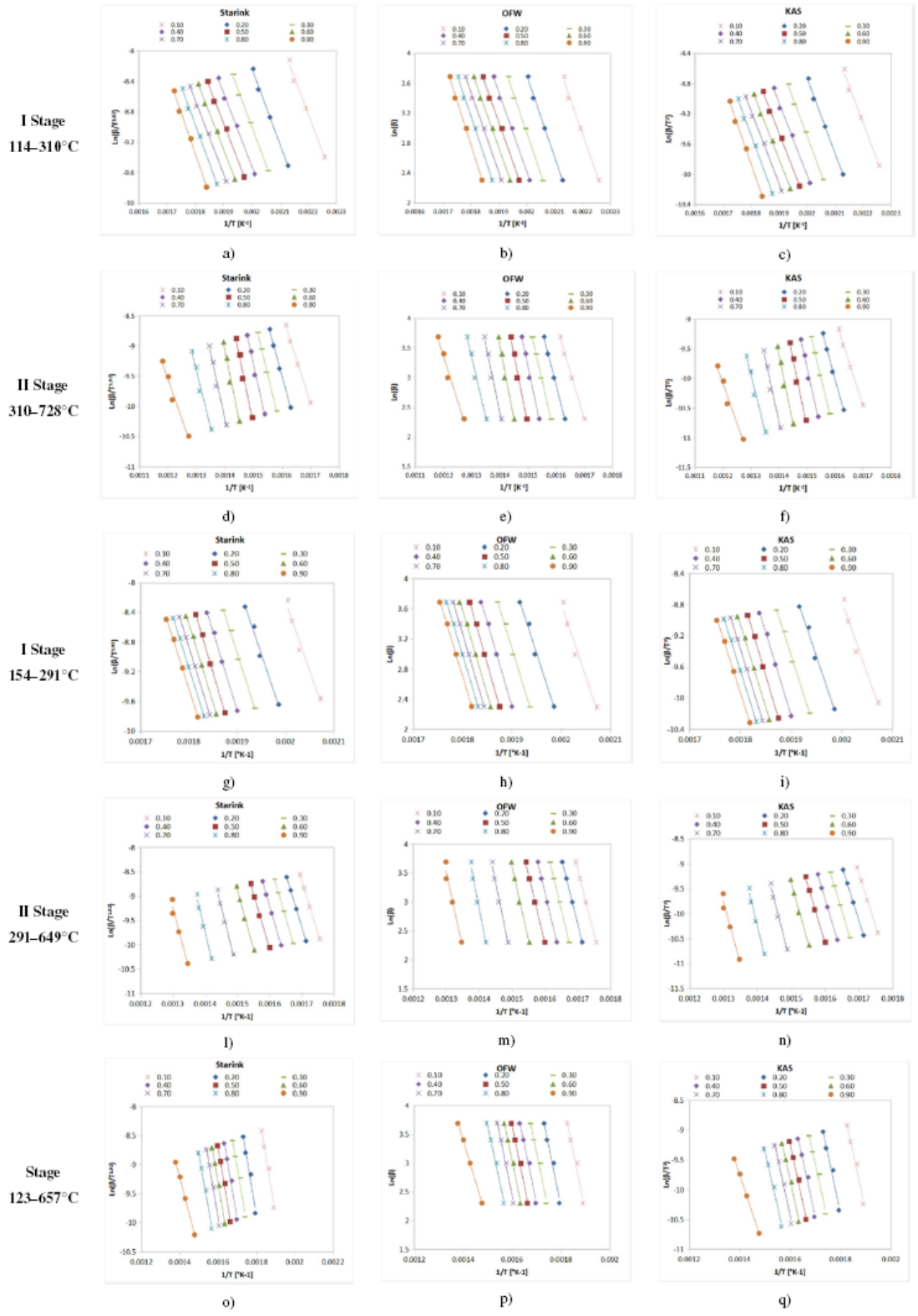

Figure A.5: *Kinetic fitting results in N_2 atmosphere based on STK, OFW, and KAS methods for HY a–f; EGM g–n; VP o–q*

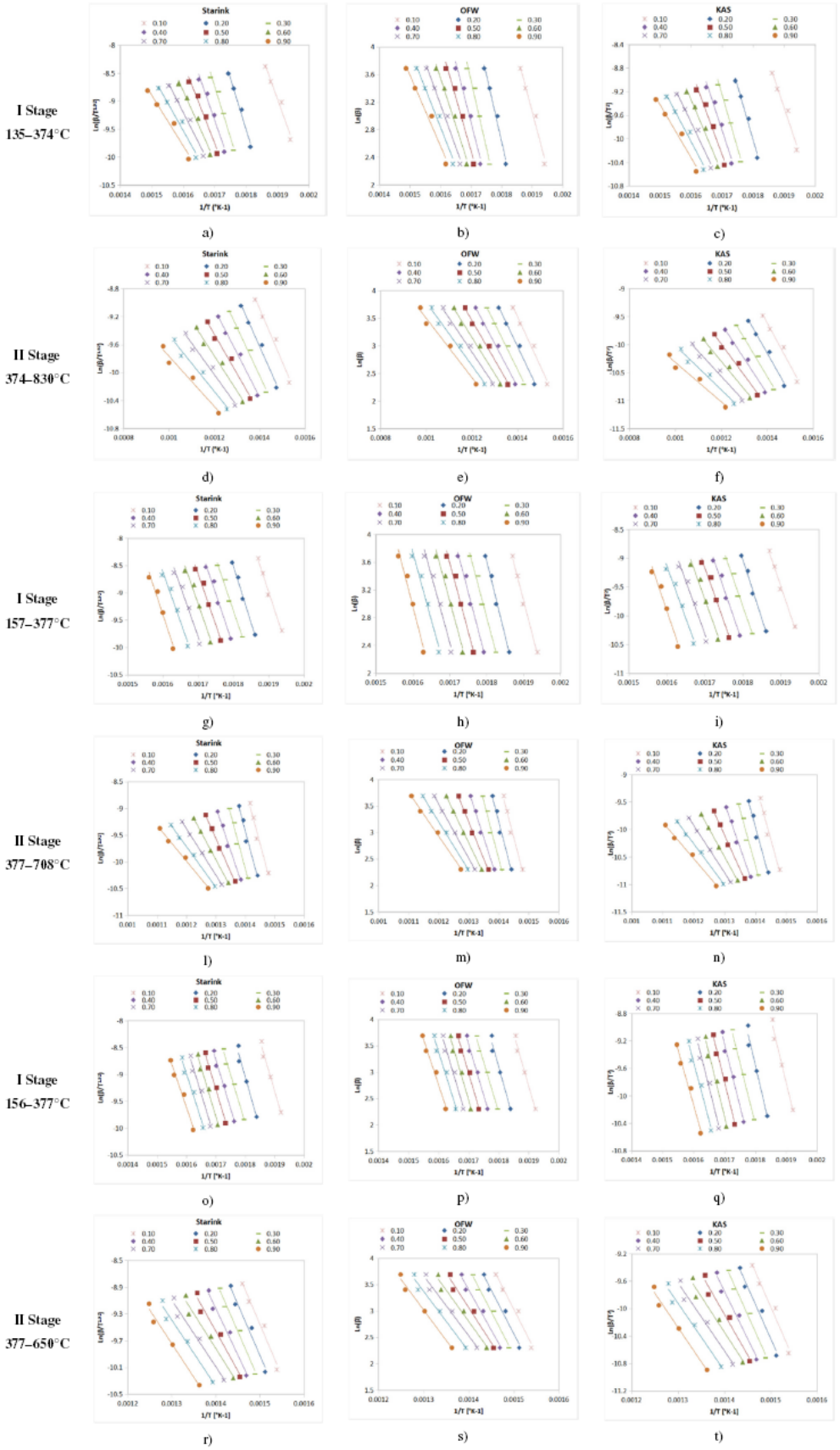

Figure A.6: *Kinetic fitting results in air atmosphere based on STK, OFW, and KAS methods for HY a–f; EGM g–n; VP o–t*

Table A.9: *Pre-exponential values from ECE method for HY, EGM, and VP at each extent of conversion α during pyrolysis.*

β	10°C/min	20°C/min	30°C/min	40°C/min	10°C/min	20°C/min	30°C/min	40°C/min
α	A $[s^{-1}]$	A $[s^{-1}]$	A $[s^{-1}]$	A $[s^{-1}]$	A $[s^{-1}]$	A $[s^{-1}]$	A $[s^{-1}]$	A $[s^{-1}]$
HY	***Stage I (114–310°C)***				***Stage II (310–728°C)***			
0.1	1.09E+06	1.12E+06	1.03E+06	1.13E+06	2.90E+07	3.58E+07	4.42E+07	4.89E+07
0.2	1.69E+06	1.72E+06	1.57E+06	1.70E+06	2.65E+09	2.95E+09	3.45E+09	3.69E+09
0.3	1.52E+06	1.54E+06	1.41E+06	1.54E+06	8.74E+10	8.98E+10	1.01E+11	1.05E+11
0.4	7.38E+05	7.66E+05	7.11E+05	7.78E+05	1.75E+12	1.68E+12	1.81E+12	1.85E+12
0.5	6.19E+05	6.46E+05	6.02E+05	6.59E+05	2.88E+13	2.58E+13	2.70E+13	2.70E+13
0.6	5.88E+05	6.14E+05	5.73E+05	6.28E+05	5.31E+13	4.70E+13	4.88E+13	4.86E+13
0.7	7.44E+05	7.72E+05	7.17E+05	7.84E+05	3.30E+12	3.11E+12	3.34E+12	3.40E+12
0.8	2.11E+06	2.12E+06	1.93E+06	2.09E+06	3.14E+10	3.30E+10	3.74E+10	3.94E+10
0.9	8.59E+06	8.29E+06	7.33E+06	7.88E+06	3.67E+06	4.76E+06	6.01E+06	6.75E+06
Avg.	1.97E+06	1.95E+06	1.76E+06	1.91E+06	9.68E+12	8.64E+12	9.01E+12	9.01E+12
a	0.2628	0.2550	0.2498	0.2479	0.2006	0.1959	0.1935	0.1920
b	-3.4275	-2.7681	-2.4279	-2.1886	-3.2597	-2.4766	-1.9749	-1.6956
EGM	***Stage I (154–291°C)***				***Stage II (291–649°C)***			
0.1	1.31E+13	1.26E+13	1.31E+13	1.39E+13	1.61E+13	1.62E+13	1.69E+13	1.69E+13
0.2	5.77E+13	5.38E+13	5.52E+13	5.82E+13	3.26E+13	3.23E+13	3.34E+13	3.34E+13
0.3	5.24E+14	4.66E+14	4.71E+14	4.90E+14	1.29E+14	1.24E+14	1.27E+14	1.25E+14
0.4	2.79E+15	2.40E+15	2.40E+15	2.47E+15	1.80E+14	1.73E+14	1.76E+14	1.74E+14
0.5	1.28E+16	1.07E+16	1.06E+16	1.08E+16	1.41E+14	1.36E+14	1.39E+14	1.37E+14
0.6	3.07E+15	2.63E+15	2.63E+15	2.71E+15	1.28E+15	1.19E+15	1.19E+15	1.15E+15
0.7	1.91E+15	1.65E+15	1.66E+15	1.71E+15	1.05E+17	8.95E+16	8.57E+16	8.04E+16
0.8	9.99E+14	8.77E+14	8.83E+14	9.15E+14	1.75E+18	1.42E+18	1.33E+18	1.22E+18
0.9	5.81E+14	5.16E+14	5.21E+14	5.42E+14	6.94E+15	6.24E+15	6.13E+15	5.87E+15
Avg.	2.53E+15	2.14E+15	2.13E+15	2.19E+15	2.07E+17	1.69E+17	1.58E+17	1.45E+17
a	0.2436	0.2386	0.2369	0.2354	0.2104	0.2066	0.2046	0.2029
b	-3.3483	-2.6058	-2.3045	-2.0179	-2.8007	-2.1293	-1.7256	-1.4282
VP	***Stage (123–657°C)***							
0.1	3.31E+12	4.23E+12	3.87E+12	3.93E+12				
0.2	4.20E+12	5.36E+12	4.88E+12	4.95E+12				
0.3	2.12E+12	2.72E+12	2.50E+12	2.55E+12				
0.4	2.17E+12	2.79E+12	2.56E+12	2.61E+12				
0.5	2.88E+12	3.69E+12	3.38E+12	3.43E+12				
0.6	2.67E+12	3.43E+12	3.14E+12	3.20E+12				
0.7	3.00E+12	3.85E+12	3.52E+12	3.58E+12				
0.8	3.67E+11	4.81E+11	4.55E+11	4.68E+11				
0.9	9.56E+06	1.41E+07	1.57E+07	1.73E+07				
Avg.	2.30E+12	2.95E+12	2.70E+12	2.75E+12				
a	0.2208	0.2183	0.2150	0.2135				
b	-3.2247	-2.5751	-2.1157	-1.8658				

Table A.10: *Pre-exponential values from ECE method for HY, EGM, and VP at each extent of conversion α during combustion.*

β	10°C/min	20°C/min	30°C/min	40°C/min	10°C/min	20°C/min	30°C/min	40°C/min
α	A $[s^{-1}]$	A $[s^{-1}]$	A $[s^{-1}]$	A $[s^{-1}]$	A $[s^{-1}]$	A $[s^{-1}]$	A $[s^{-1}]$	A $[s^{-1}]$
HY		***Stage I (135–374°C)***				***Stage II (374–830°C)***		
0.1	2.95E+09	3.53E+09	3.55E+09	3.25E+09	5.16E+01	5.48E+01	4.68E+01	4.55E+01
0.2	4.06E+11	4.50E+11	4.19E+11	3.65E+11	3.09E+01	3.36E+01	2.92E+01	2.87E+01
0.3	3.30E+11	3.67E+11	3.43E+11	2.99E+11	1.76E+01	1.95E+01	1.74E+01	1.73E+01
0.4	6.44E+09	7.62E+09	7.58E+09	6.89E+09	7.12E+00	8.18E+00	7.53E+00	7.65E+00
0.5	2.23E+08	2.78E+08	2.92E+08	2.74E+08	2.55E+00	3.05E+00	2.92E+00	3.03E+00
0.6	7.18E+06	9.45E+06	1.05E+07	1.02E+07	1.03E+00	1.27E+00	1.26E+00	1.34E+00
0.7	5.24E+05	7.18E+05	8.31E+05	8.31E+05	4.72E-01	6.04E-01	6.18E-01	6.65E-01
0.8	7.05E+04	9.97E+04	1.19E+05	1.22E+05	2.31E-01	3.04E-01	3.20E-01	3.50E-01
0.9	1.08E+04	1.57E+04	1.93E+04	2.01E+04	1.21E-01	1.63E-01	1.76E-01	1.95E-01
Avg.	8.28E+10	9.21E+10	8.59E+10	7.49E+10	1.24E+01	1.35E+01	1.18E+01	1.16E+01
a	0.2254	0.2218	0.2182	0.2159	0.1801	0.1730	0.1660	0.1621
b	-3.5558	-2.9153	-2.4345	-2.2226	-3.4003	-2.8873	-2.6044	-2.3833
EGM		***Stage I (157–377°C)***				***Stage II (377–708°C)***		
0.1	1.07E+13	9.83E+12	1.35E+13	1.00E+13	7.00E+09	5.45E+09	7.05E+09	7.05E+09
0.2	8.43E+13	7.42E+13	1.01E+14	7.32E+13	9.20E+09	7.12E+09	9.20E+09	9.18E+09
0.3	3.68E+12	3.45E+12	4.78E+12	3.57E+12	7.13E+09	5.55E+09	7.18E+09	7.18E+09
0.4	5.32E+12	4.95E+12	6.84E+12	5.10E+12	1.36E+07	1.25E+07	1.65E+07	1.74E+07
0.5	1.77E+12	1.68E+12	2.34E+12	1.76E+12	6.22E+04	6.57E+04	8.83E+04	9.79E+04
0.6	1.31E+12	1.26E+12	1.75E+12	1.32E+12	2.47E+03	2.84E+03	3.85E+03	4.40E+03
0.7	9.79E+11	9.43E+11	1.32E+12	9.96E+11	2.50E+02	3.05E+02	4.18E+02	4.87E+02
0.8	7.58E+11	7.34E+11	1.03E+12	7.79E+11	5.00E+01	6.36E+01	8.75E+01	1.03E+02
0.9	1.05E+13	9.68E+12	1.33E+13	9.86E+12	1.27E+01	1.67E+01	2.31E+01	2.76E+01
Avg.	1.33E+13	1.19E+13	1.62E+13	1.18E+13	2.59E+09	2.01E+09	2.61E+09	2.60E+09
a	0.2281	0.2234	0.2220	0.2199	0.1753	0.1707	0.1702	0.1686
b	-3.0382	-2.3706	-1.8108	-1.7841	-3.0574	-2.5263	-2.1717	-1.9066
VP		***Stage I (156–377°C)***				***Stage II (377–650°C)***		
0.1	1.11E+12	2.01E+12	2.80E+12	2.10E+12	2.62E+07	4.81E+06	6.37E+06	6.79E+06
0.2	3.19E+12	5.73E+12	7.92E+12	5.89E+12	1.74E+07	3.29E+06	4.36E+06	4.66E+06
0.3	2.62E+11	4.80E+11	6.75E+11	5.13E+11	1.46E+07	2.79E+06	3.71E+06	3.97E+06
0.4	3.43E+11	6.28E+11	8.80E+11	6.68E+11	2.30E+06	5.00E+05	6.68E+05	7.27E+05
0.5	4.68E+11	8.55E+11	1.20E+12	9.04E+11	1.05E+05	2.82E+04	3.80E+04	4.25E+04
0.6	5.72E+11	1.04E+12	1.46E+12	1.10E+12	1.20E+04	3.75E+03	5.09E+03	5.79E+03
0.7	2.27E+11	4.17E+11	5.86E+11	4.46E+11	5.70E+03	1.87E+03	2.55E+03	2.92E+03
0.8	4.05E+10	7.56E+10	1.07E+11	8.30E+10	5.22E+03	1.73E+03	2.35E+03	2.69E+03
0.9	6.64E+09	1.26E+10	1.81E+10	1.42E+10	6.43E+03	2.10E+03	2.85E+03	3.26E+03
Avg.	6.92E+11	1.25E+12	1.74E+12	1.30E+12	6.73E+06	1.27E+06	1.68E+06	1.80E+06
a	0.2255	0.2212	0.2181	0.2176	0.1834	0.1800	0.1757	0.1743
b	-3.2832	-2.5557	-2.1939	-2.0158	-2.4665	-1.9725	-1.8069	-1.4072

I Stage 114–310°C

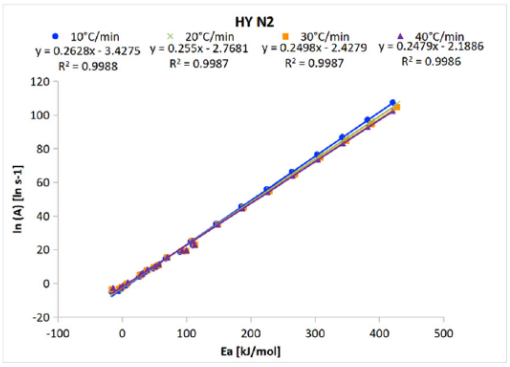

a)

II Stage 310–728°C

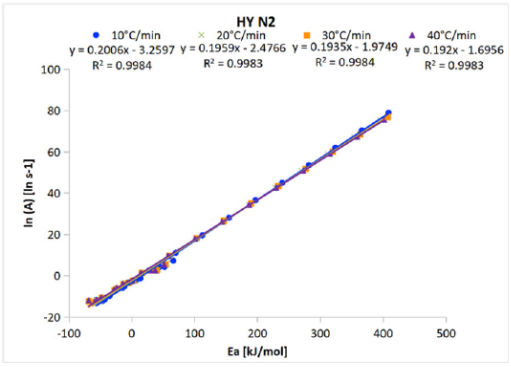

b)

I Stage 154–291°C

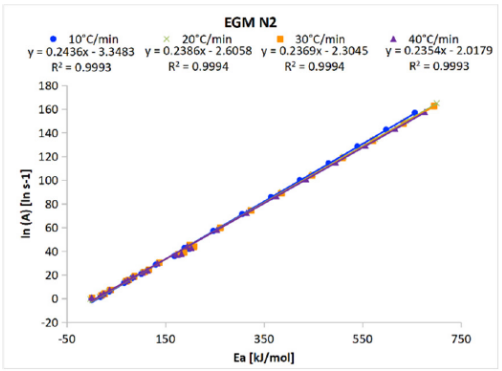

c)

II Stage 291–649°C

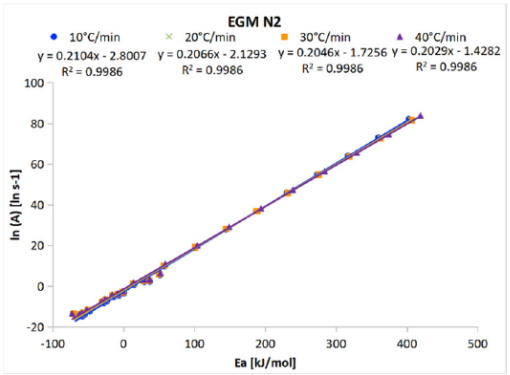

d)

Stage 123–657°C

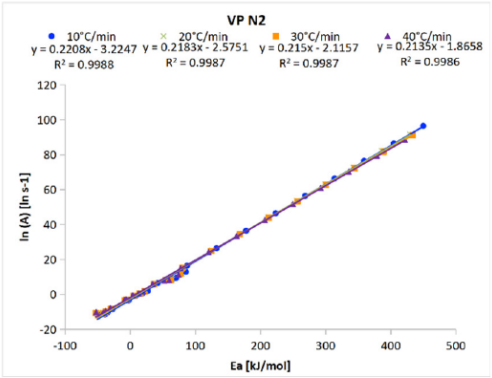

e)

Figure A.7: *Plots of E_i vs. ln(A) in N_2 atmosphere for HY a–b, EGM c–d, and VP e.*

I Stage 135–374°C

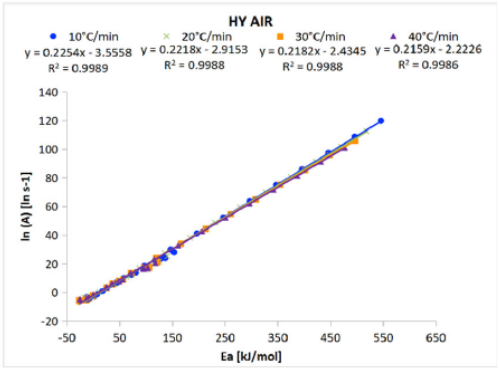

a)

II Stage 374–830°C

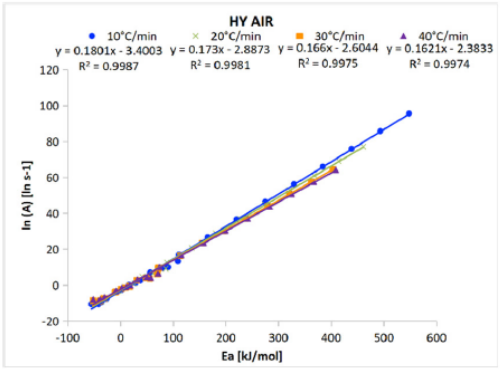

b)

I Stage 157–377°C

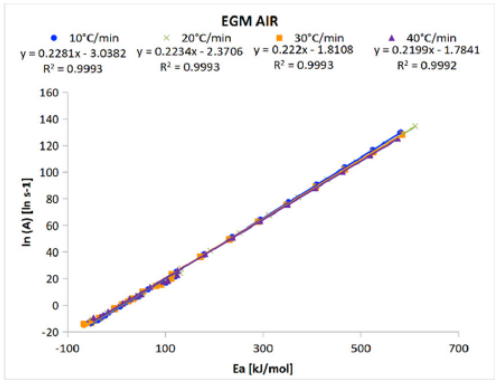

c)

II Stage 377–708°C

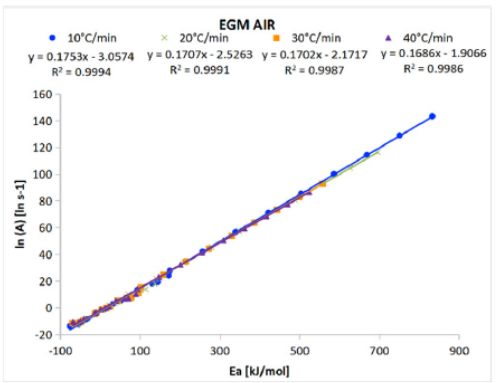

d)

I Stage 156–377°C

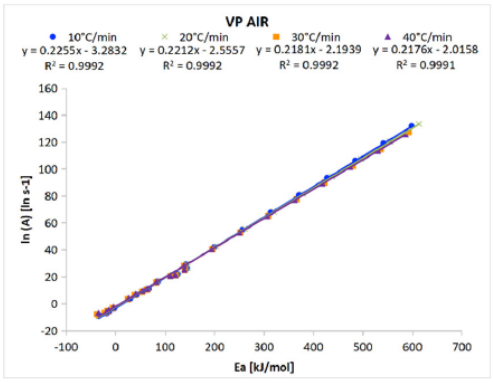

e)

II Stage 377–650°C

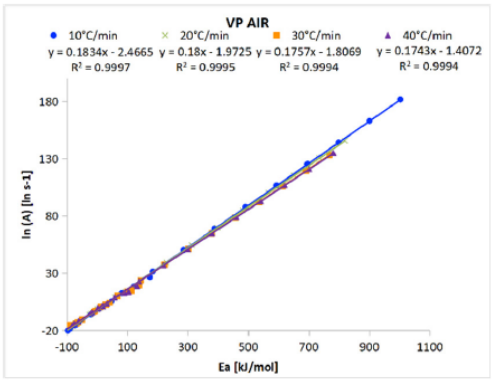

f)

Figure A.8: *Plots of E_i vs. ln(A) in air atmosphere for HY a–b, EGM c–d, and VP e–f.*

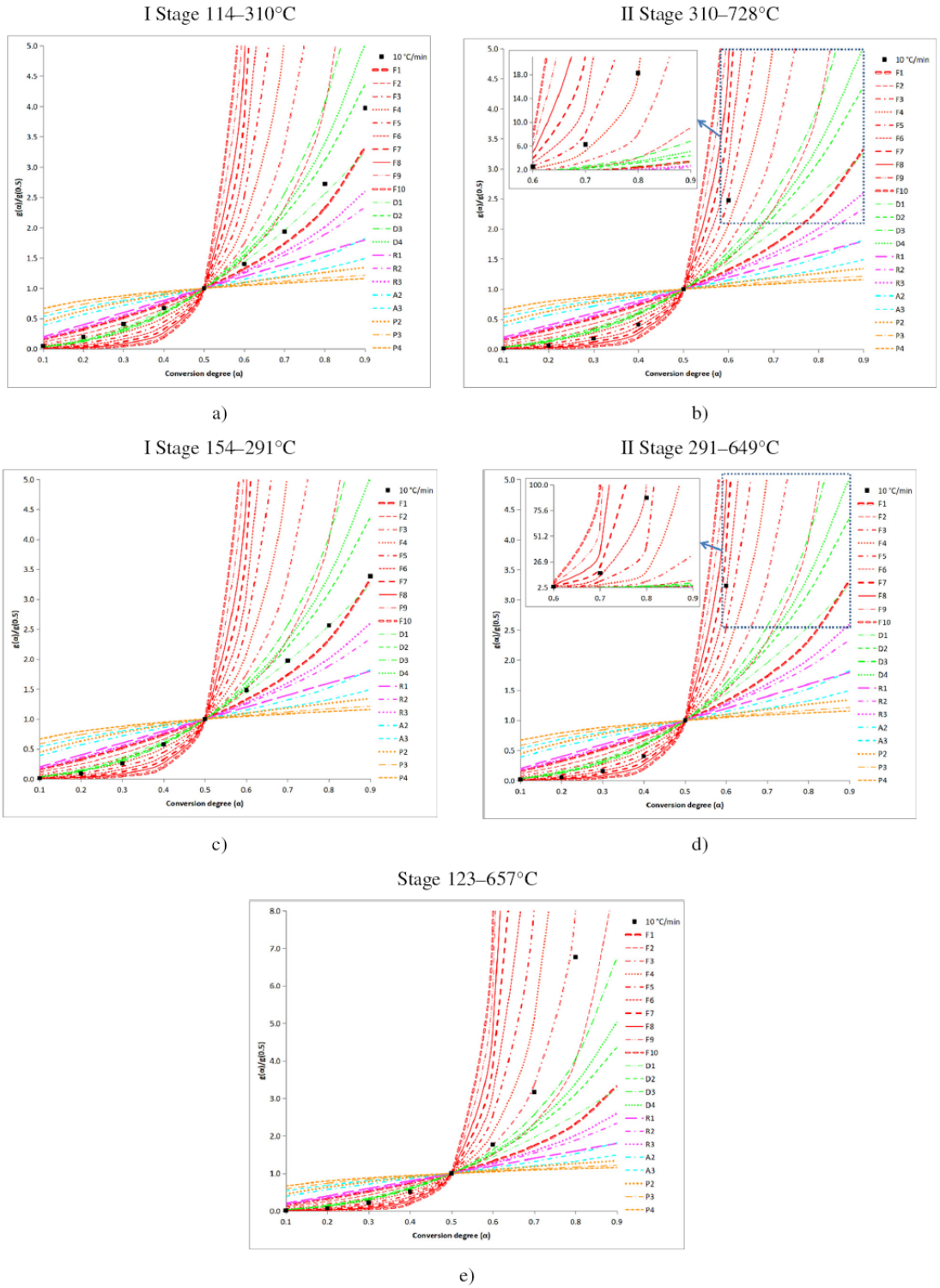

Figure A.9: *Theoretical and experimental master plots of HY a–b, EGM c–d, and VP e, during pyrolysis process.*

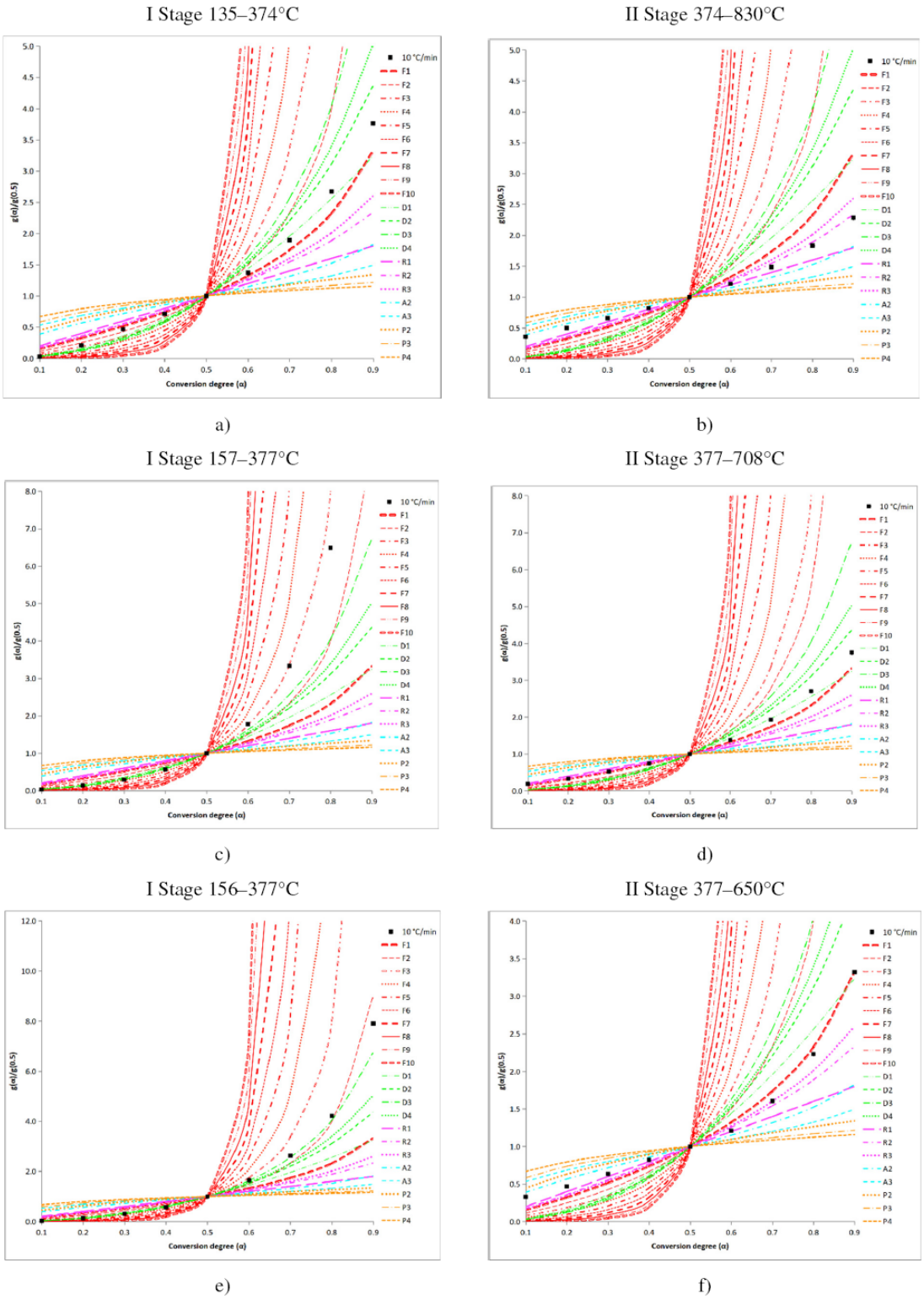

Figure A.10: *Theoretical and experimental master plots of HY a–b, EGM c–d, and VP e–f, during combustion process.*

Table A.11: *Thermodynamic parameters of HY, EGM, and VP during pyrolysis.*

	ΔH (kJ/mol)				**ΔG (kJ/mol)**				**ΔS (J/mol K)**			
α	10°C/min	20°C/min	30°C/min	40°C/min	10°C/min	20°C/min	30°C/min	40°C/min	10°C/min	20°C/min	30°C/min	40°C/min
HY Stage I (114–310°C)												
0.1	77.87	77.75	77.68	77.65	112.64	115.07	117.47	118.73	-142.74	-142.50	-143.12	-142.28
0.2	79.31	79.19	79.10	79.07	113.42	115.81	118.17	119.41	-140.02	-139.86	-140.51	-139.71
0.3	78.76	78.63	78.54	78.50	113.23	115.62	117.99	119.24	-141.47	-141.26	-141.91	-141.09
0.4	75.91	75.78	75.68	75.63	111.94	114.40	116.83	118.13	-147.87	-147.49	-148.02	-147.16
0.5	75.17	75.03	74.92	74.87	111.63	114.10	116.55	117.86	-149.66	-149.22	-149.72	-148.86
0.6	74.90	74.76	74.65	74.59	111.54	114.01	116.47	117.78	-150.38	-149.92	-150.41	-149.55
0.7	75.73	75.58	75.47	75.42	111.96	114.41	116.85	118.14	-148.70	-148.30	-148.82	-147.97
0.8	79.61	79.47	79.36	79.31	113.81	116.18	118.52	119.75	-140.36	-140.19	-140.86	-140.04
0.9	84.87	84.73	84.62	84.57	116.31	118.56	120.78	121.91	-129.04	-129.18	-130.06	-129.30
Avg.	78.01	77.88	77.78	77.74	112.94	115.35	117.74	118.99	-143.36	-143.10	-143.72	-142.88
HY Stage II (310–728°C)												
0.1	117.45	117.31	117.23	117.19	160.46	161.34	161.39	161.70	-117.11	-115.52	-113.91	-113.11
0.2	139.76	139.63	139.56	139.52	169.19	169.88	169.87	170.07	-80.13	-79.37	-78.17	-77.63
0.3	157.03	156.91	156.85	156.80	175.94	176.49	176.43	176.55	-51.49	-51.39	-50.50	-50.17
0.4	171.83	171.70	171.66	171.60	181.73	182.16	182.05	182.10	-26.97	-27.44	-26.81	-26.67
0.5	185.64	185.50	185.47	185.42	187.15	187.46	187.30	187.29	-4.11	-5.12	-4.73	-4.76
0.6	188.52	188.38	188.34	188.29	188.33	188.61	188.45	188.43	0.52	-0.62	-0.28	-0.34
0.7	174.48	174.31	174.28	174.22	182.96	183.36	183.24	183.28	-23.09	-23.73	-23.11	-23.02
0.8	151.04	150.84	150.79	150.71	173.97	174.56	174.50	174.65	-62.43	-62.23	-61.17	-60.83
0.9	105.50	105.19	105.11	105.00	156.47	157.44	157.52	157.87	-138.76	-137.07	-135.17	-134.35
Avg.	154.58	154.42	154.37	154.31	175.13	175.70	175.64	175.77	-55.95	-55.83	-54.87	-54.54
EGM Stage I (154–291°C)												
0.1	150.51	150.42	150.39	150.37	152.62	152.73	152.65	152.51	-7.78	-8.21	-7.89	-7.32
0.2	156.42	156.33	156.31	156.27	155.36	155.42	155.30	155.11	3.90	3.25	3.52	3.94
0.3	165.36	165.28	165.25	165.21	159.42	159.41	159.23	158.98	21.85	20.85	20.97	21.29
0.4	172.15	172.08	172.04	172.00	162.50	162.44	162.21	161.91	35.46	34.20	34.21	34.46
0.5	178.35	178.28	178.24	178.20	165.31	165.20	164.93	164.58	47.92	46.41	46.33	46.51
0.6	172.44	172.37	172.32	172.28	162.68	162.61	162.38	162.08	35.87	34.61	34.61	34.85
0.7	170.46	170.38	170.33	170.30	161.80	161.75	161.53	161.24	31.80	30.62	30.63	30.91
0.8	167.76	167.68	167.64	167.60	160.61	160.58	160.38	160.11	26.30	25.22	25.28	25.58
0.9	165.51	165.43	165.38	165.34	159.61	159.59	159.41	159.16	21.68	20.69	20.78	21.10
Avg.	166.55	166.47	166.43	166.40	159.99	159.97	159.78	159.52	24.11	23.07	23.16	23.48
EGM Stage II (291–649°C)												
0.1	172.60	172.52	172.47	172.43	175.00	174.98	174.89	174.88	-7.28	-7.71	-7.06	-7.14
0.2	175.83	175.74	175.69	175.65	176.42	176.49	176.28	176.29	-1.79	-2.33	-1.73	-1.86
0.3	182.24	182.15	182.10	182.06	179.19	179.43	179.00	179.04	9.27	8.51	9.02	8.82
0.4	183.74	183.64	183.59	183.55	179.87	180.15	179.67	179.72	11.74	10.91	11.41	11.18
0.5	182.46	182.35	182.30	182.27	179.38	179.63	179.19	179.23	9.36	8.52	9.07	8.86
0.6	192.79	192.68	192.63	192.60	183.84	184.36	183.56	183.65	27.23	26.03	26.45	26.10
0.7	213.47	213.36	213.31	213.29	192.72	193.78	192.27	192.46	63.10	61.22	61.33	60.72
0.8	226.60	226.48	226.42	226.41	198.41	199.81	197.84	198.11	85.71	83.38	83.30	82.52
0.9	199.99	199.86	199.77	199.76	187.24	187.97	186.90	187.03	38.76	37.17	37.51	37.13
Avg.	192.19	192.09	192.03	192.00	183.56	184.07	183.29	183.38	26.24	25.08	25.48	25.15
VP Stage (123–657°C)												
0.1	159.32	159.27	159.20	159.17	165.83	165.31	165.67	165.69	-19.33	-17.25	-18.10	-18.00
0.2	160.17	160.11	160.03	160.00	166.24	165.70	166.06	166.08	-18.04	-15.98	-16.87	-16.77
0.3	156.92	156.86	156.78	156.73	165.06	164.57	164.94	164.97	-24.17	-22.05	-22.84	-22.73
0.4	156.91	156.84	156.76	156.71	165.10	164.61	164.98	165.01	-24.33	-22.22	-23.00	-22.91
0.5	158.09	158.01	157.93	157.88	165.59	165.08	165.44	165.46	-22.27	-20.20	-21.01	-20.93
0.6	157.67	157.58	157.51	157.46	165.46	164.95	165.32	165.35	-23.14	-21.07	-21.86	-21.79
0.7	158.11	158.02	157.94	157.88	165.66	165.15	165.51	165.53	-22.45	-20.38	-21.18	-21.13
0.8	148.45	148.36	148.27	148.21	162.02	161.67	162.07	162.13	-40.31	-38.06	-38.61	-38.46
0.9	100.33	100.13	100.02	99.92	143.75	144.21	144.80	145.06	-129.01	-126.02	-125.29	-124.65
Avg.	150.66	150.58	150.49	150.44	162.75	162.36	162.76	162.81	-35.89	-33.69	-34.31	-34.15

Table A.12: *Thermodynamic parameters of HY, EGM, and VP during combustion.*

	ΔH (kJ/mol)				ΔG (kJ/mol)				ΔS (J/mol K)			
α	10°C/min	20°C/min	30°C/min	40°C/min	10°C/min	20°C/min	30°C/min	40°C/min	10°C/min	20°C/min	30°C/min	40°C/min
HY Stage I (135–374°C)												
0.1	126.42	126.35	126.27	126.23	150.63	151.08	150.28	152.27	-77.76	-76.24	-76.63	-77.07
0.2	147.97	147.90	147.84	147.79	159.73	159.86	159.71	160.87	-37.77	-36.87	-37.91	-38.73
0.3	146.92	146.83	146.78	146.71	159.35	159.50	159.32	160.51	-39.94	-39.05	-40.01	-40.85
0.4	129.37	129.28	129.21	129.13	152.08	152.48	151.77	153.63	-72.93	-71.52	-72.02	-72.54
0.5	114.37	114.27	114.20	114.10	145.86	146.48	145.33	147.76	-101.10	-99.29	-99.39	-99.63
0.6	99.07	98.95	98.84	98.75	139.51	140.36	138.75	141.75	-129.86	-127.64	-127.39	-127.31
0.7	87.39	87.26	87.12	87.03	134.67	135.69	133.73	137.18	-151.83	-149.30	-148.80	-148.47
0.8	78.41	78.28	78.11	78.01	130.96	132.12	129.89	133.68	-168.74	-165.97	-165.29	-164.79
0.9	70.00	69.85	69.66	69.55	127.49	128.77	126.29	130.40	-184.60	-181.61	-180.78	-180.13
Avg.	111.10	111.00	110.89	110.81	144.48	145.15	143.90	146.45	-107.17	-105.27	-105.36	-105.50
HY Stage II (374–830°C)												
0.1	58.09	57.87	57.63	57.50	159.76	167.52	167.75	174.90	-227.66	-227.33	-229.17	-229.44
0.2	55.04	54.79	54.52	54.37	158.82	166.65	166.79	174.02	-232.37	-231.92	-233.65	-233.83
0.3	51.73	51.44	51.15	50.98	157.79	165.69	165.74	173.05	-237.47	-236.88	-238.49	-238.55
0.4	46.54	46.21	45.86	45.69	156.12	164.15	164.04	171.48	-245.35	-244.53	-245.95	-245.84
0.5	40.68	40.29	39.88	39.71	154.23	162.40	162.12	169.71	-254.22	-253.16	-254.39	-254.07
0.6	35.49	35.04	34.56	34.36	152.55	160.85	160.42	168.14	-262.11	-260.85	-261.94	-261.45
0.7	31.01	30.49	29.93	29.72	151.12	159.53	158.97	166.80	-268.94	-267.53	-268.55	-267.91
0.8	26.86	26.26	25.60	25.37	149.81	158.32	157.63	165.57	-275.28	-273.78	-274.78	-274.00
0.9	23.07	22.38	21.59	21.36	148.62	157.21	156.42	164.46	-281.11	-279.55	-280.61	-279.65
Avg.	40.95	40.53	40.08	39.89	154.31	162.48	162.21	169.79	-253.84	-252.84	-254.17	-253.86
EGM Stage I (157–377°C)												
0.1	158.54	158.45	158.42	158.38	161.44	161.70	160.92	161.71	-10.11	-10.85	-8.19	-10.66
0.2	167.41	167.32	167.29	167.25	165.56	165.71	164.86	165.59	6.43	5.37	7.95	5.29
0.3	153.59	153.49	153.47	153.41	159.30	159.62	158.87	159.70	-19.91	-20.47	-17.70	-20.17
0.4	155.12	155.02	155.00	154.93	160.04	160.34	159.58	160.39	-17.14	-17.74	-15.00	-17.50
0.5	150.21	150.12	150.08	150.01	157.84	158.19	157.47	158.32	-26.57	-26.96	-24.18	-26.62
0.6	148.83	148.75	148.70	148.63	157.24	157.61	156.90	157.76	-29.31	-29.62	-26.84	-29.27
0.7	147.46	147.38	147.32	147.24	156.66	157.04	156.34	157.21	-32.06	-32.29	-29.53	-31.93
0.8	146.24	146.16	146.10	146.02	156.15	156.55	155.85	156.73	-34.52	-34.71	-31.92	-34.32
0.9	157.66	157.56	157.52	157.43	161.41	161.67	160.89	161.68	-13.08	-13.71	-11.04	-13.61
Avg.	153.90	153.81	153.77	153.70	159.52	159.83	159.07	159.90	-19.58	-20.11	-17.38	-19.86
EGM Stage II (377–708°C)												
0.1	164.46	164.30	164.26	164.21	195.67	197.22	195.74	195.71	-72.55	-74.89	-72.93	-73.06
0.2	165.88	165.72	165.68	165.62	196.26	197.81	196.35	196.33	-70.61	-73.01	-71.06	-71.24
0.3	164.29	164.12	164.09	164.01	195.71	197.26	195.79	195.76	-73.04	-75.40	-73.43	-73.62
0.4	128.48	128.27	128.20	128.11	182.39	183.83	181.88	181.63	-125.34	-126.41	-124.37	-124.12
0.5	97.66	97.41	97.29	97.18	170.93	172.27	169.92	169.47	-170.34	-170.34	-168.27	-167.67
0.6	79.15	78.86	78.69	78.56	164.07	165.34	162.76	162.19	-197.41	-196.79	-194.76	-193.97
0.7	65.99	65.66	65.42	65.27	159.20	160.43	157.67	157.03	-216.69	-215.65	-213.71	-212.80
0.8	56.69	56.32	56.02	55.86	155.77	156.98	154.10	153.40	-230.34	-229.04	-227.20	-226.22
0.9	48.74	48.33	47.97	47.78	152.85	154.03	151.05	150.30	-242.02	-240.52	-238.81	-237.77
Avg.	107.93	107.66	107.51	107.40	174.76	176.13	173.92	173.54	-155.37	-155.78	-153.84	-153.38
VP Stage I (156–377°C)												
0.1	151.41	151.33	151.27	151.26	160.40	158.91	158.19	159.01	-28.49	-23.74	-21.02	-23.40
0.2	155.90	155.81	155.74	155.74	162.31	160.81	160.03	160.86	-20.33	-15.67	-13.01	-15.44
0.3	144.69	144.60	144.53	144.51	157.79	156.30	155.67	156.49	-41.47	-36.62	-33.85	-36.14
0.4	145.80	145.71	145.63	145.61	158.28	156.79	156.14	156.96	-39.50	-34.67	-31.91	-34.23
0.5	147.10	147.02	146.93	146.91	158.84	157.35	156.68	157.50	-37.17	-32.35	-29.62	-31.96
0.6	147.92	147.83	147.74	147.72	159.20	157.71	157.03	157.86	-35.74	-30.93	-28.22	-30.56
0.7	143.74	143.65	143.55	143.54	157.53	156.04	155.42	156.24	-43.66	-38.79	-36.05	-38.31
0.8	136.02	135.93	135.82	135.80	154.41	152.94	152.43	153.23	-58.22	-53.24	-50.42	-52.57
0.9	127.90	127.80	127.69	127.65	151.14	149.68	149.28	150.07	-73.58	-68.48	-65.56	-67.64
Avg.	144.50	144.41	144.32	144.30	157.77	156.28	155.65	156.47	-42.02	-37.17	-34.41	-36.70
VP Stage II (377–650°C)												
0.1	123.48	123.38	123.25	123.19	172.13	177.83	180.23	178.54	-118.74	-133.08	-130.75	-130.49
0.2	121.16	121.05	120.91	120.87	171.30	176.90	179.38	177.64	-122.36	-136.50	-134.17	-133.85
0.3	120.12	120.00	119.85	119.81	170.94	176.50	179.01	177.26	-124.03	-138.10	-135.75	-135.43
0.4	109.98	109.83	109.67	109.63	167.16	172.28	175.15	173.17	-139.58	-152.63	-150.26	-149.80
0.5	93.08	92.90	92.70	92.67	160.84	165.22	168.69	166.35	-165.40	-176.75	-174.37	-173.68
0.6	81.20	80.99	80.77	80.74	156.40	160.27	164.16	161.56	-183.56	-193.75	-191.36	-190.52
0.7	77.05	76.82	76.58	76.55	154.88	158.56	162.60	159.91	-189.97	-199.79	-197.38	-196.52
0.8	76.47	76.22	75.98	75.94	154.70	158.36	162.42	159.72	-190.95	-200.77	-198.35	-197.49
0.9	77.47	77.19	76.97	76.91	155.13	158.84	162.86	160.18	-189.55	-199.56	-197.08	-196.28
Avg.	97.78	97.60	97.41	97.37	162.61	167.19	170.50	168.26	-158.24	-170.10	-167.72	-167.11

A.3 Supplementary material Chapter 5

Supplementary material *Section 5.1*

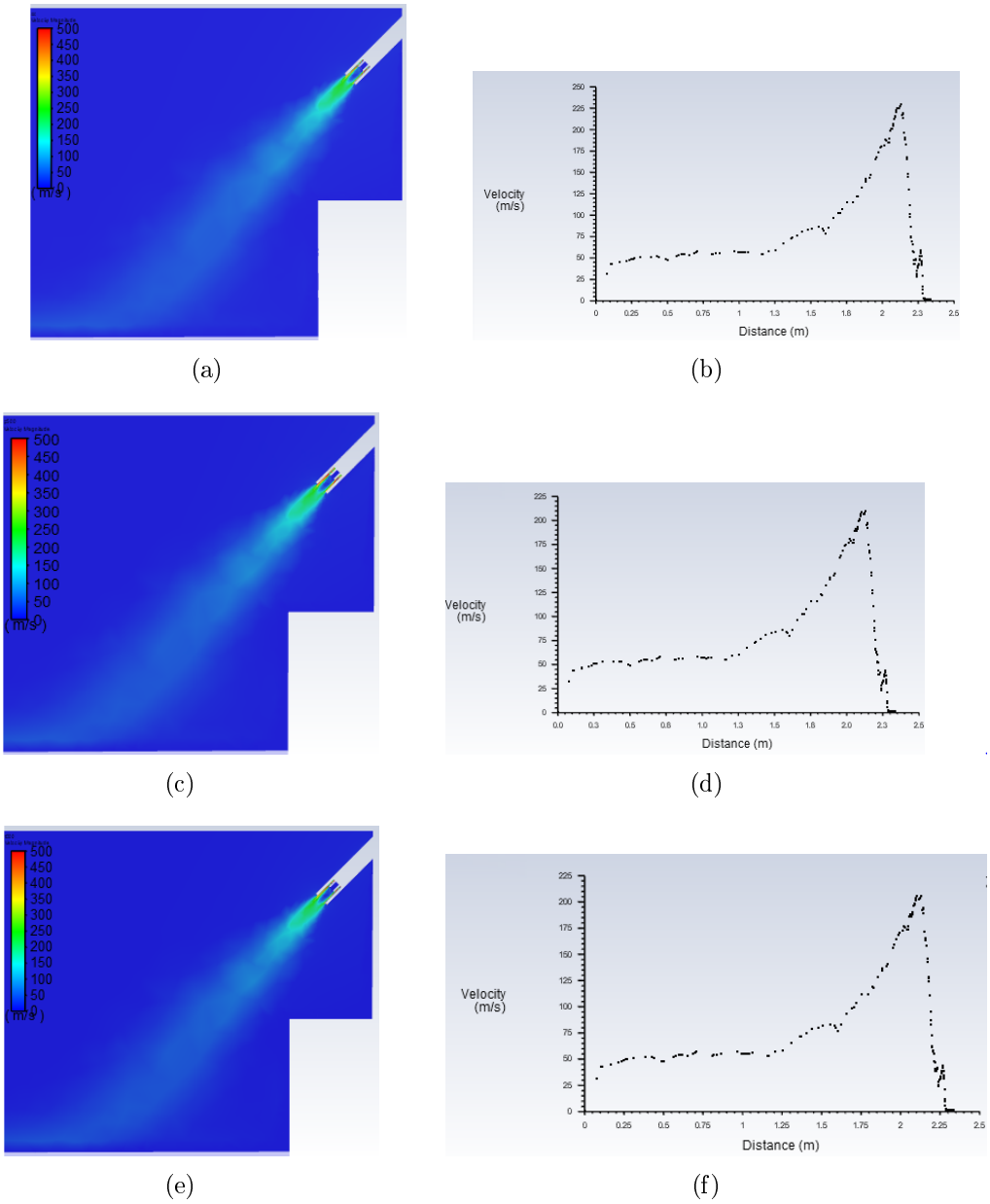

Figure A.11: *Velocity magnitude and velocity distribution profile for anthracite (a,b), P500 (c,d) and T300 (e,f).*

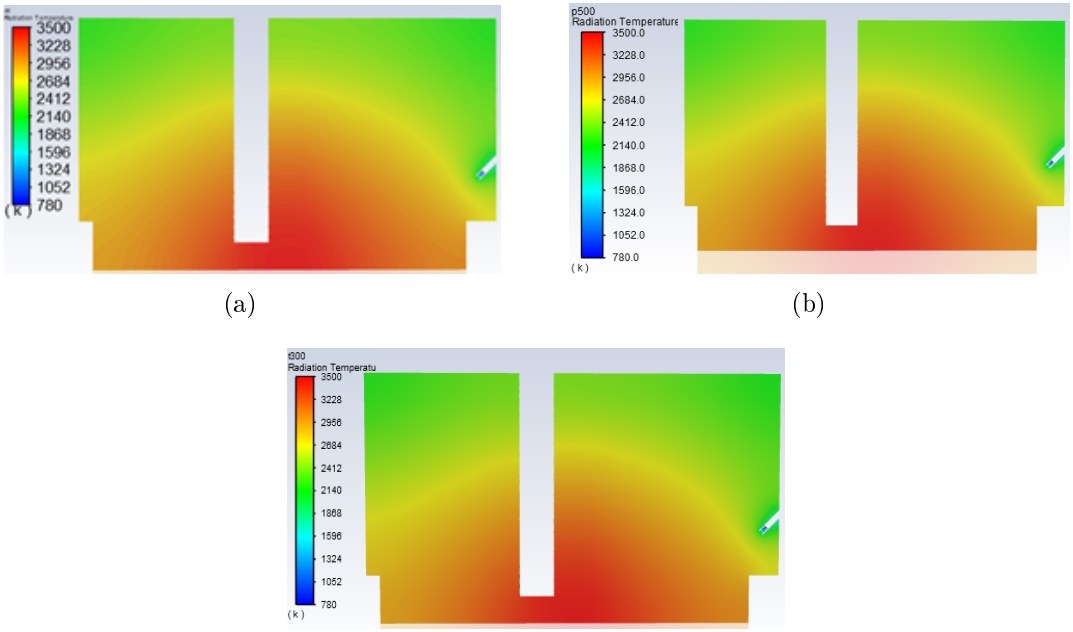

Figure A.12: *Radiation temperature profile for anthracite (a), P500 (b) and T300 (c).*

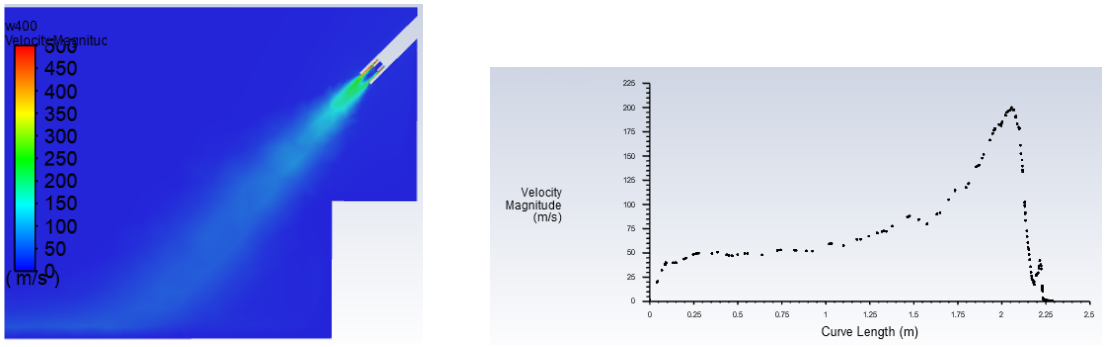

Figure A.13: *Velocity magnitude a) and velocity distribution profile b) for W400.*

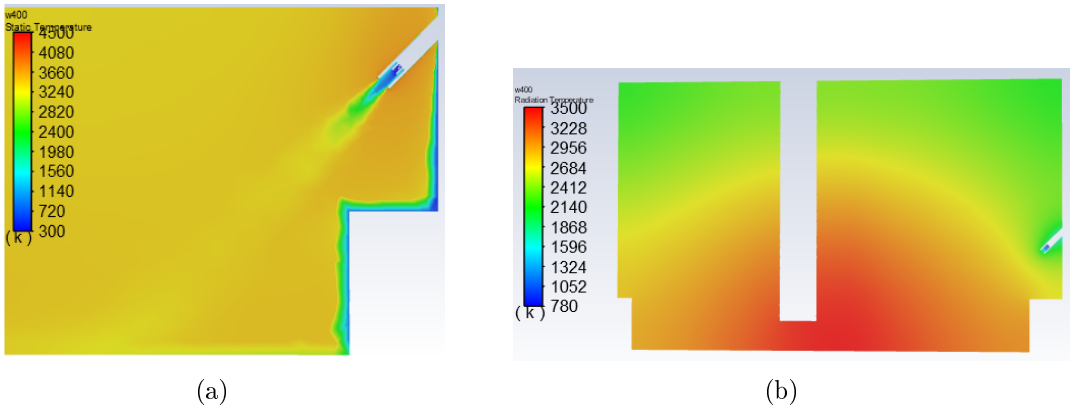

Figure A.14: *Static temperature a) and radiation temperature profile b) for W400.*

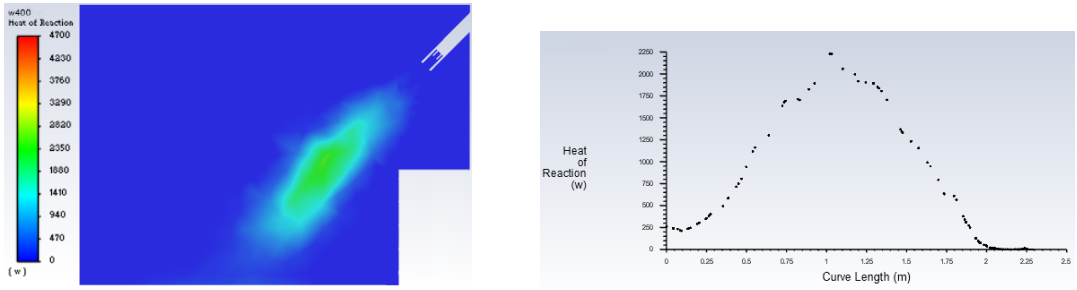

(a) (b)

Figure A.15: *Static temperature a) and radiation temperature profile b) for W400.*

Supplementary material *Section 5.2*

Table A.13: *Characterisation impact results of the production and usage of hydrochar.*

Impact category	Unit	Ereact	Estirr	Efiltration	Edryer	Emill	Epump	Anaerobic Digestion	Transport
Global warming	kg CO2 eq	2.71E+01	1.92E-02	7.56E-01	2.49E+00	5.07E-01	3.45E-02	1.32E+00	5.13E+00
Stratospheric ozone depletion	kg CFC11 eq	6.12E-06	1.24E-08	4.90E-07	5.63E-07	3.29E-07	2.24E-08	7.95E-07	3.61E-06
Ionizing radiation	kBq Co-60 eq	2.61E-02	1.63E-04	6.44E-03	2.40E-03	4.31E-03	2.94E-04	7.91E-03	4.15E-02
Ozone formation. Human health	kg NOx eq	1.74E-02	3.31E-05	1.30E-03	1.60E-03	8.73E-04	5.95E-05	1.79E-03	7.72E-03
Fine particulate matter formation	kg PM2.5 eq	4.84E-03	2.18E-05	8.59E-04	4.45E-04	5.75E-04	3.92E-05	1.18E-03	4.35E-03
Ozone formation. Terrestrial ecosystems	kg NOx eq	1.81E-02	3.37E-05	1.33E-03	1.66E-03	8.89E-04	6.06E-05	1.82E-03	8.15E-03
Terrestrial acidification	kg SO2 eq	1.43E-02	6.41E-05	2.52E-03	1.31E-03	1.69E-03	1.15E-04	3.44E-03	9.65E-03
Freshwater eutrophication	kg P eq	6.17E-05	7.73E-07	3.05E-05	5.67E-06	2.04E-05	1.39E-06	3.42E-04	6.38E-04
Marine eutrophication	kg N eq	6.20E-06	5.12E-08	2.02E-06	5.70E-07	1.35E-06	9.22E-08	9.90E-04	1.06E-05
Terrestrial ecotoxicity	kg 1.4-DCB	1.92E+00	6.02E-02	2.37E+00	1.76E-01	1.59E+00	1.08E-01	3.14E+00	7.62E+01
Freshwater ecotoxicity	kg 1.4-DCB	1.20E-03	6.52E-06	2.57E-04	1.10E-04	1.72E-04	1.17E-05	2.05E-03	1.27E-02
Marine ecotoxicity	kg 1.4-DCB	5.43E-02	4.46E-05	1.76E-03	4.99E-03	1.18E-03	8.03E-05	4.74E-03	5.81E-02
Human carcinogenic toxicity	kg 1.4-DCB	4.33E-02	2.46E-04	9.69E-03	3.98E-03	6.50E-03	4.43E-04	2.53E-02	6.23E-02
Human non-carcinogenic toxicity	kg 1.4-DCB	2.14E-01	4.45E-03	1.75E-01	1.97E-02	1.17E-01	8.01E-03	6.25E-01	1.45E+00
Land use	m2a crop eq	8.53E-02	5.47E-04	2.16E-02	7.85E-03	1.44E-02	9.85E-04	2.89E-02	2.39E-01
Mineral resource scarcity	kg Cu eq	6.77E-03	3.84E-05	1.51E-03	6.23E-04	1.01E-03	6.91E-05	3.30E-03	1.26E-02
Fossil resource scarcity	kg oil eq	1.12E+01	5.83E-03	2.30E-01	1.03E+00	1.54E-01	1.05E-02	2.98E-01	1.74E+00
Water consumption	m3	9.05E-03	3.48E-04	1.37E-02	8.32E-04	9.19E-03	6.27E-04	-1.36E-01	9.75E-03

Table A.14: Characterisation impact results of the production and usage of fossil coal.

Impact category	Unit	F-EAF	Anode	Argon	EAF converter	Ferrosilicon	Hard coal	Iron scrap	Natural gas	Nitrogen	Oxygen	Quicklime	Refractory	Electricity	EAF dust	EAF secondary metallurgy slag	EAF slag	Inert waste for final disposal
Global warming	kg CO2 eq	4.41E+01	2.98E+00	1.51E+00	4.90E+00	3.29E-01	5.49E+00	3.85E+01	4.84E+00	8.02E-01	1.33E+01	6.86E+01	2.94E+01	2.22E+02	4.83E+00	5.01E+00	4.76E+01	5.68E-02
Stratospheric ozone depletion	kg CFC11 eq	0.00E+00	2.39E-06	7.31E-07	1.42E-06	1.08E-05	1.47E-06	1.90E-05	5.90E-06	3.88E-07	6.43E-06	7.25E-06	7.06E-06	1.45E-04	7.49E-07	7.76E-07	7.26E-06	3.62E-08
Ionizing radiation	kBq Co-60 eq	0.00E+00	5.97E-02	5.57E-02	2.01E-02	2.23E-01	1.43E-02	3.91E-01	3.03E-03	2.93E-02	4.89E-01	1.54E-01	6.93E-02	1.90E+00	1.47E-02	1.32E-02	1.42E-01	6.45E-04
Ozone formation, Human health	kg NOx eq	8.99E-02	7.34E-03	2.72E-03	1.60E-02	9.06E-02	2.45E-02	2.50E-01	9.34E-03	1.50E-03	2.42E-02	4.24E-02	6.27E-02	3.72E-01	1.20E-02	1.25E-02	1.17E-01	4.33E-04
Fine particulate matter formation	kg PM2.5 eq	3.26E-02	5.90E-03	2.23E-03	1.03E-02	1.83E-01	1.32E-02	1.01E-01	3.80E-03	1.18E-03	1.96E-02	2.13E-02	2.77E-02	2.33E-01	3.98E-03	4.12E-03	3.90E-02	1.22E-04
Ozone formation, Terrestrial ecosystems	kg NOx eq	9.76E-02	7.64E-03	2.74E-03	1.66E-02	9.51E-02	2.47E-02	2.55E-01	1.00E-02	1.52E-03	2.44E-02	4.36E-02	6.39E-02	3.78E-01	1.22E-02	1.26E-02	1.19E-01	4.42E-04
Terrestrial acidification	kg SO2 eq	6.02E-02	1.58E-02	5.60E-03	3.00E-02	1.17E-01	4.11E-02	2.50E-01	1.16E-02	2.98E-03	4.93E-02	5.45E-02	5.23E-02	6.94E-01	9.80E-03	1.02E-02	9.59E-02	2.71E-04
Freshwater eutrophication	kg P eq	0.00E+00	9.81E-04	1.70E-04	3.40E-04	1.58E-03	1.60E-03	4.46E-03	3.52E-05	9.07E-05	1.50E-03	2.03E-03	4.20E-03	8.41E-03	2.42E-04	2.33E-04	2.23E-03	1.02E-05
Marine eutrophication	kg N eq	0.00E+00	4.62E-06	6.42E-06	7.25E-05	1.18E-04	2.22E-05	2.90E-04	5.31E-06	3.37E-06	5.60E-05	1.65E-05	6.43E-05	3.84E-04	5.53E-06	5.73E-06	5.42E-05	3.39E-07
Terrestrial ecotoxicity	kg 1,4-DCB	4.61E+02	4.67E+00	1.73E+00	4.45E+01	5.06E+01	5.25E+00	1.09E+03	1.03E+00	1.09E+00	1.61E+01	1.12E+02	3.53E+01	2.33E+02	1.08E+01	1.11E+01	1.00E+02	4.67E-01
Freshwater ecotoxicity	kg 1,4-DCB	1.37E-02	3.43E-03	5.68E-04	1.52E-02	1.64E-02	2.45E-03	8.39E-02	1.13E-03	2.96E-04	4.60E-03	8.79E-03	1.48E-00	4.80E-02	3.64E-01	7.39E-02	2.08E+01	9.31E-05
Marine ecotoxicity	kg 1,4-DCB	3.10E-01	1.36E-02	2.14E-03	4.30E-02	5.03E-02	6.69E-03	6.25E-01	1.13E-02	1.26E-03	1.94E-02	9.67E-02	2.06E-00	2.32E-01	5.48E-01	1.22E-01	3.12E+01	4.03E-04
Human carcinogenic toxicity	kg 1,4-DCB	1.04E-01	5.82E-02	1.35E-02	5.47E-01	4.87E-01	3.91E-02	1.25E+00	2.86E-02	6.79E-03	1.11E-01	1.00E-01	2.28E+00	1.24E+00	2.83E+01	6.01E+00	1.77E+03	7.15E-04
Human non-carcinogenic toxicity	kg 1,4-DCB	2.94E+01	3.32E-01	3.20E-01	3.03E+00	7.06E-00	2.98E-01	5.63E+01	1.10E-01	1.71E-01	2.82E-00	2.60E+00	7.25E+01	2.72E+01	5.06E+01	6.43E+00	7.24E+01	1.10E-02
Land use	m2a crop eq	0.00E+00	1.47E-01	4.60E-02	1.39E+00	7.21E-01	3.33E-01	4.55E+00	7.93E-02	2.23E-02	3.64E-01	3.48E-01	3.66E-01	5.07E+00	1.47E-01	1.52E-01	1.43E+00	-3.28E-03
Mineral resource scarcity	kg Cu eq	0.00E+00	4.25E-03	2.01E-03	1.16E-01	8.90E-02	6.43E-03	6.30E-01	5.30E-03	1.10E-03	1.78E-02	7.25E-03	7.64E-02	2.06E-01	1.83E-02	1.90E-02	1.81E-01	1.31E-04
Fossil resource scarcity	kg oil eq	0.00E+00	2.79E+00	4.09E-01	1.11E+00	9.08E+00	6.94E+00	1.14E+01	7.33E+00	2.15E+01	3.50E+00	6.45E+00	5.21E+00	6.76E+01	6.99E-01	7.24E-01	6.81E+00	3.00E-02
Water consumption	m3	4.25E+00	7.84E-03	8.35E-02	4.66E-02	1.93E-01	1.07E-02	2.30E-01	3.44E-03	4.41E-02	7.38E-01	3.30E-02	5.30E-02	3.96E+00	1.68E-02	1.75E-02	1.66E-01	1.12E-03

List of Figures

List of Tables

Acknowledgements

...